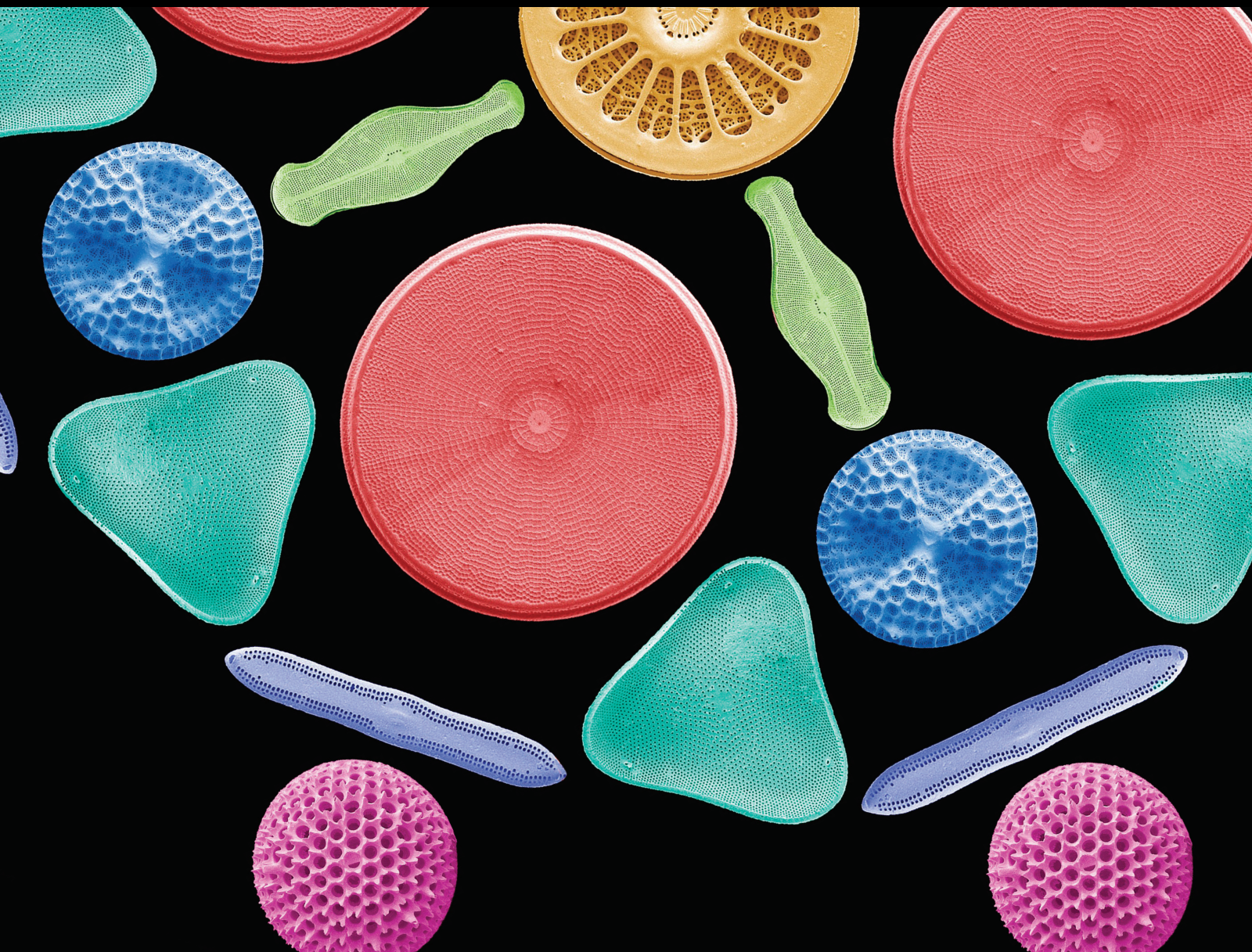


Scanning

Characterization of the Corroding Interface using Scanning Techniques

Lead Guest Editor: Jian Chen

Guest Editors: Yan Xin Qiao, James J. Noel, Peter G. Keech, and R. Matthew Asmussen





Characterization of the Corroding Interface using Scanning Techniques

Scanning

Characterization of the Corroding Interface using Scanning Techniques

Lead Guest Editor: Jian Chen


Guest Editors: Yan Xin Qiao, James J. Noel, Peter G.
Keech, and R. Matthew Asmussen




Chief Editor

Guosong Wu, China

Associate Editors


Richard Arinero , France

Daniele Passeri , Italy

Andrea Picone , Italy


Academic Editors

David Alsteens, Belgium


Igor Altfeder , USA

Jose Alvarez , France

Lavinia C. Ardelean , Romania

Renato Buzio , Italy

J. Chen, Canada

Ovidiu Cretu , Japan


Nicolas Delorme , France


Hendrix Demers , Canada

Jonathan R. Felts, USA


Marina I. Giannotti, Spain


Federico Grillo , United Kingdom


Anton V. Ievlev , USA

Heng Bo Jiang , China

Berndt Koslowski , Germany

Jessem Landoulsi , France


Jason L. Pitters , Canada

Michela Relucenti , Italy

Francesco Ruffino , Italy

Senthil Kumaran Selvaraj , India

Stefan G. Stanciu, Romania

Andreas Stylianou , Cyprus

Christian Teichert , Austria

Marilena Vivona , United Kingdom

Shuilin Wu, China

Contents

Stress Corrosion Cracking Behavior of TP 439 and 690 TT under Film-Forming Amine Environment

Lu Jundong , Jiang Xiaobin, Sun Ke, Liu Bin, Li Xinmin, and Ni Qinwen

Research Article (8 pages), Article ID 6668537, Volume 2021 (2021)

Theoretical and Experimental Analysis of Thin-Walled Curved Rectangular Box Beam under In-Plane Bending

Long Yanze , Zhang Ke, Shi Huaitao , Li Songhua, and Zhang Xiaochen 


Research Article (19 pages), Article ID 8867142, Volume 2021 (2021)

Prediction of Welding Deformation and Residual Stress of a Thin Plate by Improved Support Vector Regression

Lei Li , Di Liu, Shuai Ren, Hong-gen Zhou, and Jiasheng Zhou




Research Article (10 pages), Article ID 8892128, Volume 2021 (2021)

Establishment and Verification of Multiaxis Fatigue Life Prediction Model

Zhuo Fu , Xiang Li, Sha Zhang, Hanqing Xiong, Chi Liu, and Kun Li

Research Article (6 pages), Article ID 8875958, Volume 2021 (2021)

High-Temperature Oxidation Behavior of a Cu-Bearing 17Cr Ferritic Stainless Steel

Mengqi Zhang , Ying Han , Guoqing Zu, Jiapeng Sun, Weiwei Zhu, Hua Chen, and Xu Ran 




Research Article (11 pages), Article ID 8847831, Volume 2020 (2020)

Available Relevant Study on Stress Analysis and Static Strength Prediction of Fiber Metal Laminates

Xiaochen Zhang, Weiying Meng , Jiancheng Guo, and Yu Zhang

Review Article (13 pages), Article ID 8874830, Volume 2020 (2020)

Mechanical Properties and Failure Behavior of 3D-SiC_f/SiC Composites with Different Interphases

Deng-hao Ma , En-ze Jin, Jun-ping Li , Zhen-hua Hou , Jian Yin, Xin Sun, Jin-ming Fang, Xiaodong Gong, and Li-na Huang

Research Article (7 pages), Article ID 6678223, Volume 2020 (2020)

Influence of Oxidation Damages on Mechanical Properties of SiC/SiC Composite Using Domestic Hiconical Type SiC Fibers

Enze Jin, Denghao Ma, Zeshuai Yuan, Wenting Sun, Hao Wang, Jiajia Zhang, Xiaodong Gong, Lina Huang, Botao Han, Xin Sun, Zhihai Feng, and Junping Li 






Research Article (8 pages), Article ID 8840963, Volume 2020 (2020)

Characterization of the Microstructure and Bonding Properties of Zirconium-Carbon Steel Clad Materials by Explosive Welding

Hui Zhao 

Research Article (8 pages), Article ID 8881898, Volume 2020 (2020)

Effect of Double Transition Metal Salt Catalyst on Fushun Oil Shale Pyrolysis

Xiaoyang Liu , Haodan Pan , Chuang Guo , Xiaojing Di , and Hongxiang Hu 

Research Article (14 pages), Article ID 6685299, Volume 2020 (2020)

Effect of Iron Ion on Corrosion Behavior of Inconel 625 in High-Temperature Water

Huiling Zhou , Yipeng Chen , Yi Sui, Yunfei Lv , Zhiyuan Zhu , Lanlan Yang, Zhen He , Chengtao Li, and Kewei Fang




Research Article (8 pages), Article ID 9130362, Volume 2020 (2020)

Quality Prediction and Control of Assembly and Welding Process for Ship Group Product Based on Digital Twin

Lei Li , Di Liu, Jinfeng Liu, Hong-gen Zhou, and Jiasheng Zhou

Research Article (13 pages), Article ID 3758730, Volume 2020 (2020)

Corrosion Resistance of Waterborne Epoxy Resin Coating Cross-Linked by Modified Tetrabutyl Titanate

Lingli Xu , Zheng Chen, Fei Huang, Yinze Zuo, Xingling Shi , and Xiaowei Zhou 


Research Article (9 pages), Article ID 1392385, Volume 2020 (2020)

The Effects of Sand Particles on the Synergy of Cavitation Erosion-Corrosion of MIG Welding Stainless Steel Coating in Saline Water

Haodan Pan , Jun Tao, Meng E, Hongxiang Hu , and Zhengbin Wang

Research Article (10 pages), Article ID 8876406, Volume 2020 (2020)

Microstructure, Mechanical Properties, and Residual Stress Distribution of AISI 316L Stainless Steel Part Fabricated by Laser Metal Deposition

Jiayang Gu, Ruifeng Li , Yi Qiu, Hangyu Yue, Bin Liu, and Heng Gu

Research Article (10 pages), Article ID 4831798, Volume 2020 (2020)

Research Article

Stress Corrosion Cracking Behavior of TP 439 and 690 TT under Film-Forming Amine Environment

Lu Jundong¹, Jiang Xiaobin,¹ Sun Ke,² Liu Bin,¹ Li Xinmin,¹ and Ni Qinwen¹

¹Suzhou Nuclear Power Research Institute, Suzhou, 215800 Jiangsu, China

²Guangdong Nuclear Power Joint Venture Co., Ltd., Shenzhen, 518000 Guangdong, China

Correspondence should be addressed to Lu Jundong; lujundong@cgnpc.com.cn

Received 3 October 2020; Accepted 18 May 2021; Published 9 June 2021

Academic Editor: Jian Chen

Copyright © 2021 Lu Jundong et al. This is an open access article distributed under the Creative Commons Attribution License, which permits unrestricted use, distribution, and reproduction in any medium, provided the original work is properly cited.

Film-forming amines have been widely used in thermal power plants for maintenance after shutdown, and there are more and more applications and researches in nuclear power secondary circuits for this purpose. However, in the direction of stress corrosion cracking, there is not much research on the influence of film-forming amines on metal materials. This article uses the high temperature slow strain rate test (SSRT) method to evaluate the influence of a commercial film-forming amine on the stress corrosion cracking behavior of two conventional island materials for PWR nuclear power plants. These two metal materials are the heat exchange tube materials of the high-pressure heater and steam generator in the high-temperature operation area of the secondary circuit of a nuclear power plant: TP 439 stainless steel and 690 TT alloy. The test analyzed the mechanical properties and fracture morphology. The test results show that in the test concentration range (<5 mg/kg), the film-forming amine will not affect the SCC of TP 439 stainless steel and 690 TT alloy under the condition of slow strain rate. The behavior has a significant impact. In practical applications, the general dosage of film-forming amine is 1-2 mg/kg. This data is lower than the film-forming amine concentration used in the experiment. Therefore, there is no need to worry about the obvious impact on the SCC behavior of TP 439 stainless steel and 690 TT alloy.

1. Introduction

Film-forming amine (FA) is a specific chemical which can form a hydrophobic layer on the metal surface in liquid or vapor phase. This type of chemicals usually contains a primary, secondary, or tertiary amine structure (or a combination thereof) linked to a hydrocarbon chain, usually with more than 10 carbon atoms, such as octadecylamine and oleyl-1,3-propanediamine. Commercial film-forming amine products (FAP) are simply a FA (or multiple), or a compound formed by the dispersion and mixing of a FA (or multiple) and other chemicals.

Presently, in the thermal power industry, the utilization of FAPs into implementing medium- and long-term boiler maintenance after shutdown has become one of the main maintenance methods [1, 2]. The operating experiences of many thermal power plants showed that the shutdown protection of FAPs can effectively reduce the corrosion rate dur-

ing the shutdown period. The unit has the following advantages after startup: water quality qualified time is shortened and start-up time is shortened.

In the nuclear power industry, there is almost no relevant literature reported. Since 2011, the successful utilization of FAP (ODACON) in Almaraz 1/2# units has attracted the attention of researchers [3, 4]. As a new choice of water chemistry methods to reduce corrosion rate, research institutions that are at the forefront of research in the nuclear power industry have started corresponding research plans.

The published literatures study the physical and chemical properties of FAs [4–7], dissociation constant and distribution coefficient [8, 9], reaction mechanism and influence on metal materials [10–16], the influence on the chemical parameters in the loop such as pH and conductivity [17–20], the decomposition products [18, 21], the influence on the heat exchange performance [22–26], and

TABLE 1: The chemical compositions of TP 439 SS and 690 TT alloy (wt%).

Element	Ni	Cr	Fe	C	Si	Mn	P	S	N	Al	Ti	Cu
690 TT	59.83	30.39	9.88	0.023	0.07	0.22	0.006	0.002	0.02	/	/	/
TP 439	0.247	17.84	81.06	0.014	0.179	0.262	0.025	0.0015	0.020	0.028	0.278	0.079

the influence on the online chemical instrument detection [27]. However, there is not much research work on the stress corrosion cracking behavior of materials at sensitive locations in the FA environment [28]. This article is conducting related research work, using a commercial FA that has been applied on the secondary circuit side of a PWR nuclear power plant for evaluation. The test metal material is the heat exchange tube material of the high-pressure heater and steam generator in the high-temperature operation area of the secondary circuit of a nuclear power plant: TP 439 stainless steel and 690 TT alloy. Different from the information [28], the evaluation in this paper is completed by the high temperature slow strain rate test (SSRT) method.

2. Experimental

The materials used in present work is TP 439 stainless steel (SS) and 690 TT alloy. The chemical compositions of TP 439 SS and 690 TT are shown in Table 1. Figure 1 shows the microstructure morphology of 690 TT alloy. The structure of 690 TT alloy presents a typical equiaxed austenite type, with carbides distributed continuously at the grain boundaries. Table 2 shows the components of the 690 TT used. The slow strain rate test (SSRT) tests for TP 439 SS and 690 TT were conducted in simulated secondary water environment according to the GB/T 15970.7-2000.

The size of the sample is shown in Figure 2. Prior to the test, the samples were cleaned in ethanol using an ultrasonic cleaner, then dried and sealed for later use. The SSRT tests were conducted using the American CORTEST high-temperature and high-pressure slow strain rate tensile tester.

The strain rate for TP 439 SS and 690 TT is 1×10^{-6} /s and 5×10^{-7} /s, respectively.

The chemical environment of each test are shown in Table 3.

3. Results and Discussion

3.1. Analysis of Mechanical Properties. The main principle of macroscopic evaluation of SCC sensitivity is that SCC will cause a significant decrease in material plasticity indicators, such as the material's maximum breaking stress, total elongation, reduction of area, and fracture absorption energy (area under the load-elongation curve). Comparing the same sample exposed to the test environment and exposed to the inert environment, the farther the ratio deviates, the higher the cracking sensitivity.

$$I_{\text{sc}} = \left(1 - \frac{t_0 - t}{t_0}\right) \times 100\%. \quad (1)$$

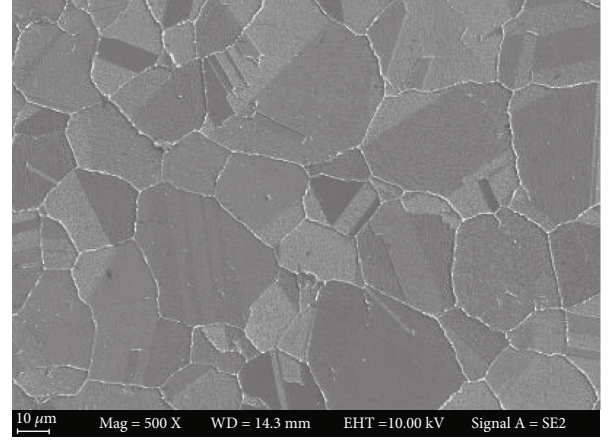


FIGURE 1: The SEM microstructure of 690 TT alloy. FA: a commercial FA product; emulsion, 1% content.

In the formula I_{sc} represents the stress corrosion cracking sensitivity index of the sample, t_0 is the test result of the sample in an inert medium, and t is the test result of the sample in the test environment.

Since the fracture absorption energy of the sample is the area under the load-elongation curve, which contains two parameters of load and elongation, it is relatively comprehensive, so the fracture absorption energy is used to calculate the stress corrosion sensitivity index of the material in different environments. From the calculation results, the stress corrosion sensitivity of TP 439 SS and 690 TT alloy is basically the same in FA and non-FA environments. The use of FAs will not significantly affect the SCC behavior of TP 439 SS and 690 TT alloy under slow strain rate conditions.

The stress-strain curve of TP 439 SS in FA, non-FA, and argon atmosphere is plotted in Figure 3. As is seen in the figure, the stress and strain of TP 439 SS in the three environments have all undergone elastic deformation \rightarrow yield \rightarrow plastic deformation \rightarrow reach tensile strength \rightarrow fracture process. The slow strain rate test data of the sample is listed in Table 3. The stress-strain curves of TP 439 SS in the two environments are basically the same and lower in compared with that in the inert gas argon, so the TP 439 SS has the susceptibility to stress corrosion cracking.

The stress-strain curves of 690 TT alloy in FA, non-FA, and argon atmosphere are plotted in Figure 4. As is seen in Figure 3, it is obvious that the stress corrosion sensitivity of 690 TT alloy is basically equal in the FA and non-FA environments. Alloy 690 TT also has the susceptibility to stress corrosion cracking.

TABLE 2: The mechanical properties obtained from the SSRT test.

Material	Environment	Temperature $T/^{\circ}\text{C}$	Maximum tensile strength σ_b/MPa	Elongation rate $A/\%$	Rate of reduction in area $Z/\%$	Absorption area before fracture	Sensitivity index I_{SCC}^*
TP 439	FA	260	388	21.9	48.6	91	6%
TP 439	Non-FA	260	388	11.4	53.6	89	8%
TP 439	Argon	260	412	27.1	89.1	97	/
690 TT	FA	284	570	45.4	70.6	245	9%
690 TT	Non-FA	284	568	39.0	68.8	242	11%
690 TT	Argon	284	661	45.4	53.8	272	/

*The stress corrosion sensitivity index is calculated based on the fracture absorption energy.

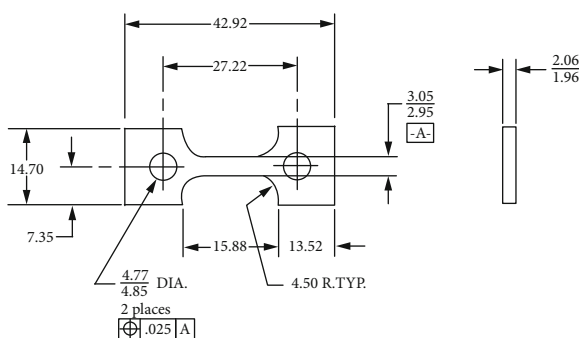


FIGURE 2: SSRT test specimen size (mm).

TABLE 3: The SSRT test parameters.

Material	Environment
TP 439 SS	FA 260°C, DO < 10 µg/kg, 3.5 mg/kg NH ₃ pH 9.7, FA 5 mg/kg
	FA-free 260°C, DO < 10 µg/kg, 3.5 mg/kg NH ₃ pH 9.7
	Argon Inert gas environment
690 TT	FA 284°C, DO < 10 µg/kg, 3.0 mg/kg NH ₃ pH 9.52, FA 5 mg/kg
	FA-free 284°C, DO < 10 µg/kg, 3.0 mg/kg NH ₃ pH 9.52
	Argon Inert gas environment

3.2. Fracture Morphology Analysis

3.2.1. Analysis of the Fracture Surface of TP 439 Stainless Steel. Figures 5–7 show the morphology of the TP 439 SS in FA, non-FA, and argon, respectively. The fracture shows obvious necking, and it present a large number of dimples with holes, which do not make much difference. It shows that the use of FAs will not significantly affect the SCC behavior of TP 439 stainless steel, and the fracture is a ductile fracture, which is consistent with the results of its fracture mechanics performance curve.

3.2.2. Fracture Morphology Analysis of 690 TT Alloy. Figures 8–10 are the fracture morphologies of 690 TT alloy in FA, non-FA, and argon atmosphere, respectively. The fracture morphology of 690 TT alloy in the two environments is similar to that of the inert medium, and there is no obvious difference. Microscopically, to a certain

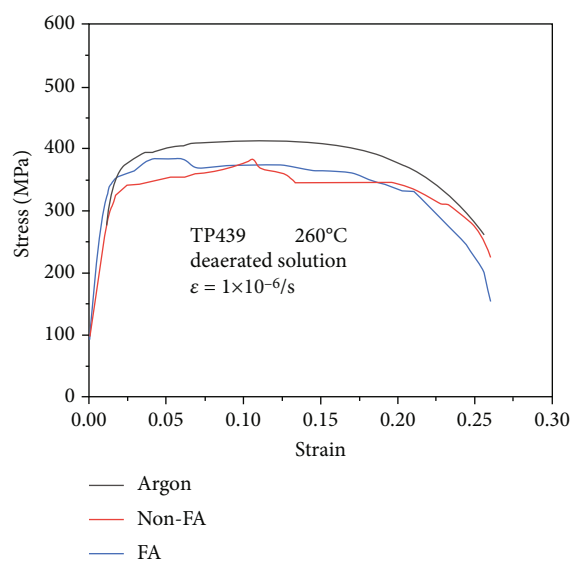


FIGURE 3: The stress-strain curves of TP 439 SS in different environments.

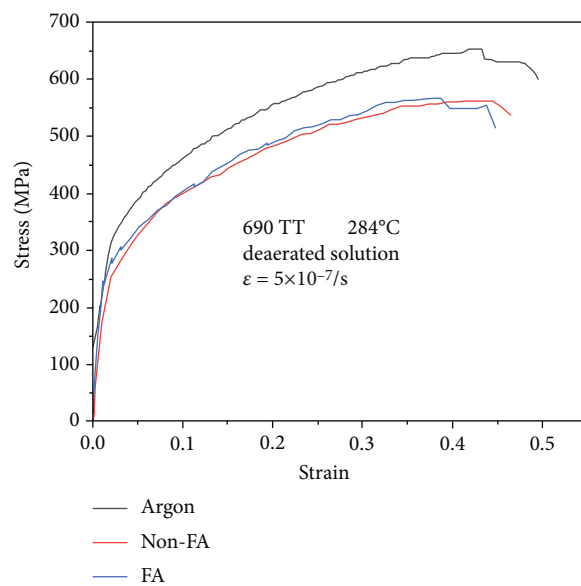


FIGURE 4: The stress-strain curves of 690 TT alloy in different environments.

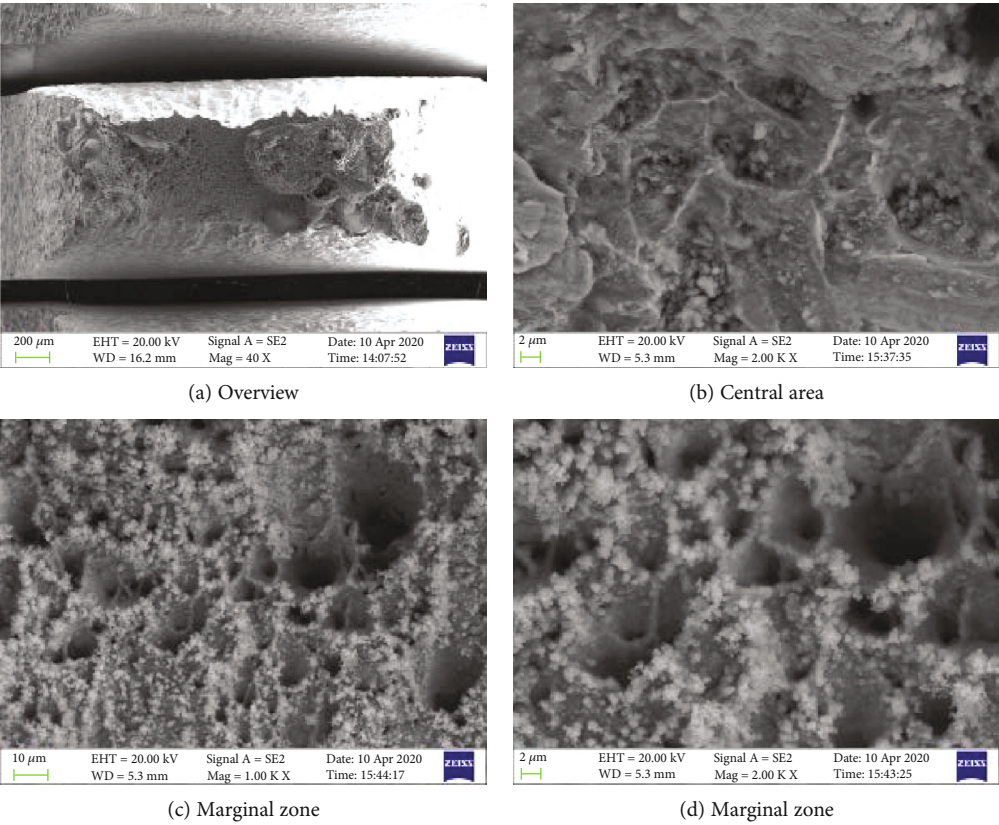


FIGURE 5: The fracture morphologies for TP 439 SS after SSRT test solution with FA.

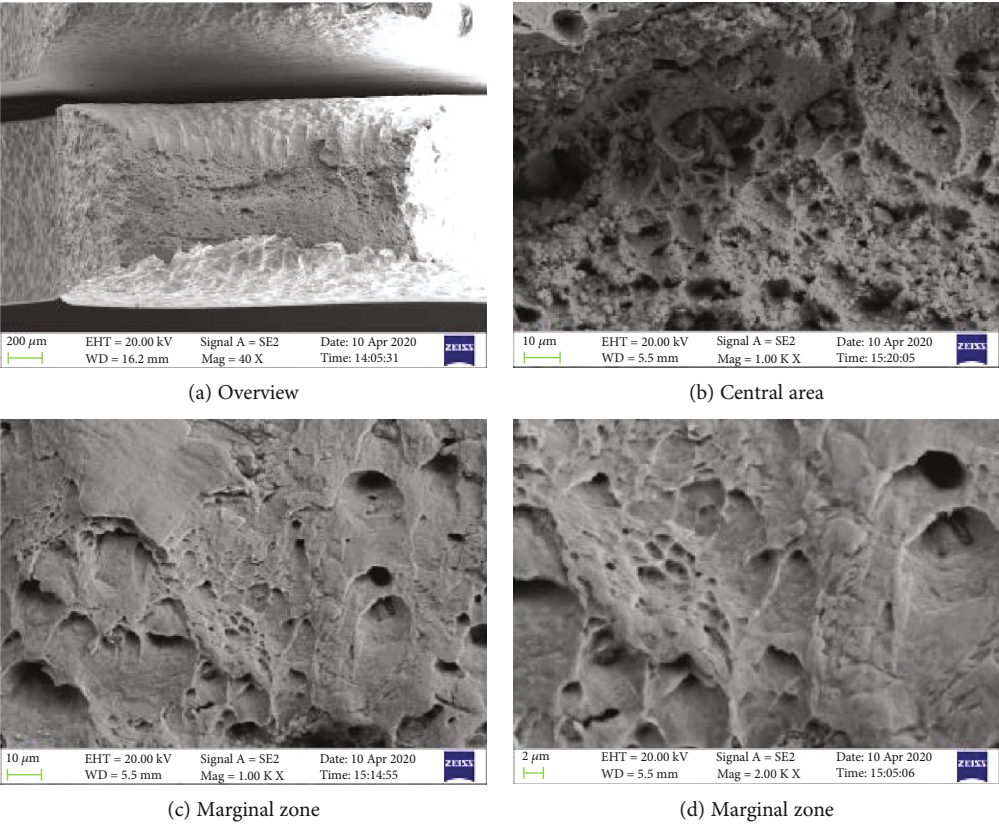


FIGURE 6: The fracture morphologies for TP 439 SS after SSRT test solution without FA.

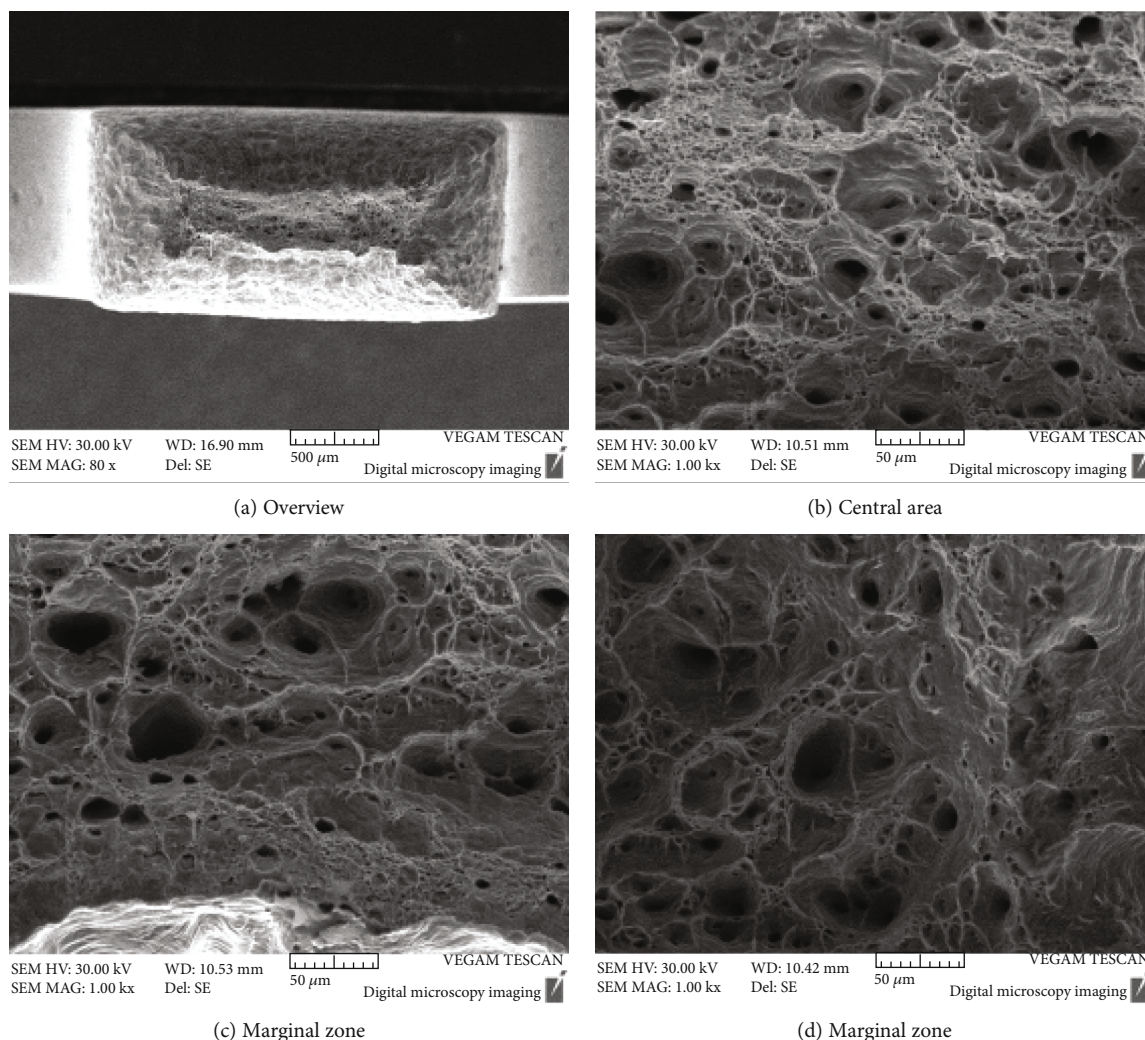


FIGURE 7: The fracture morphologies for TP 439 SS after SSRT in argon atmosphere.

extent, the fracture surface shows a mixed morphology of intergranular cracking and dimples. The reason for the intergranular cracking of 690 TT alloy is the TT treatment in the manufacturing process, which makes the 690 TT alloy grain boundary distribute a layer of continuous carbide $M_{23}C_6$, as shown in Figure 7, so it will show a certain degree of intergranularity under tensile stress. The cracking characteristics are not the appearance of intergranular stress corrosion cracking, which can be proved by the fracture in the argon atmosphere. Therefore, combined with the stress-strain curve of Figure 3, the 690 TT alloy does not exhibit stress corrosion characteristics in FA and non-FA environments.

4. Discussion

The test selected a commercial FA, as well as the heat exchange tube materials of the high-pressure heater and steam generator in the high-temperature operation area of a nuclear power plant: TP 439 stainless steel and 690 TT alloy. And the high-temperature slow strain rate test

(SSRT) method was used to evaluate the effect of the FA on the stress corrosion cracking behavior of two metal materials. The test analyzes both mechanical properties and fracture morphology. The test results show that the fracture absorption energy of the sample is basically the same in FA and non-FA environments, so the FA used in the test will not significantly affect the SCC behavior of TP 439 stainless steel and 690 TT alloy under slow strain rate conditions within the test concentration range.

According to the existing practical application in the secondary circuit of nuclear power, the general dosage of FA is 1-2 mg/kg. This data is lower than the FA concentration used in the experiment. That is to say, from the practical application point of view, when the application concentration of FA is lower than 5 mg/kg, the test FA will not significantly affect the SCC behavior of TP 439 stainless steel and 690 TT alloy under slow strain rate conditions. Perhaps, this FA will have an impact on the SCC behavior of TP 439 stainless steel and 690 TT alloy, so the value of 5 mg/kg has not reached the threshold for this effect. This requires further research.

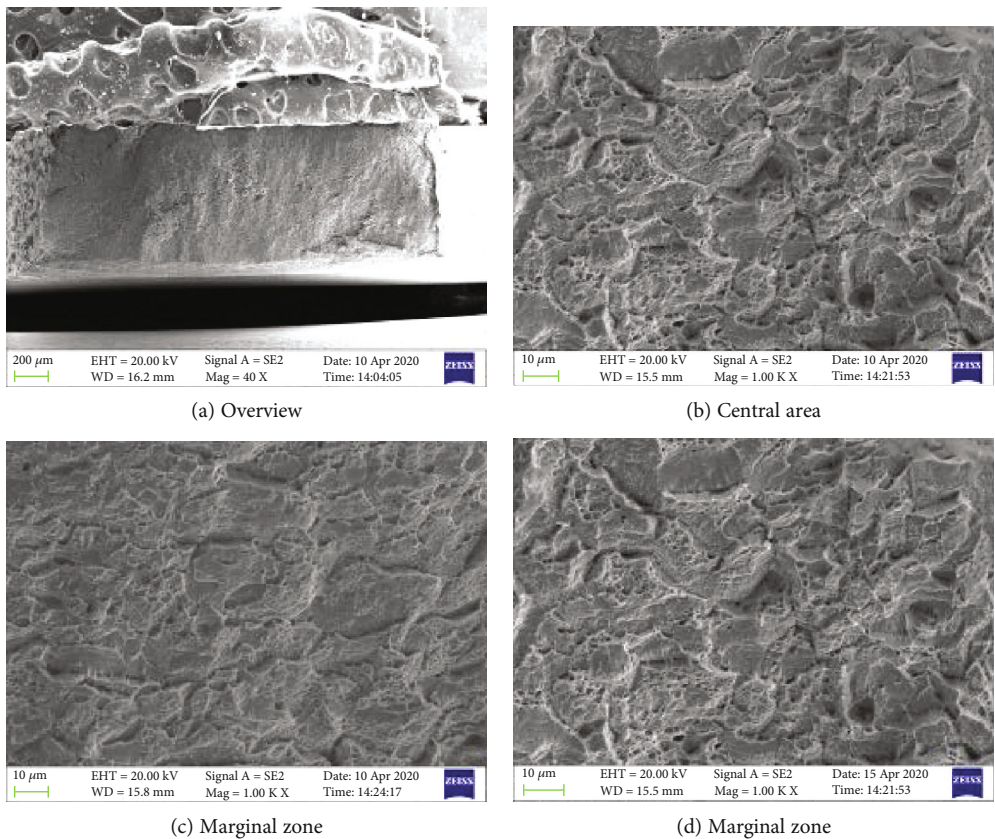


FIGURE 8: High temperature SSRT test fracture of 690 TT in the environment with FA.

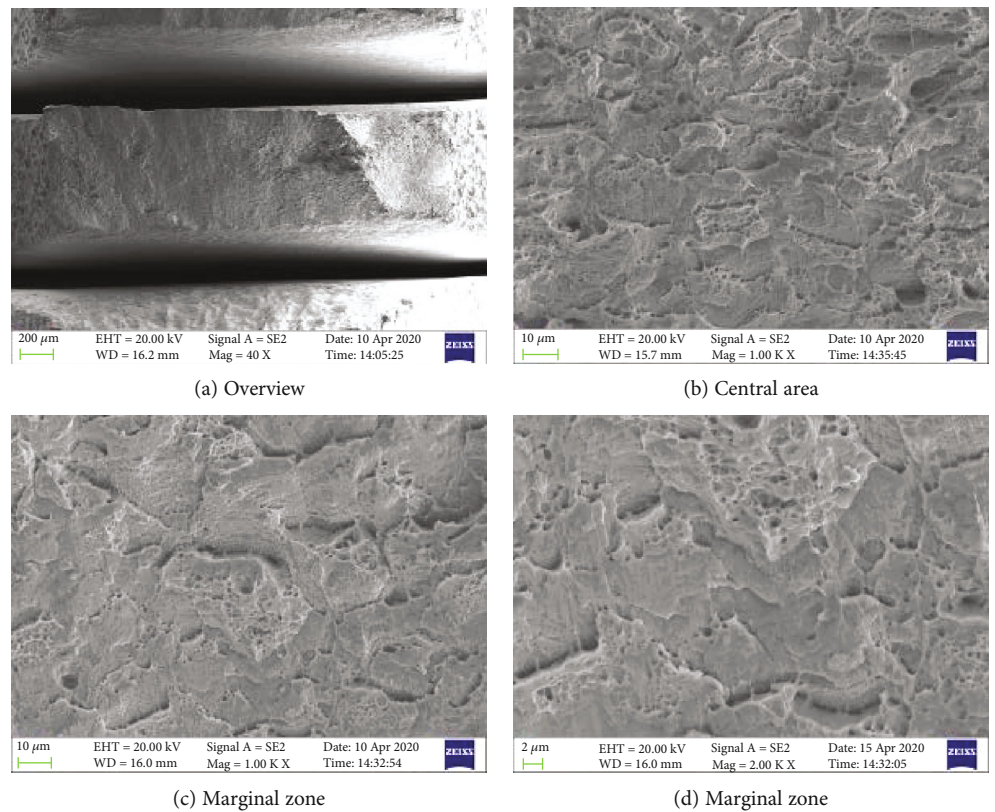


FIGURE 9: High temperature SSRT test fracture of 690 TT in the environment without FA.

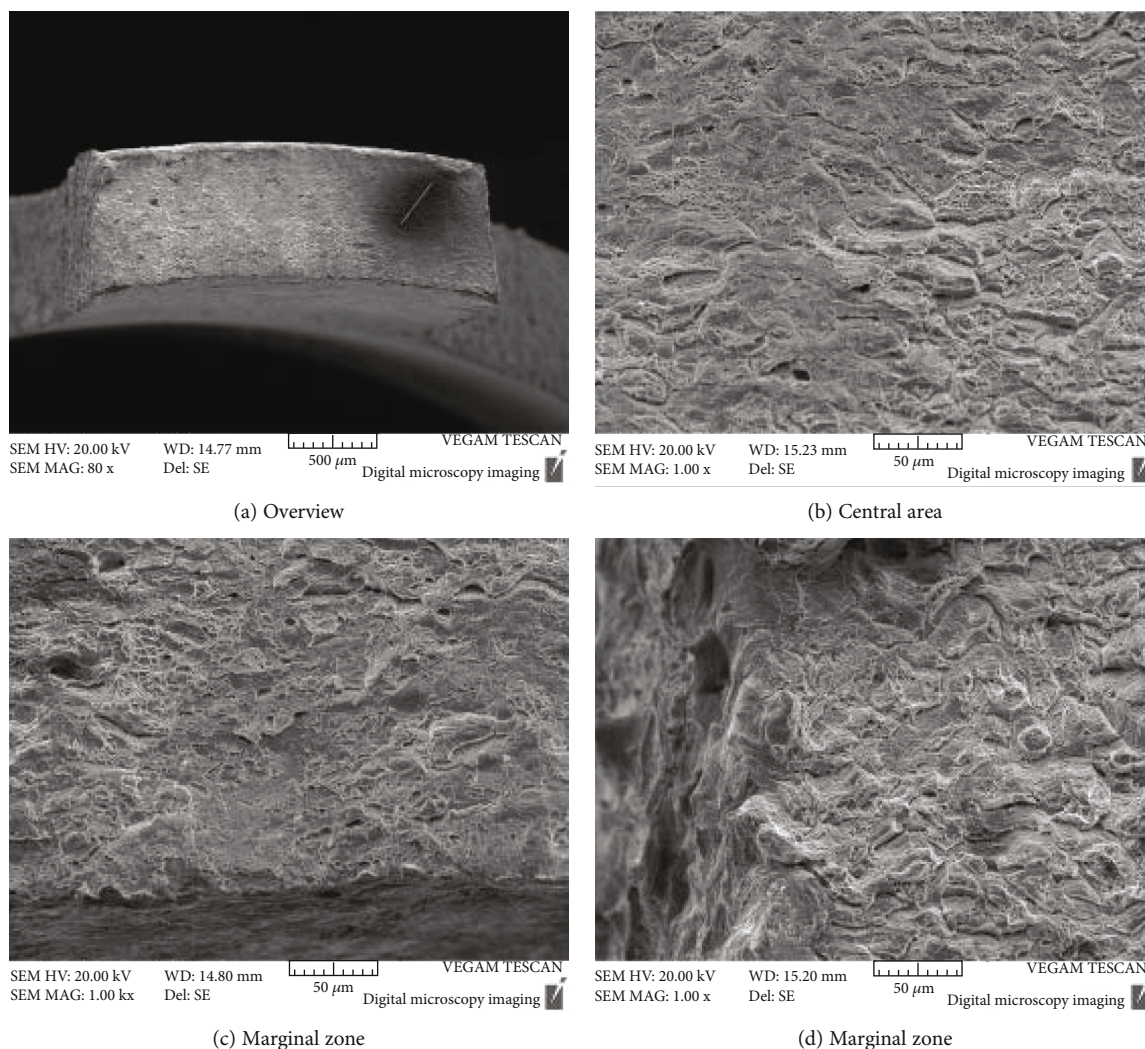


FIGURE 10: High temperature SSRT test fracture of 690 TT alloy under argon.

5. Conclusion

The test adopted the SSRT method. Under the environment of 5 mg/kg FA, SCC evaluation was carried out on two materials of TP 439 stainless steel and 690 TT alloy. The test results indicated that:

- (1) Under the condition of slow strain rate, the stress corrosion behavior of the two materials is relatively consistent in the two environments of FA and non-FA, and neither shows obvious stress corrosion sensitivity
- (2) Under the test conditions, the FA (<5 mg/kg) will not significantly affect the SCC behavior of TP 439 stainless steel and 690 TT alloy under the condition of slow strain rate
- (3) In actual application, the general dosage of FA is 1-2 mg/kg. This data is lower than the FA concentration used in the experiment. Therefore, there is no need to worry about the obvious impact on the SCC behavior of TP 439 stainless steel and 690 TT alloy

Data Availability

The data used to support the findings of this study are available from the corresponding author upon request.

Conflicts of Interest

The authors declare that they have no conflicts of interest.

References

- [1] J. Savelkoul and R. Van Lier, "Operational experience with organics in industrial steam generation," *Power Plant Chemistry*, vol. 7, no. 12, pp. 733-739, 2005.
- [2] E. V. Chernyshev, E. N. Veprov, V. A. Petrov et al., "Increasing the corrosion resistance of equipment due to the use of film-forming amines," *Power Technology and Engineering*, vol. 40, no. 1, pp. 34-37, 2006.
- [3] M. I. Mendizabal, C. B. Herrera, A. Barrera et al., "Film forming amine application at Embalse nuclear power plant refurbishment outage," in *EPRI SGMP 2016 Steam Generator Secondary Side Management Conference*, Orlando, FL, 2016.

- [4] U. Ramminger, *Film Forming Amines: Chemical Qualification*, AREVA GmbH, Erlangen, Germany, 2016.
- [5] Z. H. Tian, L. J. Song, K. W. Fang, G. X. Lin, and H. L. Zhou, "Corrosion behavior of 304L stainless steel in a B-Li coolant for a nuclear power plant," *Materiali in Tehnologije*, vol. 53, no. 5, pp. 643–647, 2019.
- [6] Y. X. Qiao, Y. P. Chen, L. L. Li et al., "Corrosion behavior of a nickel-free high-nitrogen stainless steel with hydrogen charging," *JOM*, vol. 73, no. 4, pp. 1165–1172, 2021.
- [7] H. Topp, *On the Interaction of Chemically Conditioned Water with Steel Heating Surfaces During Saturated Pool Boiling-an Experimental Thermotechnical Approach*, [Ph.D. thesis], University of Rostock, Rostock, Germany, 2010.
- [8] A. Drexler, V. Schneider, and J. Fandrich, "Chemistry related on-line monitoring of PWRs," *Power Plant Chemistry*, vol. 12, no. 12, pp. 700–707, 2010.
- [9] S. Choi, *Pressurized water reactor secondary side filming amine application:scoping assessment*, EPRI,3002008187, pp. 2–21, 2016.
- [10] S. A. Cao, J. Y. Hu, J. L. Xie, Q. Q. Liang, and L. Yin, "Research on the film-forming characteristics of octadecylamine at high temperatures," *Anti-Corrosion Methods and Materials*, vol. 60, no. 1, pp. 14–19, 2013.
- [11] H. H. Ge, G. D. Zhou, Q. Q. Liao, Y. G. Lee, and B. H. Hoo, "A study of anti-corrosion behavior of octadecylamine-treated iron samples," *Applied Surface Science*, vol. 156, no. 1-4, pp. 39–46, 2000.
- [12] W. Zhang, A. de Bache, and T. Petrick, "Dry lay-up of steam generators with film-forming amines:studies and field experiences," *Power Plant Chemistry*, vol. 16, no. 5, pp. 284–292, 2014.
- [13] M. Kreider, *Notice Regarding the Technical Meeting on AREVA's Filming Amine at DEI on August 10-11, 2016*, DEI Memo No. M-5711-00-01, Dominion Engineering, Inc., Reston, VA, 2016.
- [14] D. Disci-Zayed, J. Jasper, and W. Hater, "Adsorption of oleyl propylenediamine on metal surfaces," *Power Plant Chemistry*, vol. 21, no. 3, pp. 146–154, 2019.
- [15] N. Voges and W. Hater, "Distribution ratio and average surface coverage of film forming amines," *Powe Plant Chemistry*, vol. 12, no. 3, pp. 132–138, 2010.
- [16] J. W. Wu, Y. X. Qiao, Y. Chen, L. L. Yang, X. Z. Cao, and S. X. Jin, "Correlation between corrosion films and corrosion-related defects formed on 316 stainless steel at high temperatures in pressurized water," *Journal of Materials Engineering and Performance*, vol. 30, 2021.
- [17] W. Hater, B. Smith, P. McCann, and A. de Bache, "Experience with the application of a film forming amine in the connah's quay triple stage combined cycle gas turbine power plant operating in cycling mode," *Power Plant Chemistry*, vol. 20, no. 3, pp. 136–144, 2018.
- [18] X. J. Zhang, Y. Li, Y. Q. Deng, R. T. Ni, and D. D. Qi, "Effects of lay-up protective agent on water and steam cation conductivity," *Electric Power*, vol. 48, no. 1, pp. 60–63, 2015.
- [19] W. Hater and D. Olivet, "The chemistry and properties of organic boiler feed water additives based on film-forming amines and their use in steam generators," in *PREPRINT – ICPWS XV*, Berlin, 2008.
- [20] W. Hater and A. de Bache, "Considerations on conductivity and pH in water/steam cycles using organic cycle chemistry," *Power Plant Chemistry*, vol. 15, no. 4, pp. 289–301, 2013.
- [21] F. Song, H. Chen, P. Li, Y. Q. Deng, F. Liu, and J. Yang, "Effect of shutdown protection agents on steam water quality of direct air-cooling units," *Thermal Power Generation*, vol. 44, no. 4, pp. 92–95, 2015.
- [22] H. Garg, "The Effect of Coatings and Surfaces on Dropwise Condensation," Technical Note N-1041, Naval Civil Engineering Laboratory, Port Hueneme, CA, 1969.
- [23] C. Gasnier and D. Lister, "The effects of chemical additives on magnetite deposition in boiling heat transfer," in *Proceedings of International Conference on Heat Exchanger Fouling and Cleaning*, Budapest, Hungary, 2013.
- [24] L. Rudolph, J. Fandrich, and U. Ramminger, "CFD calculation method for the assessment of the impact of film-forming amines on local deposition at the tube sheet of steam generators, paper no. 61," in *NPC 2016*, Brighton, October 2016.
- [25] H. Topp, W. Hater, A. De Bache, and C. Zum Kolk, "Film forming amines in shell boilers," *Power Plant Chemistry*, vol. 14, no. 1, pp. 38–48, 2012.
- [26] C. Arias, A. Usón Boned, U. Ramminger, and J. Fandrich, "Five years experience with filming amines at NPP Almaraz," in *EPRI SGMP 2016 Steam Generator Secondary Side Management Conference*, Orlando, FL, 2016.
- [27] M. Lendi and P. Wuhrmann, "Impact of film-forming amines on the reliability of online analytical instruments," *Power Plant Chemistry*, vol. 14, no. 9, pp. 560–567, 2012.
- [28] R. Verlet and C. Vautier, *Influence of Film Forming Amine ODA on Stress Corrosion Cracking of Nickel Based Alloys*, MAI, 2018.

Research Article

Theoretical and Experimental Analysis of Thin-Walled Curved Rectangular Box Beam under In-Plane Bending

Long Yanze , Zhang Ke, Shi Huaitao , Li Songhua, and Zhang Xiaochen 

School of Mechanical Engineering, Shenyang Jianzhu University, Shenyang 110168, China

Correspondence should be addressed to Long Yanze; longyanze@sjzu.edu.cn

Received 1 October 2020; Revised 5 March 2021; Accepted 15 March 2021; Published 30 April 2021

Academic Editor: Heng Bo Jiang

Copyright © 2021 Long Yanze et al. This is an open access article distributed under the Creative Commons Attribution License, which permits unrestricted use, distribution, and reproduction in any medium, provided the original work is properly cited.

Thin-walled curved box beam structures especially rectangular members are widely used in mechanical and architectural structures and other engineering fields because of their high strength-to-weight ratios. In this paper, we present experimental and theoretical analysis methods for the static analysis of thin-walled curved rectangular-box beams under in-plane bending based on 11 feature deformation modes. As to the numerical investigations, we explored the convergence and accuracy analysis by normal finite element analysis, higher-order assumed strain plane element, deep collocation method element, and inverse finite element method, respectively. The out-of-plane and in-plane characteristic deformation vector modes derived by the theoretical formula are superimposed by transforming the axial, tangential, and the normal deformation values into scalar tensile and compression amounts. A one-dimensional deformation experimental test theory is first proposed, formulating the specific contributions of various deformation modes. In this way, the magnitude and trend of the influence of each low-order deformation mode on the distortion and warping in the actual deformation are determined, and the significance of distortion and warping in the actual curved beams subjected to the in-plane loads is verified. This study strengthens the deformation theory of rectangular box-type thin-walled curved beams under in-plane bending, thus providing a reference for analyzing the mechanical properties of curved-beam structures.

1. Introduction

Because of their high strength-to-weight ratios, the curved beam members and particularly those with rectangular cross-sections are widely used in mechanical engineering and building structures. This geometry is the first choice for engineering applications when working in the direction of a fixed load. However, studies of the accuracy of the strength and deformation of thin-walled curved beams have mainly considered the distortion and warping of thin-walled curved beam structures and the complexity of other factors, causing difficulties in obtaining the mechanical properties of thin-walled curved beam structures. The earliest research on thin-walled beams [1] began with Vlasov, while Dabrowski expanded into thin-walled curved beam theory [2]. The analysis of the beam by Y.Y. Kim and J.H. Kim (1999,2000) is accurate in that deformation is mainly caused by distortion and warping [3, 4], which increases the accuracy of the analysis of the curved beam. Y. Kim and Y.Y. Kim analyzed the

one-dimensional high-order theory of the in-plane thin-walled curved box beam under the action of in-plane loading [5, 6]. Zhang et al. proposed a new finite element method which is considering eight cross-sectional deformation modes [7–9]. This requires the introduction of a section feature deformation described by a high-order function, that is, a high-order feature deformation. The strain values of the deformed configuration were calculated in terms of the displacement values and the initial curvature by Afnani et al. [10]. Fazlali et al. presented an analytical solution for the elastic-plastic pure bending of a linear kinematic-hardening curved beam with a rectangular cross-section [11].

However, previous literature has made assumptions regarding deformation theory, the rigidity of the section, and the effect of curvature, in the above articles on thin-walled curved beams, whether in finite-element analysis, linear viscoelastic analysis [12], one-dimensional high-order theory [13], or cross-section deformation mode analysis [14, 15]. In theoretical analysis, the analysis is always

predictive, regardless of its accuracy. Thus, current analysis lack analytical methods based on actual experimental data.

As to the finite element analysis factors of plane problems on beam structures, accuracy and convergence are the most important issues among them. In one of the most recent works in the fields of assumed strain elements, Rezaiee-Pajand published some numerical articles [16–21] related to high-order strains, which expanded the authors' general view of numerical analysis.

Some researchers studied the surrogate of FEM by deep learning, which mainly trains the deep neural networks from datasets obtained from FEM. Hongwei Guo et al. [22] proposed a deep collocation method (DCM) for thin plate bending problems, which predicted maximum transverse with increasing layers is studied in order to show the convergence of deep collocation method in solving the plate bending problem. E. Samaniego et al. [23] explore the possibility of using a Deep Neural Network- (DNN-) based solver for Partial Differential Equations (PDEs). Solving them is a crucial step towards a precise knowledge of the behavior of natural and engineered systems.

To enable shape sensing analyses of beam structures undergoing bending deformation, Marco Gherlone et al. demonstrated that the recently presented iFEM for beam is reliable when experimentally measured strains are used as input data [24, 25]. Adnan Kefal developed a new eight-node curved inverse-shell (iCS8) element based on iFEM methodology, in which the high accuracy and practical utility of the iCS8 element are demonstrated for different cylindrical marine structures through examining coarse iCS8 discretizations with dense and sparse sensor deployments [26–29].

In this paper, we present experimental and theoretical analysis methods for the static analysis of a thin-walled curved rectangular box beam under in-plane bending based on 11 feature deformation modes. The experimental method for measuring the actual deformation of each section in a curved beam structure is proposed, using a one-dimensional deformation experimental test theory. Numerical investigations is explored the convergence and accuracy analysis by normal finite element analysis, higher-order assumed strain plane element, deep collocation method element, and inverse finite element method, respectively. The out-of-plane and in-plane characteristic deformation modes derived in the formula are superimposed by transforming the axial, tangential, and normal deformation values into tensile and compression components. The one-dimensional deformation experimental test theory is first proposed, formulating the specific contributions of various deformation modes. In this way, the magnitude and trend of the influence of each low-order deformation, distortion, and warping mode on the actual deformation are determined, and the significance of distortion and warping in actual curved beams subjected to in-plane loads is verified. This theory can be used in cases where it is difficult to measure and apply the measurement of the deformation distribution of various elastomer materials and structures to better understand the mechanical properties of the structure. The actual influence of distortion and warping in high-order deformation on deformation is reflected by actual data and a predictive curve.

The low-order and high-order deformation modes of the box curved beam subjected to an in-plane load are thus obtained.

2. Theoretical Analysis

The geometrical dimensions of the thin-walled curved box beam shown in Figure1 include ρ , Φ , and y , where ρ is the radial coordinate, Φ is the angular coordinate starting from the fixed end, and y is the ordinate. The height and width of the thin-walled curved beam structure are h and b , respectively, and the thicknesses of the wall are t_1 and t_2 , respectively. The cantilever beam structure of the thin-walled curved beam mechanism is fixed at one end, and the load is applied to the other free end. The load in the plane comprises the tangential force T , radial force V , and in-plane bending moment M .

In order to determine the contour displacement field, the cross-section analysis of the thin-walled curved rectangular box beam is utilized. Firstly, research on all deformations of the predecessors is performed, and the high-order deformation is extracted by removing the low-order deformation components from the deformation [9]. A feature deformation is identified, and its shape function is defined to eliminate the influence of that feature deformation in the next function mode. The shape function of the section deformation and the wall envelope area are iterated. Eleven feature deformations are identified, in which the deformations 1st, 2nd, 3rd, 7th, 8th, and 9th are low-order deformation modes; the 4th, 5th, and 6th are high-order deformation modes of in-plane distortion, and 10th and 11th are high-order warping deformation modes.

According to the Timoshenko theory, the six low-order deformations include the translational displacement of the section by torsion, axial expansion, and rotational displacement about the x - and the y -axis. Modes 4th–6th are thus torsional distortion, uniaxial symmetric bending distortion, and biaxial symmetric bending distortion; modes 10th and 11th are torsional warping and bending warping, respectively, in the out-of-plane high-order deformation.

The actual deformation of the cross-section of all thin-walled curved rectangular box beams is the superposition of vectors of the above low- and high-order deformations [5]. The low- and high-order deformations are composed of axial, tangential, and normal components. By superimposing the out-of-plane and in-plane deformations, this study experimentally determines the actual deformation of the section via only tension and compression components. The axial deformation of the wall is perpendicular to the cross-section, with the negative value perpendicular to downward face, meaning that tension is positive. As for the normal and tangential deformation, the outer contour of the siding is positive, and the inside of the contour is negative. The deformation vectors of the above three directions are extracted into scalar deformation types in a unified plane by tension and compression. The out-of-plane deformation by modes 7th–11th is thus transformed to an in-plane scalar form, as shown in Figure2, which can be superimposed with the deformation vectors 1st–6th to determine the actual deformation of any point on the wall.

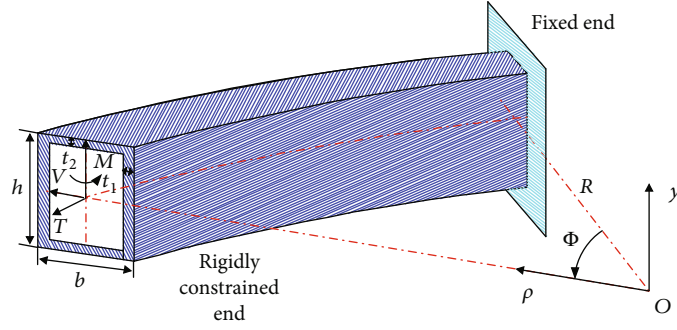


FIGURE 1: Geometry and coordinate system for cantilevered thin-walled curved box beam subjected to external loads.

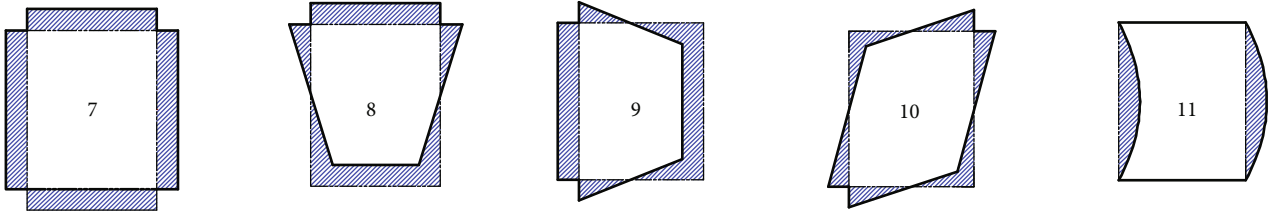


FIGURE 2: Cross-sectional deformation modes from out-of-plane into in-plane.

In order to obtain the in-plane section deformation function of the thin-walled curved box beam, it is necessary to consider the eleven types of section deformation modes listed in the previous section (as shown in Figure 3). We consider the four walls of the rectangular section of the box beam as the research objects, to accurately calculate the expressions of various deformed shape functions. As shown in Figure 1, the thin-walled curved box beam is subjected to in-plane radial loading. The deformation is not symmetrical about y because of the curvature. This deformation can be decomposed into symmetric, asymmetric, and high-order modes, namely, low-order and high-order modes.

A local coordinate system of the wall, as shown in Figure 4, is established, in which n and s represent the normal and tangential directions, respectively.

The deformation expression $\chi_b(\phi)$ of the contour displacement component of the rectangular section of the curved beam [7] can be expressed as

$$u_{nj}(s_j, \phi) = \psi_{nj}^{\chi_b}(s_j) \chi_b(\phi), \quad (1)$$

$$u_{sj}(s_j, \phi) = \psi_{sj}^{\chi_b}(s_j) \chi_b(\phi), \quad (2)$$

$$u_{\phi j}(s_j, \phi) = \psi_{\phi j}^{\chi_b}(s_j) \chi_b(\phi). \quad (3)$$

$\psi_{rj}^{\chi_b}(s_j)$ represents the shape function of the wall of the beam and is used to describe the shape of the line in the profile of the section; j indicates the j th wall, r is the direction of the deformation in the section wall, such as $r = n, s, \phi$, respectively, for the normal, tangential, and radial directions. χ_b denotes the generalized displacement of a point on the midline of the section, which is used to describe the amplitude variation of the in-plane and out-of-plane feature deformations along the axis.

The load of the analyzed curved beam is the in-plane bending load, while ignoring the unloading effect and shear lag. An approximate shape function must be derived using a one-quarter or one-half model of the entire section model. Because both the geometry and the external load are curved by the inner plane, the curvature is symmetric about the two axes of the hollow rectangular section.

Three orthogonal displacement components are used to represent the displacement of the point (α, s) on the midline of the section at time t : the axial component \tilde{u}_r , the tangential component \tilde{v}_r , and the normal component \tilde{w}_r , in which the three displacement components are along the coordinate axis (α, s, n) direction is positive. The three displacement components can be expressed in the form of the sum of finite terms by modal superposition method, namely,

$$\tilde{u}_r(\alpha, s; t) = \sum_{i=1}^{11} \chi_{ri}(\alpha; t) \varphi_{ri}(s), \quad (4)$$

$$\tilde{v}_r(\alpha, s; t) = \sum_{i=1}^{11} \chi_{ri}(\alpha; t) \psi_{ri}(s), \quad (5)$$

$$\tilde{w}_r(\alpha, s; t) = \sum_{i=1}^{11} \chi_{ri}(\alpha; t) \phi_{ri}(s), \quad (6)$$

where $\chi_{ri}(\alpha; t)$ represents the generalized displacement of a point (α, s) on the midline of the section at time t , which is used to describe the amplitude change of the in-plane and out-of-plane characteristic deformation along the axis; while $\varphi_{ri}(s)$, $\psi_{ri}(s)$, and $\phi_{ri}(s)$ also known as generalized coordinates, it is used to describe the shape change of the section along the center line of the section profile. Considering the influence of the axial and tangential displacement due to

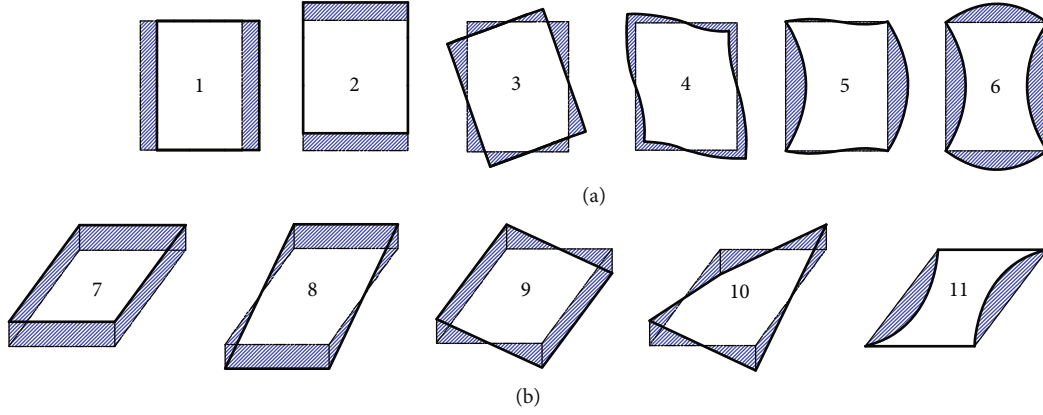


FIGURE 3: Cross-sectional deformation modes of a thin-walled rectangular beam.

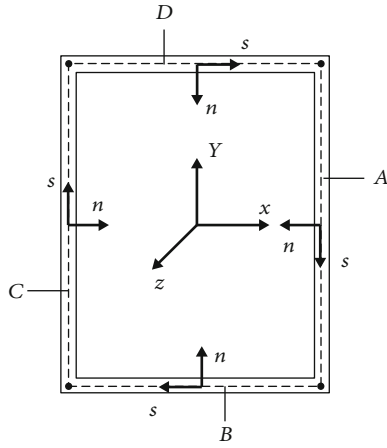


FIGURE 4: Local system of wall.

Kirchhoff's hypothesis on bending problem is adopted for the strain field and stress field: straight line hypothesis, namely, the thickness is constant; the normal stress on the midplane is much smaller than the other stress component hypothesis, and the midplane has no expansion and contraction assumption. At the same time, using linear elastic constitutive relationship expressed as

$$\sigma_r = E_r \varepsilon_r, \quad (11)$$

where σ_r represents stress component column vector, ε_r represents strain component column vector, which could be obtained easily according to the geometric equations and matrix expressions, while it should be noted the constitutive matrix E_r in the plane stress is expressed as

$$E_r = \begin{bmatrix} E_1 & 0 & E_1 \nu \\ 0 & G & 0 \\ E_1 \nu & 0 & E_1 \end{bmatrix}, \quad (12)$$

$$E_1 = \frac{E}{1 - \nu^2}, \quad (13)$$

$$G = \frac{E}{2(1 + \nu)}, \quad (14)$$

the deflection of the wall, the three-dimensional displacement component vector is obtained from the two-dimensional displacement component vector expressed as

$$\mathbf{x}_r = H_r \mathbf{X}_r, \quad (7)$$

where 2D displacement component vector \mathbf{X}_r obtained by Equation(7), 3D displacement component vector \mathbf{x}_r and conversion matrix H_r expressed as

$$\mathbf{x}_r = [u_r(\alpha, s, n; t) \ v_r(\alpha, s, n; t) \ v_r(\alpha, s, n; t) \ w_r(\alpha, s, n; t)]^T, \quad (8)$$

$$H_r = \begin{bmatrix} 1 & 0 & -n \frac{\partial}{\rho \partial \alpha} \\ 0 & 1 & -n \frac{\partial}{\partial s} \\ 0 & 0 & 1 \end{bmatrix}^T, \quad (9)$$

$$\mathbf{X}_r = [\tilde{u}_r(\alpha, s, n; t) \ \tilde{v}_r(\alpha, s, n; t) \ \tilde{w}_r(\alpha, s, n; t)]^T. \quad (10)$$

where E , and G represent the Young's modulus and shear modulus of the material, respectively; ν represents the Poisson constant.

The kinematic equation of the curved beam segment is established by the energy method, it is necessary to determine the strain energy, external force potential energy, and kinetic energy of the structure; the strain energy of a curved beam is express as

$$U = \frac{1}{2} \int \int \varepsilon_r^T \sigma_r dA dz, \quad (15)$$

where the two integrations are performed on the integration space of the beam axis direction and the cross-sectional area,

respectively, regardless of nonlinear factors; the external force potential energy of the beam is expressed as

$$U_p = - \int \int x_r^T p_r dA dz - \int \int (x_r^T q_r d\Omega)_{n=-t_r/2} dz - \int [x_r^T \bar{\sigma}_r]_{z=z_1}^{z=z_2} dA, \quad (16)$$

where z_1 and z_2 represent axial coordinates at both ends of the beam ($z_1 < z_2$); Ω represents integral space of the s coordinate along the midline of the section; p is the force sequence vector of the body distribution acting on the middle surface; and q is the force sequence vector of the surface distribution acting on the beam surface; $\bar{\sigma}_r$ is the vector of force series acting on the cross section of the beam. In which the first integral range refers to the integral space of the beam axis direction and the cross-sectional area, the second integral range refers to the integral space of the cross-sectional area and the integral space of the s -coordinate along the center line of the section, and the third integral range refers to the direction of the beam axis. The kinetic energy is expressed as

$$T = \frac{1}{2} \int \int \frac{\partial u_r}{\partial t} \Psi_r^T H_r^T \eta H_r \Psi_r \frac{\partial u_r}{\partial t} dA dz. \quad (17)$$

The Hamilton principle and Lagrange function are used to derive the kinematic differential equation of the curved beam. The Hamilton principle can be expressed as

$$\delta H = \delta \int_{t_1}^{t_2} L dt, \quad (18)$$

where H represents Hamilton and L represents Lagrange function.

$$L = T - U - U_p. \quad (19)$$

3. Numerical Investigations

3.1. Finite Element Analysis. A full model representation includes supports and loading, in which the top end of the beam are totally restrained at the position of $\varphi = 0^\circ$, acting as fixed supports, and a point load is applied at the free end of the beam; this load will create a moment under total loads of 300 N and 1000 N and the forces applied at the position of $\varphi = 90^\circ$ along the y -axis. Analysis is carried out by linearly increasing the load from zero to a maximum value given by the expected total capacity of the structure, whose model is meshed into thin shell elements having the material parameters of $E = 200$ MPa. Finite model is meshed into 809 elements and 2046 nodes with thin shell element, which the results obtained under the load of 1000 N in shown in Figure 5.

Generally speaking, the field variable selection is the most important step in finite element technology. Obviously, the accuracy of this approximation depends on the interpolation function assigned to the element. Different types of mathe-

tical functions can be used to express these functions. However, one of the most stable forms is a polynomial basis of degree \mathcal{P} :

$$\mathcal{P}^{\mathcal{P}} = [x \quad y \quad x^2 \quad xy \quad y^2 \quad \dots \quad y^{\mathcal{P}}] \tilde{a}, \quad (20)$$

$$\tilde{a} = [a_{i1} a_{i2} \dots]^T. \quad (21)$$

The approximation field consists of two main parts: (a) interpolation function—the order of this function determines the accuracy and speed of convergence to achieve a precise response. The degree of convergence and sustainability gradient depends on the degree of \mathcal{P} . (b) Additional carrier—according to the formula method, its definition is different. In some formulas based on displacement, it is called a degree of freedom vector. In the displacement field method, these parameters are obtained by various methods, but in the natural assumed strain method, these strain states are based on the application of a series of optimal criteria to reduce the stress, according to the degree of freedom and derived from the distribution of geometric shapes. The number of degrees of freedom required. The most commonly used best criteria are balance and compatibility equations. In addition to forcing a minimum energy level to the finite element, applying balance can also increase the convergence speed of the resulting element.

3.2. Higher-Order Assumed Strain Plane Element. The traditional plane element analysis needs to be divided into a very fine mesh to get accurate results, and the convergence speed is too slow. In order to improve the convergence speed and accuracy of finite element analysis for planar elements, in this paper, we adopted a new robust membrane finite element for the analysis of plane problems proposed by Rezaiee-Pajand, which has triangular geometry with four nodes and 11 degrees of freedom for the element, in which each of the three vertex nodes has three degrees of freedom, two displacements, and one drilling. The fourth node that is located inside the element has only two translational degrees of freedom. Three different meshes are used to analyze this structure, namely, 1×6 , 2×12 , and 4×24 . These mesh styles are named based on the number of quadrilateral elements used in them. Of note, to analyze using triangular elements, each quadrilateral element is divided into two triangular elements.

In order to compare the convergence rate and accuracy of various element types, tip deflection of the curved beam under applied load was computed, which proposed element in the analysis of curved structures; a thin curved cantilever beam loaded by a transverse load at its free end is analyzed. The beam is made of the elastic material with a modulus of elasticity and Poisson's ratio equal to 10^7 and 0.25, respectively, and its inner radius and thickness are 4.12 and 0.1 unit. The beam is analyzed by three different mesh and the results of vertical displacement of the structural tip are listed in Table 1. The near-exact value is reported by Choo et al. (2006) is equal to 0.08734 [30]. The convergence curves for different elements are depicted in Figure 6.

A: Static structural
Figure
Type: Equivalent elastic strain
Unit: mm/mm
Time: 1
2018/12/29 11:29

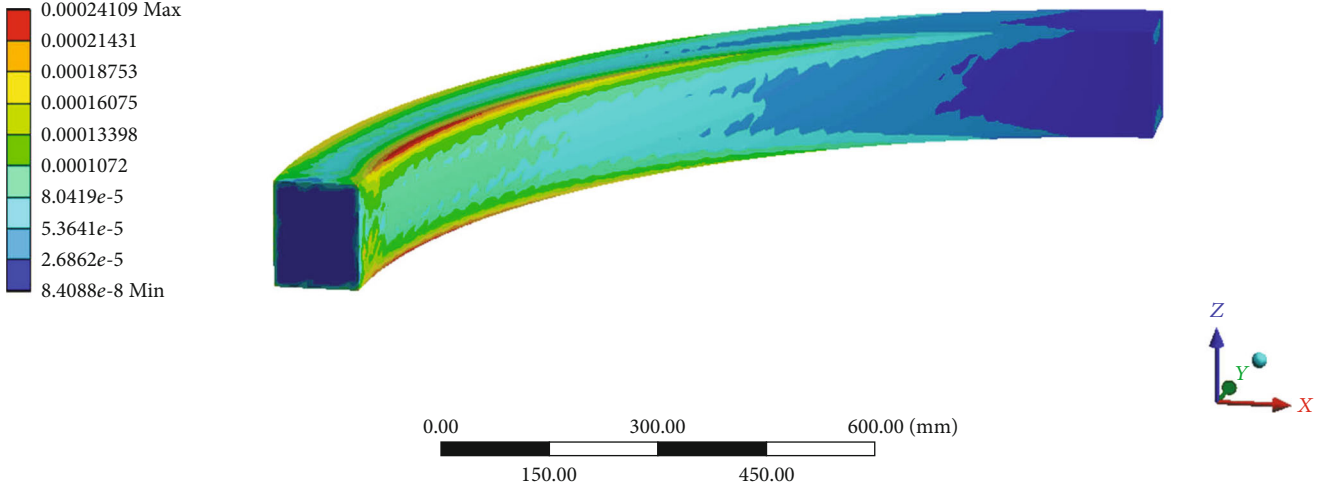


FIGURE 5: Finite element analysis of curved beam structure under load.

TABLE 1: Normalized tip deflection of the thin curved beam.

	Mesh density		1×6	2×12	4×24
Element type	Node	Degree of freedom	Normalized deflection		
Quadrilateral elements					
RY-Q10	5	10	-0.08901	-0.08844	-0.08846
RY-Q14D	5	14	-0.08748	-0.08898	-0.08925
RY-Q18	9	18	-0.08745	-0.08840	-0.08850
Triangular elements					
RGR-T10	5	10	-0.06305	-0.08493	-0.08609
RGR-T11D	7	11	-0.08291	-0.08434	-0.08691
RGR-T10D	4	10	-0.06486	-0.08501	-0.08650
Standard reference value is 0.08734*					

As shown in Table 1, the tip deflection values of element analysis with different mesh densities from 1×6 to 2×12 and 4×24 can be seen that the convergence of the triangular elements is significant; in the triangular element, the convergence speed and accuracy of the triangular element with 4 nodes and 10 degrees of freedom are better than the elements with 5 nodes and 10 degrees of freedom and 7 nodes and 10 degrees of freedom, besides the element with 6 nodes and 10 degrees of freedom (all translational degrees of freedom, no rotational degrees of freedom) excluded for high order analysis.

Even the obtained results show that triangular plane elements with four-node and 11 degree of freedoms [31] perform better than the other elements shown in Figure7. All of the above, as to finite plane element analysis of the curved beam structures, the triangular element with 4 nodes and 11

degrees of freedom has fast convergence speed and high analysis accuracy.

3.3. Deep Collocation Method. This deep collocation method can be seen as a truly mesh-free method without the need of background grids.

This section introduces the deep collocation method used to solve the Kirchhoff board bending problem. This method is a widely used method to find the numerical solutions of normal, partial differential, and integral equations. Among the control theories, it is a popular method for trajectory optimization. Usually, a set of randomly distributed points (also called collocation points) is used to represent the required trajectory, which minimizes the loss function while satisfying a set of constraints. The collocation method is often relatively insensitive to instability and is a feasible method for training deep neural networks.

First, the collocation point is expressed as a discretized physical domain. Another set of collocation points is used to discretize the boundary conditions. Then, the feed forward deep neural network [23] is used to approximate the lateral deflection w . Therefore, a loss function can be constructed to find optimal hyperparameters by approximating the boundary conditions to the minimization of the governing equations. The purpose of this section is to seek a series of approximate deflection parameters to minimize the loss function (θ). If the function value is small, the approximate deflection value is very close to the value that satisfies the driving equation. The thin plate bending problem solved by the deep collocation method can be simplified into an optimization problem. In the deep learning Tensorflow framework, various optimizers are used. One of the most widely used optimization methods is the Adam optimization algorithm, which is also used in the numerical research of this article. The idea is to decrease at the collocation point x_i ,

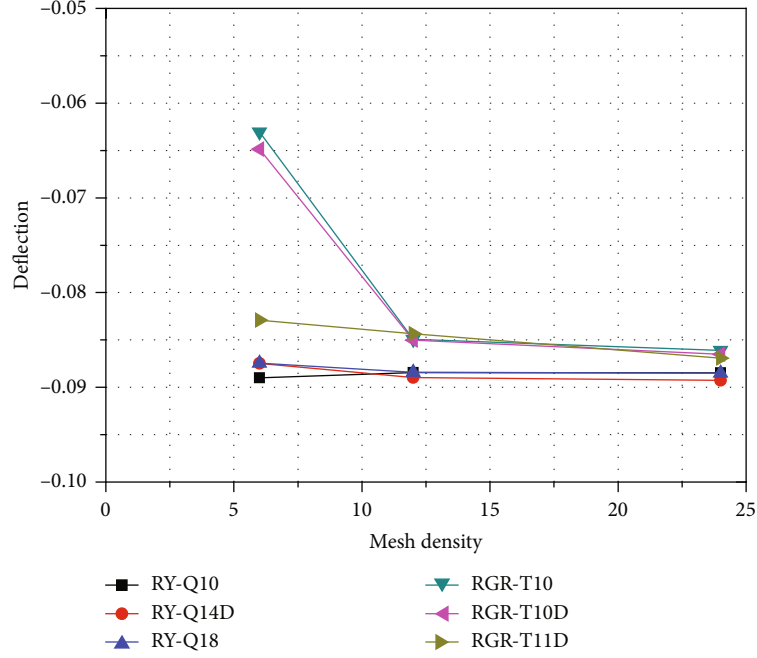


FIGURE 6: Convergence of the normalized tip deflection of the thin curved beam.

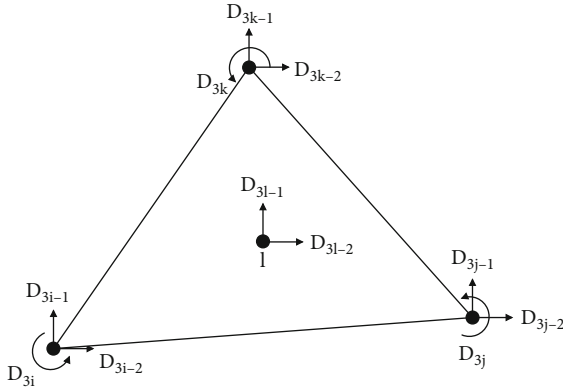


FIGURE 7: Four-node triangular element with incomplete second-order strain field.

using the Adam-based learning rate α_i , and then the process in Equation (22) is repeated until a convergence criterion is satisfied.

$$\theta_{i+1} = \theta_i + \alpha_i \nabla_{\theta} L(x_i; \theta), \quad (22)$$

where ∇ is commonly called biharmonic operator.

For the clamped load situation, a deep feedforward neural network with increased layers and neurons was studied to verify the convergence of the scheme. First, the maximum center deflection is shown in Table 2, which is calculated for the number of different layers and neurons and compared with Timoshenko's exact solution shown in Figure 8. The result of deep collection is the most consistent with the exact solution. However, for a neural network with a single hidden layer, even with 60 neurons, the result is not very accurate. As the number of neurons increases, the results are indeed more

TABLE 2: Maximum deflection predicted by deep collocation method.

Clamped square plate Number of hidden layers	Predicted maximum deflection			
	20 neurons	30 neurons	40 neurons	50 neurons
1	0.860568	1.152175	1.195843	1.24987
2	1.257226	1.257759	1.265145	1.261974
3	1.26178	1.260374	1.261743	1.258893
Exact solution is 1.260000*				

accurate for neural networks with a single hidden layer. This can be observed for the other two hidden layer types. In addition, as the number of hidden layers increases, the result is much more accurate than that of a single hidden layer neural network.

3.4. Inverse Finite Element Method. The Timoshenko beam theory is adopted, and the discretization using the C0 continuous inverse element is adopted through the variational principle. The three-dimensional displacement field of the beam structure is reconstructed under the condition of ensuring the least squares compatibility between the measured strain and the strain interpolated by the inverse element. Then, describe the experimental setup. Thin-walled cantilever beams bear different static and dynamic loads. First, the measured surface strain is used as input data for shape sensing through a single inverse element. For the same test case, more and more inverse elements are also used to study convergence. Then, compare the deflection recovered by iFEM with the deflection measured experimentally. For static loads, the accuracy and convergence of iFEM measurement errors are proved.

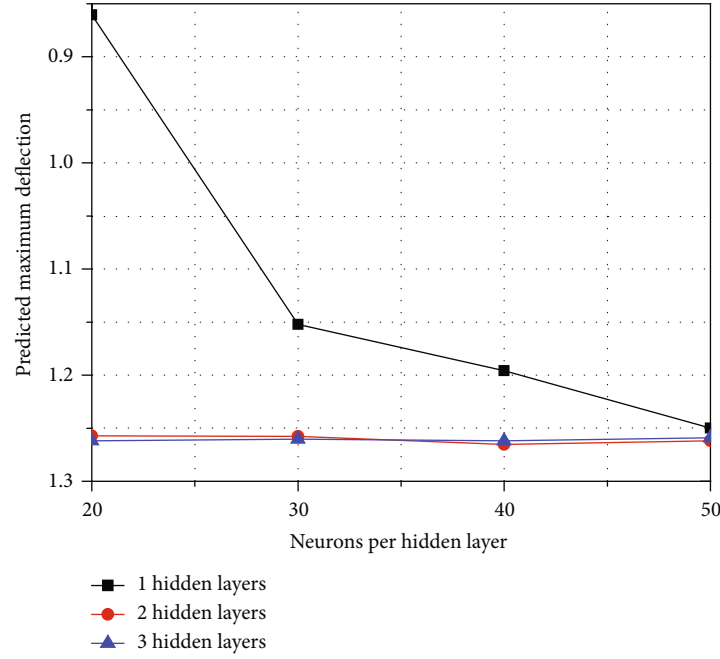


FIGURE 8: The relative deflection with varying hidden layers and neurons.

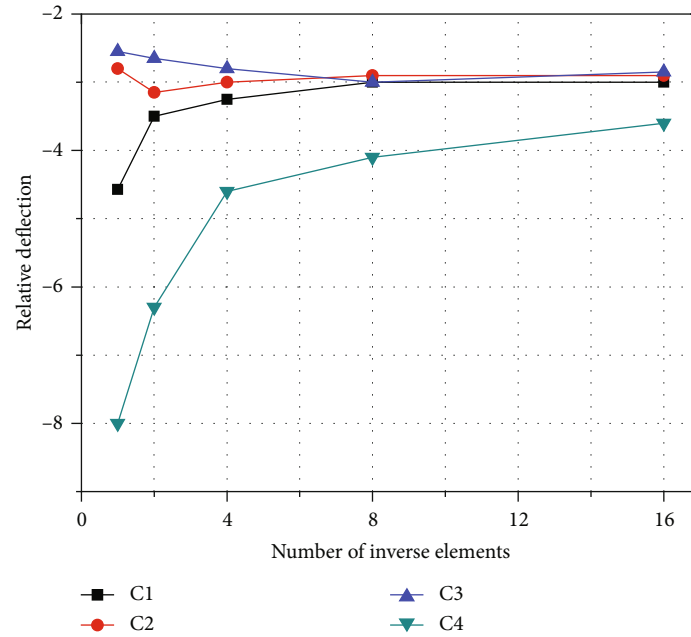


FIGURE 9: Relative tip deflection in iFEM-predicted of different strain gauges arrangement. C1: six strain gauges in one axial location; C2: six strain gauges in two axial locations; C3: eight strain gauges in two axial locations; C4: eight strain gauges in three axial locations.

As an example to illustrate the analysis of convergence and accuracy under the shape sensing of the inverse finite element method. Under the condition of tip force in static testing, one end is fully constrained, and the free end is loaded. The analysis of the working conditions under the load condition evaluates the accuracy of the solution by predicting the percentage difference of the displacement and the rotation relative to the experimentally measured rotation. The percentage difference is defined as the relative error between

the predicted value of the end deflection and the actual measured value. It mainly analyzes the change value caused by the number of inverse elements. For all load conditions and using any strain gauge configuration considered, the end deflection predicted by iFEM. The difference with the measured value meets the error requirement range.

As shown in Figure 9, more and more inverse elements obtained the end displacement results under load conditions. All elements are distributed with strain gauges corresponding

to each curve. As the number of antielements increases, the percentage difference in the predicted iFEM deflection will converge to a value less than 6%. Each input strain is obtained by linear fitting to three different values. When using fitted strain data, the main advantage of applying the fitting process to the original data is that a large number of inverse elements can be used to discretize the frame members without the need to obtain additional data. In this case, it is advantageous to use higher fidelity discretization for the iFEM model. Generally, the number of antielements to be used is related to the complexity of the applied load and the expected structural deformation. Using the fitted data, the results obtained by using different strain gauge configurations will converge to almost the same value. At the same time, the more strain gauges, the higher the convergence efficiency. At the same time, the strain gauges are distributed at the most, with the same amount of strain. The more the instrument is distributed, the faster the convergence efficiency. Therefore, as the iFEM algorithm, in discretization applications, more strain gauges should be used, and they should be evenly distributed in each position of the structure, which will help the convergence speed and achieve the accurate value faster.

4. Experimental Investigation

4.1. Test Specimens. The curved plates of the curved beam structure are formed by bending two flat plates to have a certain radius of curvature and then welding them with the upper and lower flat plates. At this point, the two curved plates are marked before bending. A butt-welded square box cross-sectional shape is used in the curved beams. Each wall plate is composed of Q235 (235 MPa) normal strength steel, and the steel plate with a thickness of 2.2 mm is flame-cut.

The beam is of width $b = 120$ mm, height $h = 150$ mm, wall thickness $t = 2.2$ mm, section radius of centerline $R = 1$ m, and central angle $\varphi = 90^\circ$. The experimental sample structure is welded from four Q235-grade steel plates to form a thin-walled curved beam; it was stored at rest for half a year after welding. In order to prevent the influence of uniqueness on the data, four samples with the same materials and parameters were tested. To research the properties of a thin-walled curved box beam, the fixed end fully and rigidly constrained by a rigid plate. The in-plane load V is applied as a radial load of 1000 N, and the load direction is as shown in Figure10.

4.2. Specimen Labeling. The mark number of each detection point is ijk as shown in Figure 11, where i represents the section of the central axis of the curved beam section with the point O as the origin, and curve PQ is the central axis of the section of the thin-walled curved box beam $i = 1, 2, 3, 4$, and 5, with point P as the reference point, according to the angle Φ_i of $\Phi_1 = 1.72^\circ$, $\Phi_2 = 22.5^\circ$, $\Phi_3 = 45^\circ$, $\Phi_4 = 67.5^\circ$, and $\Phi_5 = 88.28^\circ$, as shown in Figure 9, respectively. To ensure the test points are evenly distributed, the angle between the 1th and 5th sections is defined by the necessary distance of 20 mm to the end to avoid the welding position; point P of the section is the constraint position.

Point Q represents the loading position, as shown in Figure12, j represents the j th wall of the i th section, which has four walls.

A indicates the wall of the outer diameter, and the other wall plates are arranged in clockwise order, with wall plate B located below, C at the inner diameter, and D above, k represents the position of the axially arranged resistance strain gauge where the j th wall of the i section is located; each wall has three positions in every section, for a total of 12 positions in each section. $k = 1$ is the starting test point, the other test points are arranged clockwise, where the o'clock position relative to the edge of the wall is $e = 20$ mm in order to avoid the welding position of the end, point 2 is the center position of each wall, and points 3 and 1 are symmetric about point 2 (as shown in Figure 13).

Strain gauges were attached to each of the 60 positions of the five sections on each of the four curved beam samples, and the strain values at each position were tested by a DH3820 high-speed static strain analysis system.

4.3. Test Results. The four sets of experimental data are similar. The results shown in Figure14 show the strain value amplified by 2×10^6 , because the experimental strain values are otherwise too small to see. The deformation diagram of positions 1-5 in the cross-section are shown in the figure. The shapes are formed by the strain values at the 12 test locations on each section; the thick solid line is the deformed shape, while the double dotted line is the nondeformed shape. The thin red solid line represents the strain value used to test the deformation change of the k point for this position; the shape is determined by this parameter. Because the experimental process can only measure the tensile or compressive strain of the test point at the test point itself, it is impossible to measure the strain at a certain position by in-plane deformation or out-of-plane deformation.

Therefore, in the experiment, the nondeformed cross-sectional outline is set to a positive value as the tensile strain, and the negative value is the compressive strain inward, formed as shown in the figure. As shown in Figure15, compared with the experiment, the theoretical analysis has a small error, within the allowable range, and mutually verified its accuracy.

5. One-Dimensional Deformation Experimental Test Theory

The strain value of each position of each wall of each section measured by the experimental method is scalar and composed of the axial, normal, and tangential strains. Although the actual deformation on the theoretical level is formed by distortion and warping in the low- and high-order deformation, the influence of the various deformation forms on the actual deformation must be determined. This study proposes an experimental test theory, which first calculates the expressions of various deformation modes in the axial, normal, and tangential components and then uses the undetermined coefficient method to calculate the influence coefficient $\chi_b(\phi)$ of the various deformation modes. By substituting this coefficient into the formulas of low-order, distortion, and warping

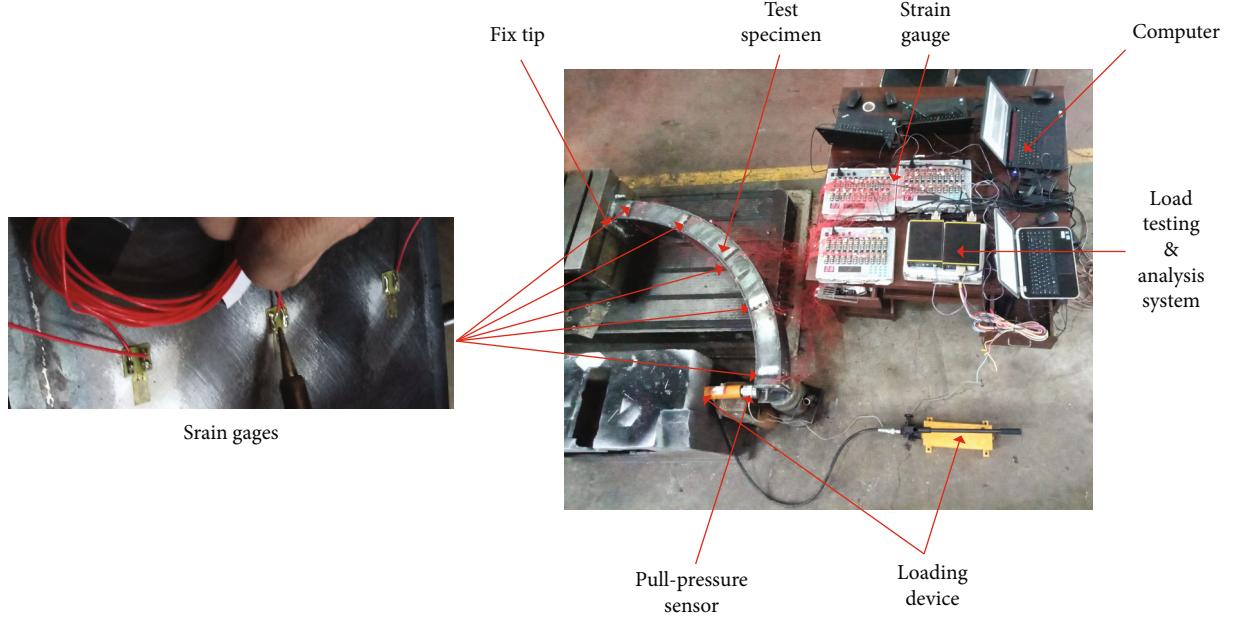


FIGURE 10: Typical test setup.

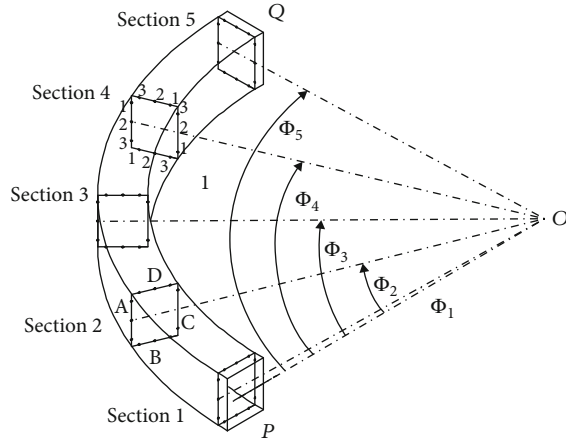


FIGURE 11: Test mark information in the curved beam.

effects, the respective influences are obtained, and the distribution of the test points at each position of the curved beam is used to infer the distribution of the entire curved beam. It thus can be determined whether there is any shape deformation effect that can be ignored.

$$u_T(s_j, \phi) = u_L(s_j, \phi) + u_D(s_j, \phi) + u_W(s_j, \phi). \quad (23)$$

The one-dimensional deformation effect formula for the thin-walled curved rectangular box beam is shown in Equation (23), where u_L is the low-order effect and u_D and u_W are the effects of distortion and warping, respectively.

The low-order effect indicates six kinds of deformation mode in Equation (16), where $\psi_L^{X_b}$ is a low-order shape function matrix concluding the six basic low-order deformation modes, while χ_b^L is a low-order influence coefficient matrix.

Equation (17) illustrates the distortion effect, where $\psi_D^{X_b}$ and χ_b^D represent the distortion effect shape function matrix and the distortion influence coefficient matrix, respectively, and the distortion types include bending and torsional distortion.

For the warping influence equation, $\psi_W^{X_b}$ and χ_b^W represent the warping function matrix and warping influence coefficients matrix, respectively, and the warping forms include two types of bending and torsion warping as shown in Equation(18).

Low-order effect:

$$u_L(s_j, \phi) = \psi_L^{X_b}(s) \chi_b^L, \quad (24)$$

$$\chi_b^L = [\chi_{b1}^L, \chi_{b2}^L, \chi_{b3}^L, \chi_{b7}^L, \chi_{b8}^L, \chi_{b9}^L], \quad (25)$$

$$\psi_L^{X_b}(s) = [\psi_{n1}^{X_b}(s), \psi_{n2}^{X_b}(s), \psi_{n3}^{X_b}(s), \psi_{\phi7}^{X_b}(s), \psi_{\phi8}^{X_b}(s), \psi_{\phi9}^{X_b}(s)]^T. \quad (26)$$

Distortion effect:

$$u_D(s_j, \phi) = \psi_D^{X_b}(s) \chi_b^D, \quad (27)$$

$$\chi_b^D = [\chi_{b5}^D, \chi_{b6}^D], \quad (28)$$

$$\psi_D^{X_b}(s) = [\psi_{n5}^{X_b}(s), \psi_{n6}^{X_b}(s)]^T. \quad (29)$$

Warping effect:

$$u_W(s_j, \phi) = \psi_W^{X_b}(s) \chi_b^W, \quad (30)$$

$$\chi_b^W = [\chi_{b10}^W, \chi_{b11}^W], \quad (31)$$

$$\psi_W^{X_b}(s) = [\psi_{n10}^{X_b}(s), \psi_{n11}^{X_b}(s)]^T. \quad (32)$$

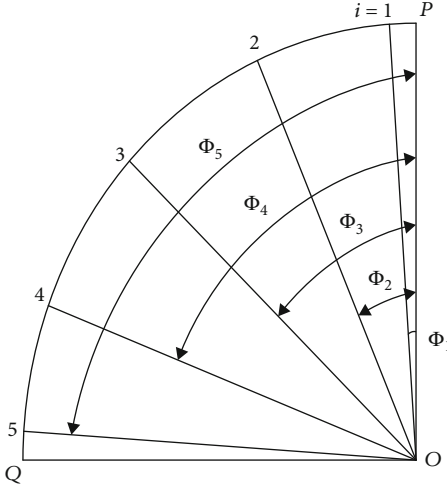


FIGURE 12: Test section distribution in curved beam.

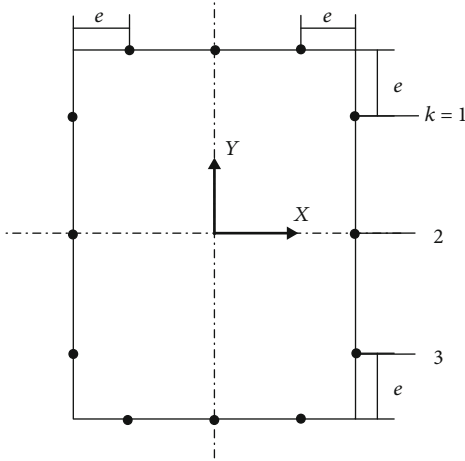


FIGURE 13: Test location markings on the cross-section.

This theory can be used in cases where it is difficult to measure the feature deformation modes, and it is impossible to distinguish between the out-of-plane and in-plane deformation modes. At the same time, the theory can be applied to the measurement of the deformation distribution of various elastomer materials and structures, to better understand the mechanical properties of the structure.

5.1. Derivation of Deformation Function Expression

5.1.1. Derivation of Low-Order Shape Function Expression. The deformation of the lower-order features can cause the main deformation of the section, which is the main deformation feature. The six low-order deformations include translational displacement by torsion, axial expansion, and rotation of the section about the x -axis and the y -axis, respectively. The characteristic deformations 1st, 2nd, and 3rd are normal deformations, and the characteristic deformations 7th, 8th, and 9th are axial deformations. The above deformation modes are, respectively, used as the main forms of low-order deformation, and the expression [1] is given by

$$\psi_{n1}^{x_b}(s) = \begin{cases} -1, & s \in [s_{AD}, s_{AB}), \\ 0, & s \in [s_{AB}, s_{BC}), \\ 1, & s \in [s_{BC}, s_{CD}), \\ 0, & s \in [s_{CD}, s_{DA}), \end{cases} \quad (33)$$

$$\psi_{n2}^{x_b}(s) = \begin{cases} 0, & s \in [s_{AD}, s_{AB}), \\ 1, & s \in [s_{AB}, s_{BC}), \\ 0, & s \in [s_{BC}, s_{CD}), \\ -1, & s \in [s_{CD}, s_{DA}), \end{cases} \quad (34)$$

$$\psi_{n3}^{x_b}(s) = \begin{cases} -(s - s_{AD}) + \frac{h}{2}, & s \in [s_{AD}, s_{AB}), \\ -(s - s_{AB}) + \frac{b}{2}, & s \in [s_{AB}, s_{BC}), \\ -(s - s_{BC}) + \frac{h}{2}, & s \in [s_{BC}, s_{CD}), \\ -(s - s_{CD}) + \frac{b}{2}, & s \in [s_{CD}, s_{DA}), \end{cases} \quad (35)$$

$$\psi_{\varphi 7}^{x_b}(s) = 1, \quad (36)$$

$$\psi_{\varphi 8}^{x_b}(s) = \begin{cases} -\frac{2}{h}(s - s_{AD})^2 + 1, & s \in [s_{AD}, s_{AB}), \\ 1, & s \in [s_{AB}, s_{BC}), \\ \frac{2}{h}(s - s_{BC})^2 + 1, & s \in [s_{BC}, s_{CD}), \\ -1, & s \in [s_{CD}, s_{DA}), \end{cases} \quad (37)$$

$$\psi_{\varphi 9}^{x_b}(s) = \begin{cases} -1, & s \in [s_{AD}, s_{AB}), \\ \frac{2}{b}(s - s_{AB}) - 1, & s \in [s_{AB}, s_{BC}), \\ 1, & s \in [s_{BC}, s_{CD}), \\ -\frac{2}{b}(s - s_{CD}) + 1, & s \in [s_{CD}, s_{DA}). \end{cases} \quad (38)$$

5.1.2. Derivation of Distortion Shape Function Expression. The high-order influence mainly comprises of the influences of distortion and warping, which is analyzed based on Zhang et al. [9]. The distortion is caused by the deflection of the section wall, and the bending moment on the wall is directly related. Because of the force of the structure of the cantilever beam, the direction and form of each wall plate can be inferred to determine the bending moment on the cross-section according to the identified distortion shape (as shown in Figure 16).

The cross-sectional dimension of the curved beam section is much larger (>5) than the wall thickness thus satisfying the applicable range of the Euler-Bernoulli beam theory. Therefore, the normal deformation function $\psi_{sj}^{x_b}(s_j)$ can be approximated as a cubic polynomial:

$$\psi_{nj}^{x_b}(s) = a_j^3 s^3 + a_j^2 s^2 + a_j^1 s + a_j^0. \quad (39)$$

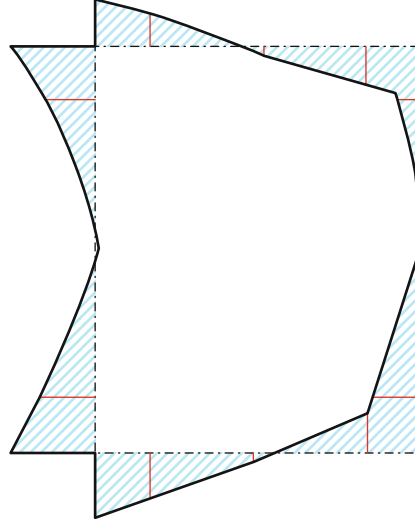


FIGURE 14: Sectional strain of each test point.

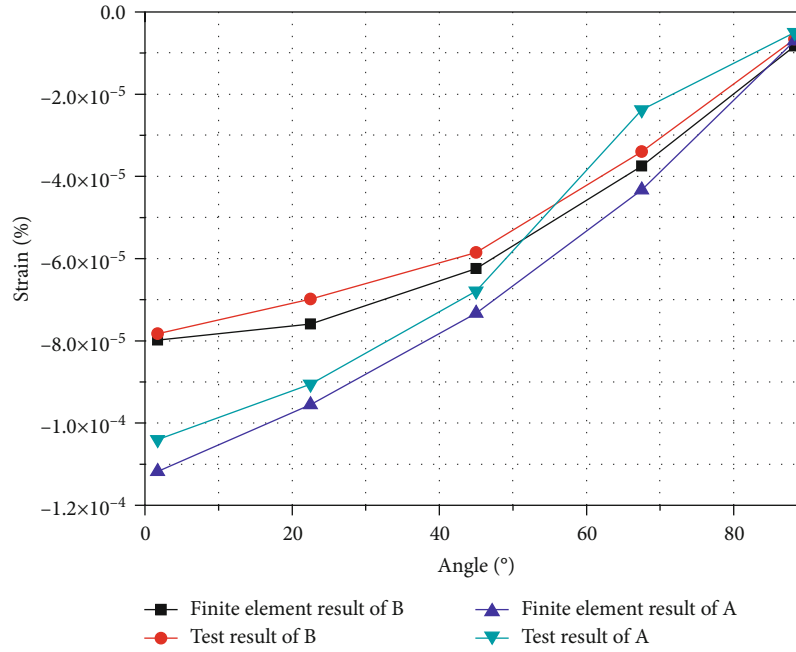


FIGURE 15: Comparison of finite element analysis and experimental results of strain at various positions on curved surface of curved beam.

The superscripts “+” and “-” indicate the approach directions of the tangential coordinates in Equation (39); a_j^i ($i = 0, 1, 2, 3, j = 5$), where i denotes the power of the polynomial and j denotes the j th shape deformation. Because the force mode determines the curved rectangular shape, the distortion type is only a single axis-symmetrical distortion type, so j can only be equal to 5, and the Euler-Bernoulli beam theory is determined by combining the geometric symmetry of the section and the bending moment balance condition. The other basic assumptions that must be used include:

- (1) Right angles must be maintained at the junctions of adjacent walls
- (2) The lateral expansion and contraction of the wall section can be ignored
- (3) The displacement on the same wall plate can be continuously differentiated
- (4) The displacement of both sides of the same node is continuous

According to the symmetry of the deformation and load on the x -axis, the distortion model of the section is simplified to the half-model shown in Figure 17(a). The antisymmetric property about the y -axis is reused, and the section deformation model is further simplified to the quarter model shown in Figure 17(b).

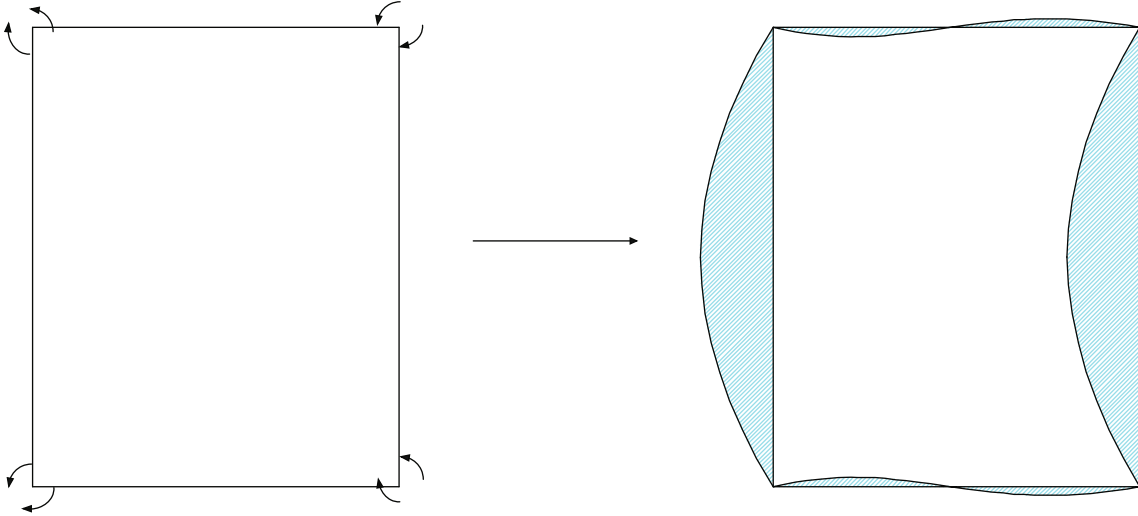


FIGURE 16: The bending moment of the wall on the section.

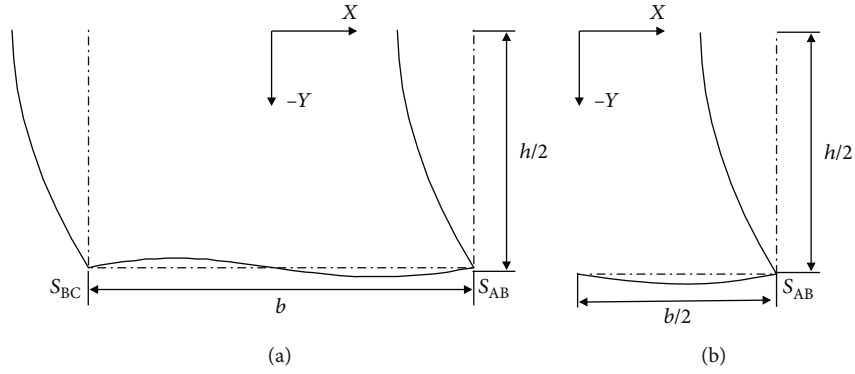


FIGURE 17: Rectangular section deformation under uniaxial symmetrical bending distortion. (a) Half-model. (b) Quarter-model.

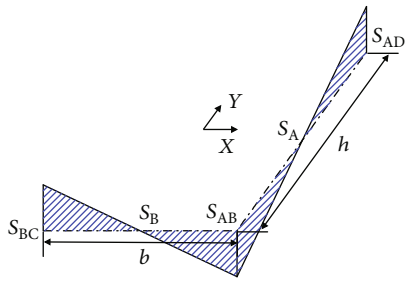


FIGURE 18: Torsion warping section deformation.

Because the bending distortion is independent of the torsion, the deformation characteristics are shown in Figure10, and it is assumed that the wall is not telescopic, in order to consider that the section has no tangential displacement ($\psi_{sj}^{X_b}(s) = 0$). For the cubic polynomial describing the quarter-model deformation function, the eight unknown coefficients are determined according to the following conditions:

- (1) According to the displacement continuity condition, the tangential displacement and the normal

displacement at the intersection of the faces A and B must satisfy

$$\psi_{n5}^{X_b}(s) \Big|_{s_{AB}^-} = -\psi_{s5}^{X_b}(s) \Big|_{s_{AB}^+}, \quad (40)$$

$$\psi_{n5}^{X_b}(s) \Big|_{s_{AB}^+} = -\psi_{s5}^{X_b}(s) \Big|_{s_{AB}^-}. \quad (41)$$

- (2) According to the bending moment balance condition at the corner joint, the deformation on both sides is opposite to that at the angular joint:

$$t_1^3 \frac{d^2 \psi_{n5}^{X_b}(s)}{ds^2} \Big|_{s_{AB}^-} = t_2^3 \frac{d^2 \psi_{n5}^{X_b}(s)}{ds^2} \Big|_{s_{AB}^+} = 0. \quad (42)$$

- (3) According to symmetric conditions about the x -axis:

$$\frac{d\psi_{n5}^{X_b}(s)}{ds} \Big|_{s_{AD}+h/2} = 0. \quad (43)$$

- (4) According to the antisymmetric conditions on the y -axis:

$$\psi_{n5}^{X_b}(s)|_{s_{AB}+b/2} = 0. \quad (44)$$

- (5) According to the assumption that the corners are kept at right angles, the angles of the two side wall plates are equal

$$\left. \frac{d\psi_{n5}^{X_b}(s)}{ds} \right|_{s_{AB}} = \left. \frac{d\psi_{n5}^{X_b}(s)}{ds} \right|_{s_{AB}^+}. \quad (45)$$

According to the principle of normalization, the amplitude of middle point of wall A shown in Figure10 is 1:

$$\psi_{n5}^{X_b}(s)|_{s_{AD}+h/2} = 0. \quad (46)$$

The eight linear independent equations in the simultaneous Equation(21), and the symmetric relationships yield the normal deformation function of the model:

$$\psi_{n5}^{X_b}(s) = \begin{cases} \frac{4}{h^3} \left(\frac{h}{2} - s + s_{AD} \right)^3 - \frac{6}{h^2} \left(\frac{h}{2} - s + s_{AD} \right)^2 + 1, & s \in \left[s_{AD}, s_{AD} + \frac{h}{2} \right), \\ \frac{4}{h^3} \left(s - s_{AD} - \frac{h}{2} \right)^3 - \frac{6}{h^2} \left(s - s_{AD} - \frac{h}{2} \right)^2 - 1, & s \in \left[s_{AD} + \frac{h}{2}, s_{AB} \right), \\ \frac{12}{b^2 h} (s - s_{AB})^3 - \frac{3}{h} (s - s_{AB}), & s \in \left[s_{AB}, s_{AB} + \frac{b}{2} \right), \\ -\frac{12}{b^2 h} (b - s + s_{AB})^3 + \frac{3}{h} (b - s + s_{AB}), & s \in \left[s_{AB} + \frac{b}{2}, s_{BC} \right), \\ -\frac{4}{h^3} \left(\frac{h}{2} - s + s_{BC} \right)^3 + \frac{6}{h^2} \left(\frac{h}{2} - s + s_{BC} \right)^2 - 1, & s \in \left[s_{BC}, s_{BC} + \frac{h}{2} \right), \\ -\frac{4}{h^3} \left(s - s_{BC} - \frac{h}{2} \right)^3 - \frac{6}{h^2} \left(s - s_{BC} - \frac{h}{2} \right)^2 + 1, & s \in \left[s_{BC} + \frac{h}{2}, s_{CD} \right), \\ -\frac{12}{b^2 h} (s - s_{CD})^3 + \frac{3}{h} (s - s_{CD}), & s \in \left[s_{CD}, s_{CD} + \frac{b}{2} \right), \\ \frac{12}{b^2 h} (b - s + s_{CD})^3 - \frac{3}{h} (b - s + s_{CD}), & s \in \left[s_{CD} + \frac{b}{2}, s_{DA} \right). \end{cases} \quad (47)$$

Because the axial deformations are orthogonal to each other, the axial deformation becomes 0:

$$\psi_{\varphi 5}^{X_b}(s) = 0. \quad (48)$$

According to the rule of strain measurement, the above deformation is not axially deformed, that is:

$$\psi_5^{X_b}(s) = \psi_{n5}^{X_b}(s). \quad (49)$$

5.1.3. Derivation of Warping Shape Function Expression. Warping is caused by uneven expansion of the siding. Based on the identified deformation characteristics of the characteristic deformations 10 and 11, the function is approximated

by a quadratic polynomial:

$$\psi_{nj}^{X_b}(s) = a_j^2 s^2 + a_j^1 s + a_j^0. \quad (50)$$

The coefficients in the formula are consistent with those mentioned in the previous section and are determined by the section deformation characteristics and geometric symmetry characteristics. According to the central symmetry characteristic of the torsional warping deformation, the biaxial symmetry characteristic of the cross-section can be simplified to solve the torsion warping model of the section to the shape function of the half-model (shown in Figure 18).

For the half-model, the next six conditions are used as the boundary conditions for determining the plane profile deformation function of the two side wall plates of the corner node:

- (1) Because the deformations on walls A and B are, respectively, opposed to S_A and S_B , the axial shape at the symmetry point becomes 0, that is,

$$\psi_{n10}^{X_b}(s)|_{s_{AD}+h/2} = \psi_{n10}^{X_b}(s)|_{s_{AB}+b/2} = 0. \quad (51)$$

- (2) The slopes at the two points of the central symmetry are equal, and the displacements are opposite. Taking the two end points of the wall plate as an example, joint continuity is assumed:

$$\left. \frac{d\psi_{n10}^{X_b}(s)}{ds} \right|_{s_{AD}^+} = \left. \frac{d\psi_{n10}^{X_b}(s)}{ds} \right|_{s_{AB}^-}, \quad (52)$$

$$\left. \frac{d\psi_{n10}^{X_b}(s)}{ds} \right|_{s_{AB}^+} = \left. \frac{d\psi_{n10}^{X_b}(s)}{ds} \right|_{s_{BC}^-}, \quad (53)$$

$$\psi_{n10}^{X_b}(s)|_{s_{AD}} = -\psi_{n10}^{X_b}(s)|_{s_{AB}}, \quad (54)$$

$$\psi_{n10}^{X_b}(s)|_{s_{AB}} = -\psi_{n10}^{X_b}(s)|_{s_{BC}}. \quad (55)$$

The six linear independent equations in the simultaneous Equation (23) are solved and substituted into the quadratic polynomial. The axial deformation function of the half-model of the rectangular section:

$$\psi_{\varphi 10}^{X_b}(s) = \begin{cases} -\frac{2}{h} (s - s_{AD}) + 1, & s \in [s_{AD}, s_{AB}), \\ \frac{2}{b} (s - s_{AB}) - 1, & s \in [s_{AB}, s_{BC}), \\ -\frac{2}{h} (s - s_{BC}) + 1, & s \in [s_{BC}, s_{CD}), \\ \frac{2}{b} (s - s_{AD}) - 1, & s \in [s_{CD}, s_{DA}). \end{cases} \quad (56)$$

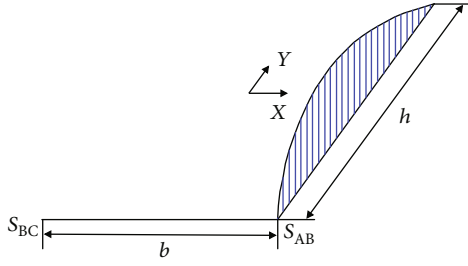


FIGURE 19: Bending warping section deformation.

According to the warping deformation characteristics and geometric symmetry characteristics of the warping deformation, the bending warping model of the section is simplified to be solved by the half-model as shown in Figure19.

According to the half-model shown in Figure20, the following six conditions are used as boundary conditions for determining the plane profile function of the two side wall plates of the corner node:

- (1) The deformation on wall A is symmetrical about the center point of wall A, and the slope of the axial deformation function at the symmetry point is 0:

$$\left. \frac{d\psi_{\varphi 11}^{x_b}(s)}{ds} \right|_{s_{AD}+h/2} = 0. \quad (57)$$

- (2) The axial deformation of wall B is 0:

$$\psi_{\varphi 11}^{x_b}(s)|_{s_{AB}} = 0. \quad (58)$$

- (3) The amplitude of the center point of wall A shown in Figure 12 is 1:

$$\psi_{\varphi 11}^{x_b}(s)|_{s_{AD}+h/2} = 1. \quad (59)$$

The six linear independent equations are combined in the joint solution, solved, and substituted in the quadratic polynomial. According to the symmetry characteristics, the axial deformation function of the model is obtained:

$$\psi_{11}^{x_b}(s) = \psi_{\varphi 11}^{x_b}(s) = \begin{cases} -\frac{4}{h^2}(s-s_{AD})^2 + \frac{4}{h}(s-s_{AD}), & s \in [s_{AD}, s_{AB}), \\ 0, & s \in [s_{AB}, s_{BC}), \\ \frac{4}{h^2}(s-s_{BC})^2 - \frac{4}{h}(s-s_{BC}), & s \in [s_{BC}, s_{CD}), \\ 0, & s \in [s_{CD}, s_{DA}). \end{cases} \quad (60)$$

The above is the expression of the shape function of each feature deformation mode. After substituting the above equation into the experimental structure, each coefficient χ_b^L , χ_b^D ,

and χ_b^W for each section is solved and returned to the original equation to obtain the values. The effects of distortion and warping in the low- and high-order modes under the action of the thin-walled curved beam under the in-plane load are clearly shown in Figure20.

6. Results

As the experimental results show, the values of 60 positions in the walls are as shown in Table 3. The strain at the test position of wall A is negative, that is, a compression value, while those at the locations of wall C are positive, or tensile, the value of 2 position approaches 0. The value of B and D walls near wall A, that is, the 3 locations in wall B and 1 position in wall D are positive values, that is, tensile, while the far wall A is negative, and the value of the 2 position point is the middle value of the 1 position point and the 3-position point value.

Taking a typical 3-position point in wall A and 1-position point in wall B as examples, the strain change of the entire curved beam is represented. The value is as shown in Figure21. It also can be seen from the figure that the strain value of locations in compression and tensile of the curved beam are basically the same; the values decrease from the constrained end to the free end, which conforms to the trend of force deformation.

Figure22 shows the results of the experimental test A3 position and the results of the one-dimensional experimental test theory. The graph compares the actual deformation with the low-order, distortion, and the warping effects.

The low-order effect is the main influencing factor of the deformation which is marked by red line, and the influence value is larger than those for distortion and warping. The low-order effect value becomes larger and then smaller, and the maximum value occurs at the second test point of 22.5° which finally approach 0.

The distortion effect is mostly compression amount which is marked by blue line, for tensile effect; the value changes from large to small and becomes larger after approaching 0. The maximum value also occurs at the 22.5° test position, before decreasing again and approaching 0. In warping marked by green line, the influence has a positive value, that is, the tensile effect. The influence value first changes from large to small. The minimum extreme point also occurs near the 22.5° position; the value then increases to the maximum extreme point at 45° test position and then decreases until it approaches 0.

For low-order influence, the above actual deformation value derivation and one-dimensional test theory can obtain the deformation form and its composition. The respective influences of various low-order characteristic deformations under the action of in-plane loading are illustrated in Figure23, with the low-order effects obtained after calculation $u_{L1}(s, \phi)$, $u_{L2}(s, \phi)$, $u_{L3}(s, \phi)$, $u_{L7}(s, \phi)$, $u_{L8}(s, \phi)$, and $u_{L9}(s, \phi)$. The influences of the six low-order strains show that the low-order deformation, except the ninth characteristic deformation mode, is near 0, and the influences are smaller than that of the ninth characteristic deformation mode. In

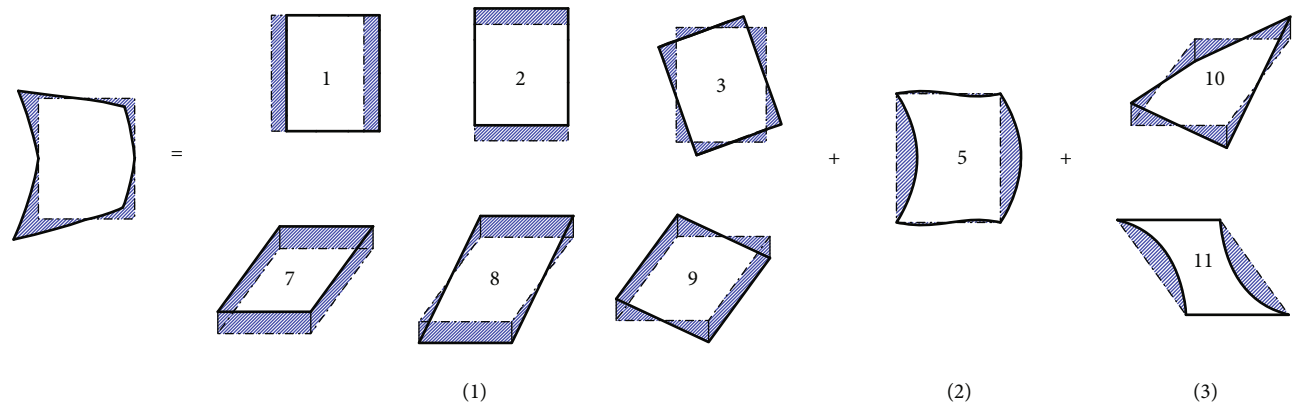


FIGURE 20: Deformation mode and its composition.

TABLE 3: Variation in test deformation in the entire curved beam.

Wall	Section Position	1			2			3			4			5		
		1	2	3	1	2	3	1	2	3	1	2	3	1	2	3
A	Sign	—	—	—	—	0	—	—	0	—	—	0	—	—	0	—
B		—	+	+	—	+	+	—	+	+	—	+	+	—	0	+
C		+	+	+	+	0	+	+	0	+	+	0	+	+	0	+
D		+	—	—	+	—	—	+	—	—	+	—	—	+	—	—

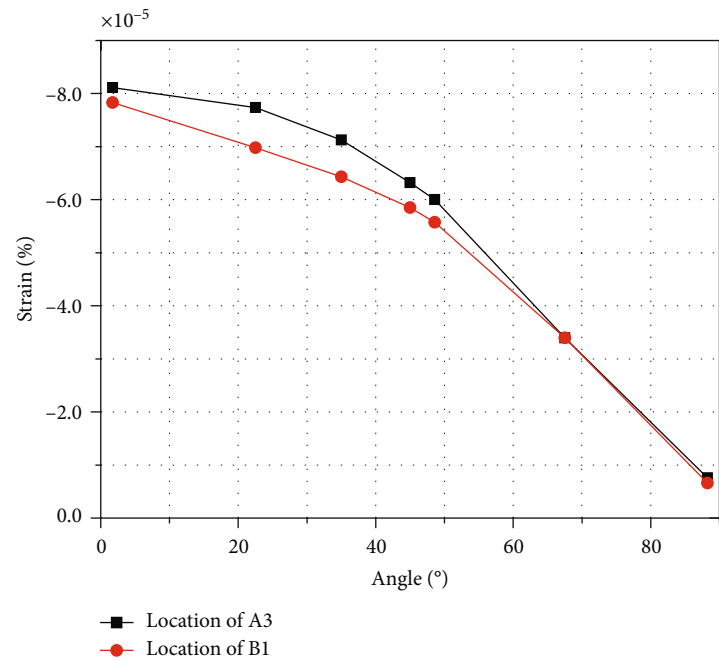


FIGURE 21: Test deformation varies of location

the low-order deformation effect, the ninth characteristic deformation mode has the greatest influence, which means that the displacement clockwise along the y -axis is the largest. This direction is consistent with the direction of load application, which determines the low-order influence throughout

the deformation, with a trend matching the overall low-order effect. The first deformation mode is translation along the x -axis, and the deformation from the constrained position to 32° along the curved beam is in the direction of the outer

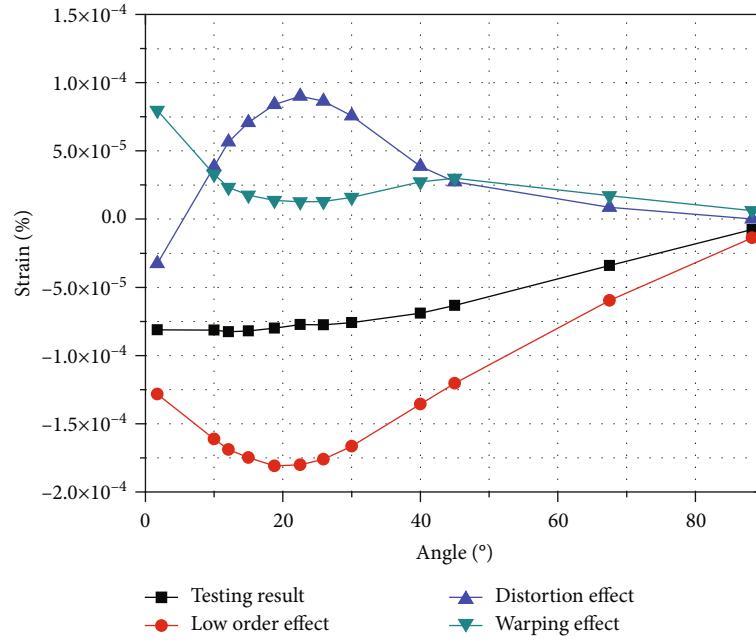


FIGURE 22: Low-order, distortional, and warping effects.

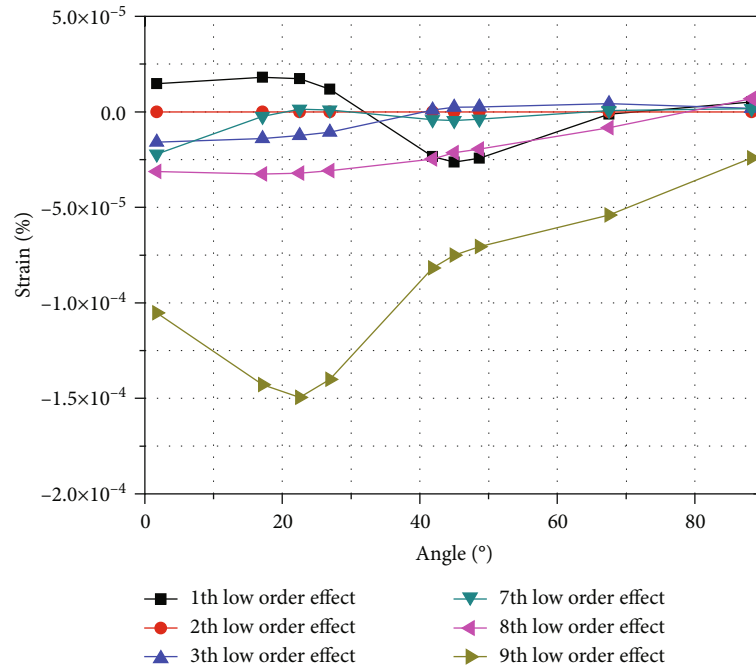


FIGURE 23: Six low-order effects.

diameter along the x -axis. From this area to the load application position, the negative direction along the x -axis is the reverse translation of the inner diameter, and the influence value changes from small to large. The maximum extreme point occurs at 45° and then becomes smaller until it approaches zero. The second characteristic deformation mode of low-order deformation has no effect, that is, the curved beam under the in-plane load has no translation along the y -direction. The third and seventh deformation

modes have little influence, that is, rigid rotation along the z -axis and the axial expansion are both negative and gradually approaching zero. Rigid rotation around the x -axis (the eighth deformation mode) is clockwise, and the influence value changes from large to small and finally approaches zero.

The 10th deformation mode in the warping effect is the torsional warping effect, and the 11th mode is the bending warping effect. Figure 24 shows that the two warping forms

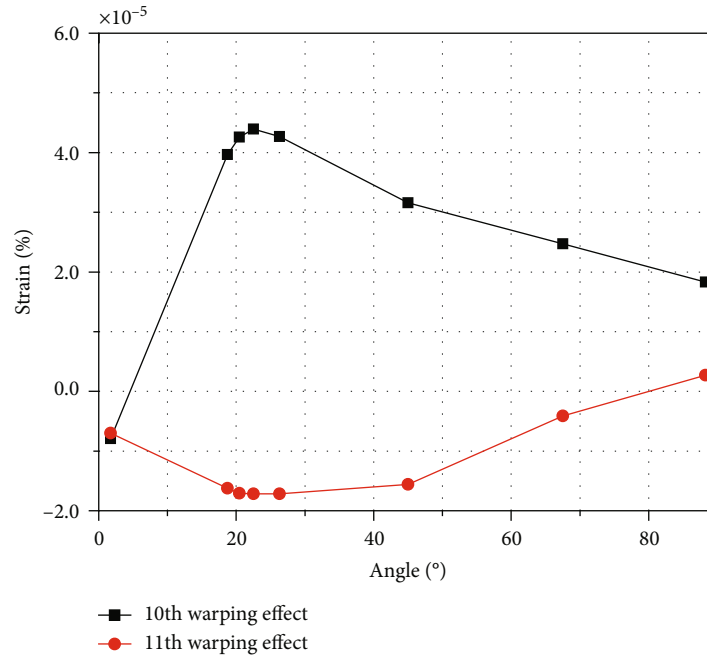


FIGURE 24: Bending torsional warping effects.

affect the curved beam under in-plane loading, the torsional effect is greater than the bending effect, and both vary from large to small, with the maximum extreme points occurring at the 22.5° test point.

7. Conclusion

A new method of one-dimensional deformation experimental test theory has been proposed for calculating and judging the contributions of low-order deformation effect and the high-order distortion and warping effects to the actual deformation of a thin-walled curved rectangular box beam under in-plane bending loads. Because the vector of deformation cannot be directly measured, we converted vectors in three directions containing axial, tangential, and normal deformations into superimposable tensile and compressive amounts, which are scalars that can be superimposed and matched with experimental data. As to the finite element analysis of plane problem on curved beam, four nodes triangular element performs better property on higher accuracy and faster convergence, then the deep collocation method element; more neurons and hidden layers could obtain better results, while the inverse finite element method experimentally measured strains are used as input data, in which more strain gauges should be used. This theory can be implemented in elastomeric materials and structures to measure the deformation distribution of various elastomer materials and structures and other mechanical properties of the structure. An experimental test system was established to obtain the deformation distribution of the entire curved beam structure at any position. The deformation value of the entire curved beam structure under the bending load was determined by marking 60 test locations evenly distributed on the four walls at five cross-sectional locations on the curved beam structure.

The significance of the distortion and warping components in the actual deformation and the main role of low-order deformations are verified. The magnitude and variation trends of the eleven deformation modes are obtained; no radial translation of the curved beam structure occurs under in-plane bending.

Data Availability

The data used to support the findings of this study are available from the corresponding author upon request.

Conflicts of Interest

The authors declare that they have no conflicts of interest.

Acknowledgments

This work was supported by the Major Science and Technology Project of Liaoning Province (2020JH1/10100012), "Seedling Cultivation" Project for Young Scientific and Technological Talents of Liaoning Education Department (lnqn202008/lnqn201908), National Natural Science Foundation of China (Grant no. 52005352), the National Key Research and Development Program of China (2017YFC0704003/2017YFC0703903), and the National Key Technology R&D Program of China (2011BAJ02B07).

References

- [1] V. Z. Vlasov, *Thin Walled Elastic Beams, Seconded*, The Israel Program for Scientific Translations, Jerusalem, 1961.
- [2] R. Dabrowski, "Curved thin-walled girders," Cement and Concrete Association, London, 1968.

- [3] Y. Y. Kim and J. H. Kim, "Thin-walled closed box beam element for static and dynamic analysis," *International Journal for Numerical Methods in Engineering*, vol. 45, no. 4, pp. 473–490, 1999.
- [4] J. H. Kim and Y. Y. Kim, "One-dimensional analysis of thin-walled closed beams having general cross sections," *International Journal for Numerical Methods in Engineering*, vol. 49, pp. 653–668, 2000.
- [5] Y. Kim and Y. Y. Kim, "Analysis of thin-walled curved box beam under in-plane flexure," *International Journal of Solids and Structures*, vol. 40, no. 22, pp. 6111–6123, 2003.
- [6] N. I. Kim, Y. S. Park, C. C. Fu, and M. Y. Kim, "Stiffness matrix of thin-walled curved beam for spatially coupled stability analysis," *International Journal of Mechanical Sciences*, vol. 50, no. 4, pp. 788–803, 2008.
- [7] L. Zhang, Z. Zhu, G. Shen, and G. Cao, "Free vibration analysis of thin-walled rectangular box beams based on generalized coordinates," *Journal of Vibroengineering*, vol. 16, no. 8, pp. 3900–3911, 2014.
- [8] L. Zhang, Z. Zhu, G. Shen, and G. Cao, "A finite element for spatial static analyses of curved thin-walled rectangular beams considering eight cross-sectional deformation modes," *Arabian Journal for Science and Engineering*, vol. 40, no. 12, pp. 3731–3743, 2015.
- [9] L. Zhang, *Study on Dynamic Behaviors of Walking Sinking Platform for the Construction of Shafts with Depth over 1000 Meters*, [Ph.D. thesis], China University of Mining and Technology, 2016.
- [10] A. Afnani, R. E. Erkmen, and V. Niki, "An efficient formulation for thin-walled beams curved in plan," *International Journal of Steel Structures*, vol. 17, no. 3, pp. 1087–1102, 2017.
- [11] M. R. Fazlali, J. Arghavani, and M. Eskandari, "An analytical study on the elastic-plastic pure bending of a linear kinematic hardening curved beam," *International Journal of Mechanical Sciences*, vol. 144, pp. 274–282, 2018.
- [12] M. T. Piovan and V. H. Cortinez, "Linear viscoelastic analysis of straight and curved thin-walled laminated composite beams," *International Journal of Solids and Structures*, vol. 45, no. 11–12, pp. 3466–3493, 2008.
- [13] I. S. Choi, G. W. Jang, S. Choi, D. Shin, and Y. Y. Kim, "Higher order analysis of thin-walled beams with axially varying quadrilateral cross sections," *Computers and Structures*, vol. 179, no. 2017, pp. 127–139, 2017.
- [14] Y. Y. Kim and Y. Kim, "A one-dimensional theory of thin-walled curved rectangular box beams under torsion and out-of-plane bending," *International Journal for Numerical Methods in Engineering*, vol. 53, no. 7, pp. 1675–1693, 2002.
- [15] Z. Zhu, L. Zhang, G. Shen, and G. Gao, "A one-dimensional higher-order theory with cubic distortional modes for static and dynamic analyses of thin-walled structures with rectangular hollow sections," *Acta Mechanica*, vol. 227, pp. 2451–2475, 2016.
- [16] M. Rezaiee-Pajand, M. Ramezani, and N. Gharaei-Moghaddam, "Using higher-order strain interpolation function to improve the accuracy of structural responses," *International Journal of Applied Mechanics*, vol. 4, article 2050026, 2020.
- [17] M. Rezaiee-Pajand, N. Gharaei-Moghaddam, and M. Ramezani, "Higher-order assumed strain plane element immune to mesh distortion," *Engineering Computations*, vol. 37, no. 9, pp. 2957–2981, 2020.
- [18] M. Rezaiee-Pajand, N. Gharaei-Moghaddam, and M. Ramezani, "Strain-based plane element for fracture mechanics' problems," *Theoretical and Applied Fracture Mechanics*, vol. 108, article 102569, 2020.
- [19] M. Rezaiee-Pajand, N. Gharaei-Moghaddam, and M. Ramezani, "A new higher-order strain-based plane element," *Scientia Iranica*, vol. 26, pp. 2258–2275, 2019.
- [20] M. Rezaiee-Pajand, N. Gharaei-Moghaddam, and M. Ramezani, "Two triangular membrane elements based on strain," *International Journal of Applied Mechanics*, vol. 4, 2019.
- [21] S. Li, C. Wei, and Y. Long, "Deformation analysis of engineering reinforcement straightening based on Bauschinger effect," *International Journal of Steel Structures*, vol. 20, no. 1, pp. 1–12, 2020.
- [22] H. Guo, X. Zhuang, and T. Rabczuk, "A deep collocation method for the bending analysis of Kirchhoff plate," *Computers, Materials and Continua*, vol. 58, no. 2, pp. 433–456, 2019.
- [23] E. Samaniego, C. Anitescu, S. Goswami et al., "An energy approach to the solution of partial differential equations in computational mechanics via machine learning: concepts, implementation and applications," *Computer Methods in Applied Mechanics and Engineering*, vol. 362, pp. 112790.1–112790.29, 2020.
- [24] M. Gherlone, M. Mattone, M. di Sciuva, A. Tessler, and A. Tessler, "Shape sensing of 3D frame structures using an inverse finite element method," *International Journal of Solids & Structures*, vol. 49, no. 22, pp. 3100–3112, 2012.
- [25] M. Gherlone, P. Cerracchio, M. Mattone, M. di Sciuva, and A. Tessler, "An inverse finite element method for beam shape sensing: theoretical framework and experimental validation," *Smart Materials & Structures*, vol. 23, no. 4, article 045027, 2014.
- [26] K. Adnan and Y. Mehmet, "Modeling of sensor placement strategy for shape sensing and structural health monitoring of a wing-shaped sandwich panel using inverse finite element method," *Sensors*, vol. 17, no. 12, article 2775, 2017.
- [27] A. Kefal, E. Oterkus, A. Tessler, and J. L. Spangler, "A quadrilateral inverse-shell element with drilling degrees of freedom for shape sensing and structural health monitoring," *Engineering Science and Technology, an International Journal*, vol. 19, no. 3, pp. 1299–1313, 2016.
- [28] A. Kefal, A. Tessler, and E. Oterkus, "An enhanced inverse finite element method for displacement and stress monitoring of multilayered composite and sandwich structures," *Composite Structures*, vol. 179, pp. 514–540, 2017.
- [29] A. Kefal, J. B. Mayang, E. Oterkus, and M. Yildiz, "Three dimensional shape and stress monitoring of bulk carriers based on iFEM methodology," *Ocean Engineering*, vol. 147, pp. 256–267, 2018.
- [30] Y. S. Choo, N. Choi, and B. Chai Lee, "Quadrilateral and triangular plane elements with rotational degrees of freedom based on the hybrid Trefftz method," *Finite Elements in Analysis and Design*, vol. 42, no. 11, pp. 1002–1008, 2006.
- [31] Y. Long, K. Zhang, H. Shi, and S. Li, "Theoretical and experimental study on strain distribution of curved beam in-plane force considering pre-bending," *Journal of the Brazilian Society of Mechanical Sciences and Engineering*, vol. 42, no. 11, pp. 1–15, 2020.

Research Article

Prediction of Welding Deformation and Residual Stress of a Thin Plate by Improved Support Vector Regression

Lei Li , Di Liu, Shuai Ren, Hong-gen Zhou, and Jiasheng Zhou

School of Mechanical Engineering, Jiangsu University of Science and Technology, Zhenjiang 212003, China

Correspondence should be addressed to Lei Li; lilei0064@sina.com

Received 25 September 2020; Revised 11 November 2020; Accepted 15 February 2021; Published 3 March 2021

Academic Editor: Jian Chen

Copyright © 2021 Lei Li et al. This is an open access article distributed under the Creative Commons Attribution License, which permits unrestricted use, distribution, and reproduction in any medium, provided the original work is properly cited.

Thin plates are widely utilized in aircraft, shipbuilding, and automotive industries to meet the requirements of lightweight components. Especially in modern shipbuilding, the thin plate structures not only meet the economic requirements of shipbuilding but also meet the strength and rigidity requirements of the ship. However, a thin plate is less stable and prone to destabilizing deformation in the welding process, which seriously affects the accuracy and performance of the thin plate welding structure. Therefore, it is beneficial to predict welding deformation and residual stress before welding. In this paper, a thin plate welding deformation and residual stress prediction model based on particle swarm optimization (PSO) and grid search (GS) improved support vector regression (PSO-GS-SVR) is established. The welding speed, welding current, welding voltage, and plate thickness are taken as input parameters of the improved support vector regression model, while longitudinal and transverse deformation and residual stress are taken as corresponding outputs. To improve the prediction accuracy of the support vector regression model, particle swarm optimization and grid search are used to optimize the parameters. The results show that the improved support regression model can accurately evaluate the deformation and residual stress of butt welding and has important engineering guiding significance.

1. Introduction

Welding is a process of forming permanent connection by heating or pressing the material of the workpiece to achieve the combination of atoms. Compared with riveted parts, castings, and forgings, welding products have the advantages of being lightweight, having a simple process, having low production cost, and having strong adaptability [1]. The welding technology is an indispensable processing method, which is widely used in aerospace, atomic energy, electronic technology, shipbuilding, construction, marine engineering, transportation and machinery manufacturing, and other industrial sectors [2–4]. Various welding deformations can occur in ship structures due to uneven heat and cold, local uncoordinated plastic strains, and welding residual stresses. Welding deformation and stress are important factors that affect the quality of hull construction and have a great impact on the welding performance, structural strength, toughness, aesthetics, and accuracy control of ship construction. This phenomenon is more obvious in thin plate welding [5].

Therefore, the research on prediction and control of welding deformation and residual stress of a thin plate has a very important engineering application value.

With the development of numerical analysis theory, the finite element method (FEM) has been adopted by many studies to predict welding deformation and residual stress. Since Ueda and Yamakawa analyzed the welding thermal stress and residual stress of butt and fillet welds by the thermo-elastic-plastic FEM, many researchers continued to develop this method for calculating the temperature, residual stress, and deformation [6]. At present, the FEM is also used in different welded joints and simple structure welds [7–9]. Liang et al. studied the welding deformation of aluminum alloy sheets by experiment and the TEP finite element method. The out-of-plane deformation predicted by the finite element method is in good agreement with the measured results [10]. Deng et al. used the finite element method to predict the welding deformation and residual stress of a thin plate and further investigated the influence of external constraints on welding deformation [11–14]. Shen et al.

TABLE 1: The chemical composition and mechanical properties of AH32.

C	Mn	Si	S	P	Yield strength (MPa)	Tensile strength (MPa)	Elongation (%)
≤0.18	0.70~1.60	0.10~0.50	≤0.04	≤0.04	315	440~590	22

derived the stress amplification factor considering the influence of the preliminary deformation of the thin plate on the basis of the modified thick plate calculation formula. Then, with the traditional specification of the calculation, results were compared to verify the feasibility and effectiveness of the formula [15, 16]. Hu et al. established a finite element model to study the lateral bow and direction residual stress of s690 cold-formed thin-walled steel [17].

In many cases, the deformation and residual stress are simulated by FEM and then verified by experimental measurement. However, the FEM takes a long time and requires high computer performance and the implementation of experimental measurement needs high condition and cost [5]. Therefore, it is meaningful to setup a model which can predict the deformation and residual stress before welding. In the past decade, various forecasting models have emerged. He and Li applied a support vector machine (SVM) to quantitatively evaluate the welding quality [18]. Tian and Luo established an intelligent prediction model for welding deformation of T-joint fillet weld based on combinatorial optimization algorithms [19]. Katherasan et al. adopted the artificial neural network (ANN) algorithm to determine the approximate optimal value of welding process parameters and then used particle swarm optimization (PSO) to optimize the process parameters [20]. Edwin and Kumanan discussed the application of the evolutionary fuzzy support vector regression model in welding residual stress prediction [21]. Ansari-pour et al. uses the ANN algorithm and multiobjective optimization algorithm to minimize deformation and residual stress during submerged arc welding [22]. Rong et al. analyzed the influence of the weld profile on angle distortion and predicted the angle distortion of gapless tungsten inert gas arc weld using the neural network [23]. Mathewa et al. established the prediction model of residual stress distribution of austenitic stainless steel girth-welded pipe by using the artificial neural network [24]. Sagai et al. successfully used process parameters to predict mechanical properties by using the stochastic and nonlinear parallel machining neural network model [25]. Das et al. used the machine learning algorithm to predict the welding residual stress of stainless steel [26]. Mathew et al. used the fuzzy neural network (FNN) to predict the welding residual stress of pressure vessels and achieved good results [27]. Koo et al. proposed a prediction model of residual stress in the welding area based on improved support vector regression [28].

In this paper, the corresponding inherent deformation and residual stress are obtained under different values of voltage, current, speed, and plate thickness. Based on the experimental data, a prediction model of welding deformation and residual stress of a thin plate based on particle swarm optimization and grid search-improved support vector regression (PSO-GS-SVR) was established. Then, the predicted results of the PSO-GS-SVR model are compared with

TABLE 2: Welding parameters.

Parameter	Units	Notation				
Voltage	V	U	25	27	29	31
Current	A	I	180	190	200	210
Speed	mm/s	S	5	6	7	8
Plate thickness	mm	T	3	4	5	6

the experimental results. The results show that there is a high degree of consistency between the predicted results and the experimental measurements. The research shows that the improved support regression model can more accurately evaluate the welding deformation and residual stress of butt welding than the original model.

The rest of this paper is arranged as follows. Section 2 shows that the deformation and residual stress corresponding to different welding parameters are obtained by experiments. Section 3 introduces the related algorithm theory. In Section 4, an improved prediction method of support vector regression is established. The optimized SVR model was evaluated by comparing the prediction results with the experimental results, which is shown in Section 5. Finally, in Section 6, this paper is summarized and the future research direction is pointed out.

2. The Experimental Procedure

In this experiment, two similar V-joint planes of 300×150 mm plates were selected. The workpiece material is AH32, which is high-strength steel. The chemical composition and mechanical properties are shown in Table 1. Due to the small welding deformation and residual stress, CO_2 gas-shielded welding is adopted, which is especially suitable for thin plate welding. The process parameters, namely, voltage (U), current (A), speed (S), and plate thickness (T), are varied in the range of 25–31 V, 180–210 A, 5–8 mm/s, and 3–6 mm, respectively. The detailed combination of the test process parameter design is shown in Table 2. Then, the transverse deformation and longitudinal deformation of welding are measured by a coordinate measuring machine (CMM). The residual stress of the workpiece was measured by X-ray diffraction.

2.1. Measurement of Deformation. In order to accurately measure the welding deformation value, the deformation results of V-shaped groove components after welding were measured by a coordinate measuring machine. The welding component is placed on the measuring platform, and the measuring platform is used as the zero-value point of bending deformation. Then, the transverse deformation and longitudinal deformation are obtained by measuring the marked measuring points on the workpiece surface step by step. Transverse deformation is the deformation

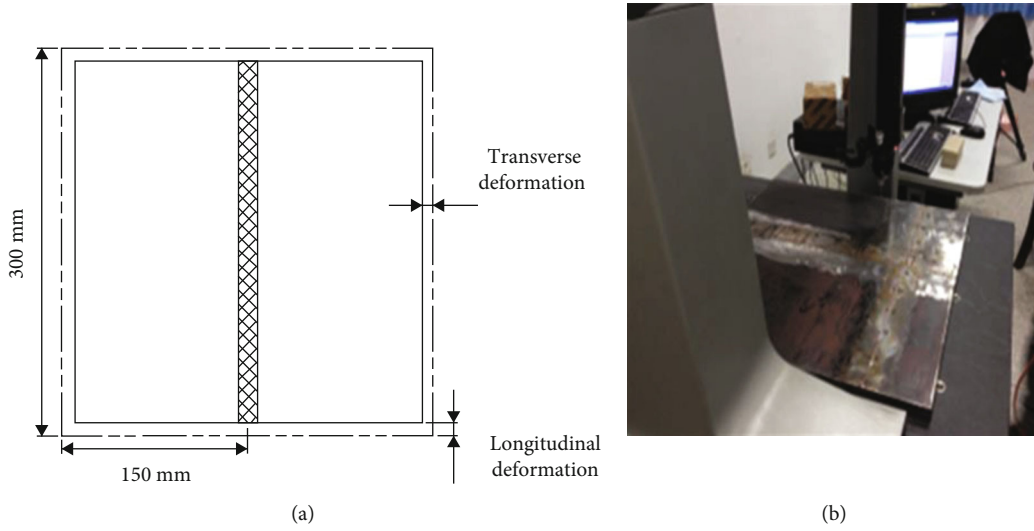


FIGURE 1: Welding deformation measurement. (a) Longitudinal and transverse deformation. (b) Experimental measurements.

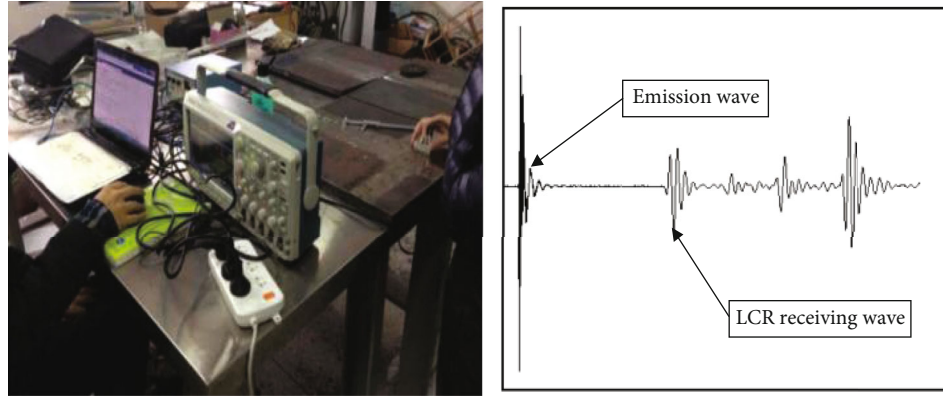


FIGURE 2: Measurement process of residual stress.

perpendicular to the direction of the weld; longitudinal deformation is the deformation parallel to the direction of the weld, as shown in Figure 1(a). The deformation measurement process is shown in Figure 1(b).

2.2. Measurement of Residual Stress. At present, there are many methods to measure welding residual stress. According to the different forms of residual stress measurement, it can be divided into destructive testing and nondestructive testing (NDT) methods [29, 30]. Nondestructive testing has been widely used for its advantages of not damaging components, such as magnetic measurement, ultrasonic measurement, and X-ray diffraction measurement [31–38]. In this paper, the ultrasonic method is selected for measurement. Because the residual stress perpendicular to the weld direction has a great influence on the structural strength, the point perpendicular to the weld direction on the half-width line of the workpiece is taken as the residual stress measurement point [39, 40]. Figure 2 shows the measurement process of residual stress.

2.3. Experimental Dataset. Through the above experimental measurement, this study consists of 24 groups of different

experimentally measured datasets. The dataset is divided into two parts. The left half is for the different U , I , S , and T process parameters. The right half is the deformation values and residual stresses corresponding to the different process parameters. All the experimental results are shown in Table 3.

3. The Related Algorithm Theory

3.1. Support Vector Regression. To solve the problem of pattern recognition, the support vector machine (SVM) is proposed by Vapnik [41]. Later, the insensitive loss function is introduced and applied to the regression estimation of nonlinear systems, which forms support vector regression (SVR). The basic theory of SVR is to map the dataset to a high-dimensional space in the way of nonlinear transformation and then regress in this space to fit a continuous function to minimize the loss function. The goal is to find an optimal classification surface that minimizes the error of all training data, in order to achieve better fitting performance and generalization ability for unknown samples. The SVR has many unique advantages in solving a small sample, nonlinear,

TABLE 3: Experimental results.

Experiment number	Voltage (V)	Current (A)	Speed (mm/s)	Plate thickness (mm)	Transverse deformation(mm)	Longitudinal deformation (mm)	Residual stress (MPa)
1	25	180	5	3	0.531	0.441	61.35
2	25	190	6	4	0.445	0.403	69.78
3	25	200	7	5	0.372	0.344	79.67
4	25	210	8	6	0.313	0.283	217.08
5	27	180	6	5	0.441	0.463	65.78
6	27	190	5	6	0.398	0.421	62.23
7	27	200	8	3	0.341	0.354	117.36
8	27	210	7	4	0.372	0.333	76.27
9	29	180	7	6	0.476	0.461	265.80
10	29	190	8	5	0.455	0.411	183.03
11	29	200	5	4	0.539	0.431	70.23
12	29	210	6	3	0.518	0.386	84.98
13	31	180	8	4	0.493	0.463	89.23
14	31	190	7	3	0.548	0.454	62.82
15	31	200	6	6	0.536	0.401	283.97
16	31	210	5	5	0.579	0.385	143.63
17	25	190	5	3	0.523	0.412	89.67
18	25	210	7	3	0.329	0.312	119.90
19	27	180	8	4	0.413	0.423	92.27
20	27	200	7	4	0.402	0.373	81.89
21	29	180	5	5	0.461	0.489	74.56
22	29	210	7	5	0.440	0.345	158.02
23	31	190	8	6	0.530	0.414	325.09
24	31	210	6	6	0.535	0.368	260.82

high-dimensional pattern recognition, and so on. It has been gradually applied to the prediction of welding deformation and residual stress. The learning ability and generalization ability of SVR are determined by the regularization coefficient C and the related parameters of kernel function. The basic model is as follows [42]:

$$f(x) = \omega \cdot \varphi(x) + b, \quad (1)$$

where $\varphi(x)$ represents the nonlinear mapping of the input sample space to the feature space, ω is the weight coefficient, and b is the offset term. The loss function is obtained by minimizing ω and b .

$$R(x) = \frac{1}{2} \|\omega\|^2 + C \left(\sum_{i=1}^l \mu_i (\xi_i + \xi_i') \right), \quad (2)$$

bound by formula (3) as follows:

$$\begin{cases} f(x_i) - y_i \leq \varepsilon + \xi_i', \\ y_i - f(x_i) \leq \varepsilon + \xi_i, \\ \xi_i, \xi_i' \geq 0, \\ i = 1, 2, \dots, l, \end{cases} \quad (3)$$

where l represents the total of training data, C denotes the regularization coefficient, ε is the insensitive coefficient, ξ_i and ξ_i' are the relaxation variables, and $(1/2)\|\omega\|^2$ is the confidence risk of the model. The SVR model is as follows:

$$f(x) = \sum_{i=1}^l (a_i - a_i') K(x, x_i) + b, \quad (4)$$

where the coefficient $a_i - a_i'$ is not equal to zero and is solved using the quadratic planning technique, the corresponding training data vectors are called support vectors, and $K(x, x_i)$ is the kernel function.

For different kernel functions, the types and quantities of parameters that need to be determined are different. Since the RBF kernel function has the advantages of less parameters and nonlinear prediction, the RBF function is selected as the kernel function of the SVR regression model. The expression of the RBF kernel function is shown in formula (5) as follows:

$$K(x, x_i) = \exp \left(-\frac{\|x - x_i\|^2}{2g^2} \right), \quad (5)$$

where g is the width parameter of the RBF kernel function, x is any input sample vector, and x_i is the center of the Gaussian RBF kernel function.

Therefore, it is important to find the optimal regularization parameter C and the width of kernel function g .

3.2. Particle Swarm Optimization. Particle swarm optimization (PSO), developed by Kennedy and Eberhart, is an evolutionary computing technology derived from the study of bird predation behavior [43]. Particle swarm optimization (PSO) has a faster convergence speed and less adjustable parameters, so it is easy to implement. Therefore, it is often used in combination with other algorithms to optimize parameters. The specific algorithm flow is as follows:

Step 1. Initialize the particle swarm optimization. Set the maximum iteration number, the maximum velocity of particles v_{\max} , the position of the space x_i , the particle swarm optimization modulus N , and the initial flight speed v_i .

Step 2. Define the moderation function. First, calculate the adaptation value for each particle and find the individual optimal solution from it. Then, the global optimal value of a group is found from the individual optimal solution. Finally, the global optimal value is compared with the historical global optimal value and updated.

Step 3. The velocity and position of particles are updated as shown in formula (6) as follows:

$$\begin{aligned} v_i &= \omega * v_i + c_1 * r_1 * i(p_{id} - x_i) \\ &\quad + c_2 * r_1 * (p_{gd} - x_i), \quad i = 1, 2, \dots, N, \\ x_i &= x + v_i, \quad i = 1, 2, \dots, N, \end{aligned} \quad (6)$$

where c_1, c_2 is the learning factor, ω is the inertia factor, $r_1, r_2 \in (0, 1)$ is the random value, p_{id} is the particle local optimal position, and p_{gd} is the global optimal position.

Step 4. If the global optimal solution position satisfies the minimum limit or reaches the maximum iteration number, it will be the output to the particle with optimal fitness.

Because particle swarm optimization has the advantages of good global search ability, fast convergence speed, and less adjustable parameters, it can find the most suitable regularization parameters C and RBF parameter g of SVR more quickly and efficiently.

3.3. Grid Search. Grid search (GS) is widely used in support vector machines for parameter search optimization [44]. It can perform comprehensive search in parallel, and its computational complexity is very prominent. Since the RBF function is chosen as the kernel function of SVR, only the optimal values of C and g had to be determined. This method maps all combinations of these two parameters to a 3D grid, and then, solves all solutions and obtains the optimal combina-

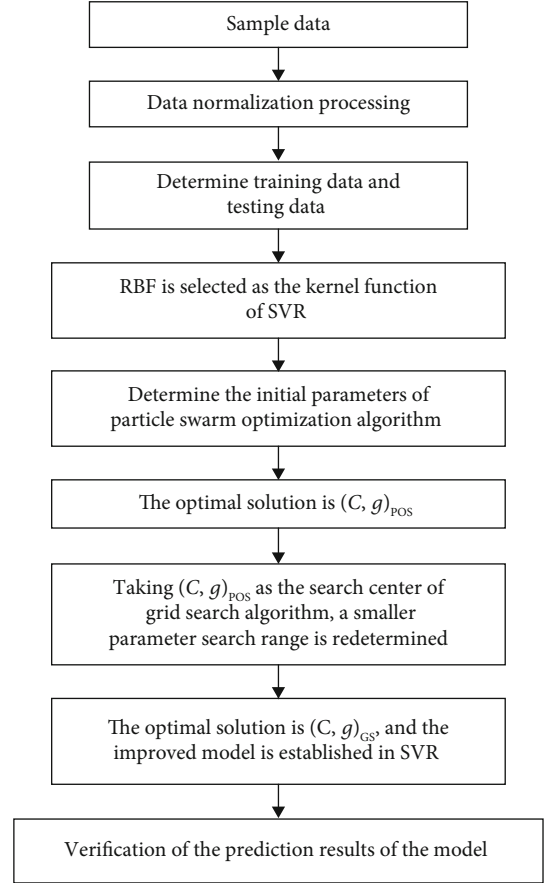


FIGURE 3: The main flow of the PSO-GS-SVR model.

tion. Finally, the groups of C and g with the highest prediction accuracy of cross-validation of the training set are selected as the optimal parameter combination.

4. The SVR Model Improved by the PSO and GS

In this paper, an improved SVR model is proposed by exploiting the advantages of particle swarm optimization and grid search. In the early stage of the algorithm, the particle swarm optimization (PSO) is used for fast rough search in a large range, and then, the population optimal solution (not necessarily the global optimal one) is found. Taking the optimal solution of the population as the initial position, the coordinate system grid of relevant parameters is established, and then, the grid search (GS) is used to search a small step between the initial positions of a small cell, which can avoid a large number of previous invalid operations. In this paper, an improved support vector regression (PSO-GS-SVR) deformation prediction model is developed to predict the weld deformation and residual stresses in butt joints with weld speed, weld current, weld voltage, and plate thickness as inputs. The improved support vector regression prediction model consists of three main steps, namely, data preprocessing, prediction model implementation, and resultant prediction validation. The main flow of the proposed PSO-GS-SVR model is shown in Figure 3.

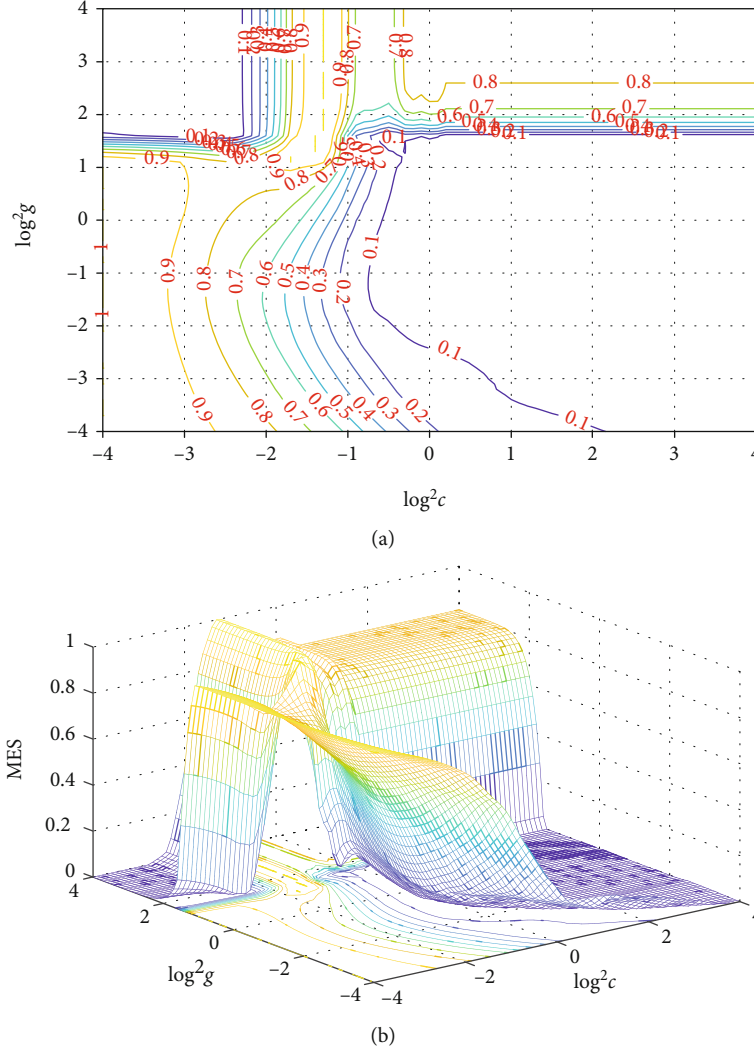


FIGURE 4: Result chart of refined parameter selection. (a) Contour map. (b) 3D view plot.

4.1. Data Preprocessing

4.1.1. Data Normalization Processing. In order to eliminate the difference between dimensions, the sample data is normalized and mapped to $[0, 1]$; the formula is as follows:

$$\bar{x} = \frac{x - x_{\min}}{x_{\max} - x_{\min}}. \quad (7)$$

4.1.2. Data Classification. The first 16 groups of data in Table 1 are used as training data, and the remaining 8 groups of data are used as test data.

4.2. Implementation of the Model. The main implementation steps are as follows:

- (1) Set initial boundary conditions. Particle swarm optimization (PSO) is used to optimize the width g and regularization coefficient C of the kernel function. The parameters involved include population size m , inertia weight w , acceleration constants

c_1 and c_2 , maximum velocity V_{\max} , and maximum algebra G_{\max} . It is determined that the population number is 20 and the population derivation algebra is 100. Because this is the first fast search, the search interval of parameter C can be set a little larger. Select the interval of two parameters as a learning factor. After all the preparatory work is completed, the first parameter optimization process can be started

- (2) After getting the optimal parameters of PSO, it is marked as $(3.151, 0.624)_{\text{POS}}$. According to the optimal parameters, the grid of the coordinate system is established with the parameters as the central starting point and the second fine mesh search of the small step length is carried out. Since the step size of traditional grid search method is generally 0.1, the step size is set to 0.05 in the small step fine search. Set the inter cell as $[2^{-4}, 2^4]$. After a small step search, the optimal solution is obtained as shown in Figure 4, which is recorded as $(3.732, 0.144)_{\text{ms}}$

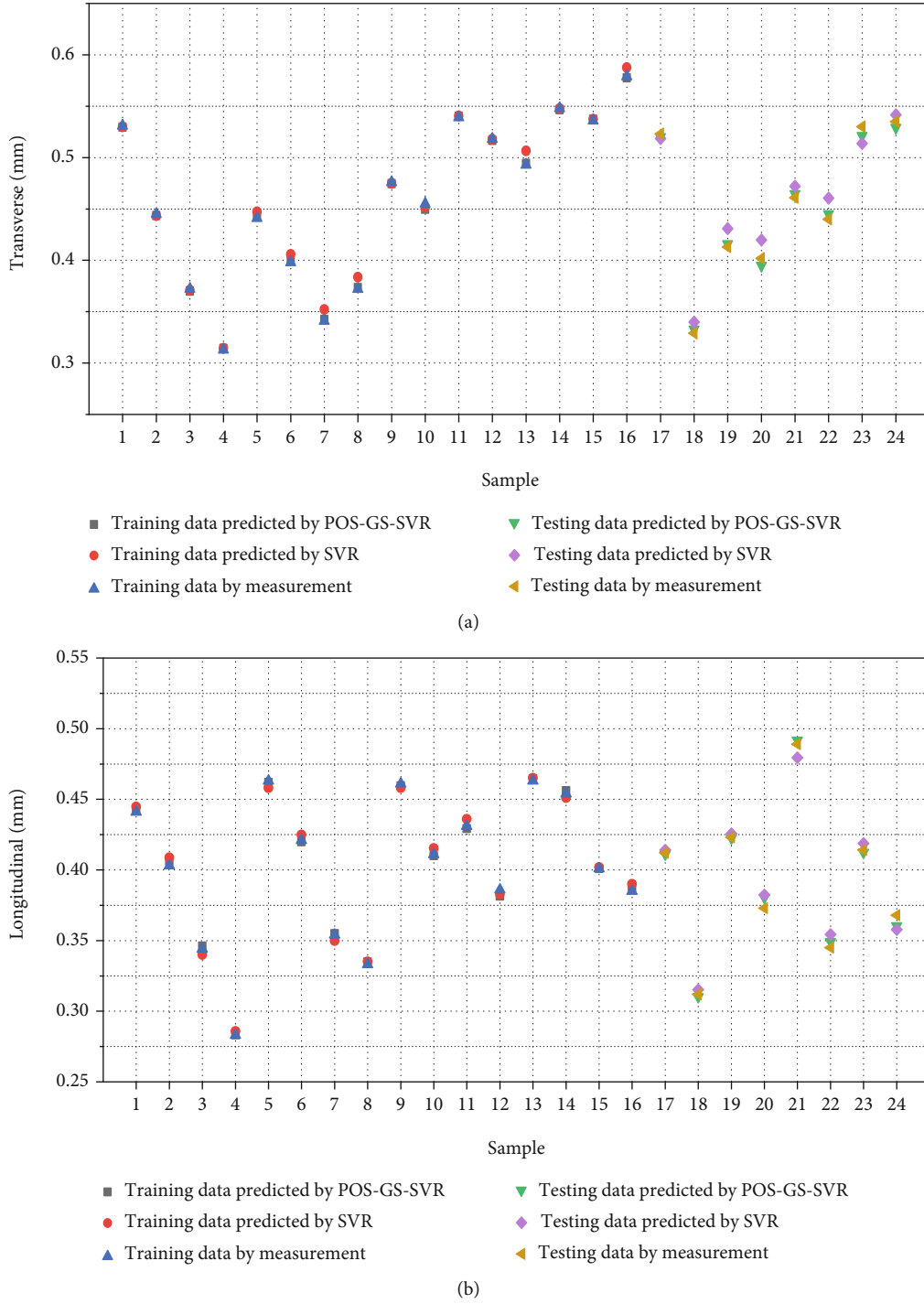


FIGURE 5: Comparison of predicted and experimental deformation values. (a) Transverse deformation. (b) Longitudinal deformation.

- (3) The optimal parameters are substituted into the SVR model and its kernel function to establish the prediction model of improved support vector regression

5. Results and Discussion

In this section, the particle swarm optimization (PSO) and grid search(GS) optimized SVR model was evaluated by

comparing the prediction results with the experimental results. Meanwhile, the accuracy of the optimized SVR model and the nonoptimized SVR model is also compared.

The prediction results of welding deformation and residual stress are shown in Figures 5 and 6, respectively. Among them, the black “■” is the training data predicted by the PSO-GS-SVR model, the red “●” represents training sample data predicted by the SVR model, the blue “▲” stands for the

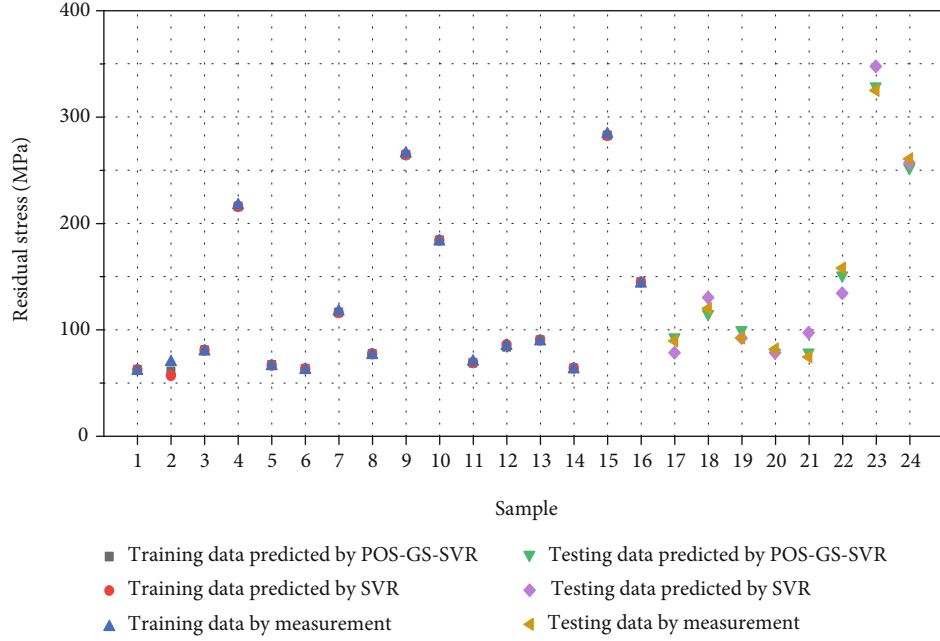


FIGURE 6: Comparison of predicted and experimental residual stress values.

TABLE 4: Prediction performance evaluation of the PSO-GS-SVR model.

		Transverse deformation			Longitudinal deformation			Residual stress		
		R^2	MAPE (%)	MSE	R^2	MAPE (%)	MSE	R^2	MAPE (%)	MSE
PSO-GS-SVR	Training	0.9931	0.5324	0.00001	0.9911	1.1496	0.00005	0.9967	1.9183	6.2346
	Testing	0.9677	1.2437	0.00004	0.9763	2.2527	0.00014	0.9745	4.3015	32.3187
SVR	Training	0.9281	1.5391	0.00010	0.9450	3.7545	0.00023	0.9809	2.2783	11.4254
	Testing	0.8619	4.2559	0.00044	0.9064	5.8612	0.00043	0.8939	9.9153	115.3360

training data of experimental measurement, the green “▼” means the testing data predicted by the PSO-GS-SVR mode, the violet “◆” denotes the testing data predicted by the SVR model, and the yellow “◀” indicates the testing data of experimental measurement. When the PSO-GS-SVR model is used, there is a small difference between the predicted values of weld deformation (as shown in Figure 5) and residual stress (as shown in Figure 6) and the experimental values. Conversely, the predictions of the SVR model are more inaccurate. In conclusion, the proposed PSO-GS-SVR model can improve the prediction accuracy.

In order to further evaluate the prediction performance of the model, we choose three indexes: coefficient of determination (R^2), mean absolute percentage error (MAPE), and mean square error (MSE). These formulas are as follows:

$$\begin{aligned}
 R^2 &= \frac{\sum_{i=1}^n (y_i - \bar{y}_i)^2}{\sum_{i=1}^n (y_i - \bar{y}_i)^2}, \\
 \text{MAPE} &= \frac{1}{n} \sum_{i=1}^n \left(\left| \frac{\hat{y}_i - y_i}{y_i} \right| \right) \times 100\%, \\
 \text{MSE} &= \frac{1}{n} \sum_{i=1}^n (y_i - \hat{y}_i)^2,
 \end{aligned} \tag{8}$$

where \hat{y}_i and y_i denote the predicted values and the experimental values and \bar{y}_i represents the mean value of experimental data. n is the number of samples.

The statistical results shown in Table 4 give the R^2 , MAPE, and MSE of deformation and residual stress. Combined with Figures 5 and 6, the two models are consistent with the overall trend of experimental data. However, further comparison between R^2 , MAPE, and MSE shows that the PSO-GS-SVR model is superior to the SVR model in all three indicators, no matter the testing data or training data. The coefficient of determination approaches is close to 1, indicating a very high degree of a match existing between the predicted values and experimental values. The value of MSE can evaluate the change degree of data. The MSE value tends to be 0, which means that the prediction model has good accuracy. The MAPE value is very small, indicating that the model is stable. Therefore, the proposed PSO-GS-SVR model is feasible to predict the deformation and residual stress of butt welding of thin plates.

6. Conclusion

This paper studies the development of particle swarm optimization and grid search-optimized SVR model for welding

deformation and residual stress of butt joint sheets, and the conclusion is as follows:

- (1) The improved support vector regression model was developed for the prediction of welding deformation and residual stress of butt welding
- (2) The transverse deformation, longitudinal deformation, and residual stress corresponding to different values of welding voltage, welding current, welding speed, and plate thickness were measured by experiments
- (3) The experimentally obtained measurements are used to train the particle swarm and grid search-improved support vector machine model, which can predict the weld deformation and residual stress well. The results show that the PSO-GS-SVR model has excellent generalization capability
- (4) Through the comparison of the three indicators, the PSO-GS-SVR model has better prediction accuracy than the SVR. It provides an effective method to predict welding deformation and residual stress of a thin plate

The current research object is simple butt welding. Considering the diversity of welded joints, our next research work is deformation prediction of a complex welding structure.

Data Availability

All the data used to support the findings of this study are included within the article.

Conflicts of Interest

The authors declare that they have no conflicts of interests.

Acknowledgments

This work was supported by the Special Funding Project for Key Technologies of Ship Intelligence Manufacturing from the MIIT of China under Grant MC-201704-Z02.

References

- [1] H. Wei, Y. Zhang, L. Tan, and Z. Zhong, "Energy efficiency evaluation of hot-wire laser welding based on process characteristic and power consumption," *Journal of Cleaner Production*, vol. 87, pp. 255–262, 2015.
- [2] D. Deng, H. Murakawa, and W. Liang, "Numerical simulation of welding distortion in large structures," *Computer Methods in Applied Mechanics & Engineering*, vol. 196, no. 45–48, pp. 4613–4627, 2007.
- [3] Q. Zhou, Y. Wang, S. K. Choi, L. Cao, and Z. Gao, "Robust optimization for reducing welding-induced angular distortion in fiber laser keyhole welding under process parameter uncertainty," *Applied Thermal Engineering*, vol. 129, pp. 893–906, 2018.
- [4] Y. Rong, G. Mi, J. Xu, Y. Huang, and C. Wang, "Laser penetration welding of ship steel EH36: a new heat source and application to predict residual stress considering martensite phase transformation," *Marine Structures*, vol. 61, pp. 256–267, 2018.
- [5] M. S. Choobi, M. Haghpanahi, and M. Sedighi, "Prediction of welding-induced angular distortions in thin butt-welded plates using artificial neural networks," *Computational Materials Science*, vol. 62, pp. 152–159, 2012.
- [6] Y. Ueda and T. Yamakawa, "Analysis of thermal elastic-plastic stress and strain during welding by finite element method," *Transactions of the Japan Welding Society*, vol. 2, no. 2, pp. 186–196, 1971.
- [7] Y. Lee, H. Jeong, K. Park, Y. Kim, and J. Cho, "Development of numerical analysis model for resistance spot welding of automotive steel," *Journal of Mechanical Science and Technology*, vol. 31, no. 7, pp. 3455–3464, 2017.
- [8] C. Li, D. Fan, X. Yu, and J.-k. HUANG, "Residual stress and welding distortion of Al/steel butt joint by arc-assisted laser welding-brazing," *Transactions of Nonferrous Metals Society of China*, vol. 29, no. 4, pp. 692–700, 2019.
- [9] Z. Lei, J. Zou, D. Wang et al., "Finite-element inverse analysis of residual stress for laser welding based on a contour method," *Optics & Laser Technology*, vol. 129, p. 106289, 2020.
- [10] W. Liang, H. Murakawa, and D. Deng, "Estimating inherent deformation in thin-plate Al-alloy joint by means of inverse analysis with the help of cutting technique," *Advances in Engineering Software*, vol. 99, pp. 89–99, 2016.
- [11] D. Deng and H. Murakawa, "Prediction of welding distortion and residual stress in a thin plate butt-welded joint," *Computational Materials Science*, vol. 43, no. 2, pp. 353–365, 2008.
- [12] D. Deng, Y. Zhou, T. Bi, and X. Liu, "Experimental and numerical investigations of welding distortion induced by CO₂ gas arc welding in thin-plate bead-on joints," *Materials & Design (1980-2015)*, vol. 52, pp. 720–729, 2013.
- [13] D. Deng, H. Murakawa, and N. Ma, "Predicting welding deformation in thin plate panel structure by means of inherent strain and interface element," *Science and Technology of Welding and Joining*, vol. 17, no. 1, pp. 13–21, 2012.
- [14] D. Deng, X. Liu, J. He, and W. Liang, "Investigating the influence of external restraint on welding distortion in thin-plate bead-on joint by means of numerical simulation and experiment," *The International Journal of Advanced Manufacturing Technology*, vol. 82, no. 5–8, pp. 1049–1062, 2016.
- [15] W. Shen, Y. Qiu, L. Xu, and L. Song, "Stress concentration effect of thin plate joints considering welding defects," *Ocean Engineering*, vol. 184, pp. 273–288, 2019.
- [16] W. Shen, Y. Qiu, C. Li, Y. Hu, and M. Li, "Fatigue strength evaluation of thin plate butt joints considering initial deformation," *International Journal of Fatigue*, vol. 125, pp. 85–96, 2019.
- [17] Y. Hu, K. Chung, H. Ban, and D. A. Nethercot, "Investigations into residual stresses in S690 cold-formed circular hollow sections due to transverse bending and longitudinal welding," *Engineering Structures*, vol. 219, p. 110911, 2020.
- [18] K. He and X. Li, "A quantitative estimation technique for welding quality using local mean decomposition and support vector machine," *Journal of Intelligent Manufacturing*, vol. 27, no. 3, pp. 525–533, 2016.
- [19] L. Tian and Y. Luo, "A study on the prediction of inherent deformation in fillet-welded joint using support vector machine and genetic optimization algorithm," *Journal of Intelligent Manufacturing*, vol. 31, no. 3, pp. 575–596, 2020.

- [20] D. Katherasan, J. V. Elias, P. Sathiya, and A. N. Haq, "Simulation and parameter optimization of flux cored arc welding using artificial neural network and particle swarm optimization algorithm," *Journal of Intelligent Manufacturing*, vol. 25, no. 1, pp. 67–76, 2014.
- [21] R. D. J. Edwin and S. Kumanan, "Evolutionary fuzzy SVR modeling of weld residual stress," *Applied Soft Computing*, vol. 42, pp. 423–430, 2016.
- [22] N. Ansari pour, A. Heidari, and S. A. Eftekhari, "Multi-objective optimization of residual stresses and distortion in submerged arc welding process using genetic algorithm and harmony search," *Proceedings of the Institution of Mechanical Engineers Part C-Journal of Mechanical Engineering Science*, vol. 234, no. 4, pp. 862–871, 2020.
- [23] Y. Rong, Y. Huang, G. Zhang, Y. Chang, and X. Shao, "Prediction of angular distortion in no gap butt joint using BPNN and inherent strain considering the actual bead geometry," *International Journal of Advanced Manufacturing Technology*, vol. 86, no. 1–4, pp. 59–69, 2016.
- [24] J. Mathewa, R. J. Moatb, S. Paddea, M. E. Fitzpatrick, and P. J. Bouchard, "Prediction of residual stresses in girth welded pipes using an artificial neural network approach," *International Journal of Pressure Vessels and Piping*, vol. 150, pp. 89–95, 2017.
- [25] F. B. A. Sagai, R. E. Raj, and M. C. Mabel, "Prediction of shear and tensile strength of the diffusion bonded AA5083 and AA7075 aluminium alloy using ANN," *Materials Science and Engineering A-Structural Materials Properties Microstructure and Processing*, vol. 692, pp. 1–8, 2017.
- [26] D. Das, A. K. Das, D. K. Pratihari, and G. G. Roy, "Prediction of residual stress in electron beam welding of stainless steel from process parameters and natural frequency of vibrations using machine-learning algorithms," *Proceedings of the Institution of Mechanical Engineers Part C-Journal of Mechanical Engineering Science*, vol. 203–210, pp. 189–196, 2020.
- [27] J. Mathew, J. Griffin, M. Alamaniotis, S. Kanarachos, and M. E. Fitzpatrick, "Prediction of welding residual stresses using machine learning: comparison between neural networks and neuro-fuzzy systems," *Applied Soft Computing*, vol. 70, pp. 131–146, 2018.
- [28] Y. D. Koo, K. H. Yoo, and M. G. Na, "Estimation of residual stress in welding of dissimilar metals at nuclear power plants using cascaded support vector regression," *Nuclear Engineering & Technology*, vol. 49, no. 4, pp. 817–824, 2017.
- [29] K. Simmen, B. Buch, A. Breitbarth, and G. Notni, "Non-destructive inspection system for MAG welding processes by combining multimodal data," *Quantitative Infrared Thermography Journal*, pp. 1–17, 2019.
- [30] S. Hong, Y. P. Wu, J. H. Wu et al., "Microstructure and cavitation erosion behavior of HVOF sprayed ceramic-metal composite coatings for application in hydro-turbines," *Renewable Energy*, vol. 164, pp. 1089–1099, 2021.
- [31] Y. X. Qiao, Y. P. Chen, L. L. Li et al., "Corrosion Behavior of a Nickel-Free High-Nitrogen Stainless Steel With Hydrogen Charging," *JOM*, 2021.
- [32] L. L. Yang, M. H. Chen, J. L. Wang et al., "Microstructure and composition evolution of a single-crystal superalloy caused by elements interdiffusion with an overlay NiCrAlY coating on oxidation," *Journal of Materials Science & Technology*, vol. 45, pp. 49–58, 2021.
- [33] Y. X. Qiao, D. K. Xu, S. Wang et al., "Effect of hydrogen charging on microstructural evolution and corrosion behavior of Ti-4Al-2V-1Mo-1Fe alloy," *Journal of Materials Science & Technology*, vol. 60, pp. 168–176, 2021.
- [34] H. L. Zhou, F. L. Fu, Z. X. Dai, Y. X. Qiao, J. Chen, and W. Liu, "Effect of laser power on microstructure and micro-galvanic corrosion behavior of a 6061-T6 aluminum alloy welding joints," *Metals*, vol. 11, no. 1, p. 3, 2021.
- [35] Y. Suzuki, H. Yamada, and K. Ikushima, "Tensile-stress dependence of magnetic hysteresis properties measured by the acoustically stimulated electromagnetic response in steel," *IEEE Transactions on Ultrasonics Ferroelectrics and Frequency Control*, vol. 1, no. 1, p. 99, 2019.
- [36] Y. Qiao, J. Huang, D. Huang et al., "Effects of laser scanning speed on microstructure, microhardness and corrosion behavior of laser cladding Ni45 coatings," *Journal of Chemistry*, vol. 2020, Article ID 1438473, 11 pages, 2020.
- [37] S. Salimi, P. Bahemmat, and M. Haghpanahi, "Study on residual stresses caused by underwater friction stir welding: FE modeling and ultrasonic measurement," *Proceedings of the Institution of Mechanical Engineers Part E Journal of Process Mechanical Engineering*, vol. 233, no. 1, pp. 118–137, 2019.
- [38] Y. X. Qiao, Z. H. Tian, X. Cai et al., "Cavitation erosion behaviors of a nickel-free high-nitrogen stainless steel," *Tribology Letters*, vol. 67, no. 1, pp. 1–9, 2019.
- [39] J. R. Nataraj, "Finite element analysis of dissimilar welding between newly developed Cr-free nickel based welding electrode and stainless steel AISI 304," *International Journal of Research in Engineering and Technology*, vol. 2, pp. 130–135, 2013.
- [40] T. Gray, D. Camilleri, and N. McPherson, *Control of Welding Distortion in Thin-Plate Fabrication*, Woodhead Publishing Limited, Cambridge, 1st edition, 2014.
- [41] V. N. Vapnik, *The Nature of Statistical Learning Theory*, Springer-Verlag, New York, NY, 1995.
- [42] V. Kecman, *Learning and Soft Computing: Support Vector Machines, Neural Networks, and Fuzzy Logic Models*, MIT Press, Cambridge, Massachusetts, 2001.
- [43] J. Kennedy and R. Eberhart, "Particle swarm optimization," in *Icnn95-international Conference on Neural Networks*IEEE.
- [44] Q. Huang, J. Mao, and Y. Liu, "An improved grid search algorithm of SVR parameters optimization," in *14th IEEE International Conference on Communication Technology*IEEE.

Research Article

Establishment and Verification of Multiaxis Fatigue Life Prediction Model

Zhuo Fu ¹, Xiang Li,² Sha Zhang,¹ Hanqing Xiong,¹ Chi Liu,¹ and Kun Li¹

¹Department of Mechanical and Electronic Engineering, Changsha University, Changsha 410022, China

²Department of Mechanical and Electronic Engineering, Central South University, Changsha 410083, China

Correspondence should be addressed to Zhuo Fu; fuzhuo2006@163.com

Received 2 October 2020; Revised 18 January 2021; Accepted 22 January 2021; Published 2 February 2021

Academic Editor: Jian Chen

Copyright © 2021 Zhuo Fu et al. This is an open access article distributed under the Creative Commons Attribution License, which permits unrestricted use, distribution, and reproduction in any medium, provided the original work is properly cited.

A fatigue life prediction model with multiaxis load is proposed. The model introduces a new effective cyclic parameter, equivalent stress on the critical surface, to modify the Suresch model. The new damage parameters are not related to empirical constants, hence more applicable for practical application in engineering. The multiaxis fatigue test was carried out with high-strength aluminum alloy 7075-T651, and the multiaxis fatigue life prediction of the test piece was conducted with the finite element software. The experiment result shows that the model proposed is effective for predicting the fatigue life under multiaxis load.

1. Establishment of Multiaxis Fatigue Life Prediction Model

Most mechanical equipment and engineering structural parts run in a complex multidimensional stress state practically. Even if they are under a uniaxial load, the local area is still in the multiaxis stress state due to their complex geometric shape [1]. The interaction of multiaxial stress is the main reason for the fatigue failure of mechanical equipment and structural parts. Therefore, it is of great value to study the multiaxis fatigue life prediction method. To date, a variety of multiaxis fatigue life prediction models [2–6] has been proposed. However, suffering from the limited experiment conditions, the complexity of loading form, and the diversity of materials [7], all the above works are not able to predict multiaxis fatigue life under different loading conditions accurately [8].

The current multiaxis fatigue life prediction mostly adopts the critical plane method, which uses the maximum shear strain plane as the damage plane of the material. The maximum shear strain γ_{\max} and the normal strain ϵ_n on the plane are considered to contribute to the fatigue damage of the material. The critical plane method is used to predict the multiaxis fatigue life. When there is a phase difference between the tensile strain and the shear strain of a material or object, that is, when it is subjected to nonproportional loading, the strain principal axis of the material or object will

periodically change with the cyclical change of the loading. The cyclical change of the strain principal axis results in that the shear strain and the normal strain on the critical plane cannot reach the maximum simultaneously, which leads to the additional strengthening effect of the material. Studies show that the bigger the phase difference angle between the tensile and torsional stresses is, the more prominent the additional effect of the strengthening is while the lower the fatigue life of the material is. Reference [9] proposed a new parameter, the normal strain, which considers that the magnitude of the normal strain amplitude between the two maximum shear strain return points is an important factor affecting the fatigue crack propagation, and meanwhile, the normal strain range can better describe the nonproportional cycle additional hardening effect of the material under the fatigue life of the phenomenon and provided the following multiaxis fatigue damage parameter model as follows:

$$\frac{\epsilon_{\text{eq}}}{2} = \sqrt{(\epsilon_n^*)^2 + \frac{1}{3} \left(\frac{\Delta \gamma_{\max}}{2} \right)^2} = \frac{\sigma'_f}{E} (2N_f)^b + \epsilon'_f (2N_f)^c, \quad (1)$$

where the normal strain equation

$$\epsilon_n^* = 0.5 \times \epsilon_n (1 + \cos \varphi). \quad (2)$$

When the equivalent strains have the same values but the ratio of shear strain to normal strains is different, the normal strain of the material varies with the phase angle, as shown in Figure 1. Figure 1 reveals the roughly positive correlation between the phase difference angle and the normal strain of the material, and the strain change is obviously larger. More detailedly, the normal strain of the material is not monotonically increasing in the range, but with the increase of the phase difference angle, it increases first and then decreases, and therefore, normal strain is not very good to describe the additional stiffening effect of the material at low strain rates.

Figure 2 depicts the relationship between the equivalent strain calculated from the Suntech model and the phase difference angle under the condition that the standard deviation of shear strain and positive strain is 0.4% and the ratio of shear strain to normal strain is different. When the phase difference angle increases, the Suntech model damage parameter also increases.

However, according to Figure 1, the normal strain of the damage parameter does not increase with the rise of the phase difference angle at the low strain ratio. Therefore, the model cannot describe the multiaxis fatigue life well under the low strain ratio. From the microscopic point of view, the fatigue crack usually occurs in the local plastic zone of the slip zone. The fatigue crack growth is the polymerization process along the crack tip shear zone. The normal strain and the normal stress on the crack surface make this polymerization accelerate, contributing to the growth of fatigue crack, so it should be considered that the normal strain and normal stress have effect on fatigue damage accumulation. When the equivalent strain of the material is the same size while the loading method is different, the fatigue life of the material will have some differences. Correspondingly, as a multiaxis fatigue damage parameter, only the equivalent strain combined with the shear strain and the normal strain on the critical plane has some limitations.

Therefore, in the multiaxis fatigue loading process, besides the contribution of strain on fatigue damage, the critical surface of the stress, to a certain extent, accelerates the formation and expansion of fatigue cracks. So, the multiaxis fatigue life prediction should consider the impact of not only strain on fatigue damage but also critical surface stress. The stress on the critical plane can be obtained by the Osgood-Ramberg equation:

$$\frac{\Delta \varepsilon_{eq}}{2} = \frac{\Delta \sigma_{eq}}{2E} + \left(\frac{\Delta \varepsilon_{eq}}{2K'} \right)^{1/n'}, \quad (3)$$

where K' is the cyclic strength factor and n' is the cyclic strain hardening factor.

Figure 3 depicts the relationship between the equivalent stress on the critical plane and the phase difference angle under the condition that the standard deviation of shear strain and positive strain is 0.4% and the ratio of shear strain to normal strain is different. The equivalent stress and the retard angle on the critical plane show a monotonically increasing relationship under the condition that the strain

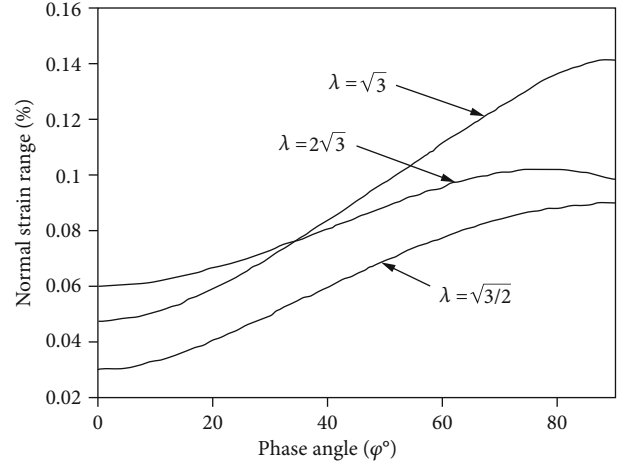


FIGURE 1: Relationship between normal strain range and phase angle.

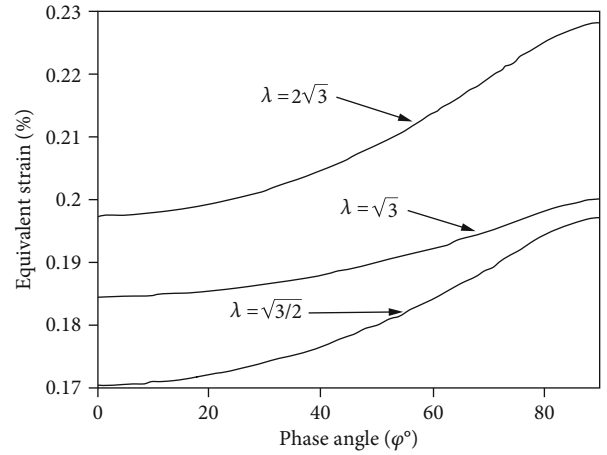


FIGURE 2: The relationship between the equivalent strain and phase angle of the model.

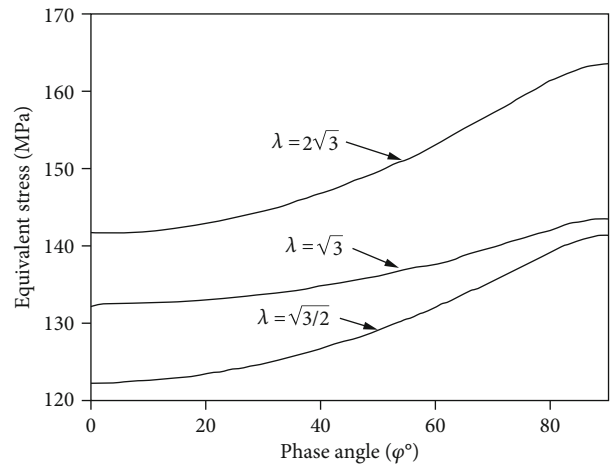


FIGURE 3: The relationship between equivalent stress and phase angle in critical plane.

TABLE 1: Chemical composition of 7075 aluminum alloys (mass fraction %).

Zn	Mg	Cu	Cr	Fe	Si	Mn	Ni	Al
5.1-6.1	2.1-2.9	1.2-2.0	0.180-28	≤0.50	≤0.40	≤0.30	≤0.05	Margin

ratio is different and reach the maximum value in 900 non-proportional loading, which is in accordance with the actual fatigue life, with the fact that the phase difference angle decreases. Comparing with Figure 2, the equivalent stress on the critical plane is used to describe the effect of the non-proportional additional effect on the multiaxial fatigue life.

In this paper, based on the existing multiaxial fatigue life prediction model, considering the different loading conditions, the equivalent stress on the critical plane is used to describe the nonproportional additional effect, and a new multiaxial fatigue life prediction model

$$\Delta\sigma_{eq} \frac{\Delta\epsilon_{eq}}{2} = (1 + \nu_e) \frac{(\sigma'_f)^2}{E} (2N_f)^{2b} + (1 + \nu_p) \sigma'_f \epsilon'_f (2N_f)^{b+c}, \quad (4)$$

where N_f is fatigue life, σ'_f is fatigue strength coefficient, ϵ'_f is fatigue ductility coefficient, b is fatigue strength index, and c is the fatigue ductility index.

The material parameters of Equation (4) can be obtained by the uniaxial fatigue test. It is also possible to estimate the fatigue material constants by means of the relevant manual and literature, which can be used to estimate the multiaxial fatigue life.

2. Multiaxial Fatigue Test

2.1. Experimental Materials. High-strength aluminum alloy 7075-T651 was employed as the study object, the chemical composition and fatigue properties of which are shown in Tables 1 and 2.

2.2. Experimental Equipment. Fatigue tests were carried out on two different fatigue testing machines, depending on the loading method. The uniaxial tensile fatigue test was carried out on an MTS-50Kg fatigue tester. In the MTS-858 is the pull-twist composite load fatigue test. Figure 4(a) is MTS-50KN, and Figure 4(b) is the MTS-858 electrohydraulic servo fatigue test system.

2.3. Specimen Shape. The test piece is made of bar nuts, and the notch is a circular groove with a radius of 1 mm at the center of the specimen. The specific shape and dimensions of the specimen are shown in Figure 5. In order to eliminate cutting marks generated in the machining process and the aluminum surface's protective film, the surface of the bar was polished using fine sandpaper before the test.

2.4. Experimental Results. The loading of the material during the test and the detailed experimental results are shown in Table 3.

TABLE 2: Uniaxial tensile fatigue properties of materials.

σ'_f (MPa)	b	ϵ'_f	c	K'	n'
1576	-0.1609	0.1575	-0.6842	747	0.0597

Detected by the Hitachi SU1500 scanning electron microscope [10, 11], the resolution of the scanning electron microscope is 50 μm and 200 μm , respectively, and the results are shown in Figures 6(a)–6(d).

3. Finite Element Simulation

It is overcomplicated to calculate the stress and strain state of the notched using the theoretical formula. In order to obtain the stress and strain state of the material quickly and effectively, the finite element analysis software is used to solve the problem. In order to make the simulation closer to the test conditions, the effective distance of the finite element model is set to 20 mm to match the effective length of the extensometer during the test. At the same time, for the convenience of loading, a 2 mm long rigid body is established at the right end of the model, and the tensile and torsional state of the finite element model is realized by loading on the rigid body. When meshing, the two-dimensional grid is firstly meshed and then rotated to generate a three-dimensional grid. The grid is divided as shown in Figure 7, where there are 30565 nodes in the range. The number of units is 15504, by which the purple part of the elastic modulus takes 108 MPa, its default for the rigid body.

The finite element analysis method is used to simulate the loading condition under the experimental conditions, and the stress and strain states at the point of danger and the corresponding damage parameter are obtained as shown in Table 4.

As Table 4 shows, in the case of proportional and unidirectional loading, the risk point of the specimen is the same node. Under nonproportional loading conditions, the risk of the specimen is transferred to the other nodes in the notch position.

The results show that the damage parameters recorded in Table 4 are brought into the multiaxial fatigue life prediction model, and the multiaxial fatigue life of the missing parts under different loading conditions is obtained. The results of the prediction are shown in Figure 8.

Figure 8 describes the relationship between the predicted life of the notch and the experimental life, where the most solid line represents the case where the test result is consistent with the predicted result. The two solid lines on the edge indicate that the predicted result is different from the experimental result, times the error factor. As can be seen from

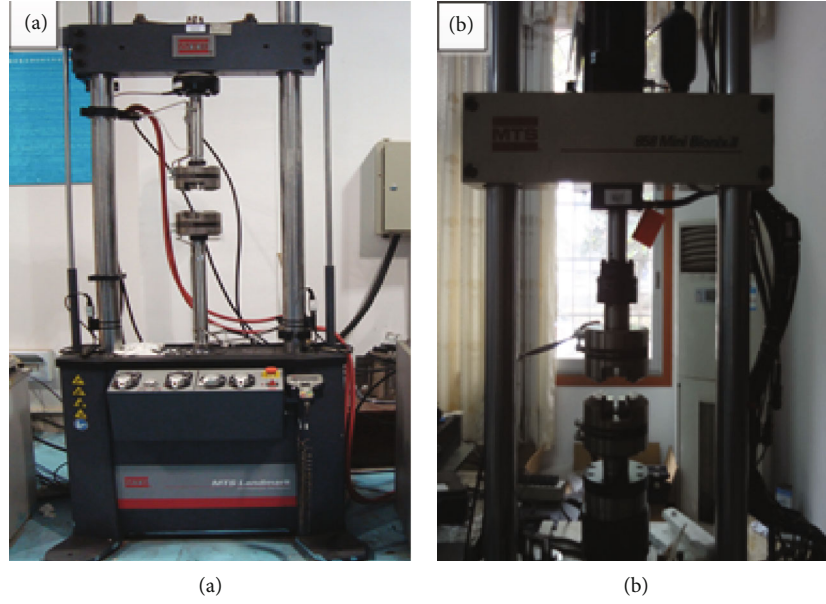


FIGURE 4: Electrohydraulic servo fatigue testing machine.

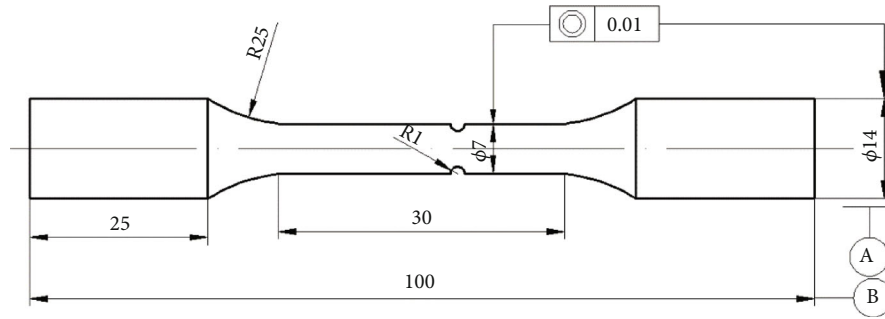


FIGURE 5: Schematic diagram showing the shape and size of fatigue specimen.

TABLE 3: Fatigue results of notch pieces.

Specimen number	Loading conditions		Phase angle (φ^0)	Life N_f
	Stretch (kN)	Twist (N*m)		
1-1	5.5	0	0	12455
1-2	5.6	0	0	10240
1-3	5.8	0	0	6152
1-4	6.0	0	0	4056
1-5	6.2	0	0	3485
1-6	6.5	0	0	2545
2-1	3.5	10	0	2854
2-2	3.0	9	0	4218
2-3	3.5	10	90	1524
2-4	3.0	9	90	2058

the figure, the prediction results are 70% (7) located within twice the error factor; the prediction accuracy is higher. At the same time, the predicted life is basically higher than

the experimental life. The reason may be that the actual stress in the sample gap is much more concentrated than in the ideal model.

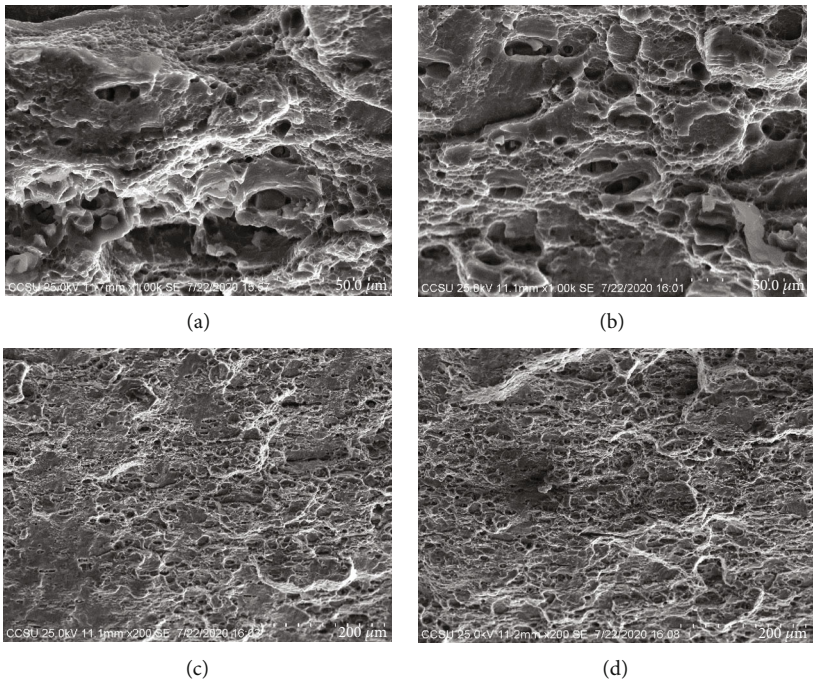


FIGURE 6: Scanning electron microscopy.

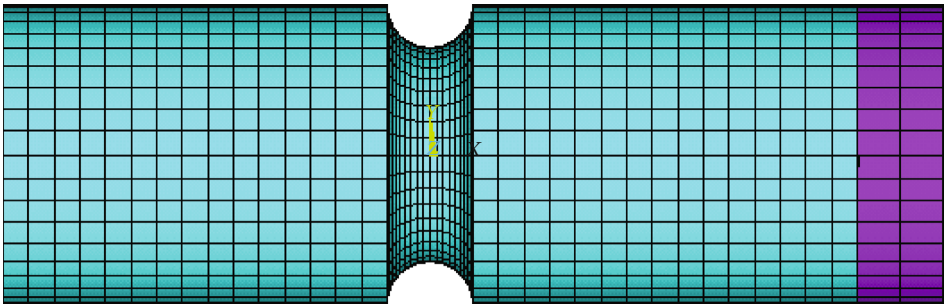


FIGURE 7: Finite element grid.

TABLE 4: Stress and strain states of the specimen at the point of danger.

Number	Dangerous node number	Stress (MPa)	Strain (%)	Shear strain (%)	Damage amount
1-1	175	336.577	0.5612	0.1554	1.913
1-2	175	342.679	0.5714	0.1582	1.983
1-3	175	354.936	0.5918	0.1639	2.127
1-4	175	367.175	0.6122	0.1695	2.2764
1-5	175	379.414	0.6326	0.1752	2.40
1-6	175	397.773	0.6632	0.1836	2.674
2-1	175	415.377	0.3571	0.8156	2.455
2-2	175	374.979	0.3265	0.7336	20.1
2-3	18791	355.91	0.357	0.8165	2.86
2-4	18791	319.189	0.306	0.7336	2.376

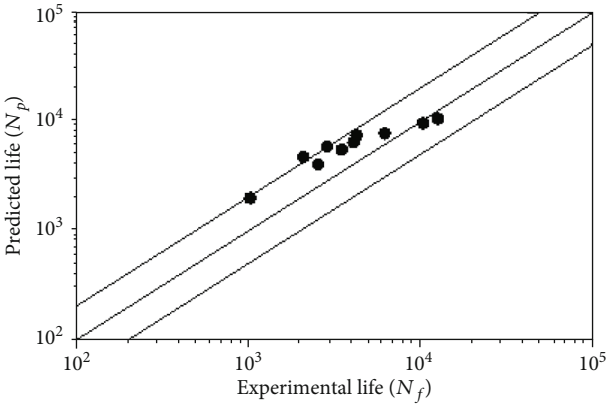


FIGURE 8: Life prediction results for missing parts.

4. Results

- (1) The results show that the normal strain on the critical plane cannot reflect the effect of the nonproportional cycle additional strengthening effect on the fatigue life under the low strain ratio
- (2) The new model of life prediction and experimental results of the comparison show that the new multi-axis life prediction model has a better prediction accuracy. The multiaxis fatigue life prediction model established in this paper is free of empirical constants and is easy to be used in engineering

Data Availability

The data used to support the findings of this study are available from the corresponding author upon request.

Conflicts of Interest

The authors declare that they have no conflicts of interest.

Acknowledgments

This work was financially supported by the youth project (11902050) of the National Natural Science Foundation of China and the youth project (2020JJ4645 and 2020JJ5613) of the Natural Science Foundation of Hunan Province, China. The authors also acknowledge the outstanding youth project (18B418, 20B068, and 20C0168) of the Education Department of Hunan Province, China.

References

- [1] K. Kanazawa, K. J. Miller, and M. W. Brown, "Low-cycle fatigue under out-of-phase loading conditions," *Journal of Engineering Materials and Technology*, vol. 99, no. 3, pp. 222–228, 1977.
- [2] D. Shang, G. Sun, J. Deng, and C. Yan, "Multiaxial fatigue damage parameter and life prediction for medium-carbon steel based on the critical plane approach," *International Journal of Fatigue*, vol. 29, no. 12, pp. 2200–2207, 2007.
- [3] A. Banvillet, T. Palin-Luc, and S. Lasserre, "A volumetric energy based high cycle multiaxial fatigue criterion," *International Journal of Fatigue*, vol. 25, no. 8, pp. 755–769, 2003.
- [4] Y. Zhao and S. O. N. G. Ying-dong, "Multi-axial fatigue life prediction model in elliptic equation form," *Journal of Mechanical Engineering*, vol. 45, no. 11, pp. 312–316, 2009.
- [5] Y.-Y. Wang and Y. Wei-Xing, "Evaluation and comparison of several multiaxial fatigue criteria," *International Journal of Fatigue*, vol. 26, no. 1, pp. 17–25, 2004.
- [6] Z. Wei, L. Yilun, and D.-L. Yang, "A fatigue life prediction model under multi-axial load," *Mechanical Design and Research*, vol. 4, pp. 71–73, 2014.
- [7] F. A. Kandile, M. W. Brown, and K. J. Miller, *Biaxial low cycle fatigue fracture of 316 stainless steel at elevated temperatures*, The Metal Society Press, London, 1982.
- [8] L. Jing, S. Qiang, L. Chunwang, Q. Yanjiang, and Z. Zhongping, "A new multi-axis fatigue life prediction method," *Chinese Journal of Mechanical Engineering*, vol. 9, pp. 285–290, 2009.
- [9] S. Deguang and D. J. Wang, "A new multiaxial fatigue damage model based on the critical plane approach," *International Journal of Fatigue*, vol. 20, no. 3, pp. 241–245, 1998.
- [10] Y. X. Qiao, J. Huang, D. Huang et al., "Effects of laser scanning speed on microstructure, microhardness and corrosion behavior of laser cladding Ni45 coatings," *Journal of Chemistry*, vol. 2020, Article ID 1438473, 11 pages, 2020.
- [11] Y. Qiao, Z. Tian, X. Cai et al., "Cavitation erosion behaviors of a nickel-free high-nitrogen stainless steel," *Tribology Letters*, vol. 67, no. 1, pp. 1–9, 2019.

Research Article

High-Temperature Oxidation Behavior of a Cu-Bearing 17Cr Ferritic Stainless Steel

Mengqi Zhang ¹, Ying Han ¹, Guoqing Zu,¹ Jiapeng Sun,² Weiwei Zhu,¹ Hua Chen,¹ and Xu Ran ¹

¹Key Laboratory of Advanced Structural Materials, Ministry of Education, Changchun University of Technology, Changchun 130012, China

²College of Mechanics and Materials, Hohai University, Nanjing 211100, China

Correspondence should be addressed to Ying Han; hanying_118@sina.com and Xu Ran; ranxu@ccut.edu.cn

Received 17 September 2020; Revised 13 November 2020; Accepted 25 November 2020; Published 16 December 2020

Academic Editor: Jian Chen

Copyright © 2020 Mengqi Zhang et al. This is an open access article distributed under the Creative Commons Attribution License, which permits unrestricted use, distribution, and reproduction in any medium, provided the original work is properly cited.

The isothermal oxidation behavior of 17Cr-0.85Si-0.5Nb-1.2Cu ferritic stainless steel in air was studied from 850°C to 1050°C by analyzing its weight gain after oxidation. The kinetic curves were plotted using the oxidation weight-gain data, and the structure, surface morphology, and element distribution of the oxide films were analyzed by XRD, SEM, and EDS. The results showed that the oxidation kinetics curves at 850°C and 950°C followed a parabolic law, and a continuous and dense oxide film composed of Cr₂O₃ and MnCr₂O₄, FeCr₂O₄, and Cu-Cr rich spinel was formed, which reveals that the steel displayed good oxidation resistance. When the temperature was increased to 1050°C, the oxidation kinetics curves gradually changed from parabolic to linear after 40 h exposure, which indicated that the oxidation resistance significantly worsened. A lower oxidation resistance was observed at 1050°C due to the formation of a large amount of Fe₂O₃ on the surface and the volatilization of the inner Cr₂O₃ layer.

1. Introduction

The materials used in automotive exhaust systems require high strength, good oxidation resistance, and satisfactory corrosion resistance because they are working in complex environments where includes cyclic oxidation and condensate corrosion [1–4]. Austenitic stainless steels are widely used to manufacture the hot-end parts of automobile exhaust systems, but in recent years, they have been gradually replaced by ferritic stainless steels due to their lower cost, smaller thermal expansion, and better high-temperature strength. Ferritic stainless steels have become one of the most promising candidates for use in exhaust manifolds [5–8].

As a relatively cheap alloying element, Cu added to Nb-bearing ferritic stainless steels are expected to greatly improve both strength and corrosion resistance; thus, Cu-Nb alloyed ferritic stainless steels have received great attention as a potential material for the hot-end parts of automotive exhaust systems [9–13]. For example, Kobayashi et al. [9, 10] investi-

gated the effect of Nb addition on the aging precipitation behavior of 18%Cr-1.5%Cu ferritic stainless steel and proved that solute Nb atoms delayed the formation of Cu-rich regions and the coarsening of Cu particles in the steel. Ota et al. [11] studied the thermal fatigue properties of 15%-21% Cr ferritic stainless steel with various Cu and Nb contents. Guo et al. [12] reported that the combination of Cu and Nb improved the corrosion resistance of ferritic stainless steel in sulfuric acid solution.

High-temperature oxidation resistance is one of the important indicators for evaluating the performance of automotive exhaust pipe materials. Moreover, improving the oxidation property is significant to expand the application range for ferritic stainless steels after all. Sun et al. [14] studied the high-temperature cyclic oxidation behavior of 1Cr17 ferritic stainless steel in air and found the oxidation kinetic curves followed a parabolic law. Wei et al. [2] reported the influence of W and Ce on the oxidation behavior of ferritic stainless steel at 950–1100°C and indicated that

the addition of W and Ce improved the density and adhesion of the oxide film, which increased the oxidation resistance. However, when the amount of W exceeded 1.0 wt.%, exfoliation of the oxide film was accelerated, leading to an increased oxidation rate. In addition, Chen et al. [15] investigated the oxidation of 441 ferritic stainless steel at 900–1050°C under a simulating automobile exhaust condition, and the results showed that the maximum service temperature is about 900°C, and the oxide film displayed a stratified structure comprised of a Mn-Cr spinel layer and a Cr₂O₃ layer. However, studies focusing on the oxidation mechanism of Cu-Nb alloyed ferritic stainless steel at high temperatures have not been reported yet. Thus, in this work, the high-temperature oxidation behavior of 17Cr-0.85Si-0.5Nb-1.2Cu ferritic stainless steel, a candidate material for automotive exhaust manifolds, was studied at 850°C, 950°C, and 1050°C in air, and the corresponding oxidation mechanism was proposed.

2. Materials and Methods

The material used in this work was 17Cr-0.85Si-0.5Nb-1.2Cu ferritic stainless steel, and the chemical composition is shown in Table 1. The steel was first hot-rolled to 10 mm and then annealed at 1100°C for 30 min, followed by water cooling. After that, specimens with sizes of 20 mm × 15 mm × 1.5 mm for the oxidation experiments were polished with SiC water-abrasive papers up to 1200 grit, washed with ethanol, and dried in a vacuum drying oven at 150°C.

Specimens that calcined to a constant weight were placed in the alumina crucibles, respectively, and stood against the inner wall of the crucible at a certain angle to ensure complete contact with air during the experiment. A box-type resistance heating furnace was used to perform continuous isothermal oxidation tests at 850°C, 950°C, and 1050°C, for 5 h, 12 h, 20 h, 40 h, 70 h, 100 h, and 140 h. Cover each crucible with a pot immediately after taking it out to avoid errors that might cause by the oxide film falling out during the cooling process. Each crucible and specimen group was weighed after air cooling, and the weight changes and oxidation rates were calculated to plot the oxidation kinetics curves. The composition of the oxide film was analyzed by X-ray diffraction (XRD, D-MAXIIA), with a scanning range of 20°–100°, with a Cu K_α radiation source and parameters of 40 kV and 40 mA. The surface and cross-section morphology and elemental composition of the oxide scale were analyzed by scanning electron microscopy (SEM, Gemini supra40) equipped with energy-dispersive X-ray spectroscopy (EDS).

3. Results and Discussion

3.1. Microstructure of Specimens. An optical micrograph of the steel after annealing at 1100°C for 30 min is shown in Figure 1(a), which reveals a typical equiaxed ferritic structure. The average grain size was measured to be 85 ± 5 μm, and a small number of precipitated particles were observed in the grains and at the grain boundaries (Figure 1(b)). These precipitated particles were analyzed by EDS, and the results are shown in Figure 1(c). It indicates that these precipitates

TABLE 1: Chemical composition of the experimental ferritic stainless steel (wt.%).

C	Si	Mn	Cr	Nb	Cu	P	S	Fe
0.01	0.85	0.25	17.14	0.5	1.2	0.008	0.004	Bal.

were residual Nb-containing compounds which have been reported by many references [16–21].

3.2. Oxidation Kinetics. Figure 2 shows the oxidation weight gain curves of the studied steel at different temperatures. The weight gain gradually increased as the test temperature increased. At 850°C and 950°C, the weight gain curves followed a parabolic law, which indicated that the oxidation reaction was mainly controlled by elemental diffusion [22, 23]. Generally, Equation (1) can be used to describe the parabolic oxidation kinetics and is defined as [24]:

$$W^2 = kt, \quad (1)$$

where W is the oxidation weight gain in mg cm^{-2} , k is the oxidation rate constant in $\text{mg}^2 \text{cm}^{-4} \text{s}^{-1}$, and t is the oxidation time in s. As we all know, the premise of the parabolic law is that there are no defects in the oxide film or at the oxide/matrix interface. However, after long-term oxidation during actual oxidation tests, cracks and other defects may form in the oxide scale, which will cause the oxidation kinetics law to deviate from the classic parabolic law. Therefore, the formula above can be modified as [16, 20]:

$$W^n = k_p t, \quad (2)$$

where n is the index of oxidation and the value of k_p is determined by the mass gain per unit area and oxidation time. Generally, a larger value of k_p indicates a higher growth rate of oxidation film [25–27]. The oxidation kinetics equations of the experimental steel at 850°C and 950°C obtained from Equation (2) are:

$$W^{1.25} = 2.92 \times 10^{-2} t (850^\circ\text{C}), \quad (3)$$

$$W^{1.52} = 6.91 \times 10^{-2} t (950^\circ\text{C}). \quad (4)$$

In these two equations, $n < 2$ indicates the formation of a loose oxide film, while the thickness of the oxide film did not increase proportionally to the element diffusion [28]. However, the oxidation still followed a parabolic law, indicating that the oxide film was protective at this time. Since $k_{p950^\circ\text{C}} > k_{p850^\circ\text{C}}$, the oxidation resistance of the steel at 850°C was better than at 950°C, and the average oxidation rates at these two temperatures were $1.17 \times 10^{-2} \text{ mg cm}^{-2} \text{h}^{-1}$ and $2.05 \times 10^{-2} \text{ mg cm}^{-2} \text{h}^{-1}$, respectively.

At 1050°C, the oxidation weight gain curve of the studied steel was segmented, and the curve displayed a parabolic shape in the first 40 h and then became linear from 40 h to 140 h, which shows that the oxidation resistance of the steel decreased rapidly. The oxidation kinetics process can be expressed by Equation (5):

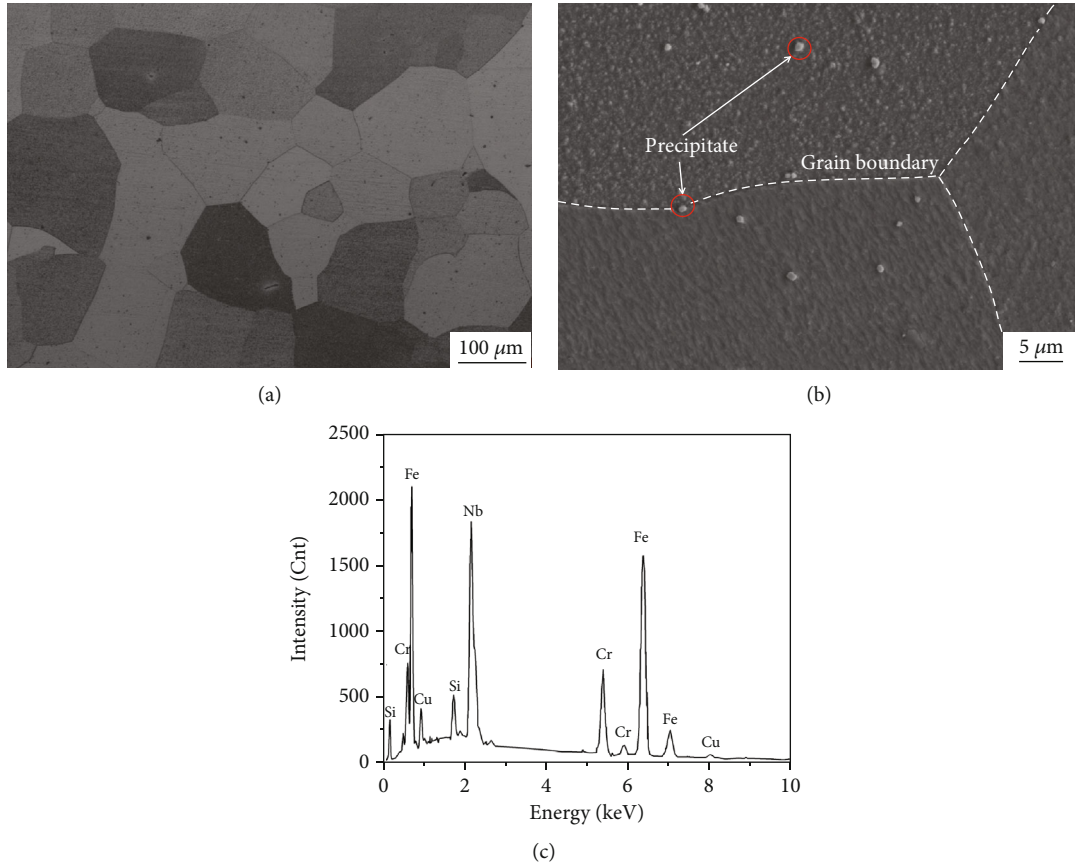


FIGURE 1: Microstructures of the annealed 17Cr-0.85Si-0.5Nb-1.2Cu ferritic stainless steel: (a) optical image of microstructure; (b) SEM image of microstructure; (c) corresponding EDS result of the precipitates in (b).

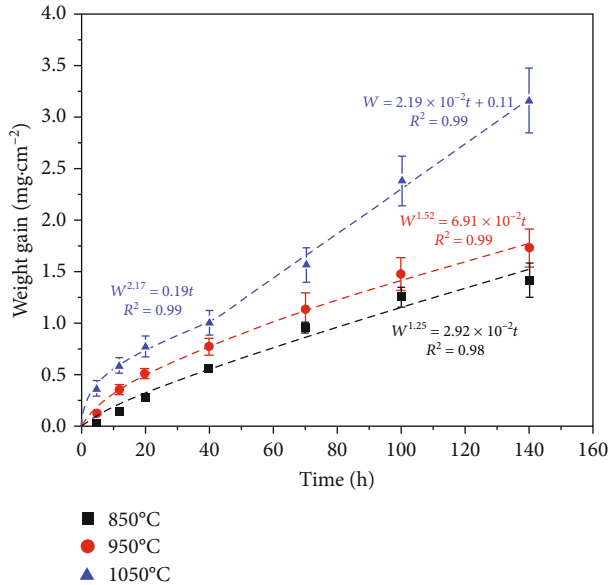


FIGURE 2: The oxidation weight gain curves of 17Cr-0.85Si-0.5Nb-1.2Cu ferritic heat-resistant stainless steel during exposure at temperatures between 850°C and 1050°C in air.

$$\begin{cases} W^{2.17} = 0.19t, & 0 \leq t \leq 40, \\ W = 2.19 \times 10^{-2}t + 0.11, & 40 \leq t \leq 140. \end{cases} \quad (5)$$

When the oxidation time was less than 40 h at 1050°C, the k_p value was 0.19, which is 2.7 and 6.5 times higher than those obtained at 850°C and 950°C, respectively. Although the oxide film was still protective at this time, the overall oxidation resistance was significantly lowered compared to that at lower temperatures. When the oxidation time exceeded 40 h, the oxidation kinetics obeyed a linear law, and the oxidation rate was no longer controlled by diffusion processes in the oxide film but instead depended on the chemical reaction. At this stage, severe macroscopic peeling of the oxide film occurred, and the matrix was not completely covered, which sharply decreased the oxidation resistance of the steel [23, 29]. When the oxidation time reached 140 h at 1050°C, the weight gain was 3.16 mg/cm², and the average oxidation rate was $3.66 \times 10^{-2} \text{ mg cm}^{-2} \text{ h}^{-1}$.

3.3. Characterization and Analysis of Oxide Films

3.3.1. Morphology and Surface Composition of Oxide Films. The surface morphology of the studied steel after oxidation at 850°C for different times is shown in Figure 3, and the compositions of these oxides were further analyzed by

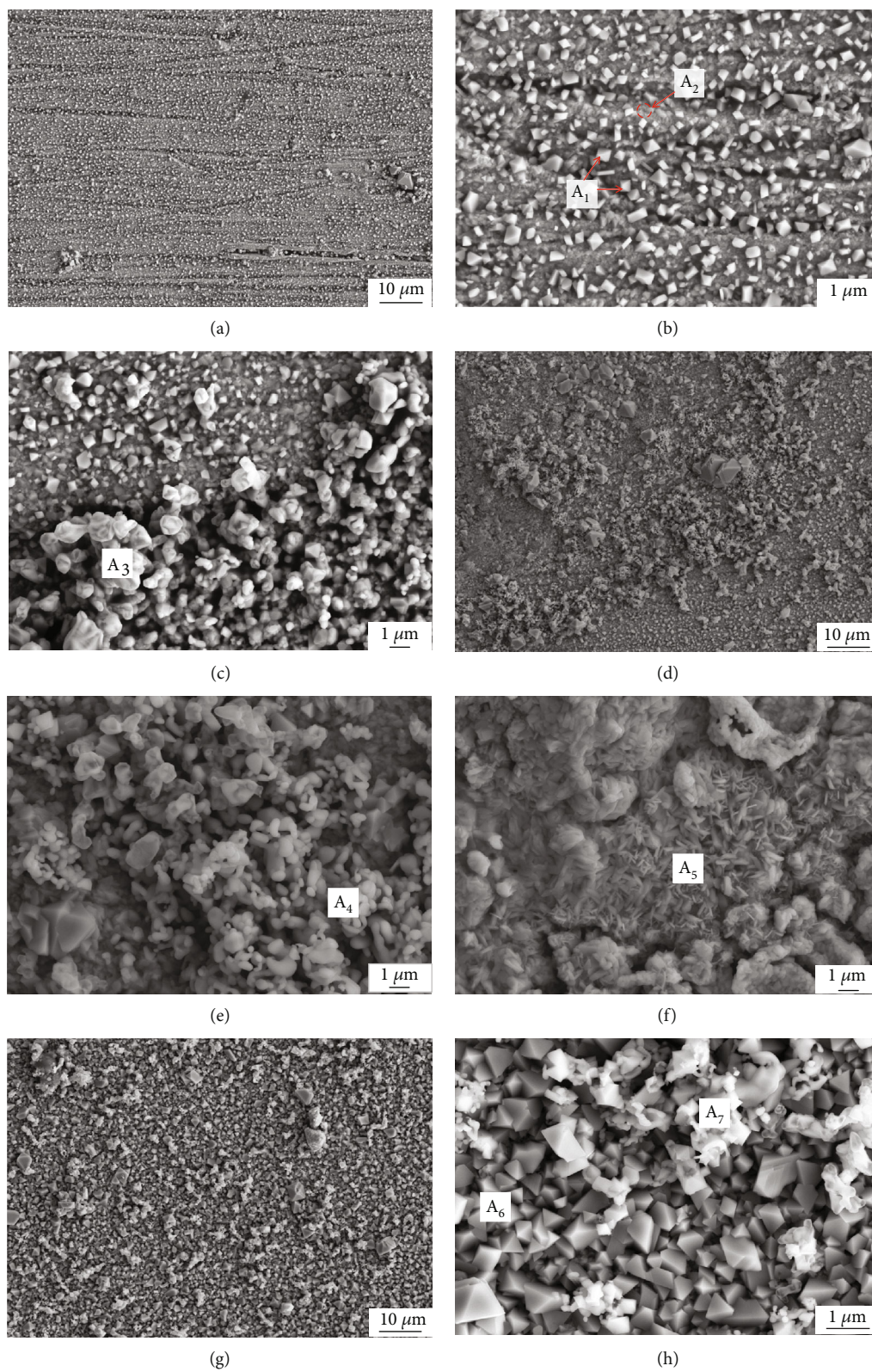


FIGURE 3: Continued.

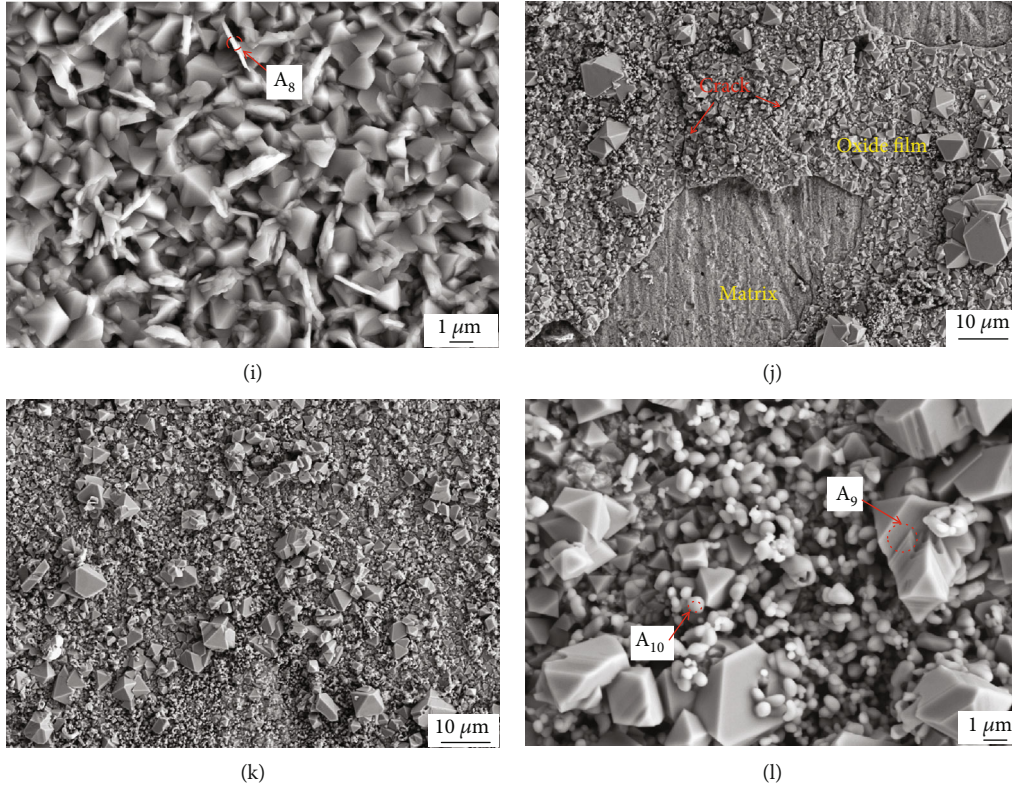


FIGURE 3: Surface morphology of oxide films at 850°C for (a–c) 5 h, (d–f) 20 h, (g–i) 70 h, and (j–l) 140 h in air.

TABLE 2: EDS quantitative analysis results of the different regions in Figure 3.

Test point	Chemical composition (at.%)					
	O	Fe	Cr	Mn	Cu	Si
A1	65.63	—	31.25	—	3.12	—
A2	39.45	9.09	49.94	—	—	1.52
A3	57.98	—	42.02	—	—	—
A4	47.86	—	52.14	—	—	—
A5	57.13	16.67	20.97	—	5.22	—
A6	34.17	—	42.77	23.06	—	—
A7	43.47	—	43.87	12.66	—	—
A8	50.42	8.72	30.96	6.44	3.46	—
A9	57.22	—	39.20	—	3.58	—
A10	52.55	—	47.45	—	—	—

EDS (Table 2). In the first 5 h (Figure 3(a)), surface scratches were apparent, indicating that the oxide film was very thin and the oxidation had just begun. At this time, the oxides were small cubes and bubble-like shapes (Figures 3(b) and 3(c)). The cubic oxides (A_1) contained Cr, O, and a small amount of Cu, region A_2 contained Cr, O, Fe, and Si, and the bubble-like particles in region A_4 were identified as Cr_2O_3 . No scratches were observed on the surface after 20 h oxidation (Figure 3(d)), and the size and quantity of the bubbly oxides on the surface increased and widely covered the thin cubic oxide film. In some areas, the bubble-like Cr_2O_3 oxides

gradually merged (A_4 in Figure 3(e)). Sparse large agglomerates and flocculent oxides (A_5 in Figure 3(f)) which contained Cr, Fe, and Cu were also observed. The oxide film was even and compact after 70 h oxidation at 850°C, and a dense spinel oxide layer formed (Figures 3(g) and 3(h)). In addition to the cubic and a low amount of bubbly oxides, thin needle-like oxides (A_8 in Figure 3(i)) also appeared. The cubic oxide films in these areas showed signs of fusion, and their geometric characteristics were not obvious. In Figure 3(h), two different oxides, A_6 and A_7 , contained Cr, O, and Mn, and the cubic oxides (A_6) contained more Mn, indicating that they were a spinel phase that contained Cr and Mn [30]. Area A_8 mainly consisted of Cr, O, and a small quantity of Fe, Mn, and Cu. When the oxidation time was lengthened to 140 h (Figures 3(j) and 3(k)), the oxide film became rougher, and some areas collapsed after cooling. Many large spinel particles were produced (Figure 3(l)), with many granular oxides (A_{10}) between them which were composed of Cr_2O_3 , while the large layered cubic spinel oxides (A_9) were mainly composed of Cr and Cu.

Figure 4 shows the surface morphology of the studied steel at 950°C and 1050°C after oxidation for 140 h in air. The surface oxide scales fell off to some degree when the time progressed to 140 h at both temperatures. It can be seen from Figure 4(a) that when the temperature was 950°C, the thickness of oxide scale was increased, and a pit-like morphology (mainly composed of Fe, Cr, Si, and O by EDS analysis) appeared in the area which experienced oxide film spallation. After oxidation at 1050°C, significant scale spalling was observed (Figure 4(b)). The remaining part of the oxide had

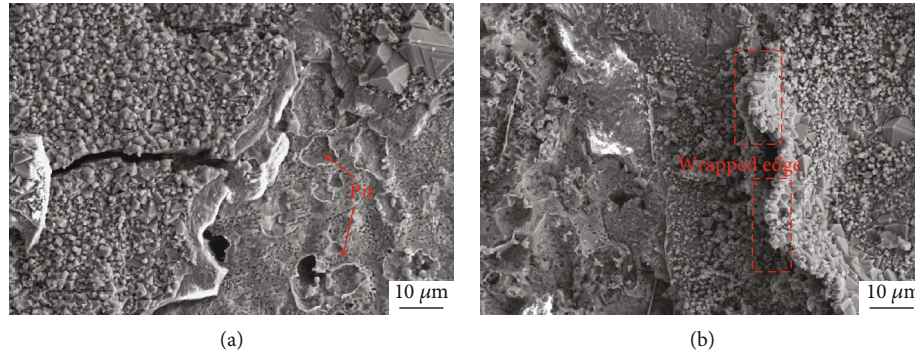


FIGURE 4: Surface morphology of oxide films formed after oxidation for 140 h in air at (a) 950°C and (b) 1050°C.

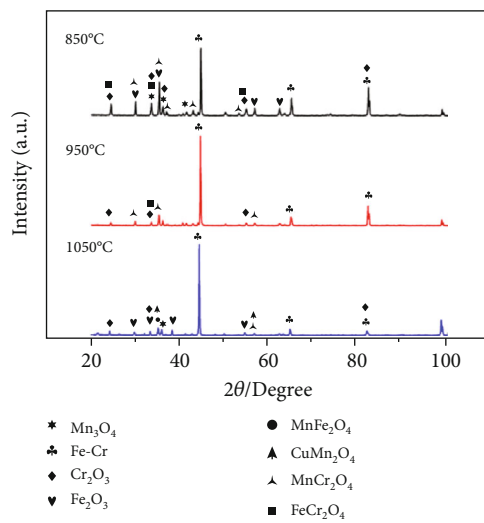


FIGURE 5: X-ray diffraction patterns of the oxide film surface after exposure at different temperatures for 140 h in air.

a warped edge and was poorly attached to the substrate, indicating a significantly lower oxidation resistance. EDS results showed that the composition of the exfoliated area was oxides containing Mn, Cr, and Cu.

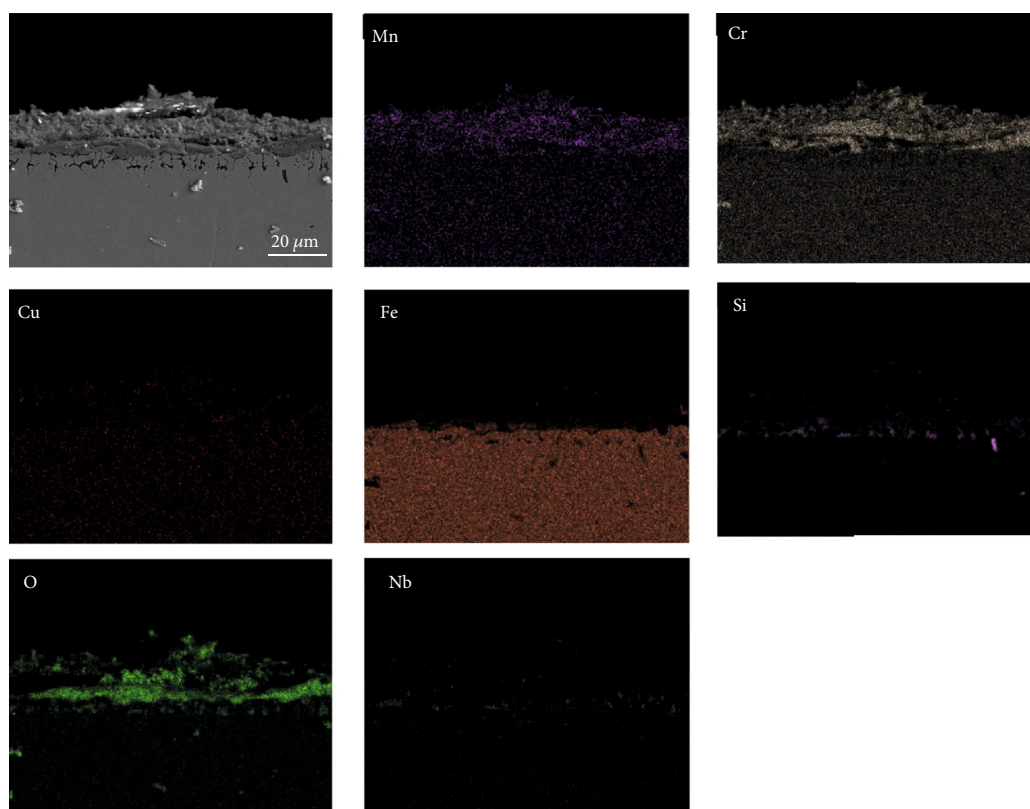
3.3.2. Phase Analysis of Oxide Films. Figure 5 presents the XRD patterns of the oxide films obtained at different temperatures for 140 h. The oxidation products were similar and were mainly composed of Fe-Cr, Cr_2O_3 , Fe_2O_3 , Mn_3O_4 , MnCr_2O_4 , and FeCr_2O_4 . But the intensities were different, indicating different phase content and/or thickness. The peaks of spinel Cu-Cr were not detected in the patterns, because their content was too low to be detected. At 1050°C, CuMn_2O_4 and more Fe_2O_3 appeared, compared to that at lower temperatures. The above results are both consistent with the EDS analysis. In addition, it can be found that as the temperature increased, the Cr_2O_3 content continued to decrease due to the further oxidation of Cr_2O_3 at high temperatures, which resulted in the formation of volatile CrO_3 . According to a previous report [31], this reaction proceeds very rapidly above 950°C, which is why Cr_2O_3

showed a low peak intensity at 1050°C. The XRD patterns also showed that the Fe-Cr peaks were heightened at higher temperatures, which could be due to severe peeling of the oxide film, which exposed more of the matrix.

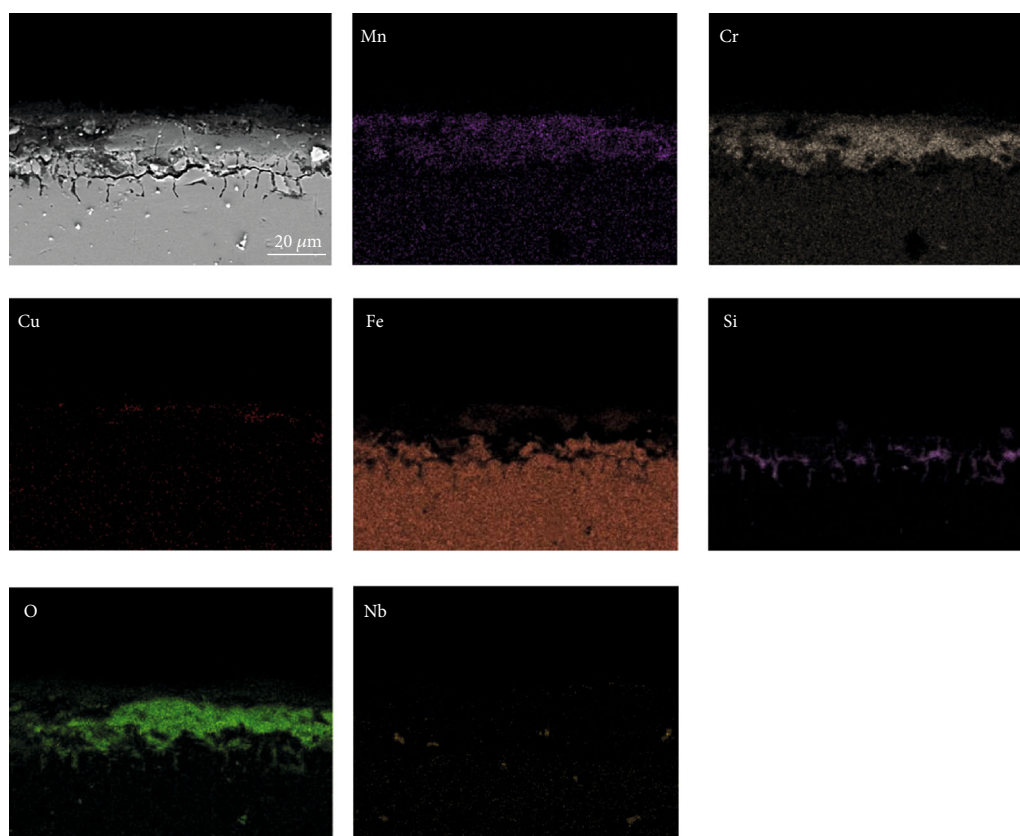
3.3.3. The Cross-Sectional Morphology of Oxide Scales. The cross-sectional morphology of the studied steel oxidized at 950°C and 1050°C for different times is shown in Figures 6 and 7, respectively. The changes in the distribution and concentration of O, Cr, Fe, Cu, Si, Nb, and Mn were detected. It can be seen from the figures that the oxygen content increased from the surface of the oxide film to the alloy substrate, and this indicated that the film at the interface of the substrate was denser than the surface oxide [1].

It can be seen from Figure 6(a) that when oxidized at 950°C for 12 h, the oxide film was still in the preliminary formation stage with a thickness of about 13.74 μm. Mn was evenly distributed throughout the entire oxide layer, but the Cr content was greater at the oxide/steel interface. A tiny amount of Cu was observed in the outer oxide layer, while nearly no Fe and Nb were detected. Moreover, some Si-rich oxides distributed sporadically near the scale/steel interface. When the oxidation time was prolonged to 100 h (Figure 6(b)), the thickness of the oxide film increased to 19.28 μm. Meanwhile, Fe began to gather near the oxide/metal interface, but Fe-rich oxides were not formed continuously or densely. A small amount of Cu was observed near the outermost side of the oxide scale, which may be related to the formation of Cu-Cr spinel oxide.

The cross-sectional element distribution of the oxide films after different oxidation times at 1050°C is shown in Figure 7. As the temperature increased, the oxide film gradually thickened and reached 18.75 μm after 12 h (Figure 7(a)), and the elemental distribution was significantly different from the specimen exposed at 950°C. Si-rich oxides were distributed near the matrix continuously, while some Nb accumulation was scattered around them. A Fe-rich oxide layer was formed above the original Cr-rich scale, and the Cr-rich layer was thinner compared with that at 950°C. The concentration of Fe throughout the entire oxide film was significantly higher than that at 950°C, indicating that Fe diffused through the oxide film and reacted with oxygen. Mn was distributed evenly throughout the oxide film, and



(a)



(b)

FIGURE 6: Cross-sectional energy spectral analysis of oxide films formed during exposure at 950°C in air: (a) for 12 h; (b) for 100 h.

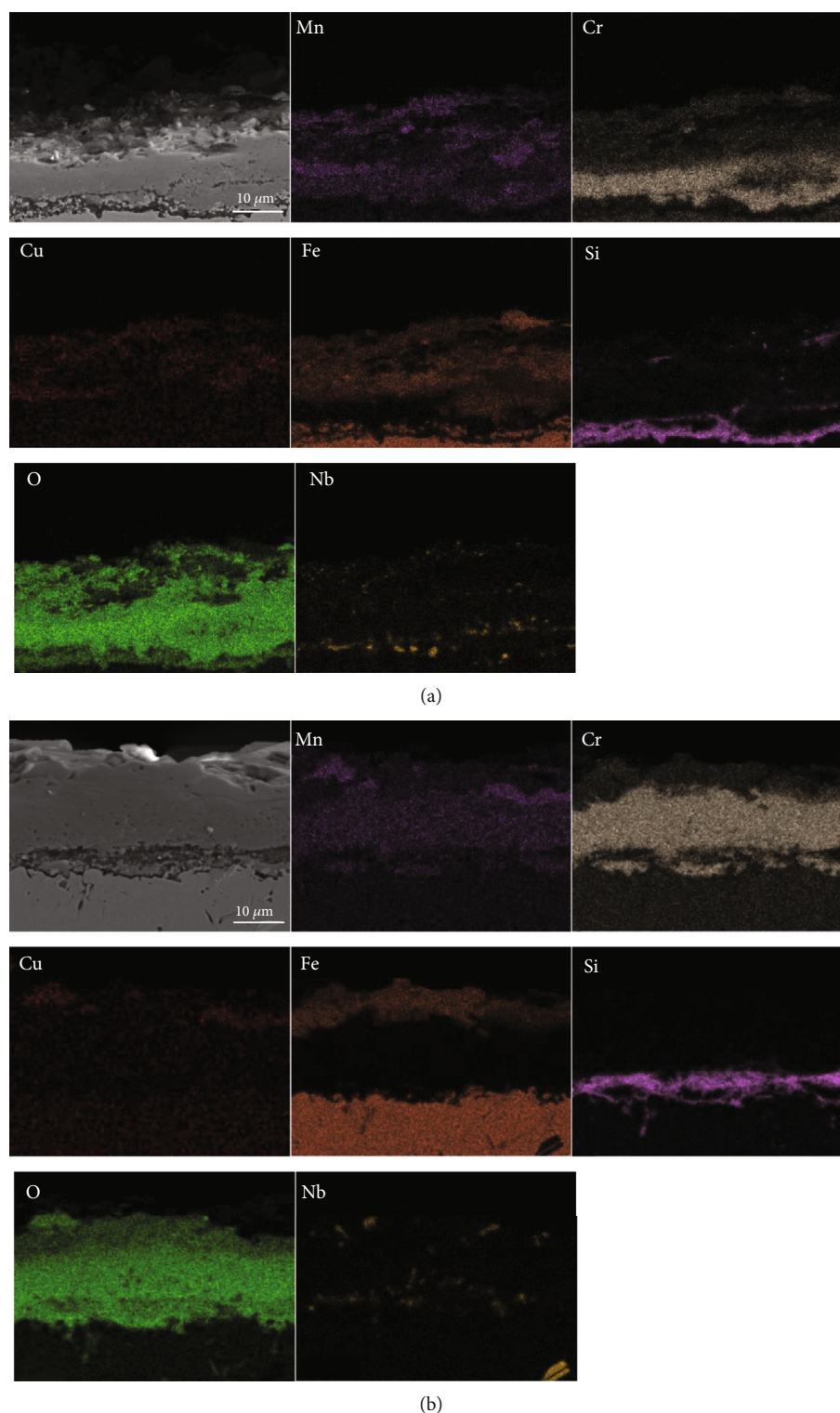


FIGURE 7: Cross-sectional energy spectral analysis of oxide films formed during exposure at 1050°C in air: (a) for 12 h; (b) for 100 h.

its concentration decreased further away from the outer layer. When the exposure time reached 100 h (Figure 7(b)), the outermost layer was a thick Fe-rich oxide, and the layer underneath was a Cr-rich oxide which was thicker than the one formed at 12 h. Large cavities also appeared in the inner

Cr-rich layer, which might have resulted in the outward diffusion and oxidation of Fe at the scale surface. Therefore, it can be inferred that after being oxidized at 1050°C for 100 h, the oxide film was stratiform, and the outer layer of the scale was composed of Fe_2O_3 and a tiny amount of

discrete CuMn_2O_4 . The middle layer was composed of Cr_2O_3 together with Mn-rich spinel oxides, and the innermost layer was SiO_2 .

3.4. Oxidation Mechanism

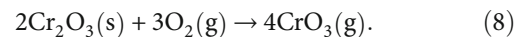
3.4.1. Oxidation Mechanism at 850°C and 950°C. According to thermodynamic theory, the affinity between oxygen and other elements in an alloy follows the order of $\text{Si} > \text{Nb} > \text{Mn} > \text{Cr} > \text{Fe} > \text{Cu}$ [2, 25, 28, 32]. During the initial oxidation stage, Si and Nb are supposed to be first oxidized at the oxide/steel interface due to their higher diffusion coefficient and oxygen affinity in steel. However, there was a strong competition between Si and Nb for the interfacial oxidation [32]. Also, since the supply amount of Si atoms was much greater than that of Nb, NbO_2 was difficult to form. This result corresponds to the result of X-ray diffraction, that is, no NbO_2 was detected. The formed SiO_2 layer was thin, porous, and discontinuous at this temperature; therefore, Cr and Mn began to diffuse outward through the SiO_2 layer to generate Cr_2O_3 and MnO, respectively. As the oxidation time increased, a denser and more continuous protective Cr_2O_3 layer was formed, while Fe began to diffuse from the metal to the middle oxide layer to form FeO. However, the protective Cr_2O_3 layer acted as a barrier to Fe diffusion to the surface of the oxide film, and FeO and MnO reacted with Cr_2O_3 , respectively, under the Cr_2O_3 layer and at the outermost oxide film surface to generate spinel oxides through the following reactions:



In addition, a small amount of Cu migrated to the outer layer of the oxide scale and reacted with Cr to form spinel oxides after longer exposure times. These spinel oxides formed on the surface were a compact barrier for the inward diffusion of O, reducing the growth of the oxide scale and acting as protective layers against oxidation [23, 33, 34].

3.4.2. Oxidation Mechanism at 1050°C. The oxidation rate of the studied steel increased significantly with increasing temperature. Si and Nb were oxidized during the initial oxidation period at 1050°C. And there are some differences from the low-temperature oxidation at 850°C–950°C. First of all, some sporadic Nb accumulation could be found. This is consistent with the finding of previous study, that is, when the content of Si in the steel is more than 0.5 wt.%, no Nb oxide aggregation layer will be formed [35]. Ali-Löytty et al. [16] also believed that the Nb-rich intermetallic precipitates remove free Nb from the alloy solution and thus made it difficult to form Nb-rich oxide layer. Therefore, based on the previous research conclusions and the phenomena observed in this experiment, we speculate that when the Si content is 0.85 wt.%, the oxidation of Nb has been severely suppressed, so the influence of Nb oxides will not be discussed here. Secondly, Si formed a continuous and dense thin oxide layer at the oxide/metal interface. It is known that Si-rich oxides are stable and protective at high temperatures [27, 36], yet a previous study [37] also found that it does not provide the high-

est oxidation resistance when a continuous Si oxide layer is formed at the steel/chromium interface. In contrast, it is better to obtain good oxidation resistance when a discontinuous Si oxide layer is formed at and below the interface with silica particles because Si does not act as a barrier for Cr diffusion to the chromium layer but rather prevents the diffusion of Cr from the matrix to the interface. Cr_2O_3 is also unstable at high temperatures, especially above 950°C, and easily reacts with oxygen to form volatile CrO_3 , which leads to the depletion of protective chromium oxides via the following reaction [25, 31, 38, 39]:



When the average Cr content of the steel was lower than the critical concentration, the matrix Fe began to oxidize. Nodular oxides formed when Fe began to diffuse along the oxide layers and oxidized outward, which made the Cr_2O_3 film unstable, thereby causing more severe oxidation [40]. From Figure 7, it can be seen that Fe rapidly diffused through the inner scale, and oxidation occurred in the upper and middle oxide layers which were originally Cr_2O_3 . Once the Fe-rich oxides which had faster oxidation rate began to form, no more dense protective chromium-rich oxide scale will be formed on the outermost surface. However, the Fe-rich oxide layer was loose and not protective, which provided more paths for the diffusion of Fe, O, Cr, and Mn [31]. It can also be observed in Figure 7(a) that the Fe-rich oxide had a bilayer structure whose outer layer was Fe_2O_3 , and the inner was Fe-Cr oxides, but they were not dense enough to impede the outward diffusion of ions. Moreover, due to the different Pilling-Bedworth ratios of these oxides, cracks also formed due to growth stress [41, 42]. The above reasons eventually led to the failure of the oxide scale at 1050°C. Some Cu-rich and Mn-rich oxides were also distributed on the outermost side of the oxide film when the exposure time was extended to 100 h. It was estimated that few CuMn_2O_4 and MnFe_2O_4 spinel oxides were formed. Previous studies have shown that when a Cu-rich phase segregates at the scale-matrix interface, it can hinder the inward diffusion of oxygen, thereby improving the oxidation resistance [43], but this phenomenon was not observed in this study. In addition, another research showed that Cu-Mn spinel oxides are good barrier to the diffusion of Cr [44–46]. However, since the nonprotective Fe_2O_3 dominated the outermost film, spinel oxides did not form a strong protective continuous dense layer, and the oxidation rate of the experimental steel increased linearly.

4. Conclusions

The isothermal oxidation behavior of 17Cr-0.85Si-0.5Nb-1.2Cu ferritic stainless steel at 850°C, 950°C, and 1050°C in air was studied, and the following conclusions were obtained:

- (1) The oxidation rate increased with the increasing temperature. The oxidation kinetics curves conformed to the parabolic law at 850°C and 950°C, while the kinetics curve followed a parabolic-linear rule at 1050°C

- (2) At 850°C and 950°C, a small amount of oxide film peeled off. The oxide film was composed of a small amount of SiO₂ and continuous and dense Cr₂O₃, FeCr₂O₄, and Cr-Mn spinel oxides. The composition of the oxide film was sufficiently stable to protect the matrix from further acute oxidation
- (3) The spallation of the oxide scale became more severe when the exposure time increased to 40 h at 1050°C. The severe volatilization of Cr₂O₃ and the enrichment of nonprotective Fe-rich oxides on the surface rapidly decrease the oxidation resistance at this high temperature

Data Availability

The raw/processed data required to reproduce these findings cannot be shared at this time as the data also forms part of an ongoing study.

Conflicts of Interest

The authors declare that they have no conflicts of interest.

Acknowledgments

This work is supported by the National Natural Science Foundation of China (No. 51604034 and 51974032), the Science and Technology Project of Jilin Education Department in 13th Five-Year (No. JJKH20181008KJ), and the Science and Technology Development Program of Jilin Province (No. 20190302003GX).

References

- [1] L. L. Wei, "An investigation on high temperature oxidation resistance of medium-chromium alloyed ferritic stainless steel," Northeastern Univ. Tech. Thesis, 2016.
- [2] L. L. Wei, J. H. Zheng, L. Q. Chen, and R. D. K. Misra, "High temperature oxidation behavior of ferritic stainless steel containing W and Ce," *Corrosion Science*, vol. 142, pp. 79–92, 2018.
- [3] G. M. Sim, J. C. Ahn, S. C. Hong, K. J. Lee, and K. S. Lee, "Effect of Nb precipitate coarsening on the high temperature strength in Nb containing ferritic stainless steels," *Materials Science and Engineering*, vol. 396, no. 1-2, pp. 159–165, 2005.
- [4] Y. Qiao, Z. Tian, X. Cai et al., "Cavitation erosion behaviors of a nickel-free high-nitrogen stainless steel," *Tribology Letters*, vol. 67, no. 1, 2018.
- [5] Y. Inoue and M. Kikuchi, "Present and future trends of stainless steel for automotive exhaust system," *Nippon Steel Technical Report*, vol. 88, pp. 62–69, 2003.
- [6] A. M. Huntz, A. Reckmann, C. Haut et al., "Oxidation of AISI 304 and AISI 439 stainless steels," *Materials Science and Engineering*, vol. 447, no. 1-2, pp. 266–276, 2007.
- [7] Y. Han, J. Q. Sun, Y. Sun, J. P. Sun, and X. Ran, "Tensile properties and microstructural evolution of an Al-bearing ferritic stainless steel at elevated temperatures," *Metals*, vol. 10, no. 1, p. 86, 2020.
- [8] Y. M. L. Y. Shao and C. X. Liu, "Annealing process optimization of high frequency longitudinal resistance welded low-carbon ferritic stainless steel pipe," *Acta Metallurgica Sinica*, vol. 55, no. 11, pp. 1367–1378, 2019.
- [9] S. Kobayashi, T. Takeda, N. Kanno, Y. Inoue, K. Nakai, and T. Sakamoto, "Effect of Nb addition on the growth and coarsening of Cu-particles in ferritic stainless steel," *ISIJ International*, vol. 54, no. 7, pp. 1697–1704, 2014.
- [10] S. Kobayashi, T. Takeda, K. Nakai, N. Kanno, and T. Sakamoto, "Effect of Nb addition on Cu precipitation in ferritic stainless steel," *ISIJ International*, vol. 51, no. 4, pp. 657–662, 2011.
- [11] H. Ota, T. Nakamura, and K. Maruyama, "Effect of solute atoms on thermal fatigue properties in ferritic stainless steels," *Materials Science and Engineering*, vol. 586, pp. 133–141, 2013.
- [12] J. J. Guo and M. S. N. Sato, "Electrochemical behavior and surface composition of ferritic stainless steels containing Cu and Nb in sulfuric acid solution," *Journal of Chinese Society for Corrosion and Protection*, vol. 10, no. 3, pp. 239–244, 1990.
- [13] X. Li, L. Shi, Y. Liu, K. Gan, and C. Liu, "Achieving a desirable combination of mechanical properties in HSLA steel through step quenching," *Materials Science and Engineering: A*, vol. 772, article 138683, 2020.
- [14] B. Sun, S. R. Wang, and Y. J. Wang, "Cyclic oxidation behavior of ferrite stainless steel at high temperature," *Hot Working Technology*, vol. 41, no. 4, pp. 43–48, 2012.
- [15] Y. S. Chen, "High temperature oxidation behavior of ferritic stainless steel for hot end of exhaust system," Shanghai Univ. Tech. Thesis, 2019.
- [16] H. Ali-Löytty, P. Jussila, and M. Valden, "Optimization of the electrical properties of Ti-Nb stabilized ferritic stainless steel SOFC interconnect alloy upon high-temperature oxidation: the role of excess Nb on the interfacial oxidation at the oxide-metal interface," *International Journal of Hydrogen Energy*, vol. 38, no. 2, pp. 1039–1051, 2013.
- [17] H. Ali-Löytty, P. Jussila, T. Juuti, L. P. Karjalainen, A. A. Zakharov, and M. Valden, "Influence of precipitation on initial high-temperature oxidation of Ti-Nb stabilized ferritic stainless steel SOFC interconnect alloy," *International Journal of Hydrogen Energy*, vol. 37, no. 19, pp. 14528–14535, 2012.
- [18] H. S. Seo, D. W. Yun, and K. Y. Kim, "Oxidation behavior of ferritic stainless steel containing Nb, Nb-Si and Nb-Ti for SOFC interconnect," *International Journal of Hydrogen Energy*, vol. 38, no. 5, pp. 2432–2442, 2013.
- [19] P. D. Jablonski, C. J. Cowen, and J. S. Sears, "Exploration of alloy 441 chemistry for solid oxide fuel cell interconnect application," *Journal of Power Sources*, vol. 195, no. 3, pp. 813–820, 2010.
- [20] A. Safikhani, M. Esmailian, T. Tinatiseresht, and G. B. Darband, "High temperature cyclic oxidation behavior of ferritic stainless steel with addition of alloying elements Nb and Ti for use in SOFCs interconnect," *International Journal of Hydrogen Energy*, vol. 41, no. 14, pp. 6045–6052, 2016.
- [21] L. Niewolak, A. Savenko, D. Grüner, H. Hattendorf, U. Breuer, and W. J. Quadackers, "Temperature dependence of laves phase composition in Nb, W and Si-alloyed high chromium ferritic steels for SOFC interconnect applications," *Journal of Phase Equilibria and Diffusion*, vol. 36, no. 5, pp. 471–484, 2015.
- [22] Y. Inoue, N. Hiraide, A. Hayashi, and K. Ushioda, "Effect of Mn addition on scale structure of Nb containing ferritic stainless steel," *ISIJ International*, vol. 58, no. 10, pp. 1850–1859, 2018.

- [23] D. N. Zou, Y. Q. Zhou, X. Zhang, W. Zhang, and Y. Han, "High temperature oxidation behavior of a high Al-containing ferritic heat-resistant stainless steel," *Materials Characterization*, vol. 136, pp. 435–443, 2018.
- [24] W. J. Qu, "Research on microstructure and high-temperature oxidation property of Al-Si coatings on 1Cr11MoNiW1VNbN stainless steel," Harbin Engineering Univ. Tech. Thesis, 2011.
- [25] X. W. Cheng, Z. Y. Jiang, B. J. Monaghan, D. B. Wei, R. J. Longbottom, and J. W. Zhao, "Breakaway oxidation behaviour of ferritic stainless steels at 1150°C in humid air," *Corrosion Science*, vol. 108, pp. 11–22, 2016.
- [26] M. Peruzzo, T. D. Beux, M. F. C. Ordoñez, R. M. Souza, and M. C. M. Farias, "High-temperature oxidation of sintered austenitic stainless steel containing boron or yttria," *Corrosion Science*, vol. 129, pp. 26–37, 2017.
- [27] H. H. Mao, X. Qi, J. Cao, L. C. An, and Y. T. Yang, "Effect of Si on high temperature oxidation of 30Cr13 stainless steel," *Journal of Iron and Steel Research, International*, vol. 24, no. 5, pp. 561–568, 2017.
- [28] T. F. Li, "High temperature oxidation and thermal corrosion of metals," Beijing: Chemical Industry Press, 2003.
- [29] H. B. Li, B. B. Zhang, Z. H. Jiang, S. C. Zhang, and H. Feng, "A new insight into high-temperature oxidation mechanism of super-austenitic stainless steel S32654 in air," *Journal of Alloys and Compounds*, vol. 686, pp. 326–338, 2016.
- [30] D. S. Li, Q. X. Dai, X. N. Cheng, R. R. Wang, and Y. Huang, "High-temperature oxidation resistance of austenitic stainless steel Cr18Ni11Cu3Al3MnNb," *Journal of Iron and Steel Research, International*, vol. 19, no. 5, pp. 74–78, 2012.
- [31] M. S. Li, *High-Temperature Corrosion of Metal*, Metallurgical Industry Press, Beijing, 2001.
- [32] Y. Kondo, "Behavior of copper and nickel during high temperature oxidation of steel containing them," *Materials Science Forum*, vol. 522–523, pp. 53–60, 2006.
- [33] G. R. Holcomb and D. E. Alman, "Effect of manganese addition on reactive evaporation of chromium in Ni-Cr alloys," *Journal of Materials Engineering and Performance*, vol. 15, no. 4, pp. 394–398, 2006.
- [34] H. Ebrahimifar and M. Zandrahimi, "Mn coating on AISI 430 ferritic stainless steel by pack cementation method for SOFC interconnect applications," *Solid State Ionics*, vol. 183, no. 1, pp. 71–79, 2011.
- [35] Y. Inoue, N. Hiraide, and K. Ushioda, "Effect of Si addition on oxidation behavior of Nb containing ferritic stainless steel," *ISIJ International*, vol. 58, no. 6, pp. 1117–1125, 2018.
- [36] D. T. Hoelzer, B. A. Pint, and I. G. Wright, "A microstructural study of the oxide scale formation on ODS Fe-13Cr steel," *Journal of Nuclear Materials*, vol. 283–287, pp. 1306–1310, 2000.
- [37] G. Bamba, Y. Wouters, A. Galerie, F. Charlot, and A. Dellali, "Thermal oxidation kinetics and oxide scale adhesion of Fe-15Cr alloys as a function of their silicon content," *Acta Materialia*, vol. 54, no. 15, pp. 3917–3922, 2006.
- [38] J. H. Kim, B. K. Kim, D. I. Kim, and P. P. Choi, "The role of grain boundaries in the initial oxidation behavior of austenitic stainless steel containing alloyed Cu at 700 °C for advanced thermal power plant applications," *Corrosion Science*, vol. 96, pp. 52–66, 2015.
- [39] Y. Qiao, J. Huang, D. Huang, J. Chen, W. Liu, and Z. Wang, "Effects of laser scanning speed on microstructure, microhardness, and corrosion behavior of laser cladding Ni45 coatings," *Journal of Chemistry*, vol. 2020, Article ID 1438473, 11 pages, 2020.
- [40] J. G. Peng, M. C. Li, and S. Z. Luo, "Oxidation characteristic of B443NT at high temperature," *Bao Steel Technology*, vol. 5, pp. 22–31, 2013.
- [41] Y. S. Chen, J. M. Zhan, Q. Z. Ni, and M. C. Li, "Oxidation behavior of type 441 ferritic stainless steel in synthetic exhaust gas," *Corrosion Science and Protection Technology*, vol. 31, no. 2, pp. 174–180, 2019.
- [42] Y. Qiao, D. Xu, S. Wang et al., "Effect of hydrogen charging on microstructural evolution and corrosion behavior of Ti-4Al-2V-1Mo-1Fe alloy," *Journal of Materials Science & Technology*, vol. 60, pp. 168–176, 2021.
- [43] S. Swaminathan, Y. S. Lee, and D. I. Kim, "Long term high temperature oxidation characteristics of La and Cu alloyed ferritic stainless steels for solid oxide fuel cell interconnects," *Journal of Power Sources*, vol. 327, pp. 104–118, 2016.
- [44] M. R. Bateni, P. Wei, X. H. Deng, and A. Petric, "Spinel coatings for UNS 430 stainless steel interconnects," *Surface and Coatings Technology*, vol. 201, no. 8, pp. 4677–4684, 2007.
- [45] N. Hosseini, M. H. Abbasi, F. Karimzadeh, and G. M. Choi, "Development of Cu_{1.3}Mn_{1.7}O₄ spinel coating on ferritic stainless steel for solid oxide fuel cell interconnects," *Journal of Power Sources*, vol. 273, pp. 1073–1083, 2015.
- [46] Z. Ranjbar-Nouri and S. Rastegari, "Applying the protective CuMn₂O₄ spinel coating on AISI-430 ferritic stainless steel used as solid oxide fuel cell interconnects," *Surface & Coatings Technology*, vol. 34, pp. 365–372, 2018.

Review Article

Available Relevant Study on Stress Analysis and Static Strength Prediction of Fiber Metal Laminates

Xiaochen Zhang, Weiyang Meng[✉], Jiancheng Guo, and Yu Zhang

School of Mechanical Engineering, Shenyang Jianzhu University, No. 25 Hunnan Middle Road, Hunnan District, Shenyang, China 110168

Correspondence should be addressed to Weiyang Meng; mengweiyang025@163.com

Received 1 October 2020; Revised 13 October 2020; Accepted 14 October 2020; Published 9 December 2020

Academic Editor: Jian Chen

Copyright © 2020 Xiaochen Zhang et al. This is an open access article distributed under the Creative Commons Attribution License, which permits unrestricted use, distribution, and reproduction in any medium, provided the original work is properly cited.

Fiber metal laminates (FMLs) are a novel type of structural material that has been extensively applied in the aerospace field. These laminates are sandwich-type composite materials that comprise alternate metal and fiber-reinforced resin layers. Because of the structural characteristics of the material, it has high-impact resistance from the metal layer and increased fracture toughness and excellent fatigue and damage tolerance properties from the fiber layer. To further develop and apply this new composite material, it is essential to understand the research status on the stress analysis of each component in FMLs and the tensile strength properties of FMLs. Therefore, in this study, the current research status on the residual stress and applied stress of the component materials in FMLs and the tensile strength of the laminates is summarized. The relationship between the applied stress of each layer and the remote stress of laminates and the relationship between the tensile properties of laminates and the component material properties in laminates are clarified. Additionally, the theoretical basis and direction of development of the related models are analyzed and studied. Consequently, all of the above are aimed at laying a foundation for further investigations of the laminate theory and for the improvement of the theoretical research system.

1. Introduction

Fiber metal laminates (FMLs) constitute a joint scientific and technological achievement of Delft University, Fokker Aircraft Company, and the National Aerospace Laboratory of the Netherlands [1]. They are sandwich-type composites that comprise alternate metal and fiber-reinforced resin composite layers. They have high-impact resistance, increased fracture toughness, excellent fatigue, and damage tolerance properties and have attracted the attention of numerous enterprises and research institutes worldwide [2].

Different material properties can be obtained by changing the thickness, quantity, and type of the metal layer, the direction and system of fibers, and the thickness, quantity, and layout order of the fiber layer. While these composites perfectly combine the performance advantages of two different materials, FMLs also improve and remedy the individual deficiencies of the two materials. That is, they overcome the shortcomings of low-fatigue strength of aluminum alloys

and the low ductility and impact strength, increased cost, and poor processability of fiber layers [3]. Compared to traditionally used aluminum alloy materials in aviation, FMLs can reduce weight by 25%–30% and increase fatigue life by a factor of 10–15 [4]. Their performance meets the requirements of the new generation of aviation equipment, although their manufacturing is complex and costly [5, 6]. Because of their light weight and high-damage tolerance, FMLs are currently used in aerospace structures instead of high-strength aluminum alloys [7], with examples including the fuselage, leading edge, and other parts of the Airbus A380 [8–10].

As shown in the schematic in Figure 1, the metal layers of FMLs can be accompanied by the fibers that resist crack growth [11, 12]. When cracks are generated and propagate in the metal layer, the fiber layer has a bridging effect that transfers a part of the load in the metal layer, and the stress of the metal layer and the stress intensity factor of the crack tip are reduced. It has also been reported that, in the process

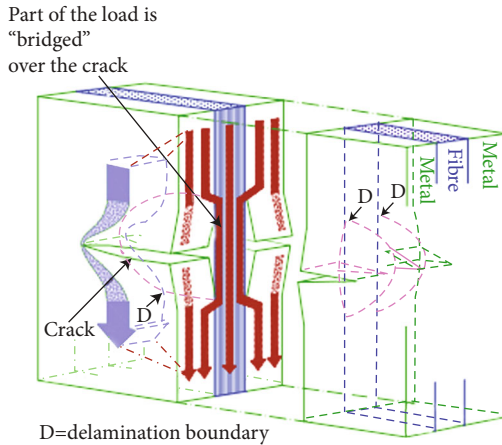


FIGURE 1: Stress path of cracked FMLs [17]. D: delamination boundary.

of fatigue, the stress in the metal layer plays a major role prior to the occurrence of the bridging mechanism, with the metal layer and bridging stresses working together upon the initiation of the bridging mechanism [13–16]. Therefore, the stress analysis of each layer in FMLs is critical when studying their fatigue properties. In addition, the study on the static strength properties of FMLs is based on stress analysis of each layer. In other words, the stress analysis of each layer in FMLs is a precondition and basis for studying their static and fatigue strengths.

Fiber metal laminates have unique structures and damage characteristics that yield the aforementioned advantages. However, FMLs also exhibit a number of characteristics that could, to a certain extent, restrict the application of laminates in the aerospace industry. Currently, a feature of Glass Reinforced Aluminum Laminates (GLARE) is their low Young's modulus compared to monolithic aluminum [8]. Young's modulus of the glass fiber layer is lower than that of the aluminum layer, and the combination of the aluminum and glass fiber layers inevitably results in a lower Young's modulus than that of a single aluminum alloy. Each layer with different material components has a different stiffness in the laminates. During a fatigue stress cycle, the layer with larger stiffness will generate more stress [12, 18]. The aluminum layer has a greater stiffness compared to the laminates, which will result in a higher stress level than the applied stress of the laminate. Another problem of FMLs is the existence of residual stresses. The FMLs are cured at an elevated temperature. After they cool down to room temperature, residual stresses will be generated in all layers of the cured laminate because of the differences in the thermal expansion coefficients. The residual stress in the aluminum layer of GLARE is tensile [12]. These two factors will result in a considerable increase in metal layer stress in the laminates under tensile loads. Therefore, it is essential to properly determine the stress of the metal layer in FMLs.

As an important structural material in the aerospace field, FMLs are primarily used as key fatigue parts. Although their fatigue performance constitutes a focus of material

research studies, the static strength constitutes a basic mechanical property of materials, and its investigation is equally important. To further develop and apply these materials, it is necessary to evaluate the static strength properties and to clarify the relationship between the tensile properties of laminates and the properties of the component materials.

This study assesses the current status of knowledge on the stress levels of each layer in FMLs and summarizes the tensile laminate properties. The basic theory pertaining to established models is reviewed to establish (a) the relationship between the stress of each layer and the remote stress of laminates and (b) the relationship between the tensile properties of laminates and the component material properties. To promote further studies of the FMLs based on the analysis of the existing models, the direction of the anticipated theoretical development is clarified.

2. Stress Analysis

So far, according to the types of fibers and metals, fiber metal laminates have mainly undergone four upgrades. They are Aramid Reinforced Aluminum Laminates (ARALL), Glass Reinforced Aluminum Laminates (GLARE), Carbon Reinforced Aluminum Laminate (CARE), and Titanium/Graphite Hybrid Laminates (TIGR). Among the four generations of fiber metal laminates, ARALL laminates and GLARE laminates have been successfully commercialized. There are some differences in structure between the two types of laminates. For ARALL laminates, there is a certain thickness of adhesive layer between the aramid fiber and aluminum alloy, but there is no adhesive layer between the glass fiber and aluminum alloy for the GLARE laminate, as shown in Figure 2. There are also some differences in metal surface treatment methods between the two kinds of laminates. For ARALL laminates, the metal surface of the bonding surface is not treated, while for GLARE laminates, the metal surface of the bonding surface is treated by sandblast, phosphoric acid anodization, and other methods, as shown in Figure 3.

2.1. Residual Stress Analysis. The preparation of fiber-reinforced metal laminates requires the bonding of each component material through curing. The curing of FMLs requires increased temperatures. When it is cooled to room temperature, residual stresses will be generated in each layer of the cured laminates because of the different thermal expansion coefficients of each material. Given that the metal layer produces residual tensile stress, the actual stress imparted to the metal layer will be further increased because of the tensile load, as shown in Figure 4. Therefore, for FMLs, the study of residual stress is critical. In addition, the residual stress of the metal was usually measured by strain gauge test, and the testing principle is shown in Figure 5.

2.1.1. Analytic Method for Solving Residual Stresses. Based on the self-balancing principle of the residual stress of composites after curing, Oken and June [20] assumed that the response of each component material in the laminate exhibits elastic properties during the cooling process. Furthermore, according to the different thermal expansion coefficients of

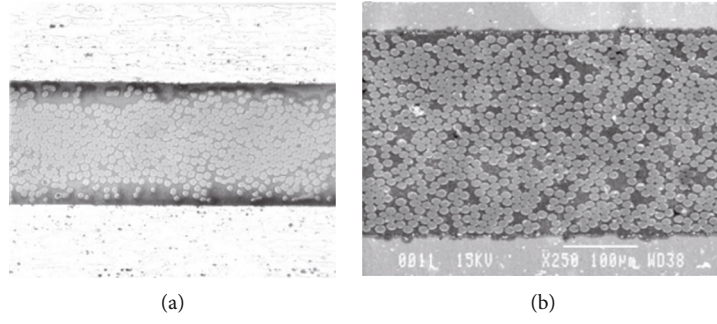


FIGURE 2: Fiber distribution in ARALL (a) and GLARE (b) [19].

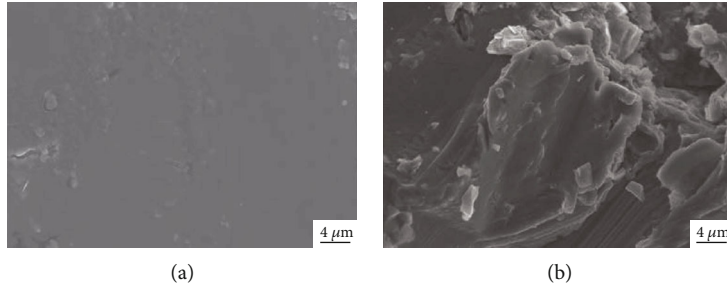


FIGURE 3: Surface morphology of metal layer in ARALL (a) and surface morphology after sandblast in GLARE (b).

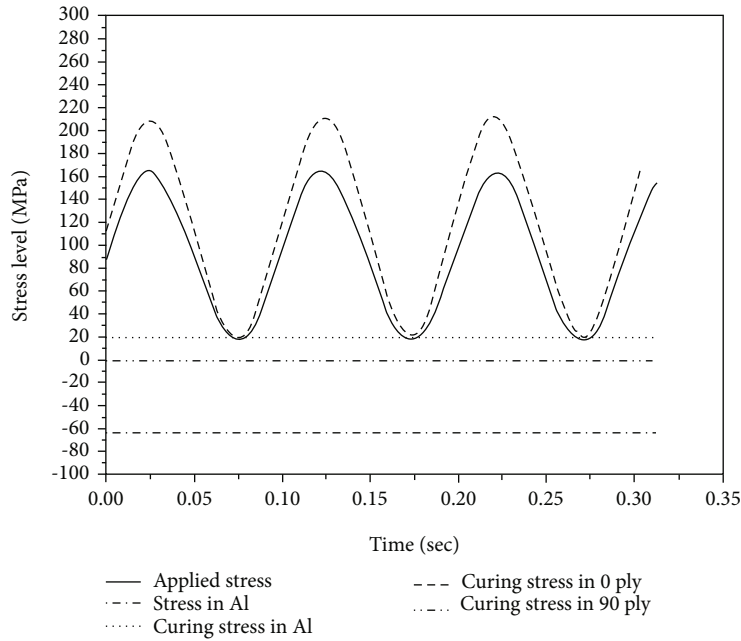


FIGURE 4: The stress level in Al layer and curing stress in each layer.

each component in the laminates, a commonly accepted formula for the calculation of residual stress of metal layers in FMLs is proposed, as follows:

$$\sigma_{r,AL} = E_{AL} \left(1 + \frac{E_{AL} t_{AL}}{E_{fm} t_{fm}} \right)^{-1} [(\alpha_{fm} - \alpha_{AL})(T_T - T_C)], \quad (1)$$

where E_{fm} and t_{fm} are the elastic modulus and thickness of the fiber resin layer in the laminates, respectively; E_{AL} and t_{AL} are the elastic modulus and thickness of the metal layer in the laminates, respectively; T_T and T_C are the test and curing temperatures, respectively; and α_{AL} and α_{fm} are the expansion coefficients of the metal and fiber resin layers, respectively.

Based on the classical laminate theory and the constitutive relationship of materials, the expression for the curing

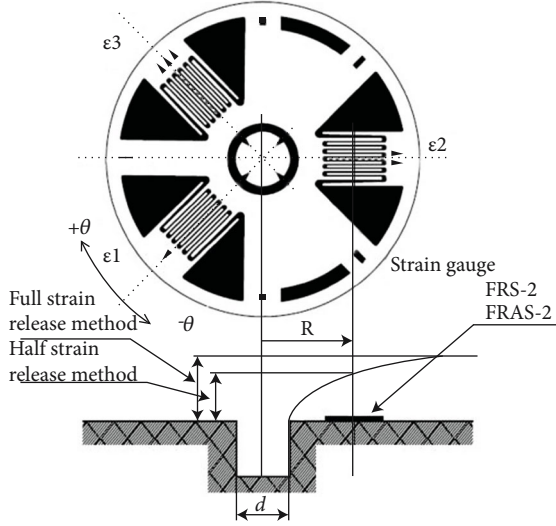


FIGURE 5: Schematic diagram of strain gauge test.

residual stress $\bar{\sigma}_{c,p}$ for each layer in FMLs was deduced by Homan [12] based on the consideration of the effect of thermal expansion coefficients of different materials on the internal stress of laminates during the curing process. The expression is as follows:

$$\bar{\sigma}_{c,p} = (S_{\varphi})_p (\bar{\varepsilon}_c - \Delta T \bar{\alpha}_p), \quad (2)$$

where $(S_{\varphi})_p$ is the stiffness matrix of each layer material at an angle φ , $\bar{\varepsilon}_c$ is the curing strain of the material, ΔT is the temperature difference before and after curing, and $\bar{\alpha}_p$ is the thermal expansion coefficient of each layer.

Khan et al. [17] further extended this theory based on the combination of the classical laminate and thermal expansion theories and proposed a new method to calculate the residual stress of each layer in the FML before and after the stress redistribution. The stress and strain curves in poststretching process are shown in Figure 6, and the expression for the metal layer stress is as follows:

$$\begin{bmatrix} \alpha_1 \\ \alpha_2 \\ \tau_{12} \end{bmatrix}_{al} = \begin{bmatrix} Q_{11} & Q_{12} & 0 \\ Q_{12} & Q_{22} & 0 \\ 0 & 0 & Q_{66} \end{bmatrix}_{al} \eta_{al}, \quad (3)$$

$$\eta_{al} = \begin{bmatrix} \varepsilon_{1,pl} \\ \varepsilon_{2,pl} \\ 0 \end{bmatrix}_{lam} + \begin{bmatrix} A_{11} & A_{12} & 0 \\ A_{12} & A_{22} & 0 \\ 0 & 0 & A_{66} \end{bmatrix}^{-1} N - \begin{bmatrix} 1 \\ 1 \\ 0 \end{bmatrix} \alpha_{al} \Delta T - \begin{bmatrix} \varepsilon_{1,pl} \\ \varepsilon_{2,pl} \\ 0 \end{bmatrix}_{al}, \quad (4)$$

where $N = N_i + N_i^T$, N_i is defined as the external load acting on laminates, N_i^T is defined as the force owing to thermal expansion, A_{ij} is defined as the extensional stiffness of the laminate, α_{al} is defined as the coefficient of thermal expansion for Al, and ΔT is defined as the temperature differ-

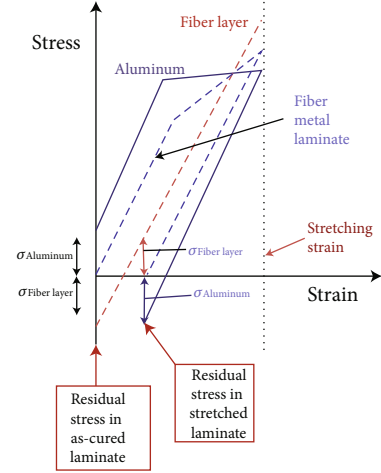


FIGURE 6: Illustration of poststretching process with stress and strain curves [17].

ence before and after curing. Before stretching, $\varepsilon_{1,pl}$ and $\varepsilon_{2,pl}$ are both equal to zero, and $N_i = 0$. After stretching, $\varepsilon_{1,pl}$ is known, $\varepsilon_{2,pl}$ can be solved using the corresponding expressions, and $N_i = 0$.

Hu et al. [21, 22] adjusted the residual stress of Aramid Reinforced Aluminum Lamina (ARALL) 3/2 laminates using prestress and prestrain methods. A prestress method using springs was used to prestretch the glass fibers before laminate curing, and strain gauges were used to detect the residual stresses of the laminates at each stage during the formation process. Finally, the relationship between the residual stress σ_1 , prestress, and the curing temperature are analyzed, and the relevant expression is as follows:

$$\frac{\sigma_1}{E_1} = -\frac{\varepsilon_0}{1 + E_1 t_1 / E_2 t_2} + \frac{1}{1 + E_1 t_1 / E_2 t_2} (\alpha_1 - \alpha_2) (T_0 - T), \quad (5)$$

where t , E , and α are the thickness, elasticity modulus, and coefficient of thermal expansion of the component materials, respectively; ε_0 is the strain of the fiber after it was prestressed; T is the current temperature; T_0 is the curing temperature; and the indices 1 and 2 denote the aluminum alloy and fiber layer, respectively. In addition, the prestrain method is used to stretch the cured laminate to produce a certain amount of plastic deformation (typically in the range of 0.4%–0.7%). Accordingly, the relationship between the residual stress σ_1 and the applied prestrain is analyzed and is found to be linear. The relevant expression is as follows:

$$\sigma_1 = \frac{D_{11} - B_{11}^2 / A_{11}}{t_1 (1.5 t_1 + t_2) - (B_{11} / A_{11}) t_1} \times \frac{1}{\rho}, \quad (6)$$

where A_{11} , B_{11} , and D_{11} are the elastic constants of the laminates, ρ is the curvature radius of laminates after corrosion, and t_1 and t_2 are the thicknesses of the metal and fiber layers, respectively.

An analytical model was proposed by Abouhamzeh et al. [23] to predict the residual stress generated during the curing of FMLs. The model was based on the classical laminate theory and on an additional term that was dependent on the curing shrinkage. Accordingly, this model (a) reflects the change of stiffness and the chemical shrinkage of the material during curing and (b) predicts the development of residual stresses during curing for both the free and constrained (molded) curing of the composite laminates.

In addition, Li et al. [24], Zhong et al. [25], amongst others, also studied the residual stresses formed during the curing of the FMLs and proposed a corresponding theoretical calculation model. Relevant experiments were conducted to test the residual stresses of FMLs, and the proposed model was validated.

2.1.2. Other Methods Used to Solve Residual Stresses. In addition to the most commonly used analytical method, there are also experimental and finite element methods that can be used to determine the residual stress of each layer in FMLs. The traditional test methods include the strain gauge embedding method, laser Raman spectroscopy, X-ray, fiber Bragg grating, and the corrosion delayering method. These traditional experimental methods are not specifically discussed in this study. Compared to the two methods presented above, the development of the finite element model is still in its infancy.

Using an incremental hole-drilling technique combined with an integration method, Ghasemi and Mohammadi [26] measured experimentally nonuniform residual stresses in each ply of FMLs. At first, the calibration coefficient matrix was calculated using finite element simulation to relate the residual stresses and relieved strains. By performing the incremental hole-drilling experiment, released strains in the FML specimens were then measured. Subsequently, the residual stresses were obtained using the calibration coefficient matrix and the measured strains in each step of the incremental hole-drilling experiment. Finally, the experimental data from the incremental hole-drilling process were evaluated by the theoretical predictions of the classical laminate theory. The strain testing process in IHD experiment is shown in Figure 7.

A quasi-three-dimensional (3D) finite element method was used by Gu et al. [27] to calculate the interlaminar residual stress of FMLs. The computation results for residual stresses in ARALL laminates were generated in free or prestressed states at various levels of service temperatures, and the residual stresses in GLARE laminates in free states were presented. The optical fiber grating technology was used to monitor the strain and temperature of the whole curing process by Hu et al. [28], as shown in Figure 8, and the residual stress of the composite laminate with an aluminum sheet was simulated numerically using the ANSYS software. A finite difference method was employed to consider the strong coupling between the curing kinetics model and the thermal-chemical model during the simulation process for transient temperature fields. Chemical shrinkage was applied to composite materials as an initial strain for each time increment in the residual stress simulation.

The residual stresses of the composite laminates and the aluminum plates were successfully simulated on the basis of the referred technology. The residual stress of GLARE laminates was obtained using X-ray, analytical (Oken and June method), and corrosion delayering methods, which were proposed by Guo and Zheng [29]. The results indicated that the analytical and corrosion delayering methods were more accurate, and the X-ray method exhibited a significant difference and a large dispersion.

In the case of the FMLs, the analysis method for solving the residual stress has been studied more extensively. The study of residual stress in the free state is mature and has attained a high-prediction accuracy. However, when the residual stress is redistributed after stretching, the study of residual stress does not take into account the influence of plastic deformation of the component materials, and its prediction accuracy is not very satisfactory. The test method of residual stress has been developed more extensively, but the prediction accuracy has certain differences, among which the strain gauge embedding and the corrosion delayering methods have higher precisions. The finite element method of residual stress is still in its infancy and exhibits a certain degree of accuracy only for the corresponding situation. Therefore, related, in-depth research needs to be conducted.

2.2. Stress Analysis of Each Layer. The stress analysis of each layer in FMLs is critical for the study of the static and fatigue strengths of laminates. In the study of the static strength, the stress analysis of each layer is the basic premise for determining the failure of the material of each layer. In a fatigue strength study, the stress analysis of each layer is necessary for the prediction of the crack initiation and propagation lifetimes. Therefore, additional studies on the development of stress in each layer in the FML are essential.

For composite laminates, a variety of properties can be solved based on the classical laminate theory, i.e., the various material properties of laminates will be solved by modifying and extending the classical laminate theory [30–35]. This study found that the current solution for the stress of each layer of the FML is similar. The primary steps used to solve the stress in each layer of the FMLs are based on laminate theory and are as follows:

2.2.1. Constitutive Relationships of Laminates and Their Components. Fiber metal laminates comprise parallel metal and nonmetal components. The constitutive relationship of all the components in the laminates is as follows:

$$\sigma_{\text{met}} = S_{\text{met}} \times \varepsilon_{\text{met}}, \varepsilon_{\text{met}} = C_{\text{met}} \times \sigma_{\text{met}}, \quad (7)$$

where σ_{met} is the stress tensor of the metal layer, ε_{met} is the strain tensor of the metal layer, S_{met} is the stiffness matrix of the metal material, and C_{met} is the compliance matrix of the metal material.

Accordingly, the stress-strain constitutive relation of laminates is as follows:

$$\sigma_{\text{lam}} = S_{\text{lam}} \times \varepsilon_{\text{lam}}, \varepsilon_{\text{lam}} = C_{\text{lam}} \times \sigma_{\text{lam}}, \quad (8)$$

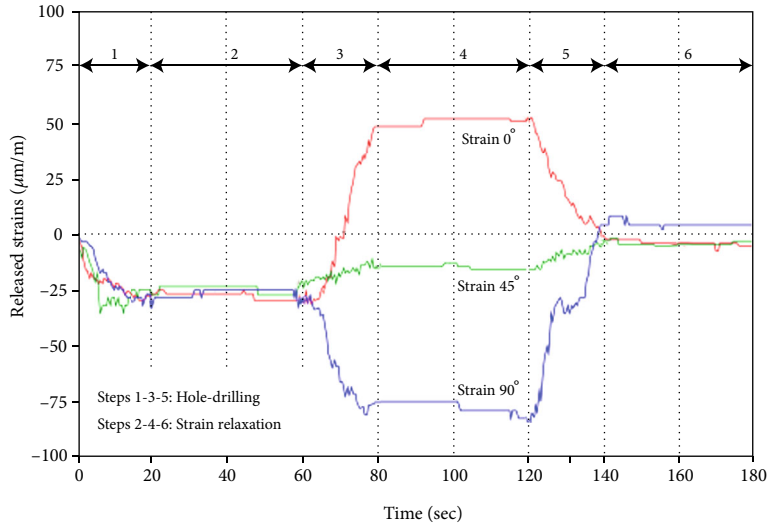
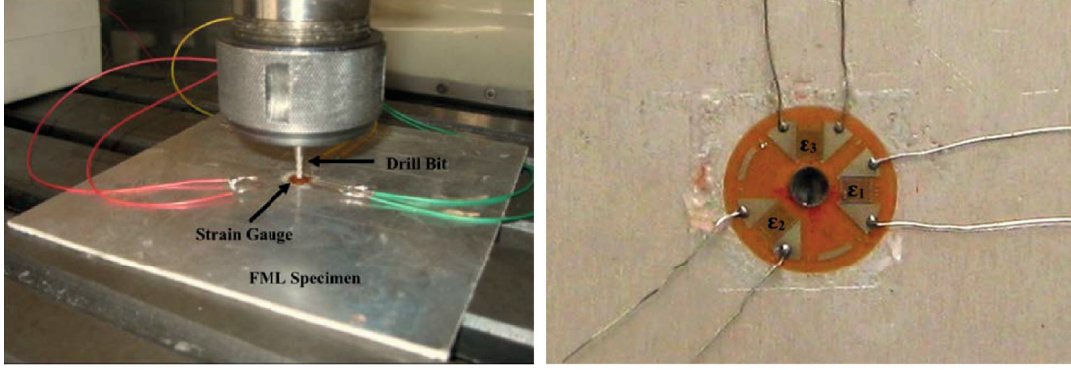


FIGURE 7: Measured strains in the IHD experiment [26].

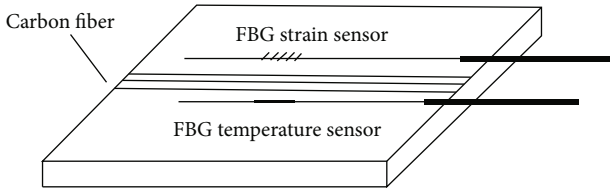


FIGURE 8: Laying method of FBG sensors [28].

where σ_{lam} is the stress tensor, ϵ_{lam} is the strain tensor, S_{lam} is the stiffness matrix, and C_{lam} is the compliance matrix of the laminates.

2.2.2. Solving the Stiffness Matrix of Laminates. The stiffness matrix \mathbf{Q} and compliance matrix \mathbf{S} of the laminates are as follows, respectively:

$$\mathbf{Q} = \sum_{k=1}^n \left([\bar{c}]_k \frac{t_k}{t_{\text{lam}}} \right), \quad (9)$$

$$\mathbf{S} = \mathbf{Q}^{-1}, \quad (10)$$

where t_k is the thickness of the k_{th} material layer and t_{lam} is the thickness of the laminates.

2.2.3. Calculation of the Stress of Each Layer. When the laminate is subjected to an external stress σ_{far} , the strain of the laminate is as follows:

$$\epsilon_{\text{lam}} = C_{\text{lam}} \times \sigma_{\text{far}}. \quad (11)$$

According to the laminate theory, the strain of the laminate is the same as that of the metal layer; therefore,

$$\epsilon_{\text{lam}} = \epsilon_{\text{met}}. \quad (12)$$

Finally, the stress of the metal layer can be expressed as follows:

$$\sigma_{\text{met}} = S_{\text{met}} \times C_{\text{lam}} \times \sigma_{\text{far}}. \quad (13)$$

2.2.4. Research Trend of Stress Solving Methods for Each Layer in FMLs. Currently, studies conducted on the stress solution method of each layer in FMLs are based on two aspects:

- (1) *Correction of the constitutive relationship of the component materials:* the constitutive relationship is corrected by considering the plasticity of the metal material. For example, Nowal [36] described a number of untypical failure modes, which have been observed during unloading in selected designs of

multilayered structures. To clarify this behavior, based on which the delamination and buckling of the external aluminum layers occurs, when the external force is released, the classical lamination theory was applied to an elastic-plastic model of aluminum layers for the analysis of the stress distribution, while the total deformation theory proposed by Hencky and Ilyushin was applied to capture the influence of the plasticity of the metal on the mechanical performance of the hybrid structure. The elastic-plastic stress analysis and damage evolution of FMLs under internal pressure and thermal residual stress were studied by Zheng and Liu [37]. The elastic stress analysis of the composite laminates was performed based on the use of the classical laminate theory. In addition, the elastoplastic stress analysis of the liner layer was conducted by employing the power hardening theory and the Hencky equation in accordance with the plastic theory

- (2) *Correction of the stiffness matrix of the laminate material:* for example, based on the classical laminate theory, Meng et al. [38] modified the calculation method of elastic modulus of laminates by introducing the concept of effective stiffness of laminates; a digital optical strain gauge was used to verify the model, as shown in Figure 9; and a more accurate prediction of the metal layer stress in the FML was realized

Numerous studies have been conducted to solve the stress of each layer in FMLs before stress redistribution. Based on current and accumulated scientific knowledge, the stress of each layer can be solved based on the classical lamination theory in conjunction with the use of the modified constitutive relationship of component materials. However, current knowledge does not allow accurate solution of the stress of each layer based on the classical lamination theory in association with the modified stiffness matrix of laminates. The current research status on the quantification of stress of each layer in FMLs after stress redistribution is still at an initial stage. The solution method fails to take into account the degradation of the properties of each component material.

3. Tensile Properties

The tensile properties of FMLs are affected by their individual components. For example, the stress-strain behavior of FMLs clearly exhibits elastic responses within a 2.0% strain and is dependent on the properties of the prepreg and metal layers, as shown in Figure 10. In addition, its toughness and notch sensitivity depend primarily on the load-bearing capacity of the stress-strain response of the plastic region of the metal layer [39]. Similar to the bulk of fiber-reinforced composites, the properties of FMLs are directional because of the influence of fiber orientation, such as for ARALL and GLARE [40, 41]. It is noted that for FMLs, the interface bond between the prepreg and the

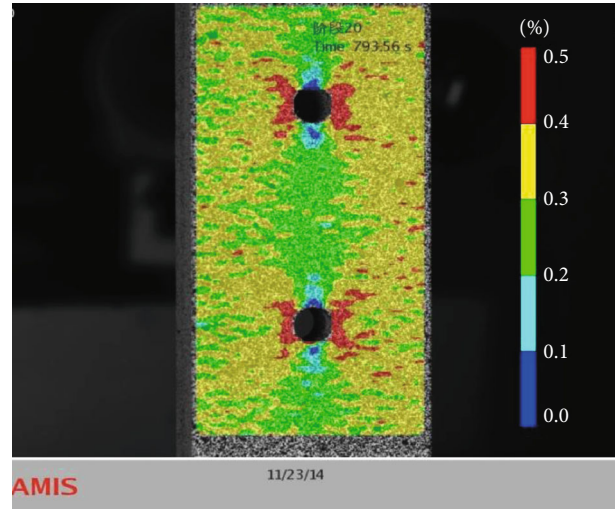


FIGURE 9: Strain diagram of specimen [38].

metal layers plays a critical role in the transfer of stress for different materials in the laminates [2].

Because of its special structure, FMLs are different not only from isotropic metal materials but also from anisotropic fiber-reinforced composites, which make the study of their mechanical properties highly complex. The failure process of FMLs is complex under tensile loading. There are multifracture modes involved in the failure of GLARE laminates, such as matrix cracks, fiber-matrix debonding, fiber fractures, fiber/matrix interfacial shear failure, and interdelamination of laminates. Under longitudinal tensile loading, fiber pull-out and interface-matrix shear modes are common failure modes of fiber layers in FMLs [42]. In addition, the metal layer plays a role in preventing multiple global longitudinal splits. In the presence of transverse tensile loading, matrix failure and matrix-fiber interface debonding/fiber splitting are the primary fracture modes in the fiber-epoxy layer of FMLs. To better understand the formation and developmental damage in FMLs, and the effect of damage on residual strength, additional studies are required. The investigation of the tensile strength of FMLs involves analytical calculations, finite element analyses, and experimental methods, alone or in combination with each other. Currently, the analytical method has matured, and this study primarily introduces the research status of analytical methods.

To date, the techniques for the estimation of the tensile strength of FMLs by using analytical methods have been based on the metal volume fraction (MVF) and classical laminate theories.

3.1. Tensile Strength Calculation Based on Metal Volume Fraction Theory. MVF is a theory proposed by Vlot and Gunnink [2]. This theory can be used to predict the tensile modulus and strength of unidirectional FMLs. The MVF value, as defined by Vlot and Gunnink, can be calculated based on the following equation:

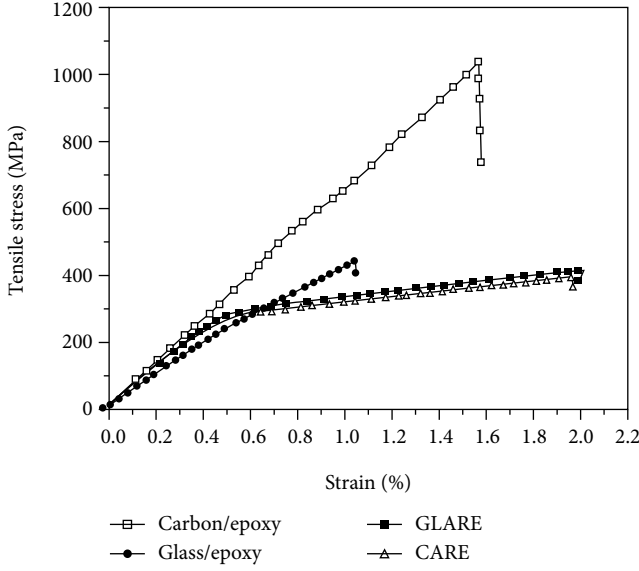


FIGURE 10: Tensile behavior of the laminates studied [39].

$$MVF = \frac{\sum_i^n t_{al}}{t_{lam}}, \quad (14)$$

where t_{lam} is the thickness of the FML, t_{al} is the thickness of a single metal sheet, and n is the layer number of the metal sheet. On the basis of this definition, Vlot and Gunnink [2] also proposed prediction formulas for the tensile properties of GLARE laminates:

$$E_{lam} = MVF \times E_{met} + (1 - MVF) \times E_{FRP}, \quad (15)$$

$$\sigma_{0.2,lam} = \left[MVF + (1 - MVF) \times \frac{E_{FRP}}{E_{met}} \right] \times \sigma_{0.2,met}, \quad (16)$$

$$\sigma_{t,lam} = MVF \times \sigma_{t,met} + (1 - MVF) \times \sigma_{t,FRP}, \quad (17)$$

where σ_t is the ultimate tensile strength, $\sigma_{0.2}$ is the tensile yield strength, E is the tensile modulus, and subscripts lam, met, and FRP denote laminates, the metal layer, and fiber-reinforced composites, respectively.

Based on the characteristics of orthogonal laminates, Ma et al. [43] modified the MVF theory, which, as proposed by Vlot and Gunnink, is only applicable to unidirectional FMLs, and further realized the prediction of the tensile properties of GLARE 3/2 laminates with 0/0° and GLARE 3/2 laminates with 0/90°. The corresponding expressions are as follows:

$$E_{lam} = MVF \times E_{met} + \alpha \times (1 - MVF) \times E_{FRP}, \quad (18)$$

$$\sigma_{0.2,lam} = \left[MVF + \alpha \times (1 - MVF) \times \frac{E_{FRP}}{E_{met}} \right] \times \sigma_{0.2,met}, \quad (19)$$

$$\sigma_{t,lam} = MVF \times \sigma_{t,met} + \alpha \times (1 - MVF) \times \sigma_{t,FRP}, \quad (20)$$

where α is the volume fraction of fibers in the tension direction, σ_t is the ultimate tensile strength, $\sigma_{0.2}$ is the tensile yield

strength, E is the tensile modulus, and subscripts lam, met, and FRP denote laminates, the metal layer, and fiber-reinforced composites, respectively.

According to the characteristics of orthogonal GLARE laminates in combination with the mixing law of elastic moduli for composite materials, Wang et al. [44] modified the MVF theory based on the consideration of the effect of fibers on the performance in two in-plane directions and accurately predicted the elastic modulus, yield stress, and tensile strength of materials. The derived expressions are as follows, respectively:

$$E_{lam} = MVF \times E_{met} + a \times E_{FRP1} + b \times E_{FRP2}, \quad (21)$$

$$\sigma_{t,lam} = \left[MVF + a \times \frac{E_{FRP1}}{E_{met}} + b \times \frac{E_{FRP2}}{E_{met}} \right] \times \sigma_{t,met}, \quad (22)$$

$$\sigma_{0.2,lam} = \left[MVF + a \times \frac{E_{FRP1}}{E_{met}} + b \times \frac{E_{FRP2}}{E_{met}} \right] \times \sigma_{0.2,met}, \quad (23)$$

where $\sigma_{0.2}$ is the tensile yield strength, σ_t is the ultimate tensile strength, E is the tensile modulus, and t is the thickness of the material layer. In addition, subscripts lam and met represent laminates and the metal layer, respectively, and FRP1 and FRP2 represent the fiber layer in the directions of 0° and 90°, respectively. The parameters MVF, a , and b can be calculated as follows: $MVF = \sum_1^3 t_{met}/t_{lam}$, $a = \sum_1^2 t_{FRP1}/t_{lam}$, and $b = \sum_1^2 t_{FRP2}/t_{lam}$.

The MVF method based on the mixing law can predict the tensile properties of FMLs. However, because of the elastic-plastic behavior of the metal layer, the elastic analysis cannot accurately predict the tensile response of FML materials. Therefore, the inelastic deformation behavior of FMLs must be considered after the alloy layer yields. To achieve a more accurate prediction of the stress-strain response and deformation behavior for FMLs, the analytical and finite element models consider that the evaluations of the plastic behavior after yielding and residual stress after curing are essential research directions.

3.2. Tensile Strength Calculation Based on Classical Laminate Theory. Taking into account the inadequacies of the MVF theory, researchers used the classical laminate theory to solve for tensile strength. The survey found that the primary steps needed for the prediction of the tensile strength of FMLs based on laminate theory are as follows:

- (1) Analyze the stress of each layer in FMLs based on the classical laminate theory. The current research status was explained above
- (2) Determine the damage state of the material using the failure criterion of the material. To analyze the failure situation of each layer in FMLs, four major strength theories (maximum tension, maximum linear strain, maximum principal shear stress, and maximum distortion-energy theories) are used for the metal layer, and the Tsai-Hill and Tsai-Wu theories are used in the prepreg layers

- (3) For each layer material that is judged to have failed, the degradation mode of material properties is analyzed based on the stiffness degradation criterion. When the material is considered to be damaged in the second step, the stiffness degradation of the material can be divided into complete and incomplete degradation. Currently, the incomplete degradation criterion is primarily used

There are two research directions used for the modification or expansion of the classical laminate theory to solve the tensile properties of FMLs:

- (1) Correction of the constitutive relationship of component materials in the laminate
- (2) Correction of the degenerate form of component materials in the laminate

The related studies are now discussed. Tensile properties of the Ti/APC-2 laminates with different fiber directions were predicted by Cortés and Cantwell [45]. To predict the tensile strength of laminates at different fiber directions, the classical laminate theory was modified by considering the effect of residual stress, and the failure criteria of Tsai-Hill, Tsai-Wu, and maximum stress were used. However, the model did not consider the effect of the metal plasticity stage. The modified classic laminate theory is as follows:

$$\{\sigma\}_{x,y}^k = \{\sigma^{\text{TH}}\}_{x,y}^k + \{\sigma^{\text{M}}\}_{x,y}^k, \quad (24)$$

$$\{\sigma^{\text{TH}}\}_{x,y}^k = Q_{x,y}^k \left(\{\epsilon^0\}_{x,y} + z\{\kappa\}_{x,y} - \{\alpha\}_{x,y}^k \Delta T \right), \quad (25)$$

$$\{\sigma^{\text{M}}\}_{x,y}^k = Q_{x,y}^k \left(\{\epsilon^0\}_{x,y} + z\{\kappa\}_{x,y} \right), \quad (26)$$

where $\{\sigma\}_{x,y}^k$ is the actual stress of the k_{th} layer in the xy -coordinate system of the laminate specimen, $\{\sigma^{\text{TH}}\}_{x,y}^k$ is the residual thermal stress of the k_{th} layer in the xy -coordinate system of the laminate specimen, $\{\sigma^{\text{M}}\}_{x,y}^k$ is the mechanical stresses of the k_{th} layer in the xy -coordinate system of the laminate specimen, $Q_{x,y}^k$ is the stiffness matrix of the k_{th} layer in the xy -coordinate system of the laminate specimen, $\{\epsilon^0\}_{x,y}$ are the midplane strains of the laminate specimen in the xy -coordinate system, z is the distance from the midplane, and $\{\kappa\}_{x,y}$ is the curvature in the xy -specimen coordinate system.

The tensile stress-strain behavior of GLARE laminates was studied by Iaccarino et al. [46]. To theoretically predict the laminate response based on the anisotropic characteristics of the metal layer, the classical lamination theory was modified to account for the inelastic behavior of aluminum, which was substituted by an “equivalent” material governed by a simple constitutive law. The maximum strain and Tsai-Hill criteria were used as the final failure conditions of aluminum and fiberglass, respectively. The equivalent constitutive relation of the metals can be expressed as follows:

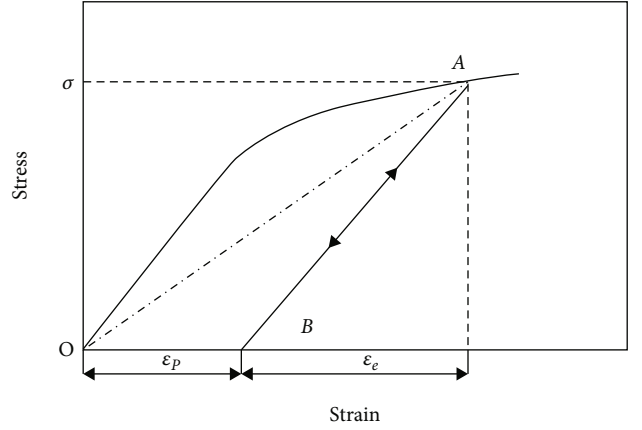


FIGURE 11: Elastic-plastic stress-strain curves for metal materials.

$$\nu_{\text{eq}} = \frac{1}{2} \left[1 - \frac{E_{\text{eq}}}{E_{\text{al}}} (1 - 2\nu_{\text{al}}) \right], \quad (27)$$

where E_{al} is the elastic modulus of aluminum; E_{eq} is the equivalent modulus of aluminum, that is, the slope of the OA segment in Figure 11; and ν_{al} is Poisson's ratio of aluminum.

Chen and Sun [47] described the elastic-plastic stress-strain relations in an ARALL laminate based on the use of classical laminate theory with proper elastic-plastic models for aluminum and modeled ARALL laminates as homogeneous orthotropic elastic-plastic solids based on the use of a three-parameter, plastic potential function. Comparison with experimental results indicated that the orthotropic plasticity model was approximately accurate up to a total strain of 1.2%, and the modified classical laminate theory was found to be capable of describing the stress-strain curves up to failure.

The nonlinear tensile responses and fracture behaviors of GLARE 4 and GLARE 5 laminates were studied by Wu and Yang [42] using inplane loading. An analytical model was proposed based on the modified classical lamination theory, which incorporated the elastoplastic behavior of the aluminum alloy to predict the stress-strain response and deformation behavior of GLARE laminates. The constitutive relationships of the laminate in the elastic and plastic states of the metal layer are as follows, respectively:

$$dN = \left\{ n^{\text{Al}} h^{\text{Al}} \left(S_{\epsilon}^{\text{Al}} \right)^{-1} + n^{\text{c}} h^{\text{c}} Q^{\text{c}} \right\} d\epsilon, \quad (28)$$

$$dN = \left\{ n^{\text{Al}} h^{\text{Al}} \left(S_{\epsilon}^{\text{Al}} + S_{\text{p}}^{\text{Al}} \right)^{-1} + n^{\text{c}} h^{\text{c}} Q^{\text{c}} \right\} d\epsilon, \quad (29)$$

where dN represents the inplane force increments per unit length; $d\epsilon$ represents the midplane strain increments per unit length; S_{ϵ}^{Al} represents the flexibility tensor of the aluminum alloy layer under elastic conditions; S_{p}^{Al} represents the flexibility tensor of the aluminum alloy layer under plastic

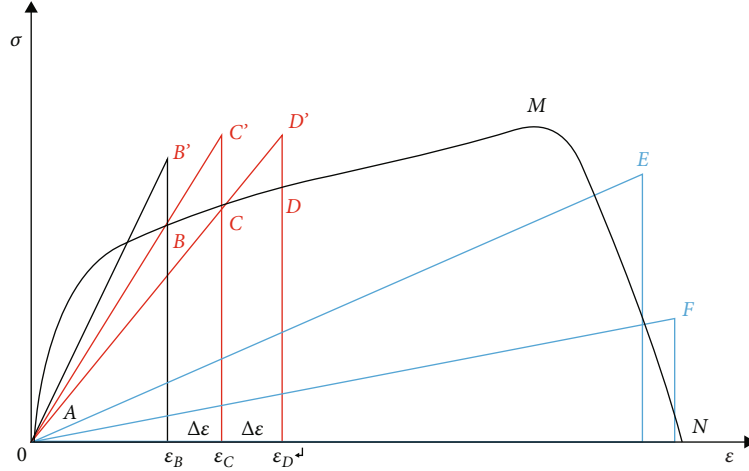


FIGURE 12: The stress-strain curve of composite under tensile loading.

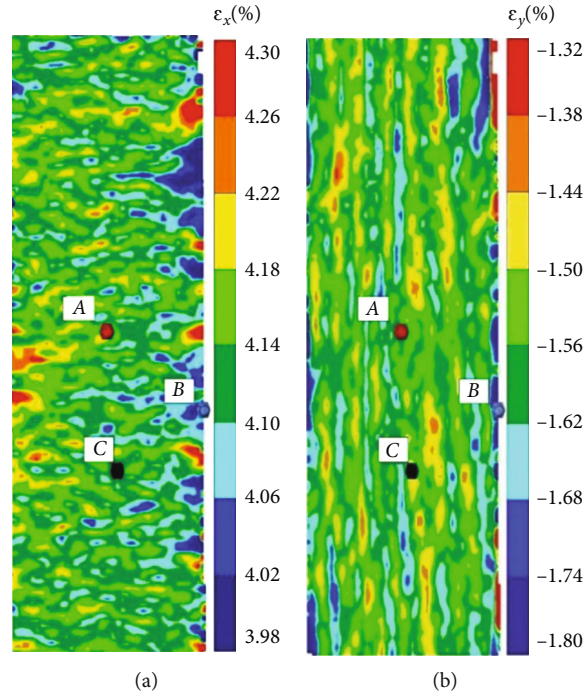


FIGURE 13: Strain distributing nephogram of GLARE2-3/2 laminates under uniaxial tensile loading [49]: (a) axial; (b) transverse.

conditions; n^{Al} and n^c are the numbers of metal and prepreg layers, respectively; h^{Al} and h^c are the thicknesses of the metal and prepreg layers, respectively; and Q^c is the stiffness matrix of the prepreg layer.

The classical laminate theory (CLT) was applied by Kawai et al. [48] to describe the off-axis inelastic behavior of GLARE 2 laminate. An incomplete stiffness degradation model was proposed, which took into account the transverse failure in glass fiber-reinforced plastic layers to cause an instantaneous degradation of transverse and shear elastic moduli based on CLT. Accordingly, the characteristic deformation behavior of GLARE 2 was accurately described. The incomplete stiffness degradation model is as follows:

$$E_{11}^d = E_{11}, E_{22}^d = 0, \nu_{12}^d = 0, G_{12}^d = 0, \quad (30)$$

where E_{11}^d degenerates into a new E_{11} , and the other parameters tend to zero.

Cortés and Cantwell [45] reported the tensile properties of Ti/APC-2 laminates under different fiber directions and proposed that the stiffness degradation of the prepreg layer was related to the loading angle. When the loading angle was less than 15° , the degenerated stiffness is as follows:

$$E_1 = 0, E_{22}^d = E_{22}, \nu_{12} = 0, G_{12} = 0. \quad (31)$$

When the loading angle is greater than 15° , the degenerated stiffness is equal to

$$E_{11}^d = E_{11}, E_2 = 0, \nu_{12} = 0, G_{12} = 0. \quad (32)$$

A general method to describe the degradation of material properties was presented by Tong et al. [49], which is simple and suitable for theoretical model calculation. When the material is in the fracture stage, as shown in the MN section of the curve in Figure 12, the degradation process of material properties can be described in the theoretical model as long as the equation of the stress-strain curve is known. It is suggested that formula (33) should be used for fitting when the stress-strain curve of the material is close to the index change and formula (34) should be used when it is close to the linear change. In addition, the distributing nephogram of the strain for the laminate before fracture was obtained by experiment, as shown in Figure 13.

$$y = A_1 e^{(-x/t_1)} + A_2 e^{(-x/t_2)} + y_0, \quad (33)$$

$$y = A_1 x + B. \quad (34)$$

A common analytical model that is independent of the configuration of the laminate was developed by Rao and Subba Rao [50] based on a hybrid degradation scheme. The model was proposed using the constant degradation factors based on the condition of the adjacent lamina. It is considered that the deterioration of the performance of each damaged layer is related to the state of its adjacent lamina. In other words, when two adjacent laminae are not damaged, the performance of the damaged lamina will degenerate to 70%. When only one adjacent lamina is damaged, it will degenerate to 50%; when both adjacent laminae are damaged, the performance of the damaged lamina will degenerate to approximately zero.

Currently, theoretical research on the tensile strength of FMLs is primarily based on the classical laminate theory. Because of the complexity of FMLs, there is no perfect theoretical system to analyze and calculate the tensile strength of FMLs. In addition, the effects of interlaminar properties on the tensile strength of FMLs are critical and cannot be ignored. Currently, the classical laminate theory fails to consider the effect of interlaminar properties, and it will be further studied by considering this effect.

4. Conclusions

In this study, the stress analysis and tensile strength of FMLs were introduced. The developments of the theoretical and experimental methods for the solution of residual stresses of laminates were expounded. The analytical models for the stress analysis of each layer in the laminates and their corresponding defects were analyzed. The two types of analytical models for tensile strength of laminates and their corresponding defects were studied and discussed.

In summary, for the analyses of the basic mechanical properties of FMLs, the residual stress and stress imposed on each layer in a free state have matured developmentally.

However, previous studies on the corresponding performance after the stress redistribution did not consider the property degradation effects of the component materials. Accordingly, additional studies on this aspect are needed. In-depth studies have been conducted on the tensile properties of FMLs based on classical laminate theory; however, only limited studies have been conducted on the interfacial bonding strength of laminates. The interfacial bonding strength plays a critical role in static strength performance. Correspondingly, the influencing factors have not been identified. In addition, the compressive properties and its failure mechanism of FMLs have not been fully studied, and the related research work considering residual stress on the compressive properties needs further development.

Conflicts of Interest

The authors declare that they have no conflicts of interest.

Acknowledgments

This work was supported by the National Natural Science Foundation of China (grant number 52005352), the Doctoral Start-up Foundation of Liaoning Province (grant number 2019-BS-198), the Key Laboratory of Vibration and Control of Aero-Propulsion System, Ministry of Education, Northeastern University (No. VCAME202007), and the "Seedling Cultivation" Project for Young Scientific and Technological Talents of Liaoning Education Department (No. Inqn201908).

References

- [1] A. Vlot, L. B. Vogelesang, and T. J. de Vries, "Towards application of fibre metal laminates in large aircraft," *Aircraft Engineering and Aerospace Technology*, vol. 71, no. 6, pp. 558–570, 1999.
- [2] A. Vlot and J. W. Gunnink, Eds., *Fibre Metal Laminates: An Introduction*, Kluwer Academic Publishers, Dordrecht, 2001.
- [3] S. Y. Wang, *Preparation and Mechanical Properties of Fiber Metal Laminates [Dissertation]*, Harbin Institute of Technology, Harbin, 2012.
- [4] J. Tao, H. G. Li, L. Pan, and Y. B. Hu, "Review on research and development of fiber metal laminates," *Nanjing University of Aeronautics and Astronautics*, vol. 47, pp. 626–636, 2015.
- [5] L. P. Jiang, "Research of glare laminate fatigue performance comprehensive evaluation," *Materials Research*, vol. 36, pp. 113–118, 2012.
- [6] C. A. J. R. Vermeeren, T. Beumler, J. L. C. G. de Kanter, O. C. van der Jagt, and B. C. L. Out, "Glare design aspects and philosophies," *Applied Composite Materials*, vol. 10, no. 4/5, pp. 257–276, 2003.
- [7] Y. J. Guo and X. R. Wu, "Phenomenological model for predicting fatigue crack growth in fiber reinforced metal laminates," *Acta Aeronaut et Astronaut Sinica*, vol. 19, pp. 275–282, 1998.
- [8] P. Y. Chang, P. C. Yeh, and J. M. Yang, "Fatigue crack initiation in hybrid boron/glass/aluminum fiber metal laminates," *Materials Science and Engineering: A*, vol. 496, no. 1–2, pp. 273–280, 2008.
- [9] R. M. Frizzell, C. T. McCarthy, and M. A. McCarthy, "An experimental investigation into the progression of damage in pin-

- loaded fibre metal laminates," *Composites Part B: Engineering*, vol. 39, no. 6, pp. 907–925, 2008.
- [10] Y. M. Fu, J. Zhong, and Y. Chen, "Thermal postbuckling analysis of fiber-metal laminated plates including interfacial damage," *Composites Part B: Engineering*, vol. 56, pp. 358–364, 2014.
 - [11] R. Marissen, *Fatigue Crack Growth in ARALL: A Hybrid Aluminum-Aramid Composite Material Crack Growth Mechanisms and Quantitative Predictions of the Crack Growth Rates, Report LR-574*, Delft University of Technology, Delft, 1988.
 - [12] J. J. Homan, "Fatigue initiation in fibre metal laminates," *International Journal of Fatigue*, vol. 28, no. 4, pp. 366–374, 2006.
 - [13] Y. J. Guo, *Fatigue Damage and Life Prediction of Fiber Reinforced Metal Laminates [Dissertation]*, Institute of Aeronautical Materials, Beijing, 1997.
 - [14] O. Kieboom, *Fatigue Crack Initiation and Early Crack Growth in Glare at Different Temperatures [Dissertation]*, Delft University of Technology, Delft, 2000.
 - [15] I. Sen, R. C. Alderliesten, and R. Benedictus, "Design optimisation procedure for fibre metal laminates based on fatigue crack initiation," *Composite Structures*, vol. 120, pp. 275–284, 2015.
 - [16] Y. Huang, J. Z. Liu, X. Huang, J. Z. Zhang, and G. Q. Yue, "Delamination and fatigue crack growth behavior in fiber metal laminates (Glare) under single overloads," *International Journal of Fatigue*, vol. 78, pp. 53–60, 2015.
 - [17] S. U. Khan, R. C. Alderliesten, and R. Benedictus, "Post-stretching induced stress redistribution in fibre metal laminates for increased fatigue crack growth resistance," *Fibre Science and Technology*, vol. 69, no. 3-4, pp. 396–405, 2009.
 - [18] A. Vasek, J. Polak, and V. Kozak, "Fatigue crack initiation in fibre-metal laminate GLARE 2," *Materials Science and Engineering A*, vol. 234-236, pp. 621–624, 1997.
 - [19] R. C. Alderliesten, "On the available relevant approaches for fatigue crack propagation prediction in GLARE," *International Journal of Fatigue*, vol. 29, no. 2, pp. 289–304, 2007.
 - [20] S. Oken and R. R. June, *Analytical and Experimental Investigation of Aircraft Metal Structures Reinforced with Filamentary Composites [Report]*, NASA CR-1859, 1971.
 - [21] H. J. Hu, H. Y. Li, and R. Q. Zheng, "Modifying residual stresses in ARALL laminates by prestressing," *Acta Mater Compos Sinica*, vol. 10, pp. 9–12, 1993.
 - [22] H. J. Hu, H. Y. Li, R. Q. Zheng, and W. Qiang, "Method of modifying residual stresses of aramid-aluminum laminates (ARALL) by prestrain," *Acta Mater Compos Sinica*, vol. 13, pp. 123–126, 1995.
 - [23] M. Abouhamzeh, J. Sinke, K. M. B. Jansen, and R. Benedictus, "Closed form expression for residual stresses and warpage during cure of composite laminates," *Composite Structures*, vol. 133, pp. 902–910, 2015.
 - [24] H. Y. Li, H. J. Hu, and R. Q. Zheng, "Analysis and measurement on residual stress of aramid aluminum laminates," *Acta Aeronaut et Astronaut Sinica*, vol. 15, pp. 596–600, 1994.
 - [25] W. H. Zhong, Z. Q. Gao, Z. G. Zhang, and H. C. Yang, "Study of residual stress in super-hybrid composite Ti/CFRP," *New carbon Maternity*, vol. 15, pp. 18–22, 2000.
 - [26] A. R. Ghasemi and M. M. Mohammadi, "Residual stress measurement of fiber metal laminates using incremental hole-drilling technique in consideration of the integral method," *International Journal of Mechanical Sciences*, vol. 114, pp. 246–256, 2016.
 - [27] Z. F. Gu, D. Y. Cui, W. H. Zhong, H. Y. Li, H. J. Hu, and R. Q. Zheng, "Analysis of residual stresses for fiber reinforced aluminium laminate," *Acta Mater Compos Sinica*, vol. 12, pp. 75–80, 1995.
 - [28] Z. H. Hu, G. R. Wang, X. D. He, and W. B. Liu, "The effect of metal mould on residual stress of composite laminated during cure process," *J Astronaut*, vol. 28, pp. 816–818, 2007.
 - [29] Y. J. Guo and R. Q. Zheng, "The residual stresses in glass fiber reinforced aluminium laminates (GLARE)," *Journal of Materials Engineering*, no. 1, pp. 28–30, 1998.
 - [30] J. Brunbauer and G. Pinter, "Fatigue life prediction of carbon fibre reinforced laminates by using cycle-dependent classical laminate theory," *Composites Part B: Engineering*, vol. 70, pp. 167–174, 2015.
 - [31] C. H. Park and A. Baz, "Comparison between finite element formulations of active constrained layer damping using classical and layer-wise laminate theory," *Finite Elements in Analysis and Design*, vol. 37, no. 1, pp. 35–56, 2001.
 - [32] P. Chaphalkar and A. D. Kelkar, "Classical laminate theory model for twill weave fabric composites," *Composites. Part A, Applied Science and Manufacturing*, vol. 32, no. 9, pp. 1281–1289, 2001.
 - [33] Q. Wang, L. L. Liang, and C. N. Peng, "Analysis of the mechanical properties of TC4-6061 composite plate based on classical laminate theory," *Applied Mechanics and Materials*, vol. 724, pp. 12–16, 2015.
 - [34] V. S. Kale and N. K. Chhapkhan, "Analysis of the response of a laminate to imposed forces using classical lamination theory and finite element technique," *Int J Eng Sci Tec*, vol. 5, pp. 1419–1426, 2013.
 - [35] H. Fukunag and G. N. Vanderplaats, "Stiffness optimization of orthotropic laminated composites using lamination parameters," *AIAA Journal*, vol. 29, pp. 641–646, 1991.
 - [36] T. Nowal, "Elastic-plastic behavior and failure analysis of selected fiber metal laminates," *Composite Structures*, vol. 183, pp. 450–456, 2018.
 - [37] J. Y. Zheng and P. F. Liu, "Elasto-plastic stress analysis and burst strength evaluation of Al-carbon fiber/epoxy composite cylindrical laminates," *Computational Materials Science*, vol. 42, no. 3, pp. 453–461, 2008.
 - [38] W. Y. Meng, L. Y. Xie, J. X. Hu, X. Lv, B. Qin, and B. W. Wang, "Strain measurement and stress prediction methods of metal layer in fiber metal laminates," *J B Univ Aeronaut Astronaut*, vol. 44, pp. 142–150, 2018.
 - [39] E. C. Botelho, R. A. Silva, L. C. Pardini, and M. C. Rezende, "A review on the development and properties of continuous fiber/epoxy/aluminum hybrid composites for aircraft structures," *Materials Research*, vol. 9, no. 3, pp. 247–256, 2006.
 - [40] J. W. Gunnink and L. B. Vogelesang, "Aerospace ARALL-the advancement in aircraft materials," in *Proceedings of the 35th International SAMPE Symposium*, pp. 1708–1721, Anaheim, California, April 1990.
 - [41] J. W. Gunnink and L. B. Vogelesang, "Aerospace ARALL: a challenger for aircraft designer," in *Proceedings of the 36th International SAMPE Symposium and Exhibition*, pp. 1509–1522, San Diego, California, April 1991.
 - [42] G. C. Wu and J. M. Yang, "Analytical modelling and numerical simulation of the nonlinear deformation of hybrid fibre-metal laminates," *Modelling Simul Mater Sci Eng*, vol. 13, no. 3, pp. 413–425, 2005.

- [43] H. Y. Ma, D. Mackay, S. Chi Lee, and W. Ying Shiu, "Aliphatic and cyclic hydrocarbons," *Journal of Materials Engineering*, no. 7, pp. 61–64, 2006.
- [44] Y. J. Wang, B. Wang, L. Zhang, and H. Y. Ma, "Tensile properties of glass fiber reinforced aluminum orthorhombic laminate," *Journal of Materials Engineering*, vol. 43, pp. 60–65, 2015.
- [45] P. Cortés and W. J. Cantwell, "The prediction of tensile failure in titanium-based thermoplastic fibre-metal laminates," *Composites Science and Technology*, vol. 66, no. 13, pp. 2306–2316, 2006.
- [46] P. Iaccarino, A. Langella, and G. Caprino, "A simplified model to predict the tensile and shear stress–strain behaviour of fibre-glass/aluminium laminates," *Composites Science and Technology*, vol. 67, no. 9, pp. 1784–1793, 2007.
- [47] J. L. Chen and C. T. Sun, "Modeling of orthotropic elastic-plastic properties of ARALL laminates," *Composites Science and Technology*, vol. 36, no. 4, pp. 321–337, 1989.
- [48] M. Kawai, M. Morishita, S. Tomura, and K. Takumida, "Inelastic behavior and strength of fiber-metal hybrid composite: glare," *International Journal of Mechanical Sciences*, vol. 40, no. 2-3, pp. 183–198, 1998.
- [49] A. S. Tong, L. Y. Xie, E. J. Bai, X. Bai, S. J. Zhang, and B. W. Wang, "Test and prediction model of statics property of fiber metal laminates," *Acta Aeronautica Et Astronautica Sinica*, vol. 39, p. 221193, 2017.
- [50] P. M. Rao and V. Subba Rao, "Estimating the failure strength of fiber metal laminates by using a hybrid degradation model," *Journal of Reinforced Plastics and Composites*, vol. 29, no. 20, pp. 3058–3063, 2010.

Research Article

Mechanical Properties and Failure Behavior of 3D-SiC_f/SiC Composites with Different Interphases

Deng-hao Ma¹, En-ze Jin¹, Jun-ping Li¹, Zhen-hua Hou², Jian Yin³, Xin Sun¹, Jin-ming Fang¹, Xiao-dong Gong¹ and Li-na Huang¹

¹Science and Technology of Advanced Functional Composite Materials Laboratory, Aerospace Research Institute of Materials & Processing Technology, Beijing 100076, China

²Jiangxi Jiajie Xinda New Materials Technology Co., Ltd, Nanchang 330096, China

³State Key Lab of Powder Metallurgy, Central South University, Changsha 410083, China

Correspondence should be addressed to Jun-ping Li; lij82020@126.com and Zhen-hua Hou; houzhenhua88@126.com

Received 3 October 2020; Revised 15 November 2020; Accepted 24 November 2020; Published 9 December 2020

Academic Editor: Jian Chen

Copyright © 2020 Deng-hao Ma et al. This is an open access article distributed under the Creative Commons Attribution License, which permits unrestricted use, distribution, and reproduction in any medium, provided the original work is properly cited.

Continuous silicon carbide fiber-reinforced silicon carbide ceramic matrix composites (SiC_f/SiC) are promising as thermal structural materials. In this work, the microstructure and static mechanical properties of 3D-SiC_f/SiC with PyC, SiC, and PyC/SiC and without an interface prepared via polymer infiltration and pyrolysis (PIP) were investigated systematically in this paper. The results show that the microstructure and static mechanical properties of SiC_f/SiC with an interphase layer were superior to the composites without an interlayer, and the interface debondings are existing in the composite without an interphase, resulting in a weak interface bonding. When the interphase is introduced, the interfacial shear strength is improved, the crack can be deflected, and the fracture energy can be absorbed. Meanwhile, the shear strength of the composites with PyC and PyC/SiC interfaces was 118 MPa and 124 MPa, respectively, and showing little difference in bending properties. This indicates that the sublayer SiC of the PyC/SiC multilayer interface limits the binding state and the plastic deformation of PyC interphase, and it is helpful to improve the mechanical properties of SiC_f/SiC.

1. Introduction

SiC_f/SiC have become the most promising structural materials for long-time high-temperature components in aerospace, owing to their excellent physical and mechanical characteristics including lower density, weaker activation, more sufficient fracture toughness, more thermostable performances, better creep resistance, and higher corrosion resistance than that of metal materials [1–8]. It has been recognized that the fiber/matrix interphase has significant effort to the mechanical properties of continuous fiber-reinforced ceramic matrix composites (CFCMCs), which can deflect the matrix microcracks propagation, enable efficient load transfer between fiber and matrix, and protect the fibers [9–14].

At present, the interfacial layers have been developed with a variety of interfacial structures, different preparation techniques, and multiple components, specifically including

weak bounding interphase, a strong bounding and layered structure interphase, a strong bounding and (X/Y) N alternating multilayer interphase, and porous structure interphase [15–17]. Studies have shown that pyrolytic carbon (PyC) interface is the most commonly used interface to improve the mechanical properties of SiC_f/SiC composites due to its typical layered structure and good chemical compatibility with SiC, but the oxidation resistance of PyC interface was poor, which restricted its use in high-temperature environment. Thus, in order to improve the comprehensive mechanical properties of SiC_f/SiC, the SiC or BN interface layer is usually deposited on the surface of the PyC interface layer [18–20]. Zhou et al. [21] prepared the alternating (PyC/SiC)_n multilayer interface layers on the surface of SiC fibers via chemical vapor deposition. It is found that the fracture toughness of the composites with multilayer interface layers is 101% higher than that without interface layer, and

the SiC sublayer can effectively prevent PyC interphase from being oxidized. Yang et al. [22] studied the effect of (PyC/BN)_n on the mechanical and oxidation properties of the 3D SiC_f/SiC composites and found that BN can be oxidized into B₂O₃ at high temperature, which plays a self-healing role on the crack and protects PyC interface layer from oxidation. It can be seen that a reasonable fiber surface design and introduction of an appropriate interface layer can give full play to the effect of fiber reinforcement and further improve the performance of composite materials. However, due to the complex mechanism of the influence of interface state on the mechanical properties of composite materials, precise quantitative analysis is still lacking. In particular, the influence of interface phase structure on the failure behavior of 3D-SiC_f/SiC composite materials needs to be further studied.

In this work, three interfacial phases of PyC, SiC, and PyC/SiC were prepared by chemical vapor deposition on the surface of SiC fiber, respectively, and then 3D SiC_f/SiC with different interfacial phases were fabricated by polymer infiltration and pyrolysis (PIP). The crack propagation and deflection were systematically analyzed in combination with the mechanical properties and the fracture morphology of the composites, and the differences of composite properties and failure behaviors were determined. Meanwhile, the relationship among interfacial shear strength, fracture toughness, and flexure strength of composites was studied systematically.

2. Experimental Procedures

2.1. Sample Preparation. In this work, the KD-IISiC fibers which were used as the reinforcement and polycarbosilane (PCS) were provided by the National University of Defense Technology (China). Typical parameters of the KD-II SiC fiber are shown in Table 1. The fiber volume fraction of the 3D SiC fiber preforms which were braided by Yixing Tian-niao High Technology Co. Ltd., China, is about 40%.

Firstly, the SiC fiber preforms were desized at 800°C in vacuum for 30 min, and then, the different interphases (PyC, SiC, and PyC/SiC) were deposited on the surface of the SiC fiber via chemical vapor deposition (CVD). The specific thickness is 0.17~0.35 μm, 0.20~0.45 μm, and 0.53~0.75 μm, respectively. At last, the SiC fiber-reinforced SiC matrix, which was prepared using the precursor infiltration and pyrolysis (PIP) method, was fabricated with different interphases, and marked as follows: S1 (no interface), S2 (SiC), S3 (PyC), and S4 (PyC/SiC), respectively. The specific preparation process is shown in Figure 1.

2.2. Sample Characterization. The fracture surfaces after the three-point bending test and polished cross-sections of the samples were observed by field emission scanning electron microscopy (FE-SEM, Hitachi SU-8000). The Instron 5565-5kN multifunctional fatigue tester was used to test the flexural strength and fracture toughness of the samples. The equipment range is 0~50 kN, load error ≤ 1%, and displacement error ≤ 1%.

TABLE 1: Parameters of SiC fiber.

SiC fiber type	Diameter (μm)	Density (g/cm ³)	Tensile strength (GPa)	Tensile modulus (GPa)
KD_II	11-13	2.66	1.8-2.5	270

3. Results and Discussion

3.1. Microstructure of the SiC/SiC with Different Interface Layers. The typical microstructure of the SiC fiber with various interface layers, such as PyC, SiC, and PyC/SiC, is shown in Figure 2. Figures 2(b) and 2(c) display the SiC fiber surfaces which are covered by the dense SiC and PyC interfacial layers, respectively, which are deposited via CVD. Figure 2(d) shows the SiC fiber with the PyC/SiC interface layer. It can be seen clearly that the SiC sublayer, which is deposited on the surface of PyC interface layer, is a thin layer with a SiC nodular interfacial phase. The main reason is that SiC grows mainly in an island pattern within a certain thickness range. In addition, it is found that the morphology of the SiC interface layer on the surface of SiC fiber and pyrolytic carbon substrate is significantly different, which may be due to the different lattice matching degree, surface energy, deposition time, and so on.

The cross-section morphologies of SiC_f/SiC composites with different interface layers were characterized by a scanning electron microscope, as shown in Figure 3. Figure 3(b) shows the microstructure of the S1 composite without interface, and it can be found that there is obvious interface debonding in the matrix and fiber. This is mainly due to the mismatch of thermal expansion coefficient between matrix and fiber and the volume effect of matrix cracking [23]. The S3 sample has a dense and uniform PyC interface, as shown in Figure 3(a), and the overall microstructure of the material is relatively complete. For S2 sample, the SiC interface layer is tightly surrounded on the surface of SiC fiber, as shown in Figure 3(c), and it can be found that the boundary has slightly nodular morphology by careful observation. For S4 composite, as shown in Figures 3(d) and 3(e), it can be clearly seen that the fiber surface is tightly wrapped by the PyC first layer and the SiC sublayer. By comparing the morphologies of SiC_f/SiC composites with different interfaces, it can be found that the introduction of the interface layer can effectively alleviate the stress concentration between fiber and matrix and improve the microstructure of composites.

3.2. Mechanical Properties and Failure Behavior of SiC_f/SiC with Different Interfacial Phases. Figure 4 shows the interfacial shear strength and fracture toughness of the composites with different interfacial layers, in which the interface shear strength is S2 (SiC) > S3 (PyC) > S4 (PyC/SiC) > S1 (no interface). The results indicate that the interfacial layer is beneficial to enhance the interfacial bonding strength of the composites. Figure 5 shows the schematic diagram of the single fiber push-out test. For the S1 sample, the fiber and matrix appear debonding, as shown in Figure 5(a), and the interface shear strength is the weakest. Due to the high modulus

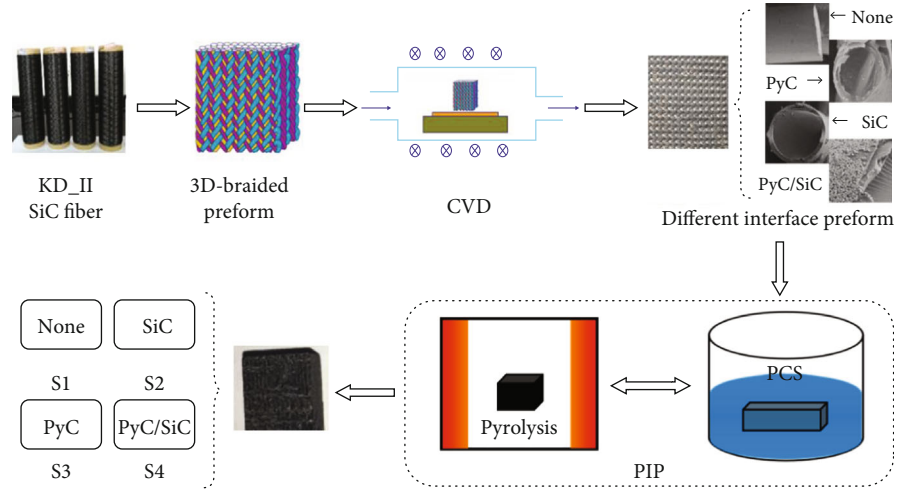


FIGURE 1: Schematic diagram of the 3D SiC_f/SiC with various interphases.

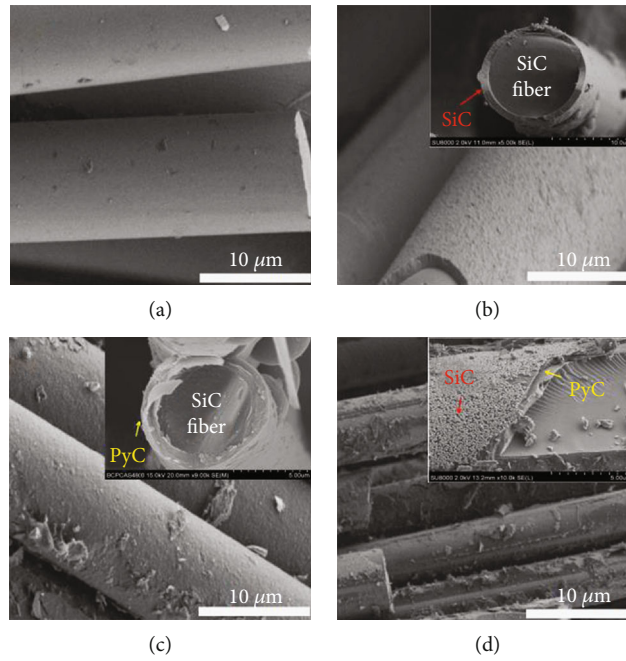


FIGURE 2: The SEM of the SiC fiber with different interface layers: (a) S1, none; (b) S2, SiC; (c) S3, PyC; (d) S4, PyC/SiC.

characteristics of CVD SiC and its high chemical compatibility with SiC fiber surface, the S2 sample has the highest interfacial shear strength. Both S3 and S4 samples have PyC interfacial layer, which effectively alleviates the thermal stress caused by the shrinkage of fiber and matrix due to cooling. At the same time, the PyC has a layered crystal structure, and the shear strength is maximum only when the interface thickness is a critical value (about 220 nm). When the PyC interface exceeds the critical thickness, the internal slip probability increases, which will weaken the interfacial shear strength of the composite. The interface thickness of PyC in S4 sample is 2~3 times of that in the S3 sample, but there is not much difference in the interface shear strength between the S3 and S4 samples, indicating that the sublayer SiC inter-

phase introduced in S4 sample is conducive to improving the overall interface bonding strength of the composite.

Meanwhile, the fracture toughness of the composite is S4 (PyC/SiC) > S3 (PyC) > S2 (SiC) > S1 (no interface), in which S1 shows the lowest fracture toughness of only $7.8 \text{ MPa m}^{1/2}$. This indicates that the relative crack propagation process is different in different interfaces. For the S1 and S2 samples, when the main crack in the matrix extends to the fiber, the crack tip stress directly acts on the surface of the fiber, leading to the destruction of the fiber, as shown in Figures 6(a) and 6(b). For the S3 sample, due to the introduction of PyC interface, its unique layered structure can help alleviate crack tip stress and effectively induce crack deflection to generate multiple microcracks and absorb more fracture energy, as shown

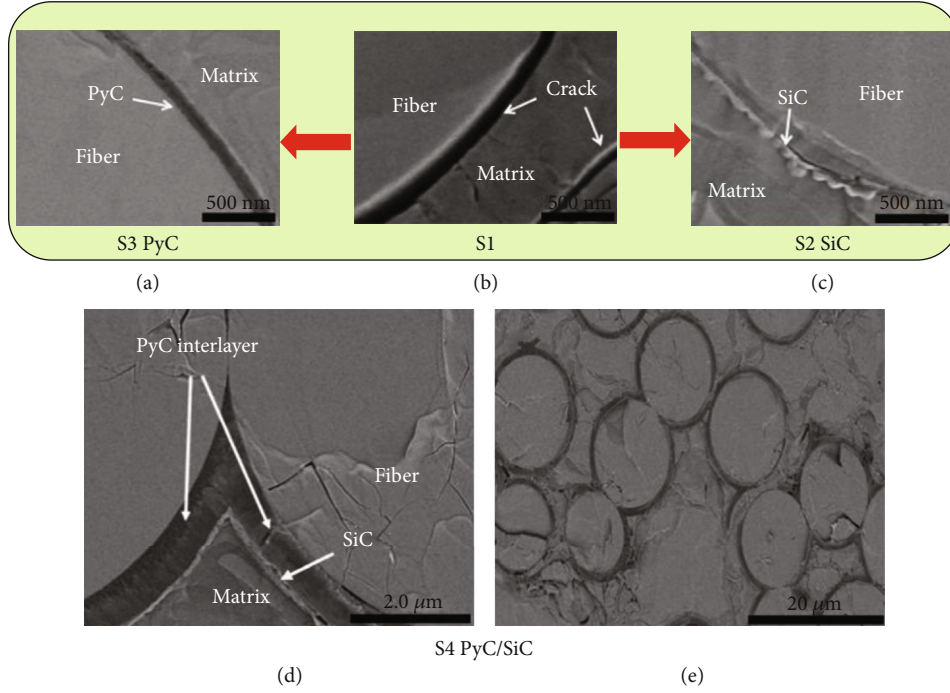


FIGURE 3: The cross-section morphology of SiC_f/SiC with different interface layers.

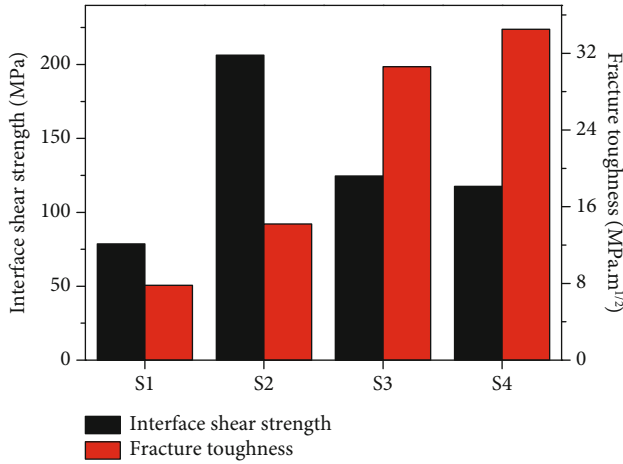


FIGURE 4: The interface shear strength and fracture toughness of the composites with different interface layers.

in Figure 6(c). For the S4 sample, the interphase includes the two-phase interface layer of PyC and SiC, in which the crack is more prone to deflection, resulting in a longer propagation path and higher fracture energy absorption, as shown in Figure 6(d). Therefore, M3 has the highest fracture toughness.

Figure 7 shows the flexural stress-displacement curves of the composites with different interface layers. It can be seen that S1 shows very low bending load and fracture displacement, and the fracture surface is relatively flat. This indicates that S1 composite absorbs little fracture energy during the fracture process, and the reinforcing and toughening effect of the fiber is not effectively exerted. S3 has the highest bend-

ing strength and has a significant fiber pull-out. At the same time, a small amount of debris remained on the fiber surface, indicating that the effective bifurcation and deflection occurred when the crack extended to the interfacial layer and absorbed a large amount of fracture energy. The failure behavior of S2 shows small deformation and obvious reduction of bending strength, but it is higher than that of S1, and a small amount of shorter fibers pulls out. This is mainly related to the excessive bonding between the fiber and matrix caused by the SiC interface, and the stress field at the crack tip cannot be effectively released at the interface, resulting in brittle fracture. For S4, its bending behavior is almost the same as that of S3, and it shows a high bending strength and large fracture displacement. Miller et al. found that the thickness of PyC has a significant influence on the flexure strength of SiC/SiC [24]. When the thickness of PyC is $0.13\text{ }\mu\text{m}$, the bending strength reaches a maximum of 420 MPa, and when the thickness of PyC is $0.58\text{ }\mu\text{m}$, the bending strength decreases sharply to 275 MPa. This is mainly due to the increase of defects in the interface layer with the increase of PyC thickness. However, the flexure strength and fracture toughness of S3 and S4 samples were similar. The results show that, compared with the single PyC interface, the sublayer SiC interface plays a certain constraint role on the PyC interface layer, which effectively reduces the overall internal slip and defects of the PyC/SiC multilayer interface and thus improves the performance of the composite.

Figure 8 shows the relationships of the interface shear strength and fracture toughness, flexural strength of the composites with different interface layers. The results show that the fracture toughness and bending strength of the composite first increase and then decrease with the increase of

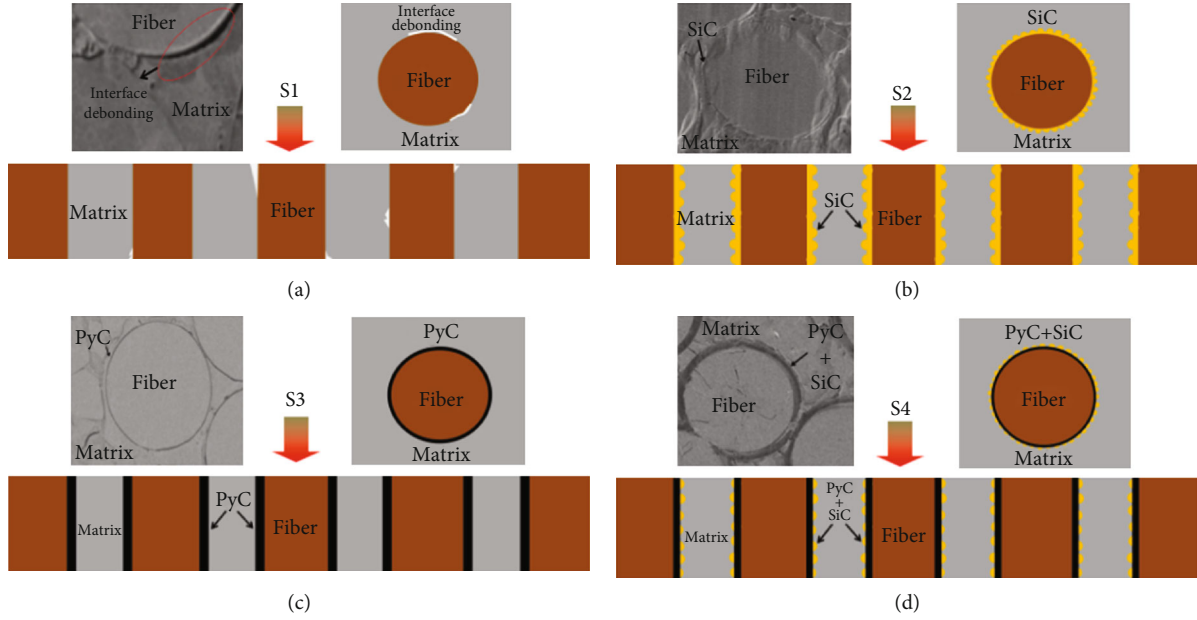


FIGURE 5: The schematic diagram of single fiber push-out test of the composites with different interface layers.

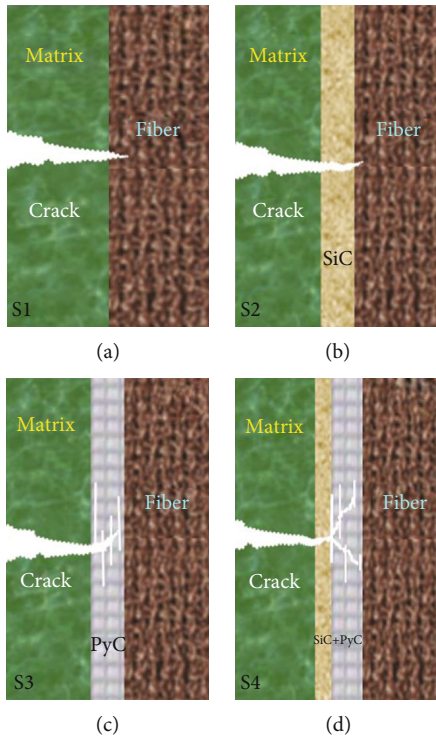


FIGURE 6: The simulation diagram of crack propagation of the composites with different interface layers.

interfacial shear strength, indicating that the moderate interfacial bond strength could effectively improve the fracture toughness and mechanical properties of the composite, which is consistent with the literature reports. At the same time, it is found that the fracture toughness of the composite decreases and the bending strength increases with the

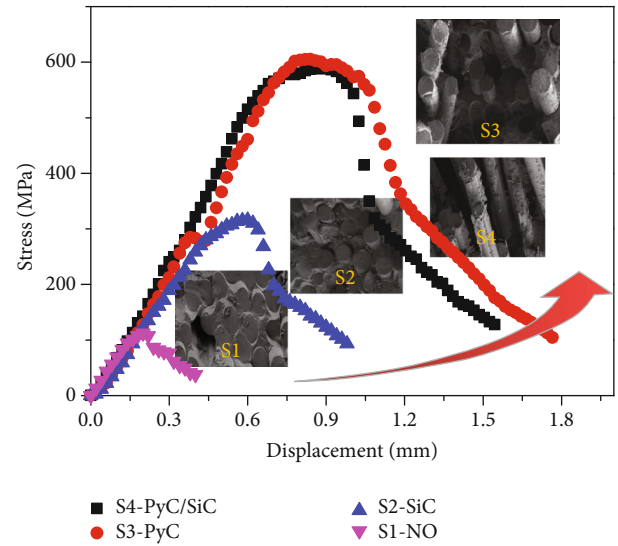


FIGURE 7: The flexural stress-displacement curves of the composites with different interface layers.

increase of the interfacial bonding strength in the area with moderate interfacial bonding strength. In conclusion, the bending properties of composite materials can be further improved through optimizing the interface phase and adjusting the interface bonding strength and fracture toughness. Meanwhile, combined with the microstructure of the interfacial phase, it can be inferred that the mechanical properties of the composites are not only affected by the interfacial bond strength and fracture toughness but also closely related to the surface roughness and shear strength of the interfacial phase itself. Therefore, in order to obtain composites with excellent mechanical properties, in addition to improving

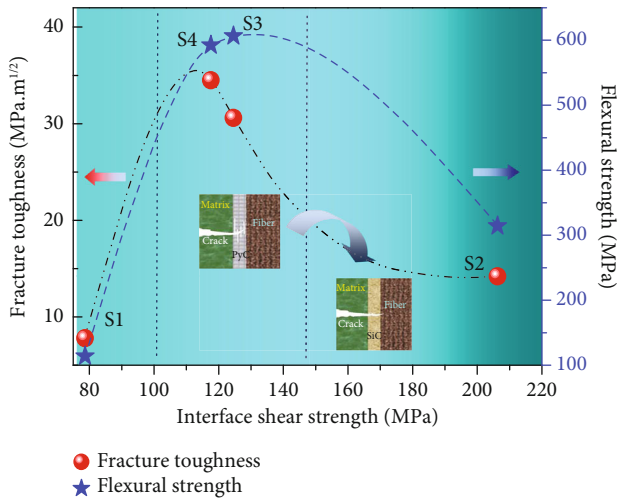


FIGURE 8: The relationships of the interface shear strength and fracture toughness, flexural strength of the composites with different interface layers.

the interfacial bonding strength between fiber-interfacial phase and interfacial phase matrix, an appropriate interfacial phases should be designed to enhance their shear strength, absorb higher fracture energy, and so as to improve the fracture toughness.

4. Conclusions

- (1) The order of the fracture toughness of different 3D-braided SiC_f/SiC is S4 (PyC/SiC) > S3 (PyC) > S2 (SiC) > S1 (no interphase), and the order of the interface shear strength is S2 (SiC) > S3 (PyC) > S4 (PyC/SiC) > S1 (no interphase). The interfacial shear strength not only depends on the state and interaction of fiber-interfacial phase and interfacial phase matrix but also is closely related to the properties of interfacial phase materials, including surface roughness and shear strength.
- (2) The introduction of PyC or PyC/SiC interphase layer is helpful to enhance the interfacial bonding state of the composites and the transition from brittle fracture mode to ductile fracture mode.
- (3) Combined with the microstructure and mechanical properties, it was found that the thickness of the PyC of the PyC/SiC multilayer interface was about 2-3 times that of the single PyC interphase layer. However, the shear strength of the two interfaces was 118 MPa and 124 MPa, respectively, showing little difference in bending properties. This indicates that sublayer SiC is beneficial to enhance the interface bonding strength of PyC/SiC multilayer interface and improve the mechanical properties of materials.

Data Availability

The data can be obtained from the article diagram.

Conflicts of Interest

We declare that we have no financial and personal relationships with other people or organizations that can inappropriately influence our work, and there is no professional or other personal interest of any nature or kind in any product, service, and/or company that could be construed as influencing the position presented in, or the review of, the manuscript entitled.

Acknowledgments

This work was supported by the National Natural Science Foundation Project (No. U19A2099) and the Equipment Research Foundation (6142906190101).

References

- [1] R. Naslain, "Design Preparation and properties of non-oxide CMCs for application in engines and nuclear reactors: an overview," *Composites Science and Technology*, vol. 64, no. 2, pp. 155–170, 2004.
- [2] Y. Qin and Y. C. Song, "Research and development of continuous SiC fibers and SiCf/SiC composites," *Journal of Inorganic Materials*, vol. 31, no. 11, pp. 1157–1165, 2016.
- [3] S. Q. Zou, C. R. Zhang, and X. G. Zhou, "Application of continuous fiber reinforced ceramic matrix composites in aeroengine," *Aeroengine*, vol. 31, pp. 55–58, 2005.
- [4] P. R. Wang, F. Liu, H. Wang, H. Li, and Y. Gou, "A review of third generation SiC fibers and SiCf/SiC composites," *Journal of Materials Science & Technology*, vol. 35, no. 12, pp. 2743–2750, 2019.
- [5] L. Z. Jin, K. Zhang, T. Xu, T. Zeng, and S. Cheng, "The fabrication and mechanical properties of SiC/SiC composites prepared by SLS combined with PIP," *Ceramics International*, vol. 44, no. 17, pp. 20992–20999, 2018.
- [6] Y. X. Qiao, D. Xu, S. Wang et al., "Effect of hydrogen charging on microstructural evolution and corrosion behavior of Ti-4Al-2V-1Mo-1Fe alloy," *Journal of Materials Science & Technology*, vol. 60, pp. 168–176, 2021.
- [7] Y. X. Qiao, J. Huang, D. Huang et al., "Effect of laser scanning speed on microstructure, microhardness and corrosion behavior of laser cladding Ni45 coatings," *Journal of Chemistry*, vol. 20, 2020.
- [8] Y. X. Qiao, Z. Tian, X. Cai et al., "Cavitation erosion behaviors of a Nickel-Free high-nitrogen stainless steel," *Tribology Letters*, vol. 67, no. 1, pp. 1–9, 2019.
- [9] R. H. Jones, "SiC/SiC composites for advanced nuclear applications," *Ceramic Engineering and Science Proceedings*, vol. 24, pp. 261–267, 2003.
- [10] H. T. Yang, Z. Lu, B. Bie, Z. Fu, J. Yue, and X. Huang, "Microstructure and damage evolution of SiCf/PyC/SiC and SiCf/BN/SiC mini-composites: a synchrotron X-ray computed microtomography study," *Ceramics International*, vol. 45, no. 9, pp. 11395–11402, 2019.
- [11] M. K. Seok and W. J. Kim, "Effects of the PyC interface coating on SiC nanowires of SiCf/SiC composite," *Journal of Nuclear Materials*, vol. 417, pp. 367–370, 2011.
- [12] Y. X. Chai, H. Zhang, X. Zhou, and Y. Zhang, "Effects of silicon ion irradiation on the interface properties of SiCf/SiC

- composites,” *Ceramics International*, vol. 44, no. 2, pp. 2165–2169, 2018.
- [13] Y. D. Xu, L. Cheng, L. Zhang, H. Yin, and X. Yin, “High toughness, 3D textile, SiC/SiC composites by chemical vapor infiltration,” *Materials Science and Engineering: A*, vol. 318, no. 1-2, pp. 183–188, 2001.
- [14] P. Colombo, G. Mera, and R. Riedel, “Polymer-derived ceramics: 40 years of research and innovation in advanced ceramics,” *Journal of the American Ceramic Society*, vol. 93, pp. 1805–1837, 2010.
- [15] S. Bertrand, R. Pailler, and J. Lamon, “Influence of strong fiber/coating interfaces on the mechanical behavior and lifetime of Hi-Nicalon/(PyC/SiC)_n/SiC minicomposites,” *Journal of the American Ceramic Society*, vol. 84, no. 4, pp. 787–794, 2001.
- [16] S. Bertrand, P. Forio, R. Pailler, and J. Lamon, “Hi-Nicalon/SiC Minicomposites with (pyrocarbon/SiC)_n nanoscale multilayered interphases,” *Journal of the American Ceramic Society*, vol. 82, no. 9, pp. 2465–2473, 1999.
- [17] S. Bertrand, C. Droillard, and R. Pailler, “TEM structure of (PyC/SiC)_n multilayered interphases in SiC/SiC composites,” *Journal of the European Ceramic Society*, vol. 20, no. 1, pp. 1–13, 2000.
- [18] O. Rapaud, S. Jacques, and H. D. Murro, “SiC/SiC minicomposites with (PyC/TiC)_n interphases processed by pressure-pulsed reactive CVI,” *Journal of Materials Science*, vol. 39, no. 1, pp. 173–180, 2004.
- [19] Y. Zhou, W. C. Zhou, and F. Luo, “Effects of dip-coated BN interphase on mechanical properties of SiCf/SiC composites prepared by CVI process,” *Transactions of Nonferrous Metals Society of China*, vol. 24, no. 5, pp. 1400–1406, 2014.
- [20] C. Chateau, L. Gelebart, and M. Bornert, “In situ X-ray microtomography characterization of damage in SiCf/SiC minicomposites,” *Composites Science and Technology*, vol. 71, no. 6, pp. 916–924, 2011.
- [21] H. J. Yu, X. G. Zhou, and W. Zhang, “Mechanical properties of 3D KD-I SiCf/SiC composites with engineered fibre-matrix interfaces,” *Composites Science and Technology*, vol. 71, no. 5, pp. 699–704, 2011.
- [22] Y. Bei, X. G. Zhou, and Y. X. Cai, “Mechanical properties of SiCf/SiC composites with PyC and the BN interface,” *Ceramics International*, vol. 41, pp. 7185–7190, 2015.
- [23] X. Yang, C. Feng, and Z. H. Peng, “Evolution of microstructure and mechanical properties of PIP-C/SiC composites after high-temperature oxidation,” *Journal of Asian Ceramic Societies*, vol. 5, pp. 370–376, 2018.
- [24] J. H. Miller, P. K. Liaw, and J. D. Landes, “Influence of fiber coating thickness on fracture behavior of continuous woven Nicalon fabric-reinforced silicon-carbide matrix ceramic composites,” *Science and Engineering: A*, vol. 317, no. 1-2, pp. 49–58, 2001.

Research Article

Influence of Oxidation Damages on Mechanical Properties of SiC/SiC Composite Using Domestic Hi-Nicalon Type SiC Fibers

Enze Jin, Denghao Ma, Zeshuai Yuan, Wenting Sun, Hao Wang, Jiajia Zhang, Xiaodong Gong, Lina Huang, Botao Han, Xin Sun, Zhihai Feng, and Junping Li 

Key Laboratory of Advanced Functional Composites Technology, Aerospace Research Institute of Materials & Processing Technology, Beijing 100076, China

Correspondence should be addressed to Junping Li; lijunpingjez@163.com

Received 1 October 2020; Revised 15 November 2020; Accepted 27 November 2020; Published 9 December 2020

Academic Editor: Jian Chen

Copyright © 2020 Enze Jin et al. This is an open access article distributed under the Creative Commons Attribution License, which permits unrestricted use, distribution, and reproduction in any medium, provided the original work is properly cited.

Here, we show that when the oxidation treatment temperature exceeded 600°C, the tensile strength of SiC/SiC begins to decrease. Oxidation leads to the damages on the PyC fiber/matrix interface, which is replaced by SiO₂ at higher temperature. The fracture mode converts from fiber pull-out to fiber-break as the fiber/matrix interface is filled with SiO₂. Oxidation time also plays an important role in affecting the tensile strength of SiC/SiC. The tensile modulus decreases with temperature from RT to 800°C, then increases above 800°C due to the decomposition of remaining CSi_xO_y and crystallization of the SiC matrix. A special surface densification treatment performed in this study is confirmed to be an effective approach to reduce the oxidation damages and improve the tensile strength of SiC/SiC after oxidation.

1. Introduction

The SiC/SiC composite is known to have high specific strength, high specific stiffness, high temperature resistance, long-term oxidation resistance, and erosion resistance [1–3], all of which are ideal properties for application as high-temperature-resistant material in many fields such as thermal protection system of aerospace vehicles and hot-end components of aircraft engines [1–3]. In addition, the SiC/SiC composite reinforced by a near-stoichiometric SiC fiber is considered the candidate material for the new-generation fuel claddings of nuclear fission reactor and the first wall material of nuclear fusion reactor due to its high irradiation resistance [4, 5].

The performance of the SiC/SiC composite oxidized in air is very important in the engineering application of this material, which draws widely interests in recent years [6, 7]. Lu et al. investigated the oxidation damages of SiC/SiC composites with pyrolytic carbon (PyC) fiber/matrix interface using high-resolution CT and SEM. The results showed that PyC interface was severely oxidized and turns into voids

above 1000°C. After oxidation at 1400°C, the brittle oxide layers filled cracks in the matrix and caused drop of tensile strength [8]. Ikarashi et al. studied the tensile properties of 3D woven SiC/SiC composites at high temperatures in air. They found that oxidative matrix crack propagation in the transverse layers strongly affected the lifetime of the SiC/SiC composites [9]. Wang et al. studied the tensile creep properties of two-dimensional (2D) woven SiC/SiC composites reinforced with low-oxygen and high-carbon SiC fibers at high temperature. The results revealed that the bridged fiber inhibited the opening of matrix cracks; on the other hand, the fiber creep promoted the growth of crack. The creep property was determined by the complete mechanisms of fibers at high temperature [10].

Domestic Hi-Nicalon type SiC fiber is a new material, and there are few studies on the oxidation damages of SiC/SiC composites prepared by this fiber [11, 12]. In this study, we will investigate the influence of oxidation damages on mechanical properties of the SiC/SiC composite reinforced by domestic Hi-Nicalon type SiC fibers under high-temperature environments.

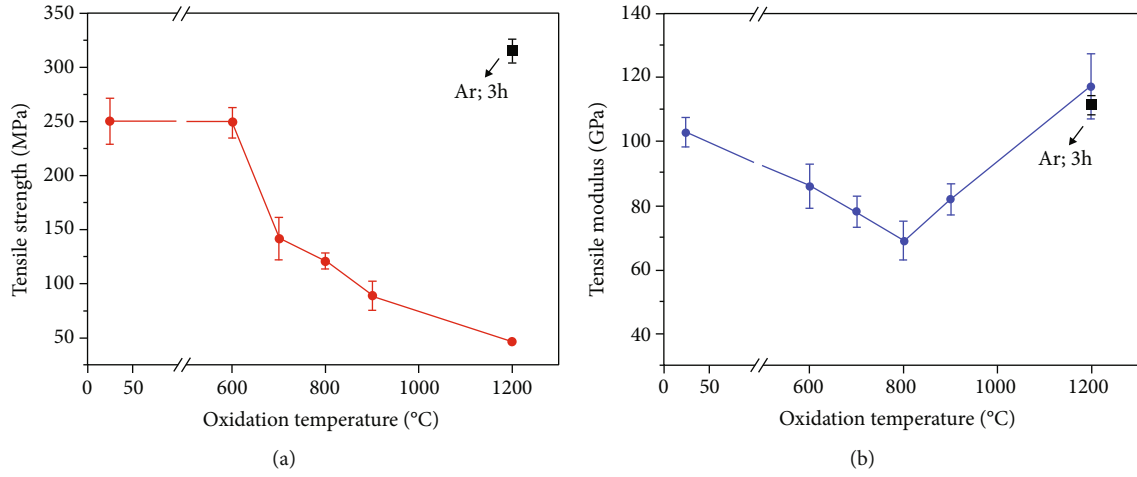


FIGURE 1: Variations of (a) tensile strength and (b) tensile modulus of SiC/SiC oxidized in air at different temperatures.

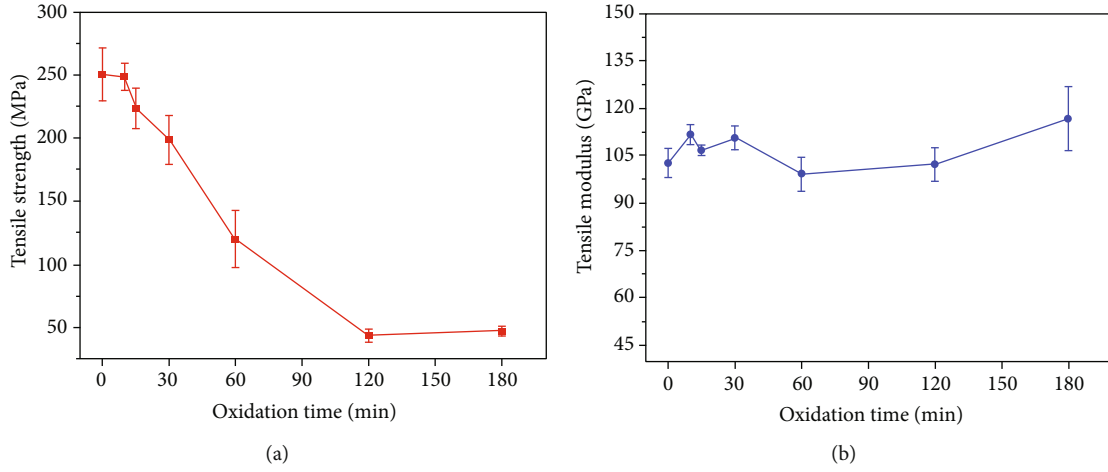


FIGURE 2: Variations of (a) tensile strength and (b) tensile modulus of SiC/SiC oxidized in air at 1200 °C for different times.

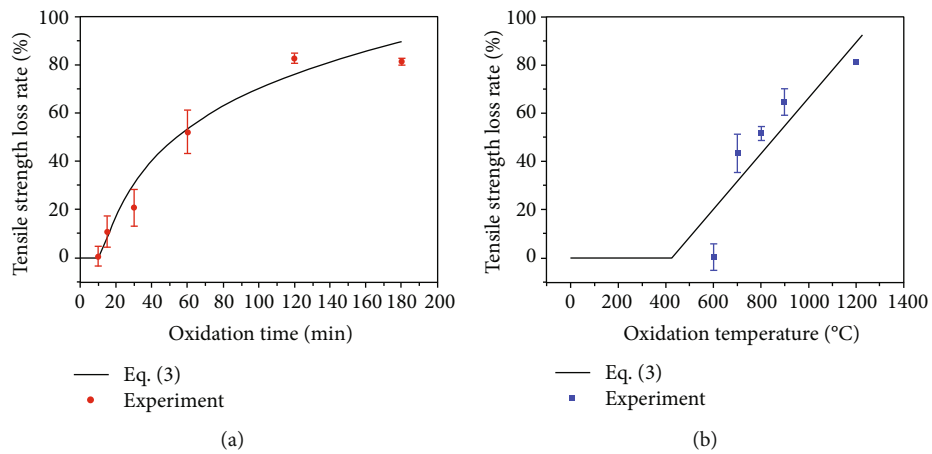


FIGURE 3: (a) Variations of tensile strength loss rate at 1200 °C for different oxidized time and (b) tensile strength loss rate oxidized at different temperature for 3 hours.

2. Materials and Methods

2D preforms were woven using domestic Hi-Nicalon type SiC fibers. The SiC fibers were provided by Xiamen Univer-

sity (Xiamen, China). The fiber diameter is 14 μm , density is 2.79 g/cm³, tensile strength is 2.7 GPa, and the modulus is 270 GPa. The oxygen content is 0.5 wt%, and the C/Si mole ratio is 1.41. The properties of the domestic Hi-Nicalon type

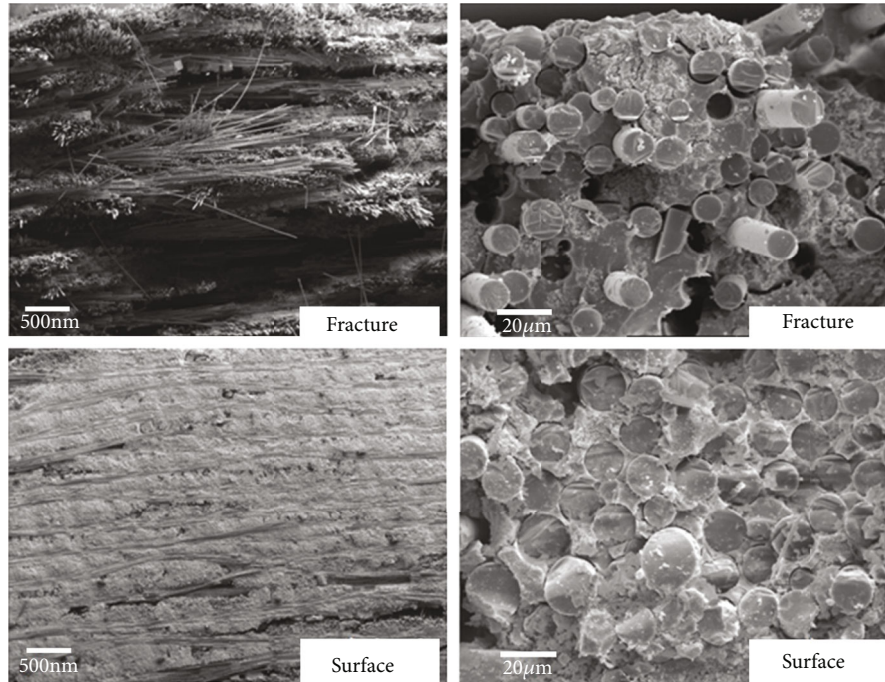


FIGURE 4: Tensile fracture morphology of SiC/SiC composites oxidized in air at 600°C for 3 hours.

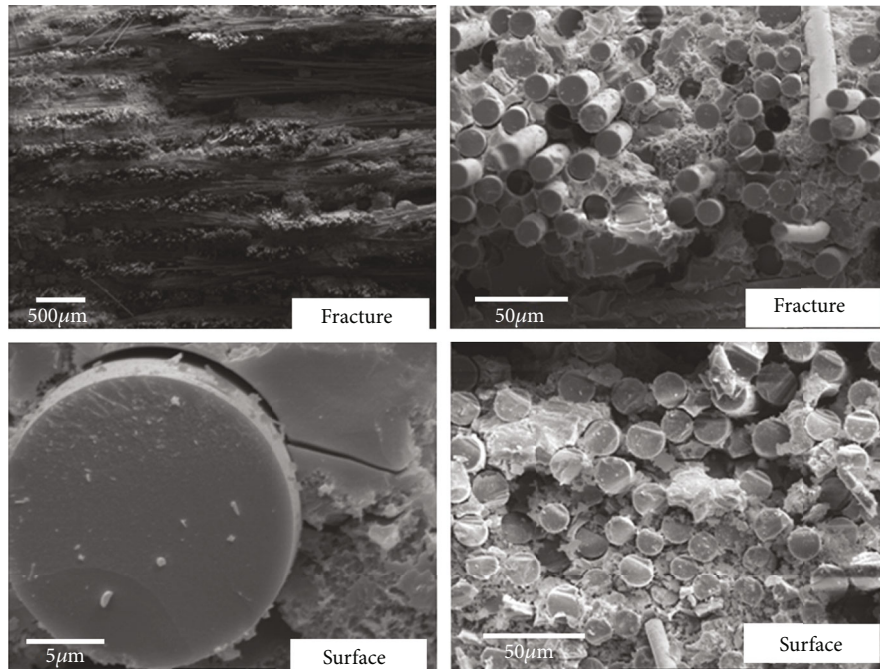


FIGURE 5: Tensile fracture morphology of SiC/SiC composites oxidized in air at 800°C for 3 hours.

SiC fiber are close to those of Hi-Nicalon fiber [13, 14]. PyC layers with a thickness of about 400 nm were coated on the surface of the preforms by chemical vapor deposition (CVD) method. SiC/SiC composites were prepared by precursor infiltration and pyrolysis (PIP) process. The preforms were impregnated with liquid-state polycarbosilane (PCS) by a vacuum infiltration method and pyrolyzed at 800°C in an inert argon atmosphere. The impregnation and pyrolysis

process were repeated 10 times until weight increase was less than 1%. Five specimens were fabricated from the composite to have an accurate calculation of density and porosity considering the Archimedes method based on ASTM C373-88 standard. The averaged porosity of the composite is 8.1%.

The machined SiC/SiC composite mechanical specimens were subjected to oxidation treatment in a muffle furnace with a temperature increasing rate of 100°C/min until the

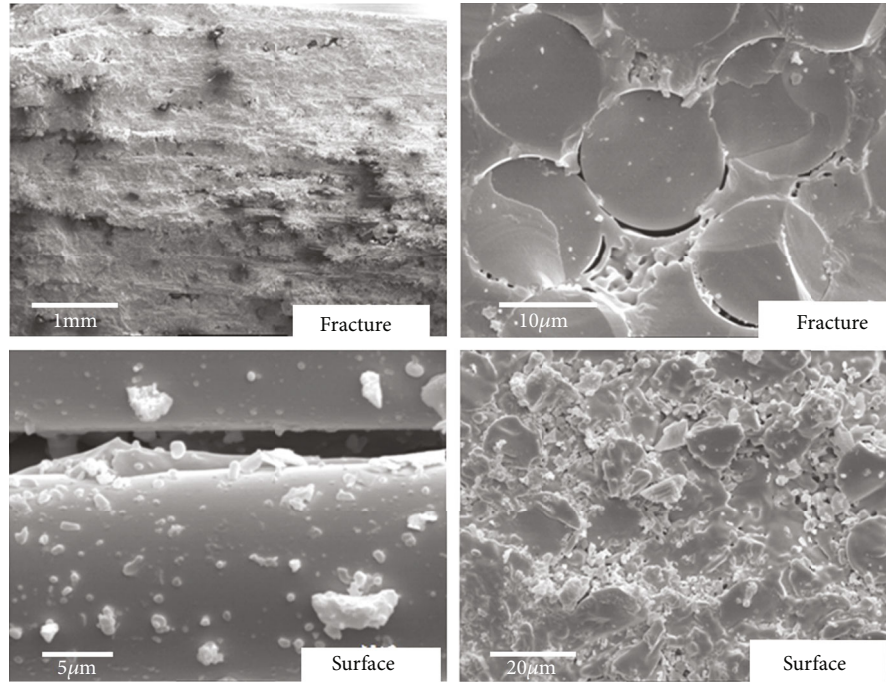


FIGURE 6: Tensile fracture morphology of SiC/SiC composites oxidized in air at 1200°C for 3 hours.

required temperature was achieved. The tensile properties of the materials were tested at room temperature using a servo-electric testing system (MTS CMT5105, China). The length, width, and height of tensile specimen are 100 mm, 5 mm, and 10 mm, respectively. Five specimens were tested for each state, and the strength was obtained by averaging the values over these five results.

3. Results and Discussion

3.1. Mechanical Property Variation. The tensile strength used in this study is the maximum stress that the SiC/SiC composite can withstand while being stretched before fracture. Young's modulus is obtained from the linear portion of the stress-strain curve in the SiC/SiC composite. The variation of tensile strength of SiC/SiC composites after oxidation for 3 hours at 600°C, 700°C, 800°C, 900°C, and 1200°C is shown in Figure 1(a). It can be seen from the results that the tensile strength of SiC/SiC composites decreases with oxidation temperature during 600–1200°C. However, the tensile strength of SiC/SiC composites treated at 1200°C under inert gas environment is slightly higher than that of as-fabricated specimens. It indicates that the reduction of tensile strength is mainly due to the oxidation damages. The tensile strength of SiC/SiC composites barely change after oxidation at 600°C for 3 hours. When the oxidation temperature exceeds 600°C, the tensile property begins to drop. After oxidation at 800°C for 3 hours, the retention of tensile strength is ~50%, and after oxidation at 1200°C, the retention of tensile strength is only ~20%.

The variations of tensile modulus of SiC/SiC composites after oxidation at different temperatures are summarized in Figure 1(b). The change of tensile modulus with temperature

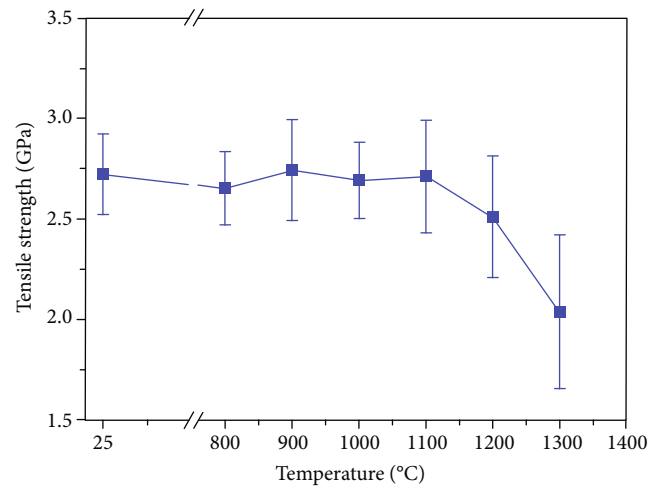


FIGURE 7: Variations of SiC fiber oxidized for 3 h in air at different temperatures.

is different with that of tensile strength. The tensile modulus decreases with temperature from 600°C to 800°C, and then, the tensile modulus increases with oxidation temperature until 1200°C.

The results of tensile property variations reveal that the oxidation damages of the SiC/SiC composite occur after 3 hours of oxidation at 600°C. The oxidation damages at 600°C only have influences on the tensile modulus of the material and have almost no influence on the tensile strength. When the oxidation temperature exceeds 600°C, the tensile strength of SiC/SiC composites begins to decline. The tensile modulus starts to increase above 800°C, which is also the preparation temperature of the SiC/SiC composite. When the temperature exceeds 800°C, the remaining CSi_xO_y

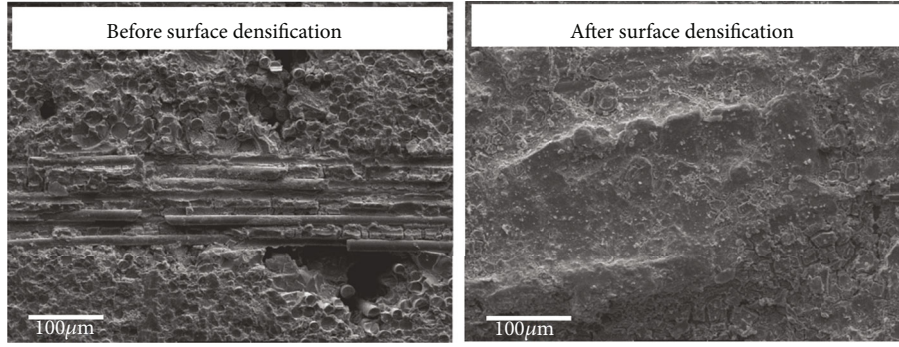


FIGURE 8: Comparison of surface morphology of SiC/SiC before and after surface densification treatment.

component in the matrix was further converted into SiC and then crystallized with the increase of temperature [15]. The modulus of the CSi_xO_y fiber (Nicalon fiber) is much lower than that of SiC fiber (Hi-Nicalon fiber) [14]. Therefore, it is reasonable to infer that the increase of modulus above 800°C is caused by the conversion of the remaining CSi_xO_y component in the matrix.

The change of tensile strength of SiC/SiC composites after oxidation at 1200°C for 10 min, 15 min, 30 min, 60 min, 120 min, and 180 min is shown in Figure 2(a). It can be seen from the results that oxidation time also plays an important role to affect the tensile strength of SiC/SiC composites. SiC/SiC composite strength begins to decrease when the oxidation time exceeds 10 min. When the oxidation time reaches 120 min, the tensile strength does not further decrease.

The variation of tensile modulus of SiC/SiC composites oxidized at 1200°C as a function of time is shown in Figure 2(b). It can be seen from the results that the effect of oxidation time on the tensile modulus of SiC/SiC is not readily observable.

Both oxidation time and temperature can affect the tensile strength of SiC/SiC composites. In this study, we use an oxidation damage parameter, q , to consider the influence of temperature and time comprehensively.

$$q = T \log(t), \quad (1)$$

where T is oxidation temperature and t is oxidation time. We define r as the tensile strength loss rate,

$$r = \frac{(\sigma_{\text{As}} - \sigma_{\text{Ox}})}{\sigma_{\text{As}}} \times 100\%, \quad (2)$$

where σ_{As} is the tensile strength of as-received SiC/SiC, σ_{Ox} is the tensile strength of SiC/SiC after oxidation treatment. We use oxidation damage parameter, q , to establish the prediction model of tensile strength loss rate, r :

$$r = \begin{cases} 0 & (\text{if } q \leq 0), \\ aT \log(t) + b & (\text{if } q > 0). \end{cases} \quad (3)$$

We can get $a = 0.051$ and $b = -80.41$ by data fitting. The relationship between tensile strength loss rate and time

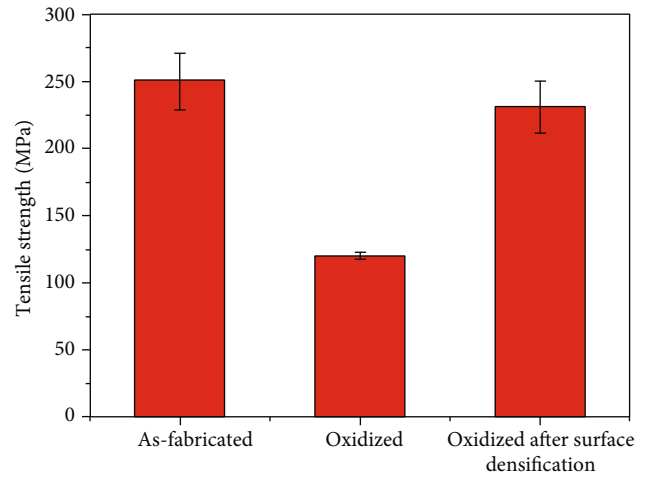


FIGURE 9: Comparison of tensile strength of SiC/SiC before and after surface densification treatment (oxidized at 1200°C for 1 hour).

oxidized at 1200°C is shown in Figure 3(a). The relationship between tensile strength loss rate and oxidation temperature (3 hours of oxidation) is shown in Figure 3(b). It can be seen that the predictive curve of SiC/SiC composite tensile strength loss rate obtained based on oxidation damage parameter is in good agreement with the experimental results.

3.2. Microstructures. The microstructures at the fracture of SiC/SiC composites were characterized by Camscan Apollo 300 scanning electron microscope (CamScan, Cambridge, UK). The failure mode and microstructure damages can be investigated in the fractures of specimens [13, 14]. The microstructures of SiC/SiC composite oxidized for 3 hours at 600°C are shown in Figure 4. It can be seen that the fractures of the SiC/SiC composite at 600°C exhibit ductile characteristics. A large number of extracted fibers can be clearly seen at the fracture, indicating that the crack was deflected at the PyC fiber/matrix interface during the loading process. The results show that the PyC fiber/matrix interface on the surface of the specimen has disappeared, while the PyC interface at the fracture still exists. It indicates that the oxidation damages at 600°C only occurred on the surface of the material. Oxygen atoms do not further oxidized the PyC interface layer inside the material.

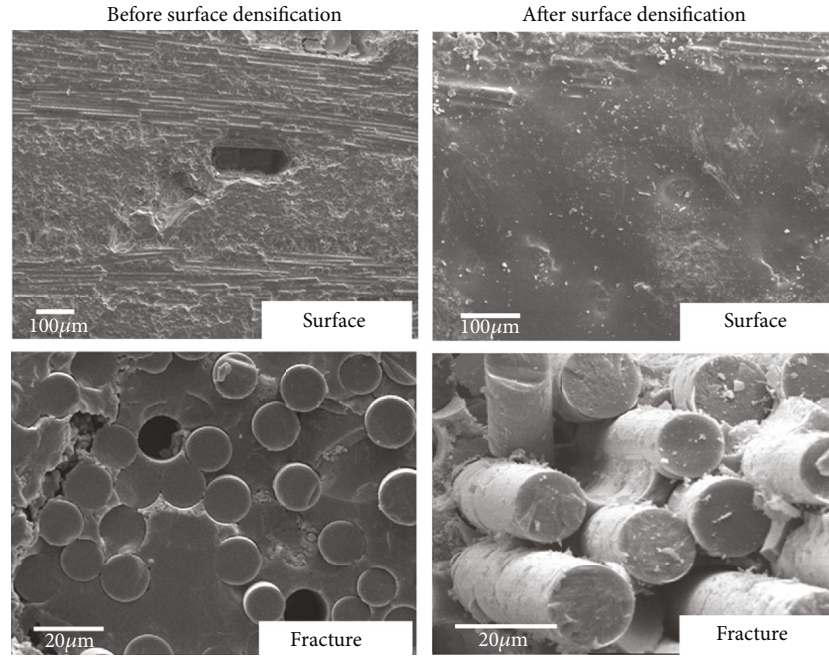


FIGURE 10: Comparison of tensile fracture morphology of SiC/SiC before and after surface densification treatment (oxidized at 1200°C for 1 hour).

The microstructures of SiC/SiC composite specimens oxidized for 3 hours at 800°C are shown in Figure 5. Compared with the composite oxidized at 600°C, the length of pulling out fibers decreases and the regions of pulling out fibers become smaller. The results show that no PyC interface at the fracture can be seen after oxidation at 800°C for 3 hours. Therefore, oxidation damage occurred inside the composite under this condition, and nearly all of the PyC interfaces have been oxidized. When the PyC at the fiber/matrix interface is oxidized, pores are formed between the fiber and matrix. Pulled-out fibers can also be seen at the fractures, indicating that cracks are deflected during the loading process. SiC/SiC composite oxidized at 800°C for 3 hours still exhibits ductile fracture behavior. However, due to the loss of the interface layer, loading stress cannot transfer effectively between the fiber and matrix. Therefore, the strength and modulus of SiC/SiC composites drop significantly on this condition. This result suggests that the rupture under constant tensile load is caused mainly by the oxidation of SiC interphase because of air ingress through the transverse crack.

The microstructures of SiC/SiC composites oxidized for 3 hours at 1200°C are shown in Figure 6. The fracture surface of the composites is very plane, and few pullout fibers can be seen. The fractures show typical brittle characteristic. It indicates that cracks are not arrested at the interface but penetrated the fiber bundles. Further observation reveals that the pores caused by the oxidation of PyC are sealed at the fiber/matrix interface. It is because the oxidations of SiC matrix and the fiber at 1200°C: $\text{SiC} + \text{O}_2 \rightarrow \text{SiO}_2 + \text{CO}_2 + \text{CO}$. SiO_2 filled the pores between the fiber and matrix becomes a new fiber/matrix interface. Pores between the fiber and matrix which are not filled completely are also shown in Figure 6. Oxida-

tion of PyC interface results in strong chemical bonding between fibers and the matrix. During the tensile process, crack initiations in SiC/SiC composites mainly appear in the matrix and gradually propagate to the fiber/matrix interface. If the fiber/matrix interface is weak enough, the crack will deflect into the interface and propagate along fiber axis direction. If the interface is too strong, the crack will not deflect but directly cause fiber break [16, 17]. Interphase usually plays a key role in determining the mechanical properties of materials [18–20]. In our previous work, both theory and experiment show that once the interface binding strength exceeds the critical value, the composite failure mode converts from fiber pull-out ductile failure mode to fiber break brittle failure mode and the tensile strength of SiC/SiC drops sharply [21]. It is worthy to mention that because sufficient SiO_2 filled the pores on the material surface, oxygen atoms prevent further entry into the material [22, 23]. It can explain the fact that the tensile strength did not further decrease with time when oxidized at 1200°C above 120 min as shown in Figure 2(a).

According to the theory of composite mechanics, the tensile strength of the SiC fiber also plays a key role in the mechanical properties of SiC/SiC. We performed the oxidation treatment on domestic Hi-Nicalon type SiC fibers at different temperatures using the same method as composite oxidation treatment. Then, the fiber tensile strength was measured by Instron tensile device using a load cell of 5 N and a crosshead speed 4.5 mm/min. The gauge length is 25 mm, and at least 50 samples were tested to calculate the average tensile strength. The variations of tensile strength of domestic Hi-Nicalon type SiC fibers with oxidation temperature are shown in Figure 7. It can be seen that the tensile strength of the SiC fiber begins to decrease above 1100°C. SiC

fibers still retain high strength after oxidized at 1200°C and retention rate is 92%. These results indicate that the drop of the SiC/SiC composite oxidized from RT to 1200°C is mainly caused by the oxidation of PyC interphase, rather than the oxidation of the SiC fiber.

3.3. Improvement. The micropores of SiC/SiC composites act as a pathway of oxygen, which are mainly caused by the shrinkage during PCS pyrolysis and machining process. In order to increase the densification of the surface and prevent the oxygen diffuse into the SiC/SiC composite, we prepared mixed precursor with 60 wt% SiC powders (Shanghai ST-Nano Co. Ltd., China, purity: 99%, grain size < 100 nm) and 40 wt% PCS to reduce the precursor shrinkage during pyrolysis. The SiC-50 wt% PCS powders were homogeneously mixed by ball milling at 250 r/min for 8 h to obtain uniformly flowing ceramic slurry, in which xylene was selected as solvent. One additional impregnation and pyrolysis process was performed using the mixed precursor to seal the micropores on the surface of as-fabricated specimens. The results show that no micropore can be seen on the surface of the composite after additional impregnation and pyrolysis process (as shown in Figure 8).

The SiC/SiC composites with densified surface were oxidized for 1 hour at 1200°C. The comparison between tensile strength of SiC/SiC with and without densified surface is shown in Figure 9. From the results, it can be seen that the tensile strength of SiC/SiC composites after surface densification is significantly improved, which is close to the strength before oxidation treatment. It indicates that the densified surface prevent the oxygen diffuse into the SiC/SiC composite and reduce the oxidation damages effectively.

The microstructures of oxidized SiC/SiC composites before and after surface densification are shown in Figure 10. It can be seen from the figure that the surface of the as-fabricated composite has obvious pores. The PyC interface is replaced by SiO₂ between the fibers and matrix in the fracture. The composites exhibit brittle characteristics. The surface of the SiC/SiC composite is covered by a dense SiO₂ film after surface densification, which effectively prevents oxygen diffusion into the composite. PyC can be seen in the fracture of the SiC/SiC composite, indicating that no oxidation damages occur inside the composite. Due to the PyC interface remaining intact, the interface strength between the fiber and matrix is low, leading to ductile fracture and improved tensile strength after oxidation.

4. Conclusions

The tensile properties of SiC/SiC reinforced with domestic Hi-Nicalon type SiC fibers oxidized at high temperature were investigated in this study. Both oxidation temperature and time have significant effects on the tensile properties of SiC/SiC. The tensile property begins to decrease with temperature when the oxidation temperature exceeds 600°C. The drop of tensile strength is mainly caused by the replacement of the PyC fiber/matrix interface by SiO₂ during oxidation. The tensile modulus decreases with temperature from RT to 800°C, then increases above 800°C due to the decompose of the

remaining CSi_xO_y and crystallization of the SiC matrix. A tensile strength loss rate model as a function of oxidation temperature and time is proposed. The prediction roughly agreed with the experimentally obtained results. Surface densification treatment is an effective way to reduce the oxidation damages and improve the tensile strength of SiC/SiC.

Data Availability

The data can be easily obtained in the figures in manuscript.

Conflicts of Interest

The authors declare that they have no conflicts of interest.

References

- [1] Y. Xue, J. Hu, H. Zhou et al., "Damage development of a woven SiC_f/SiC composite during multi-step fatigue tests at room temperature," *Ceramics International*, vol. 46, no. 14, pp. 22116–22126, 2020.
- [2] S. Zhao, Z.-C. Yang, and X.-G. Zhou, "Fracture behavior of SiC/SiC composites with different interfaces," *Journal of Inorganic Materials*, vol. 31, no. 1, pp. 58–62, 2016.
- [3] B. S. Vasile, A. C. Birca, V. A. Surdu, I. A. Neacsu, and A. I. Nicoară, "Ceramic composite materials obtained by electron-beam physical vapor deposition used as thermal barriers in the aerospace industry," *Nanomaterials*, vol. 10, no. 2, p. 370, 2020.
- [4] L. L. Snead, T. Nozawa, M. Ferraris, Y. Katoh, R. Shinavski, and M. Sawan, "Silicon carbide composites as fusion power reactor structural materials," *Journal of Nuclear Materials*, vol. 417, no. 1–3, pp. 330–339, 2011.
- [5] S. Agarwal, G. Duscher, Y. Zhao, M. L. Crespiello, Y. Katoh, and W. J. Weber, "Multiscale characterization of irradiation behaviour of ion-irradiated SiC/SiC composites," *Acta Materialia*, vol. 161, pp. 207–220, 2018.
- [6] H. Wang, Z. Chen, R. Zhang et al., "Preparation and tensile behavior of SiC_f/SiC mini composites containing different types and thicknesses of interphase," *Ceramics International*, vol. 46, no. 14, pp. 22297–22306, 2020.
- [7] M. B. Ruggles-Wrenn, D. T. Christensen, A. L. Chamberlain, J. E. Lane, and T. S. Cook, "Effect of frequency and environment on fatigue behavior of a CVI SiC/SiC ceramic matrix composite at 1200°C," *Composites Science and Technology*, vol. 71, no. 2, pp. 190–196, 2011.
- [8] Z. Lu, B. Bie, A. Pang et al., "Oxidation and microstructure of SiC_f/SiC composites in moist air up to 1600°C by x-ray tomographic characterization," *International Journal of Applied Ceramic Technology*, vol. 17, no. 3, pp. 874–885, 2020.
- [9] Y. Ikarashi, T. Ogasawara, and T. Aoki, "Effects of cyclic tensile loading on the rupture behavior of orthogonal 3-D woven SiC fiber/SiC matrix composites at elevated temperatures in air," *Journal of the European Ceramic Society*, vol. 39, no. 4, pp. 806–812, 2019.
- [10] X. Wang, Z. Song, Z. Cheng, D. Han, M. Li, and C. Zhang, "Tensile creep properties and damage mechanisms of 2D-SiC_f/SiC composites reinforced with low-oxygen high-carbon type SiC fiber," *Journal of the European Ceramic Society*, vol. 40, no. 14, pp. 4872–4878, 2020.

- [11] J. Dai, Y. Wang, Z. Xu, and L. He, "Degradation of boron nitride interfacial coatings fabricated by chemical vapor infiltration on SiC fibers under ambient air/room temperature conditions," *Ceramics International*, vol. 45, no. 6, pp. 6937–6943, 2019.
- [12] X. Luan, X. Xu, L. Wang et al., "Self-healing enhancing tensile creep of 2D-satin weave SiC/(SiC-SiBCN)_x composites in wet oxygen environment," *Journal of the European Ceramic Society*, vol. 40, no. 10, pp. 3509–3519, 2020.
- [13] S. Wu, L. Cheng, L. Zhang, Y. Xu, J. Zhang, and H. Mei, "Wet oxidation behaviors of Hi-Nicalon fibers," *Applied Surface Science*, vol. 253, no. 3, pp. 1447–1450, 2006.
- [14] G. Kister and B. Harris, "Tensile properties of heat-treated Nicalon and Hi-Nicalon fibres," *Composites Part A: Applied Science and Manufacturing*, vol. 33, no. 3, pp. 435–438, 2002.
- [15] Y. Katoh, K. Ozawa, C. Shih et al., "Continuous SiC fiber, CVI SiC matrix composites for nuclear applications: properties and irradiation effects," *Journal of Nuclear Materials*, vol. 448, no. 1–3, pp. 448–476, 2014.
- [16] C. Fellah, J. Brauna, C. Sauder, F. Sirotti, and M. Berger, "Influence of the carbon interface on the mechanical behavior of SiC/SiC composites," *Composites Part A: Applied Science and Manufacturing*, vol. 133, article 105867, 2020.
- [17] D. Ding, W. Zhou, F. Luo, M. Chen, and D. Zhu, "Mechanical properties and oxidation resistance of SiC_f/CVI-SiC composites with PIP-SiC interphase," *Ceramics International*, vol. 38, no. 5, pp. 3929–3934, 2012.
- [18] P. Chen, S. Chen, W. Guo, and F. Gao, "The interface behavior of a thin piezoelectric film bonded to a graded substrate," *Mechanics of Materials*, vol. 127, pp. 26–38, 2018.
- [19] P. Chen, J. Peng, H. Liu, F. Gao, and W. Guo, "The electromechanical behavior of a piezoelectric actuator bonded to a graded substrate including an adhesive layer," *Mechanics of Materials*, vol. 123, pp. 77–87, 2018.
- [20] P. Chen, S. Chen, J. Peng, F. Gao, and H. Liu, "The interface behavior of a thin film bonded imperfectly to a finite thickness gradient substrate," *Engineering Fracture Mechanics*, vol. 217, article 106529, 2019.
- [21] E. Jin, W. Sun, H. Liu et al., "Effect of interface coating on high temperature mechanical properties of SiC–SiC composite using domestic Hi–Nicalon type SiC fibers," *Coatings*, vol. 10, no. 5, p. 477, 2020.
- [22] C. Wan, H. Xu, J. Xia, and J. P. Ao, "Ultrahigh-temperature oxidation of 4H-SiC (0001) and gate oxide reliability dependence on oxidation temperature," *Journal of Crystal Growth*, vol. 530, no. 15, article 125250, 2020.
- [23] B. Poobalan, J. H. Moon, S. C. Kim et al., "Investigation of SiO₂ film growth on 4H-SiC by direct thermal oxidation and post-oxidation annealing techniques in HNO₃ & H₂O vapor at varied process durations," *Thin Solid Films*, vol. 570, no. 3, pp. 138–149, 2014.

Research Article

Characterization of the Microstructure and Bonding Properties of Zirconium-Carbon Steel Clad Materials by Explosive Welding

Hui Zhao 

School of Materials Science and Engineering, Xi'an Shiyou University, No.18, Electronic Second Road, Yanta District, Xi'an, Shaanxi, China

Correspondence should be addressed to Hui Zhao; huier7921@126.com

Received 1 October 2020; Revised 26 October 2020; Accepted 29 October 2020; Published 26 November 2020

Academic Editor: Jian Chen

Copyright © 2020 Hui Zhao. This is an open access article distributed under the Creative Commons Attribution License, which permits unrestricted use, distribution, and reproduction in any medium, provided the original work is properly cited.

An investigation was carried out to characterize the microstructure and bonding properties of the zirconium-carbon steel explosive clad. The microstructure and the composition of the clad were characterized using optical microscopy and scanning electron microscopy. Bonding properties were inspected by using bending and shearing tests. The examination results indicate that the R60702 and Cr70 plates were joined successfully without visible defects. The interface wave is symmetrical. There is no element diffusion across the interface of the clad plate. There are melt blocks at the interface. Bending and shearing test results indicate that the bonding properties of the clad meet the requirements of the ASTM B898 specification. And after shell rolling, no delamination appeared at the interface. Thus, it indicates that the clad plates have good bonding quality and meet the processing requirement.

1. Introduction

Zirconium (Zr) and its alloy have excellent corrosion resistance in acid and alkali environment. They show more excellent corrosion resistance than stainless steel, titanium alloy, and nickel alloy. Therefore, Zr is widely used in harsh environments, such as dehydration tower of acetic acid project in the chemical industry, synthesis tower in urea project, and reactor in alcohol production [1–7]. However, Zr is difficult to separate hafnium during refining. Therefore, the price of industrial pure zirconium is relatively expensive, which is 4–5 times that of high-grade stainless steel and 2–3 times that of titanium. Therefore, in recent years, zirconium-steel clad materials are used to replace pure Zr in chemical equipment. The processing method of zirconium-steel clad material is usually explosive welding. In this method, the explosive is used as the energy source, so that the atoms between the two metal interfaces are infinitely close, thus forming a firm combination. However, the physical and chemical properties of zirconium and steel are very different, so it is difficult to clad zirconium and steel by explosive welding method. Thus, Ti is used to the interlayer between zirconium and carbon

steel to bond them. The microstructure and properties of zirconium-steel clad materials with Ti interlayer have been investigated by more studies [8–15]. Generally, the interface is the weakness of the clad plate, but the zirconium-steel clad with interlayer has two interfaces. Thus, the study on the zirconium-steel clad materials without the interlayer is useful. However, not too much work has been implemented on zirconium-steel clad materials without the interlayer. Therefore, in this paper, the R60702-Gr70 clad material without the interlayer was prepared by explosive welding. The microstructure and mechanical properties of the clad material were characterized. The results show that the clad material meets the requirements of specification and processing.

2. Experimental Procedure

2.1. Materials. The flyer and the base plate are zirconium (ASME SB551 R60702) in solution-annealed condition and carbon steel (ASME SA Gr70) in normalization condition, respectively. The chemical compositions of R60702 and Gr70 are listed in Table 1 and Table 2. The flyer and base

TABLE 1: The components of R60702.

Material	Chemical element (%)						
	Hf	Fe+C	C	N	H	O	Zr
ASTM SB551 R60702	≤4.5	≤0.1	≤0.05	≤0.025	≤0.005	≤0.10	Bal.
Measured values	2.21	0.066	0.007	0.003	0.001	0.068	Bal.

TABLE 2: The components of Gr70.

Material	Chemical element (%)					
	C	Si	Mn	P	S	Fe
SA 516 Gr70	≤0.20	≤0.035	1.20~1.60	≤0.015	≤0.015	Bal.
Measured values	0.18	0.015	1.14	0.005	0.008	Bal.

plate were sequentially prepared with dimensions of $3 \times 2330 \times 6000$ mm and $25 \times 2330 \times 6000$ mm, respectively.

2.2. Explosive Welding Process. Figure 1 shows the assemble sketch of explosive welding. The R60702 and Gr70 plates were placed in a parallel direction. The spacers (R60702) were put on the surface of Gr70 to support the R60702 plate. The height of the spaces is about 8 mm. The ANFO explosive layer was put on the surface of the R60702 plate. The thickness of the explosive was 33-35 mm, the density was 0.75 g/cm^3 , and the velocity was 2300 m/s^{-1} . An electronic detonation was placed in the long edge of the pate. By igniting the electronic detonator, the detonation initiated the explosives, and the R60702 plate was accelerated to shock rapidly the Gr70 plate.

2.3. Specimen Characterization. Ultrasonic examination (UT) was employed to inspect the clad plates according to ASTM A578 specification with the Hanwei HS150 equipment [16]. After that, samples were cut parallel to the detonation direction. The cross-sections of specimens were grounded with SiC sandpaper up to No. 2000 and polished. The micrographs of R60702, Gr70, and the interface were examined by optical microscopy (Olympus GX51). The cross-sectional observation of the clad plate after explosive welding and their element analyses were conducted using a scanning electron microscopy (SEM, SSX-550) equipped with an energy dispersed X-ray microanalyzer (EDX). The specimens for the shearing test were prepared according to the ASTM B898[17]. The shearing test was carried out on the testing machine (DLY-10A). The shearing speed was 0.2 mm/min^{-1} . The bending test was also performed with the same instrument. The specimens for outside bending were bent up to 105° . And the specimens for inside bending were bent up to 180° (according to specification ASTM B898).

3. Results and Discussion

Explosive welding on the R60702 plate and Gr70 plate were carried out using ANFO explosives; then, the size of the clad plate was $3/25 \times 2330 \times 6000$ mm. Figure 2 shows the photographs of the clad plate. During the explosive welding process, the flyer plate impacted drastically to the base plate,

leading to the clad plate appeared apparent plastic deformation (Figure 2(a)). Thus, after explosive welding, the clad plate was flattened (Figure 2(b)). As shown in the two pictures, there is no a crack or disjoint defect on the clad plate by visual inspection. For further confirmation of bonding quality, UT was employed to check the continuities of the clad plate. During the UT process, high-frequency ultrasonic energy is introduced and propagated through the R60702 material of the clad plate in the form of pulse. Once there is a defect (such as the unbounded area) in the pulse path, parts of the energy will be reflected back from the defect surface. In the present work, the UT records show that there is no area where one or more discontinuities produced a continuous total loss of back reflection pulse. Figure 3 is a UT record of the clad plate. There are the first back reflection and the second back reflection pulses in the clad plate. According to the ASTM A578 specification, it indicates the interface of the R60702-Gr70 clad plate is continuous. Thus, the bonding quality of the clad plate meets the requirement of ASTM A578.

After UT, microstructure analysis was implemented on the R60702 plate clad, Gr70 plate, and clad plate. Optical views of the microstructures of the clad plate are shown in Figures 4 and 5. Figure 4(a) shows the microstructure of the R60702 plate. It can be seen from the picture that zirconium alloy (R60702) consists of the α phase with a large grain size (about $20\text{-}40 \mu\text{m}$). The size of α -Zr grains is about 8.5 level. The structure is made up of fully equal-axed grains. And there is no abnormal deposition in the metal structure. Figure 4(b) illustrates the microstructure of Gr70. This steel contains ferrite and pearlite grains with a band-like distribution. Figure 5 shows the optical interface micrograph of the clad plate. It can be seen from Figure 5(a) the explosive welding process led to the formation of a wavy interface along with the detonation direction. The formation mechanism of this wavy interface is when R60702 and Gr70 plate collided at a high velocity with an oblique angle; a high-velocity cumulative jet was spouted from the squeezed surface of both plates, and behaves as inviscid fluid [18]. The flow pattern of the jet depends on the destiny of the plates being joined [19]. The cumulative jet moved along the bisector of the collision angle to form a symmetrical wavy interface in the R60702-Gr70 plate because of their similar densities (shown in Figure 5(a)), as explained in the swinging wake model [20], as shown in [19–21]. And there are no visible defects like pores or cracks in the interface at high magnification (Figure 5(b)). However, during the explosive welding, the R70602 plate collided the Gr70 plate at high velocity (above $1000 \text{ m per microsecond}$); the mechanical energy released during collision leads to a rapid pressure boost, intense plastic deformation in the interface area, friction, and shear of the two materials. This leads to partial melting of the wave crest

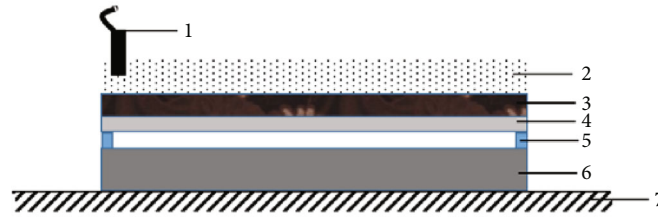


FIGURE 1: The sketch of explosive welding: (1) detonation, (2) explosives, (3) baffle, (4) R60702, (5) spacer, (6) Gr70, and (7) anvil.



(a)



(b)

FIGURE 2: Photographs of the R60702-Gr70 clad plate after (a) explosive welding and (b) flattening (plate size: $3/25 \times 2330 \times 6000$ mm).

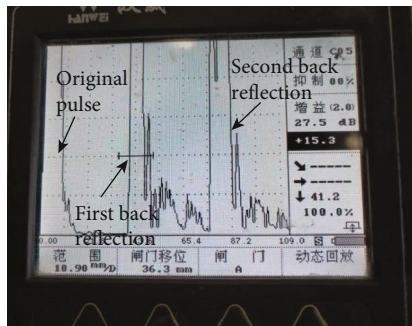


FIGURE 3: UT record of the clad plate.

regions and to the formation of melt blocks (Figure 5(b), white arrow).

To further observe the microstructure characteristic of the welded interface, the SEM was employed to investigate the bonding interface as shown in Figure 6(a). And there are also no defects like pores and cracks on the surface of the clad plate. The results are in accordance with that of optical micrographic examination. And base on the results mentioned above, high-velocity collision leading to the temperature increase in local zones, melt blocks formed at the vortices in the clad surface (Figure 6(b)). The elemental components of the melt blocks were measured using EDX at the positions marked with white arrows 1, 2, and 3, in Figure 6(b). The results are shown in Figure 7. The spectrum positions in Figure 7(a) are corresponding to the arrows in Figure 6(b). As confirmed by the EDX analysis, the region

at arrow 1 consists of 97.56% Fe, 2.06% Zr, and 0.38% Si; the region at arrow 2 consists of 100% Fe; and the region at arrow 3 consists of 44.51% Fe and 55.49% Zr (Figures 7(b) and 7(c)). Base on the EDX analysis results, it can be concluded that R60702 and Gr70 melted during the explosive welding, and the temperature at the welding interface exceeded the melting temperature of R60700 (1852°C) in a short time. The melt blocks resulted from the melting and mixing of the R60700 and Gr70 plates.

Because of the high temperature at the interface during the explosive welding, it could lead to the formation of the element diffusion across the interface [19–21]. However, Figure 6 indicates that there is no diffusion layer across the interface. In order to confirmation the element diffusion process (possible), line scanning of Fe and Zr, Cr, and Si elements are carried out away from $200\mu\text{m}$ across the interface. The results are shown in Figure 8. The R60700 and Gr70 materials contain different elements. At the bonding interface from the R60702 to Gr70, it can be seen from Figure 8(b) that the contents of Fe and Zr elements all show sharp transitions across the interface. It indicates that element diffusion during the explosive welding process is not observed under the accuracy of line scanning detection. And there is no silicon in R60702 material (Table 1), thus the silicon element in the specimen is from SiC sandpaper contamination during polishing.

Figures 9 and 10 show the mechanical properties of the R60702-Gr70 clad plate. The bending test was conducted to evaluate the bonding quality of the clad plate. Figure 9 shows the cross-sectional images of the R60702-Gr70 specimen

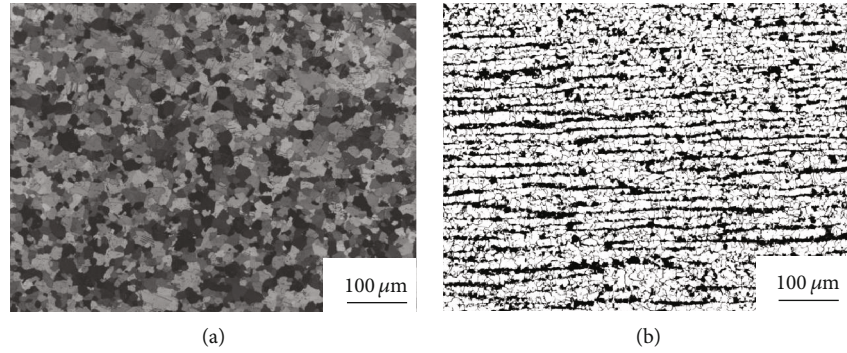


FIGURE 4: Optical micrographs of (a) R6070 and (b) Gr70.

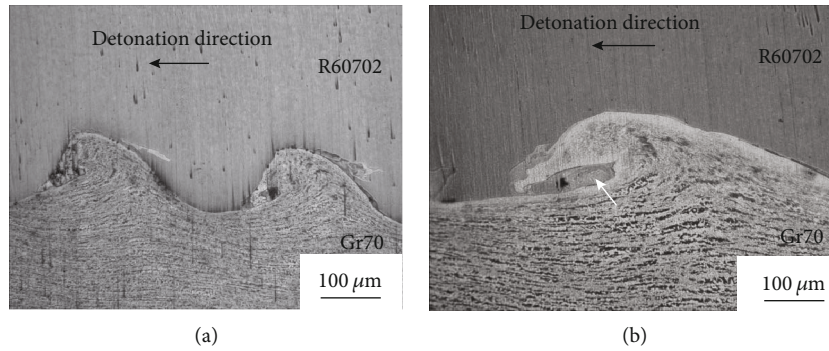


FIGURE 5: Optical micrograph of the joint cross-section (a) at low magnification and (b) at high magnification.

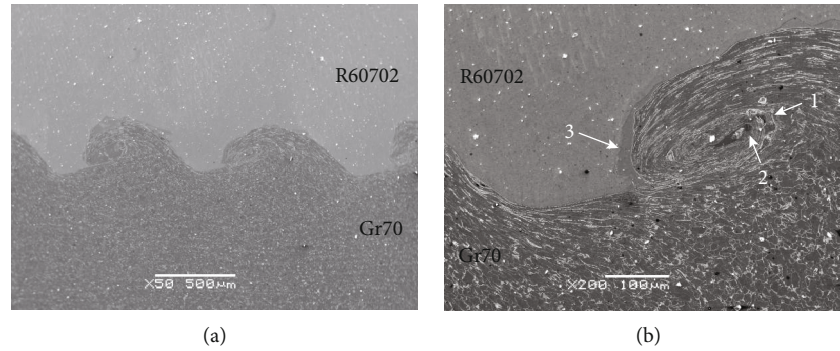


FIGURE 6: SEM microstructure of the joint cross-section (a) at low magnification and (b) at high magnification.

after the bending tests. During the face-bend test, the R60702 plate was subjected to tensile stress, and the Gr70 plate was subjected to compressive stress. During the reversed-bend test, the R60702 plate was subjected to compressive stress, and the Gr70 plate was subjected to stress. Either face-bend specimen or reversed-bend specimen was not delaminated at the interface or parent metals. The result meets the requirements of the ASTM B898 specification. The shearing test was also employed to evaluate the bonding quality of the clad plate. The shearing strength is 412 MPa. It is much higher than that of the ASTM 898 requirement (137 MPa). Figure 10 shows the shearing specimen after the shearing test. It can be seen that the separation appears at the interface. After the above examination, the clad plate was cut and rolled to the shell structure (shown in Figure 11). The diameter of

the shell is $\phi 508$ mm. During the rolling, the clad plate was not delaminated at the interface or base metals. It indicates the clad plate meets the processing requirement.

4. Conclusion

An investigation on the R60702-Gr70 explosive clad plate was carried out to understand the microstructure and bonding properties. The important findings are as follows:

- (1) The R60702-Cr70 clad plate with $3/25 \times 2330 \times 6000$ mm was successfully obtained by the explosive welding technique. UT inspection indicates that the bonding quality meets the requirement of the ASTM A578 specification

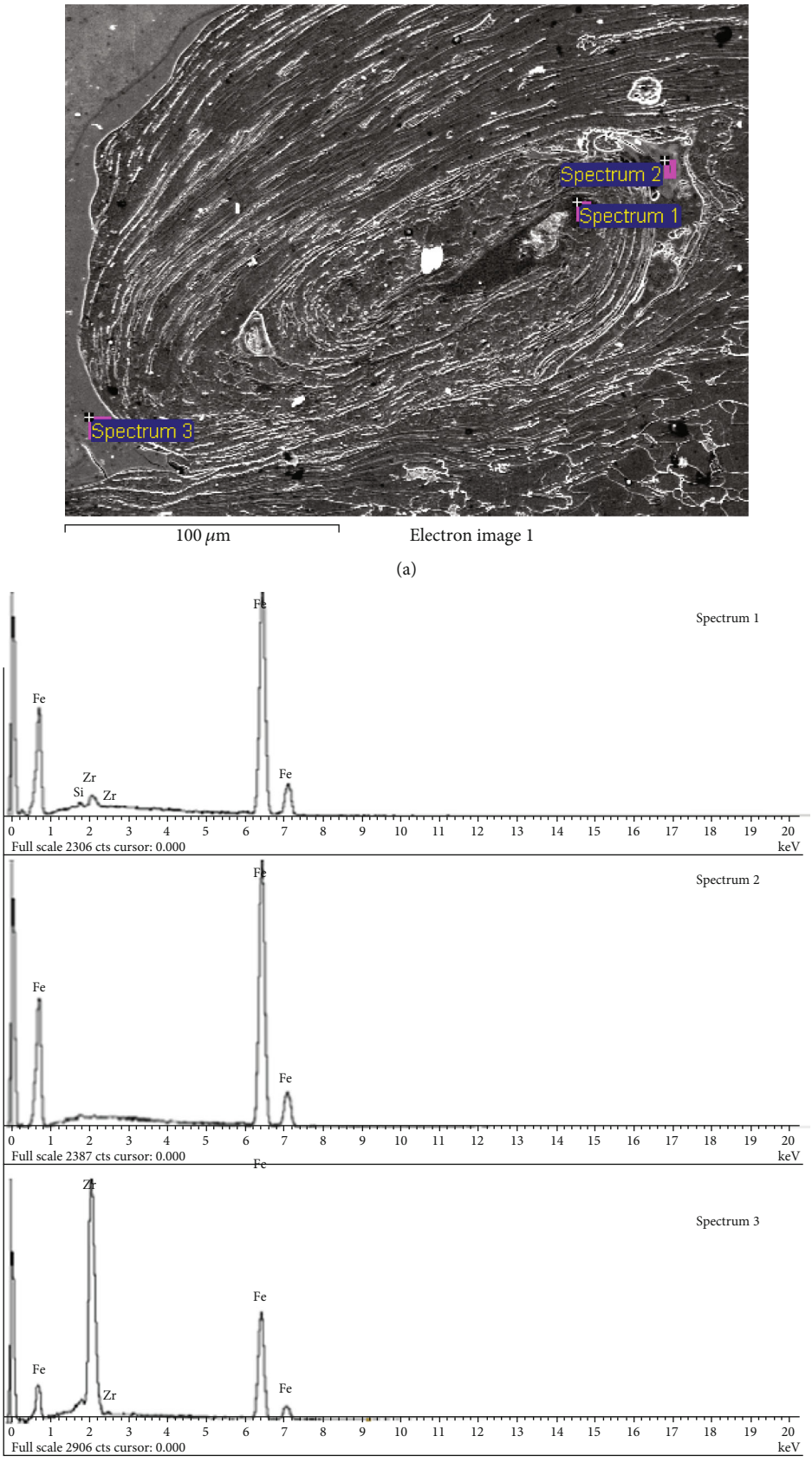


FIGURE 7: Continued.

Spectrum	Si	Fe	Zr	Total
Spectrum 1	0.38	97.56	2.06	100.00
Spectrum 2	0	100	0	100.00
Spectrum 3	0	44.51	55.49	100.00

All results in weight%

(c)

FIGURE 7: SEM micrographs of the clad plate (a) and corresponding EDX spectrums: (b) white arrow 1 (spectrum1), (c) white arrow 2 (spectrum2), and (d) white arrow 3 (spectrum3).

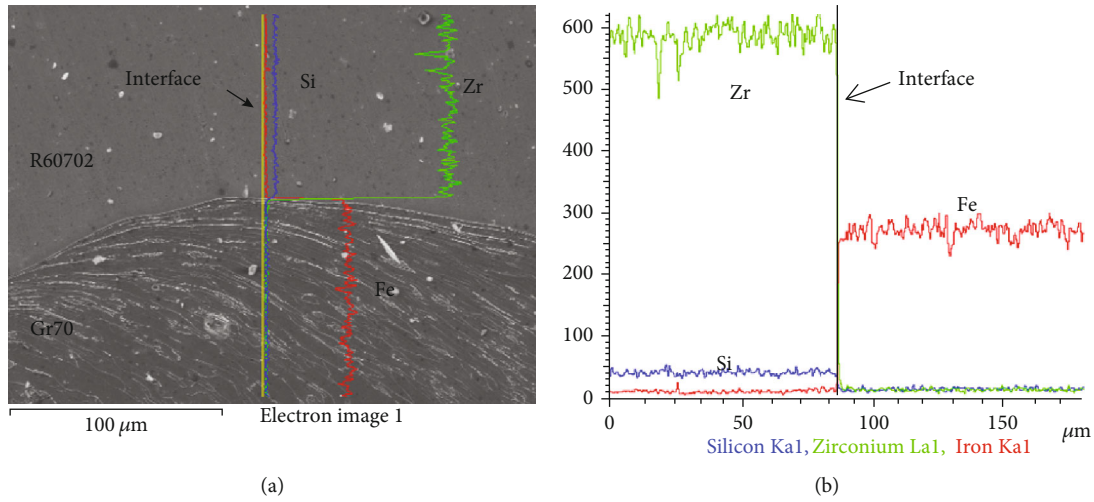


FIGURE 8: The bonding interface in the R60702-Gr70 clad plate: (a) microstructure; (b) line scan analysis from R60702 to Gr70 plates.

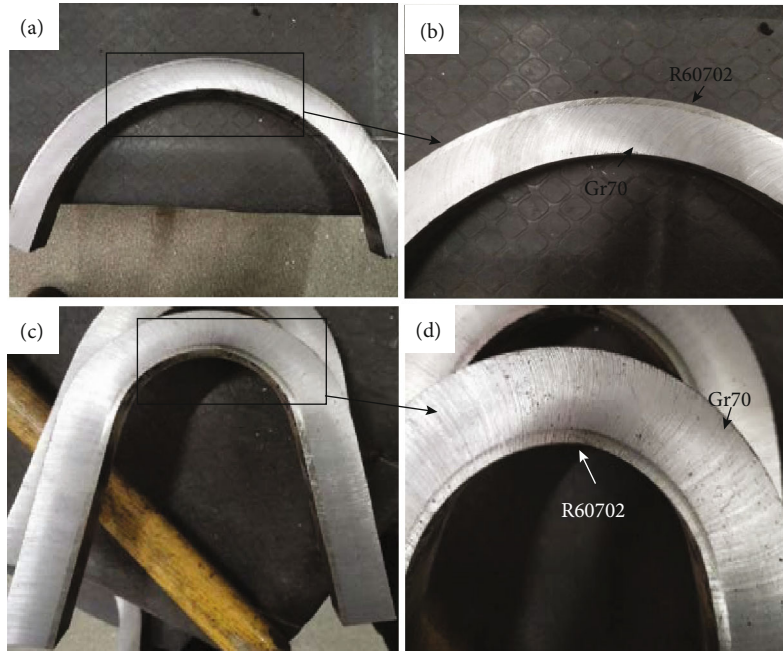


FIGURE 9: The specimens after bending test: a) and b) outside bending (bended up to 105°), c) and d) inside bending (bended up to 180°).

- (2) The R60702-Gr70 explosive clad plate has a wavy interface. The wave is symmetrical. No cracks or pore defects were observed at the interface. And there is no element diffusion across the interface of the clad plate
- (3) There are melt blocks on the interface. These melt blocks resulted from the melting and mixing of the R60702 and Gr70 materials during the high-velocity collision

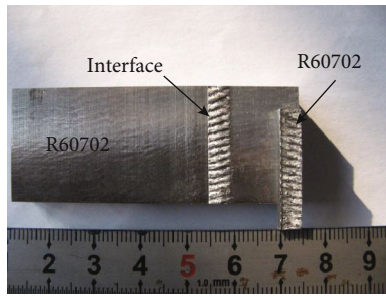


FIGURE 10: View of the samples after the shearing test.

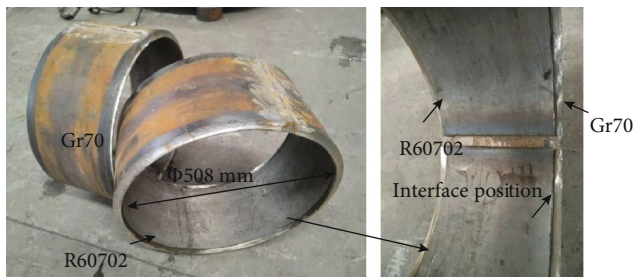


FIGURE 11: The shell structure after rolling.

- (4) Bending test results indicate that no delamination appears at the interface. And the shearing strength reaches 412 MPa. All the results meet the requirements of the ASTM B898 specification. Also, after shell rolling, there is no delamination that appears at the interface. It indicates that the clad plate has good bonding quality and meets the processing requirement

Data Availability

I declare that I do not have any commercial or associative interest that represents a conflict of interest in connection with the work submitted.

Conflicts of Interest

The authors declare that (i) no support, financial or otherwise, has been received from any organization that may have an interest in the submitted work and (ii) there are no other relationships or activities that could appear to have influenced the submitted work.

Acknowledgments

All authors acknowledge the supports of the Shaanxi innovation capability support plan, Innovation talents promotion plan—Science and technology innovation team (2018TD-035) and Xi'an Science and technology plan project (2020KJRC0100).

References

- [1] J. L. Havenga and J. T. Nel, "The Manufacturing of Zirconium Metal Powder by Means of a High Temperature Plasma Process," in *2010 Abstracts IEEE International Conference on Plasma Science*, p. 1, Norfolk, VA, 2010.
- [2] Y. Li and J. He, "Comparative and verified studies of zirconium nanocomposite nanofibres by bubble spinning," *Micro & Nano Letters*, vol. 13, no. 2, pp. 228–231, 2018.
- [3] I. V. Gayvoronsky and V. V. Girzhon, "Structural state of zirconium surface layers after laser alloying by titanium and nickel," *2015 International Young Scientists Forum on Applied Physics (YSF)*, Dnipropetrovsk, pp. 1–4, 2015.
- [4] N. S. Pushilina, V. N. Kudiiarov, and A. N. Nikolaeva, "Investigation of hydrogen distribution in zirconium alloy by means glow discharge optical emission spectroscopy," in *2014 9th International Forum on Strategic Technology (IFOST)*, pp. 489–491, Cox's Bazar, 2014.
- [5] S. Kaushik, K. Buddhadev, D. Sangita et al., "Direct non-destructive total reflection X-ray fluorescence elemental determinations in zirconium alloy samples," *Journal of Synchrotron Radiation*, vol. 27, no. 5, pp. 1253–1261, 2020.
- [6] L. L. Yang, M. H. Chen, J. L. Wang et al., "Microstructure and composition evolution of a single-crystal superalloy caused by elements interdiffusion with an overlay NiCrAlY coating on oxidation," *Journal of Materials Science & Technology*, vol. 45, pp. 49–58, 2020.
- [7] Y. X. Qiao, J. Huang, D. Huang et al., "Effects of laser scanning speed on microstructure, microhardness, and corrosion behavior of laser cladding Ni45 coatings," *Journal of Chemistry*, vol. 2020, Article ID 1438473, 11 pages, 2020.
- [8] A. Aushev, A. N. Balandina, E. N. Grishin, O. B. Drennov, A. M. Podurets, and M. I. Tkachenko, "Features of uniaxial and biaxial deformation of the contact boundary of metals during explosion welding," *Inorganic Materials: Applied Research*, vol. 9, no. 3, pp. 504–508, 2018.
- [9] M. Yang, H. M. Ao, S. Zhao, and J. F. Xu, "Application of colloid water covering on explosive welding of AA1060 foil to Q235 steel plate," *Propellants, Explosives and Pyrotechnics*, vol. 45, no. 3, pp. 453–462, 2020.
- [10] Z. R. Sun, C. Shi, F. Xu, F. Ke, and X. M. Wu, "Detonation process analysis and interface morphology distribution of double vertical explosive welding by SPH 2D/3D numerical simulation and experiment," *Materials & Design*, vol. 191, pp. 108–117, 2020.
- [11] E. V. Kuz'min, V. I. Lysak, S. V. Kuz'min, and M. P. Kerolev, "Effect of parameters of high-velocity collision on the structure and properties of joints upon explosive welding with simultaneous ultrasonication," *The Physics of Metals and Metallography*, vol. 120, no. 2, pp. 197–203, 2019.
- [12] T. T. Zhang, W. X. Wang, J. Zhou et al., "Investigation of interface bonding mechanism of an explosively welded tri-metal titanium/aluminum/magnesium plate by nanoindentation," *JOM: the journal of the Minerals, Metals & Materials Society*, vol. 70, no. 4, pp. 504–509, 2018.
- [13] S. Y. Yang and J. W. Bao, "Microstructure and properties of 5083 Al/1060 Al/AZ31 composite plate fabricated by explosive welding," *Journal of Materials Engineering & Performance*, vol. 27, no. 3, pp. 1177–1184, 2018.
- [14] J. Loiseau, W. Georges, D. L. Frost, and A. J. Higgins, "The propulsive capability of explosives heavily loaded with inert materials," *Shock Waves*, vol. 28, no. 4, pp. 709–741, 2018.

- [15] P. W. Chen, J. R. Feng, Q. Zhou et al., "Investigation on the explosive welding of 1100 aluminum alloy and AZ31 magnesium alloy," *Journal of Materials Engineering and Performance*, vol. 25, no. 7, pp. 2635–2641, 2016.
- [16] *Standard specification for straight-beam ultrasonic examination of rolled steel plates for special applications*, pp. 1–5, 2017, ASTM A578.
- [17] *Standard specification for reactive and refractory metal clad plate*, pp. 1–9, 2016, ASTM B898.
- [18] R. C. Gupta and G. S. Kainth, "Swinging wake mechanism for interface wave generation in explosive welding of metals," *Journal of Applied Mechanics*, vol. 57, no. 3, pp. 514–521, 1990.
- [19] S. P. Kiselev and V. I. Mali, "Numerical and experimental modeling of jet formation during a high-velocity oblique impact of metal plates," *Combustion Explosion & Shock Waves*, vol. 48, no. 2, pp. 214–225, 2012.
- [20] S. Saravanan and K. Raghukandan, "Thermal kinetics in explosive cladding of dissimilar metals," *Science and Technology of Welding and Joining*, vol. 28, no. 5, pp. 99–103, 2013.
- [21] T. Onzawa and Y. Ishi, *Fundamental studies on explosive welding, welding research abroad*, vol. 23, no. 3, pp. 28–36.

Research Article

Effect of Double Transition Metal Salt Catalyst on Fushun Oil Shale Pyrolysis

Xiaoyang Liu ¹, Haodan Pan ¹, Chuang Guo ², Xiaojing Di ¹ and Hongxiang Hu ³

¹College of Petroleum Engineering, Liaoning Shihua University, Fushun 113301, China

²Beijing Gas Energy Development Co. Ltd, Beijing 100000, China

³CAS Key Laboratory of Nuclear Materials and Safety Assessment, Institute of Metal Research, Chinese Academy of Sciences, Shenyang 110016, China

Correspondence should be addressed to Haodan Pan; panhaodan@126.com and Hongxiang Hu; hxhu@imr.ac.cn

Received 3 October 2020; Revised 19 October 2020; Accepted 21 October 2020; Published 4 November 2020

Academic Editor: Jian Chen

Copyright © 2020 Xiaoyang Liu et al. This is an open access article distributed under the Creative Commons Attribution License, which permits unrestricted use, distribution, and reproduction in any medium, provided the original work is properly cited.

Shale ash (SA) as the carrier, the ratio of Cu to Ni in the Cu-Ni transition metal salt being, respectively, 1 : 0, 2 : 1, 1 : 1, 1 : 2, 0 : 1, the double transition metal salt catalyst ($\text{Cu}_m\text{Ni}_n/\text{SA}$) was prepared to explore the effect of such catalysts on the pyrolysis behavior and characteristics of Fushun OS. The research results show that the temperature (T_{\max}) corresponding to the maximum weight loss rate decreased by 12.9°C, 4.0°C, and 3.6°C; and the apparent activation energy decreased by 35.2%, 33.9%, and 29.6%, respectively, after adding catalysts $\text{Cu}_0\text{Ni}_1/\text{SA}$ in pyrolysis. The addition of $\text{Cu}_0\text{Ni}_1/\text{SA}$ and $\text{Cu}_2\text{Ni}_1/\text{SA}$ further improves the shale oil (SO) yield of 3.5% and 3.1%, respectively. $\text{Cu}_0\text{Ni}_1/\text{SA}$ produces more aromatic hydrocarbons, which, however, weakens the stability of SO and is of toxicity in use. After analyzing the pyrolysis product—semicoke (SC) and SO—with ATR-FTIR and GC-MS methods, $\text{Cu}_m\text{Ni}_n/\text{SA}$ promotes the secondary cracking and aromatization of OS pyrolysis, increasing the content of the compound of olefins and aromatics in SO, and hastening the decomposition of long-chain aliphatic hydrocarbons to short-chain aliphatic hydrocarbons.

1. Introduction

With the shortage of traditional energy resources against the increasing oil demand, oil shale is considered to be a type of ideal alternative energy source to substitute oil owing to its abundant reserves. There are approximately 68.92 billion tons shale oil converted from proven oil shale in the world, which is three times the amount of crude oil reserves [1] and approximately accounts for 35% of the total global energy [2]. China is abundant in oil shale reserves, and the oil content is above the average. Among them, oil shale reserves with an oil content of more than 5% to 10% are 266.435 billion tons, and more than 10% are 126.694 billion tons [3]. Liaoning Fushun mining area, the third-largest mining area in the country, boosts approximately 3.6 billion tons of the oil shale reserves [4].

Shale oil and shale gas can be obtained through the pyrolysis of oil shale (OS). Catalytic pyrolysis increases the conversion rate of oil shale pyrolysis and the yield of shale oil as well

as its quality [5, 6]. Domestic and foreign scholars have done extensive experimental studies on the catalytic pyrolysis of oil shale with different catalysts. Gai et al. [7] studied the influence of the presence of pyrite on the pyrolysis behavior of oil shale. The iron contained in pyrite positively affects the pyrolysis behavior of oil shale and promotes its volatilization, thus increasing the yield of liquid and gas products. Cao [8] introduced a type of catalyst from oil shale rock as raw material to obtain light feedstock oil, which not only greatly reduces the cost of producing light fuel oil but also increases the oil quality by adding the catalyst. Williams et al. [9, 10] studied the effect of the ZSM-5 zeolite catalyst on the pyrolysis of oil shale in Kark, Pakistan. The addition of catalyst increases the content of gas products and shale semicoke, reducing the yield of shale oil, promoting the conversion of long-chain alkanes and olefins into low-molecular-weight and short-chain alkanes, and decreasing the total nitrogen and sulfur content in the catalyzed oil. Wang et al. [11] added alkali metal carbonates K_2CO_3 , MgCO_3 , Na_2CO_3 , and

CaCO_3 to oil shale, and the results showed that different alkali metal carbonates had different catalytic effects on oil shale. MgCO_3 has an obvious effect compared with other alkali metal carbonates, and it is especially violent at the beginning of pyrolysis. Jiang et al. [12] and Pulushev et al. [13] studied the effects of pyrolysis conditions and transition metals on the pyrolysis products and characteristics of Huadian oil shale, finding that the addition of transition metal cobalt salts to OS increases the selectivity of aromatics and promotes the aromatization of olefins. Chang et al. [14] studied the effects of $\text{FeCl}_2 \cdot 4\text{H}_2\text{O}$, $\text{CoCl}_2 \cdot 6\text{H}_2\text{O}$, $\text{NiCl}_2 \cdot 6\text{H}_2\text{O}$, and ZnCl_2 on the pyrolysis of OS, summarizing that all these four metal salts enhance the secondary cracking of shale oil, reduce oil production, and improve the pyrolysis gas production. All these studies affirm that catalyst increases either the pyrolysis conversion rate or product yield. However, there are relatively few reports on the OS pyrolysis catalyzed by shale ash (SA) with double transition metal salts as the carrier is relatively few.

In this paper, shale ash (SA) as the carrier, the ratio of Cu to Ni in Cu-Ni transition metal salt-containing being different, the double transition metal salt catalyst ($\text{Cu}_m\text{Ni}_n/\text{SA}$) was prepared to explore the effect of such catalysts on the pyrolysis characteristics of Fushun OS. The thermogravimetric method was applied to analyze the effect of the double transition metal catalysts containing different ratios Cu to Ni in $\text{Cu}_m\text{Ni}_n/\text{SA}$ groups on the pyrolysis characteristics of OS. The components of pyrolysis product shale oil (SO) were analyzed by ATR-FTIR and GC-MS, while the effects of the catalyst on the activation energy of OS pyrolysis were analyzed by the Coats Redfern model.

2. Experimental Materials and Methods

2.1. Materials. OS and SA were obtained from Fushun, Liaoning Province, China. OS and SA samples were first crushed and screened into a particle size of 10-18 mesh and 40-60 mesh before the experiment, and then cleaned with deionized water for 7-8 times, and eventually dried overnight in a blast drying oven at 80°C . The main properties of OS and SA samples are shown in Table 1.

The inorganic crystalline phases in OS and SA were analyzed by X-ray diffraction (XRD), and the results are shown in Figure 1. The XRD spectrum shows that the minerals in OS are mainly composed of quartz and aluminosilicates including kaolinite and illite, and also a small amount of carbonate. The specific components are shown in Table 2.

Figure 2 is the scanning electron microscopy (SEM) of OS and SA, presenting the maldistribution and irregular but the certain pored structure of the mineral particle size in the OS, which belongs to a type of solid sedimentary rocks composed of the scaly-structured clay kaolinite and mica mineral. Figure 2(b) clearly shows the larger pored structure of the SA compared with that of OS, enabling the SA to load transition metal salt as a carrier.

The equal volume impregnation method was applied to prepare for the catalyst samples. First, the water absorption of the carrier SA was measured. The loading amount of the

TABLE 1: Industrial analysis and elemental analysis of oil shale (OS) and shale ash (SA).

Industrial analysis, %					Elemental analysis, %				
Sample	M_{ad}	A_{ad}	V_{ad}	FC_{ad}^*	C_{ad}	H_{ad}	N_{ad}	O_{ad}^*	S_{ad}
OS	2.86	77.29	17.77	2.08	10.91	1.82	0.78	5.91	0.33
SA	0.48	90.68	5.96	2.88	5.16	0.56	1.06	0.64	0.83

* subtraction method.

transition metal salt was set as 3 wt.% for the distinct experiment statistics (the ratio of the mass of the two types of transition metal salts to the sum of the mass of the two types of transition metal salts and SA was 3 wt.%). The transition metal salt ($\text{CuCl}_2 \cdot 2\text{H}_2\text{O}$, $\text{NiCl}_2 \cdot 6\text{H}_2\text{O}$) was accurately weighed with different Cu/Ni ratios (1:0, 2:1, 1:1, 1:2, 0:1) and then dissolved in the same volume of deionized water. Mechanically stirred and mixed with a glass rod, SA was added into the solution and again fully stirred and immersed for 12 hours. After a 20-hour forced air drying at 130°C , the Cu-Ni/shale ash-based double transition metal catalyst was obtained and stored in seal preservation for later use.

The prepared SA-grouped double transition metal catalyst is named as $\text{Cu}_m\text{Ni}_n/\text{SA}$ (m for the mass fraction ratio of Cu metal salt and n for the Ni metal salt in the catalyst), and the sample of $\text{Cu}_m\text{Ni}_n/\text{SA}$ mixed with OS is expressed as $\text{OS-Cu}_m\text{Ni}_n/\text{SA}$, for example, $\text{OS-Cu}_1\text{Ni}_1/\text{SA}$ represents SA the mixed pyrolysis with a load mass fraction ratio of OS to Cu-Ni of 1:1.

The morphology analysis of SA after loading metal salt is shown in Figure 3. Compared with the initial SA, the surface of $\text{Cu}_m\text{Ni}_n/\text{SA}$ is covered with scaly material, and the pores become smaller and shallower (Figure 3(a)). Through SEM/EDS analysis, the material composition in the pores contains Ni and Cu elements, indicating that the metal salt has been loaded into the pores of SA through the impregnation method (Figure 3(b)).

2.2. Laboratory Apparatus. The Nicolet iS50 model Fourier transform attenuated total reflection infrared spectroscopy (ATR-FTIR) was applied to analyze the characteristics of OS and SO, and Netzsch STA 449 F5 thermogravimetric analyzer-mass spectrometry (TG-MS) to study OS thermal weight loss behavior and component. The SO obtained from the experimental pyrolysis was extracted with dichloromethane, and the SO component was analyzed with the GC-MS (Agilent 7890A/5975C from NYSE: A, United States). The ATR-FTIR spectrum was recorded between 4000 cm^{-1} and 400 cm^{-1} , and the spectral resolution was 4 cm^{-1} . The sensitivity of the microbalance for TG detection was less than $\pm 0.1\text{ }\mu\text{g}$, and the temperature accuracy was $\pm 0.5^\circ\text{C}$. In addition, in order to avoid the limitation of heating transfer, a blank sample was used before the experiment to baseline the influence of the buoyancy and weight loss of the crucible on the experimental data.

2.3. Experimental Methods. First, a certain amount of mixed sample ($10 \pm 0.5\text{ mg}$) of OS and SA-grouped transition metal

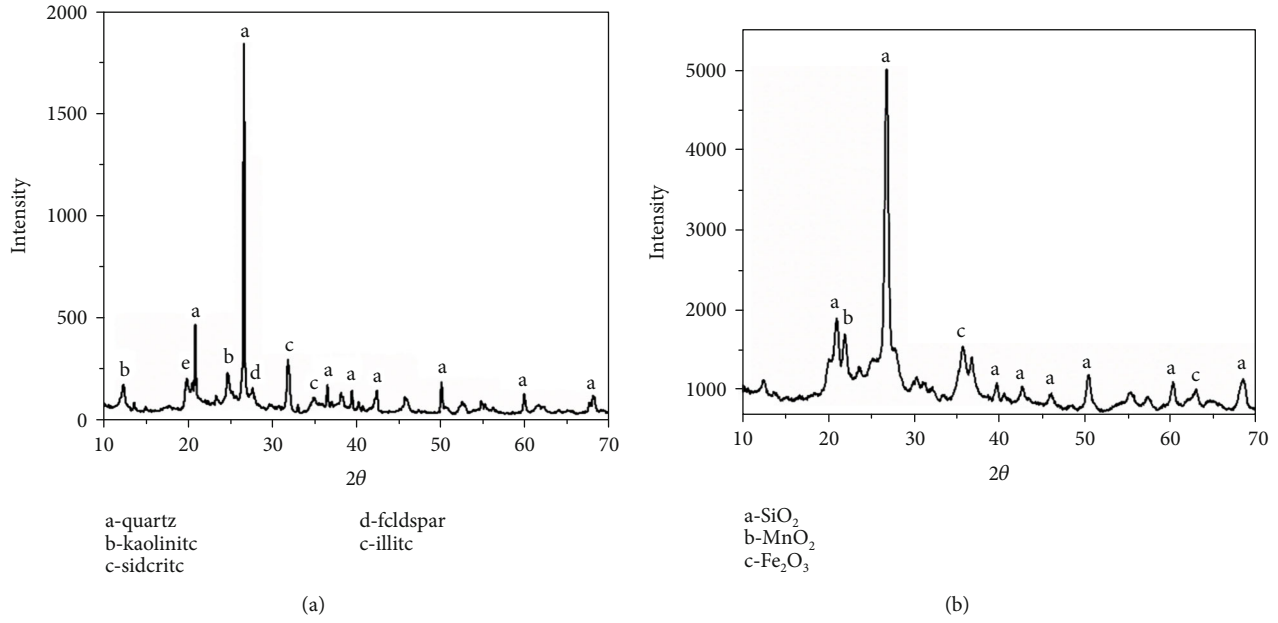


FIGURE 1: XRD patterns of oil shale (OS) and shale ash (SA): (a) OS; (b) SA.

TABLE 2: Ash XRF (X-ray fluorescence) analysis of OS and SA.

Constituent, wt %	SiO ₂	Al ₂ O ₃	Fe ₂ O ₃	K ₂ O	TiO ₂	MgO	P ₂ O ₅	SO ₃	CaO	Other
OS	40.48	13.30	9.78	1.01	0.89	0.88	0.81	0.80	0.79	31.26
SA	58.15	23.18	10.26	1.45	1.35	1.42	1.25	1.53	1.08	0.33

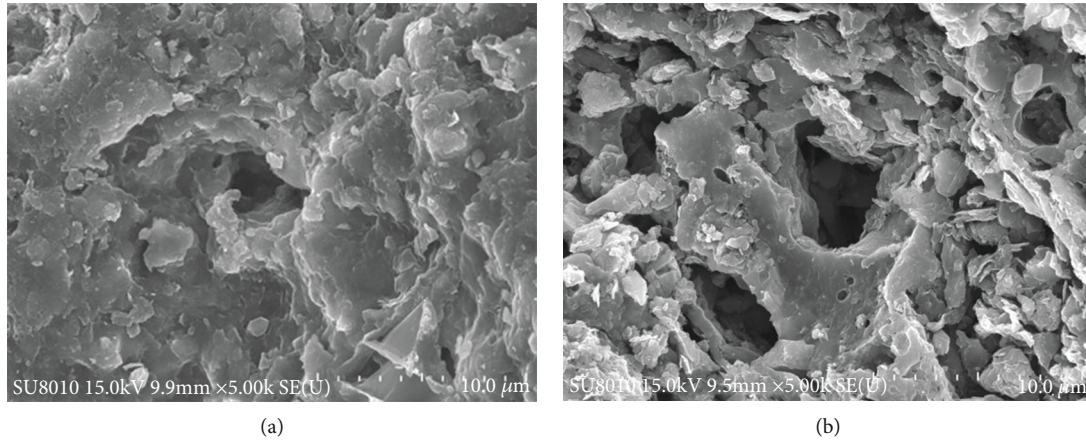


FIGURE 2: Scanning electron microscopy (SEM) of OS and SA: (a) OS; (b) SA.

salt catalyst was weighed and placed into a thermogravimetry crucible with a height of 4 mm and a diameter of 6 mm. The 50 mL/min argon was used as the purge gas, and the 30 mL/min of argon as the protective gas. Then, the temperature was lifted from room temperature to 900°C at a heating rate of 10°C/min. The mixing ratio of OS to catalyst was 2 : 1. The gas produced during the pyrolysis was purged into the mass spectrometer through the capillary column connecting to the thermogravimetric analyzer. Besides, the connecting tube between the thermogravimetry and the mass spectrom-

eter was heated to 255°C to prevent the gas from condensing in the capillary.

The weight loss rate of pure OS is calculated by formula (1):

$$M_{OS} = M_{Loss}/r_{OS} \quad (1)$$

M_{Loss} is the weight loss rate of OS during the mixed pyrolysis of transition metal salt and OS, and r_{OS} is the mass percentage of OS in the sample.

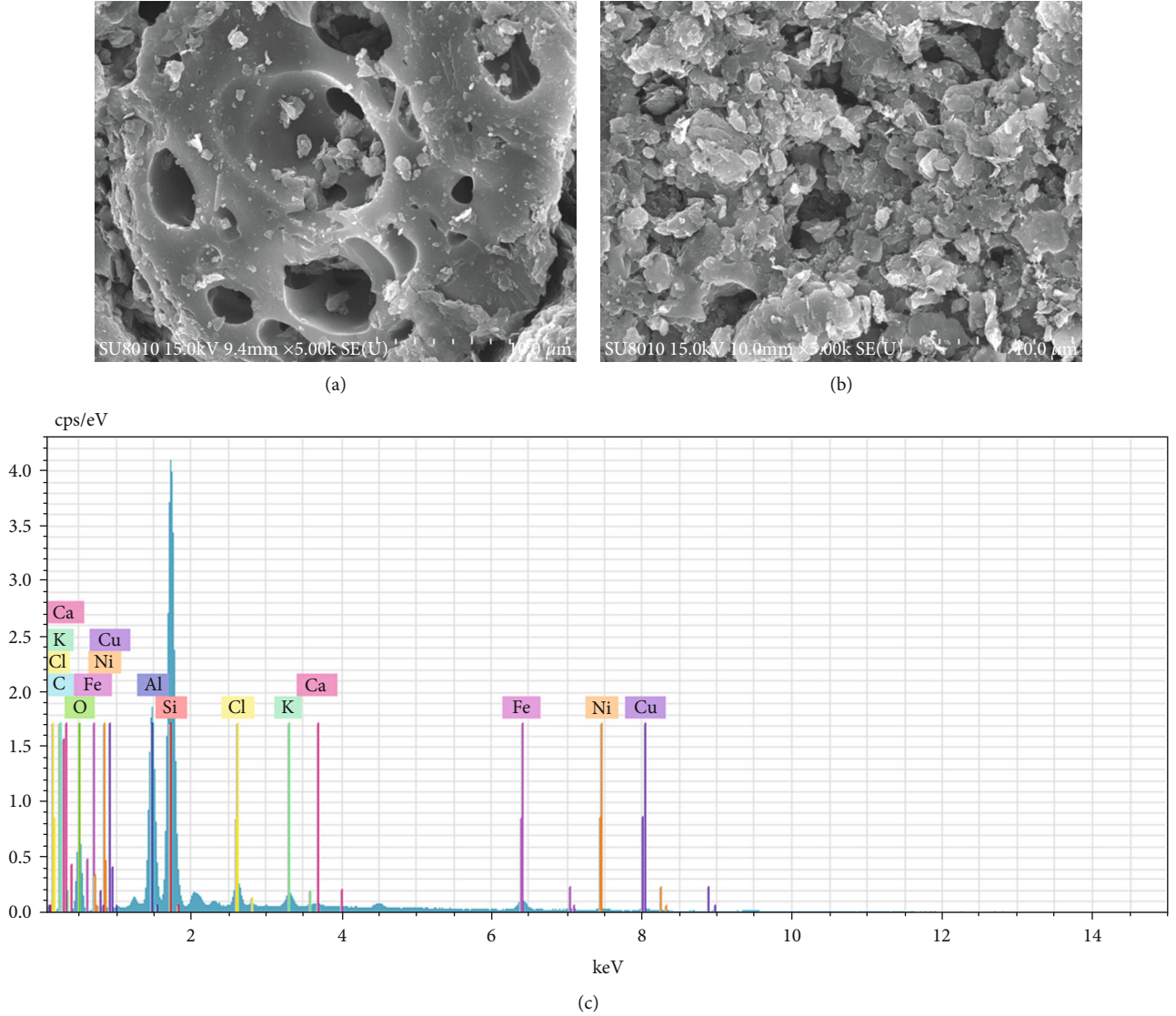


FIGURE 3: SEM/EDS analysis image of $\text{Cu}_m\text{Ni}_n/\text{SA}$. (a) Scanning electron micrograph (SEM) before SA loading metal salts. (b) SEM after SA loading metal salts. (c) Energy dispersion spectrometer (EDS) image after SA loading metal salts.

2.4. Kinetics Analysis. Assuming m_0 represents the initial quality of the oil shale. It was heated according to the preset heating program where it underwent the thermal decomposition reaction. The pyrolysis conversion rate of OS α can be expressed as (t time for the time, m_t for the mass of the sample, and m_∞ for the final mass of the residue unable to be decomposed)

$$\alpha = \frac{m_0 - m_t}{m_0 - m_\infty}. \quad (2)$$

The decomposition rate in the decomposition reaction can be expressed as

$$\frac{d\alpha}{dt} = k f(\alpha). \quad (3)$$

In this formula, k is the Arrhenius rate constant, $k = A \exp(-E/RT)$; A is the prefactor, (S^{-1}); E is the activation

energy, (kJ/mol); T is the thermodynamic temperature, (K); R is the gas constant, in units of $\text{J}/(\text{mol}\cdot\text{K})$. The overall reaction equation of OS pyrolysis can be expressed as

$$\frac{d\alpha}{dt} = A \exp\left(-\frac{E}{RT}\right) f(\alpha). \quad (4)$$

In nonisothermal conditions, the heating rate can be expressed as $\beta = dT/dt$; then, formula (3) can be rewritten as

$$\frac{d\alpha}{dT} = \frac{A}{\beta} \times \exp\left(-\frac{E}{RT}\right) f(\alpha). \quad (5)$$

The functional form of $f(\alpha)$ and its reaction order is determined by the reaction type or mechanism, normally $f(\alpha) = (1 - \alpha)^n$.

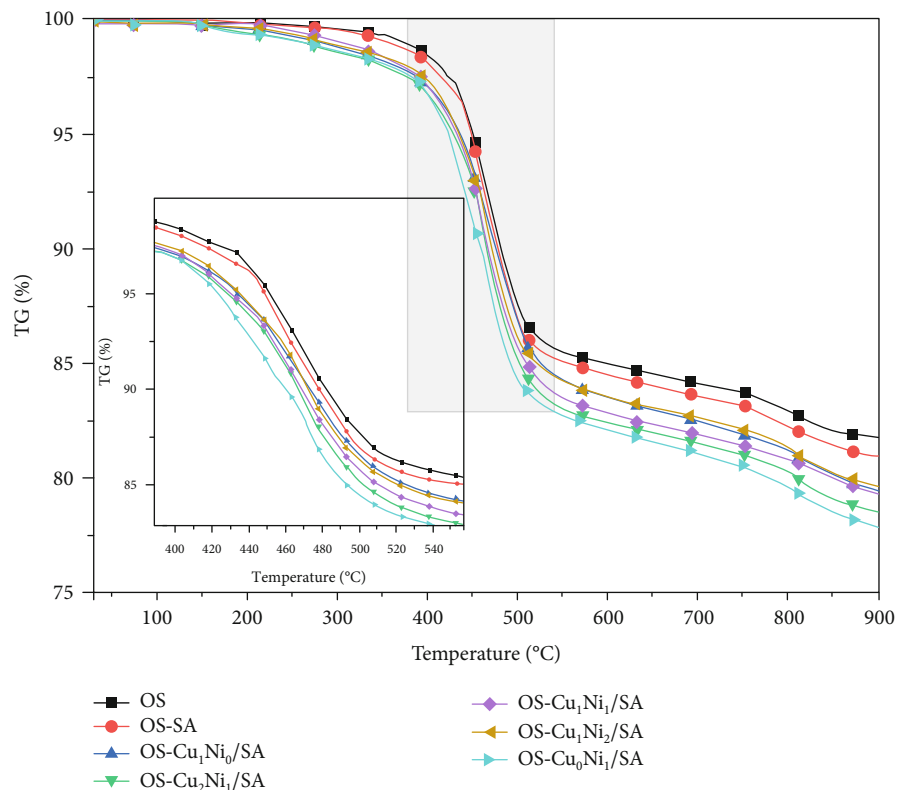


FIGURE 4: TG curves of mixed pyrolysis of OS with different $\text{Cu}_m\text{Ni}_n/\text{SA}$.

3. Experimental Results and Discussion

3.1. Effect of Transition Metal Salt Catalysts on OS Pyrolysis

3.1.1. Analysis of Catalytic Cracking Behavior. Figures 4 and 5 show the thermogravimetric (TG, DTG) curves of OS after adding different transition metal salts. The quality loss of OS involves various chemical and physical processes and can be divided into three following stages [15, 16]: the figures below show that the mass loss in stage one ($<200^\circ\text{C}$), mainly caused by the evaporation of water, especially the adsorbed water from clay minerals and interlayer water, was relatively small due to the sample's lower moisture content after the blast drying procedure. Stage two ($200\sim600^\circ\text{C}$) was the decomposition of organic matter. The kerogen molecules and other organic components in the OS were decomposed and produce asphaltenes, which then continued to decompose into various small aromatic molecules or aliphatic molecules. Technically, this stage can also be considered as the oil production stage in OS pyrolysis [12], where a series of complex reactions including ring-opening reaction, depolymerization reaction, and repolymerization reaction [17, 18] would occur when the temperature rose to a certain level. These reactions promoted the addition and rearrangement of organic matter in the OS and the production of different types of organic compounds. The rapid pyrolysis occurred between 417.2 and 519.9°C , and the weight loss rate in this stage reached as high as $13.58\text{ wt.}\%$, accounting for $65.35\text{ wt.}\%$ of the total weight loss. The maximum weight loss

peak also appeared. In the third stage ($>600^\circ\text{C}$), the decomposition of organic matter basically finished and occurred mainly the decomposition reaction of inorganic minerals (such as carbonate and clay minerals).

The figure suggests a similar trend of the curves of OS TG and DTG after adding $\text{Cu}_m\text{Ni}_n/\text{SA}$. The TG curves moved left to the low-temperature zone after adding SA and different $\text{Cu}_m\text{Ni}_n/\text{SA}$ to the direct OS pyrolysis, manifesting that the temperature of OS after adding SA and $\text{Cu}_m\text{Ni}_n/\text{SA}$ was lower than that of the direct OS pyrolysis under the same weight loss rate in its main pyrolysis stage. The volatile evolution content increased and the final coke output decreased to a certain extent. The catalytic effect of $\text{Cu}_m\text{Ni}_n/\text{SA}$ was significantly higher than that of SA, among which OS- $\text{Cu}_0\text{Ni}_1/\text{SA}$ had the minimum coke output, and the total mass loss rate in descending order was OS- $\text{Cu}_0\text{Ni}_1/\text{SA} < \text{OS}-\text{Cu}_2\text{Ni}_1/\text{SA} < \text{OS}-\text{Cu}_1\text{Ni}_1/\text{SA} < \text{OS}-\text{Cu}_1\text{Ni}_0/\text{SA} < \text{OS}-\text{Cu}_1\text{Ni}_2/\text{SA} < \text{OS}-\text{SA} < \text{OS}$. The DTG curves show three sharp weight loss peaks during the pyrolysis of OS, which, respectively, corresponds to the decomposition of moisture ($90\sim200^\circ\text{C}$), organic matter ($200\sim600^\circ\text{C}$), and inorganic minerals ($700\sim900^\circ\text{C}$). The first maximum weight loss rate in the second stage was significantly higher than that in the first and third stages, indicating that the mass-loss rate in the second stage was faster than that in the first and third stages.

Combining with Table 3, it can be seen the addition of SA and $\text{Cu}_m\text{Ni}_n/\text{SA}$ to varying degrees lowered the temperature (T_{\max}) reaching the occurrence of maximum mass loss rate.

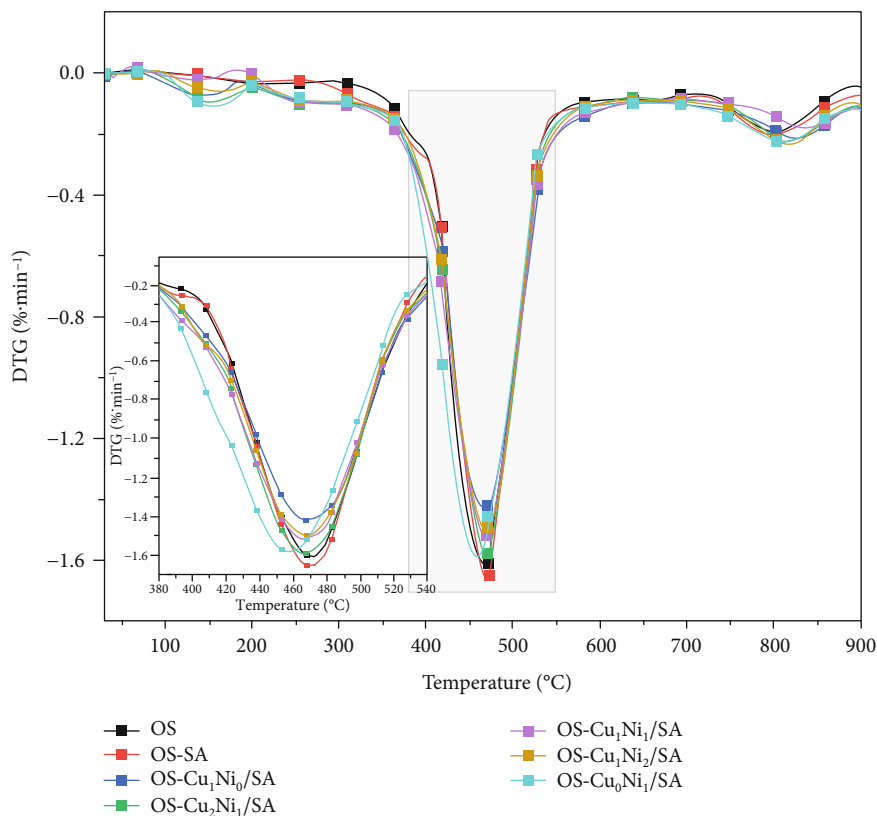


FIGURE 5: DTG curves of mixed pyrolysis of OS with different $\text{Cu}_m\text{Ni}_n/\text{SA}$.

The decrease in temperature corroborates that SA and $\text{Cu}_m\text{Ni}_n/\text{SA}$ can catalyze the cracking reaction to a certain extent and further activate the release process of volatile substances. Within an appropriate temperature range, the presence of transition metal salt ions accelerates the cleavage of branched functional groups in kerogen and promotes the formation of cracked oil gas phase, thereby lowering the reaction temperature. Among them, the T_{\max} of OS- $\text{Cu}_0\text{Ni}_1/\text{SA}$ had the sharpest decline of 2.74% compared with that of the direct OS pyrolysis. The T_{\max} of each sample in descending order was ranked as OS- $\text{Cu}_0\text{Ni}_1/\text{SA}$ < OS- $\text{Cu}_2\text{Ni}_1/\text{SA}$ < OS- $\text{Cu}_1\text{Ni}_1/\text{SA}$ < OS- $\text{Cu}_1\text{Ni}_2/\text{SA}$ < OS- $\text{Cu}_1\text{Ni}_0/\text{SA}$ < OS-SA. Moreover, the addition of $\text{Cu}_m\text{Ni}_n/\text{SA}$ lowered the start and end temperatures in the main pyrolysis stage, as well as the maximum weight loss rate to a certain extent, but expanded the devolatilization temperature range. It can also be seen from Table 3 that the samples adding SA and $\text{Cu}_m\text{Ni}_n/\text{SA}$ had a greater weight loss rate within all temperature ranges, indicating that SA and $\text{Cu}_m\text{Ni}_n/\text{SA}$ promotes the pyrolysis reaction of OS, including the decomposition of inorganic minerals. Thermal cracking behavior confirms that OS- $\text{Cu}_0\text{Ni}_1/\text{SA}$, OS- $\text{Cu}_2\text{Ni}_1/\text{SA}$, and OS- $\text{Cu}_1\text{Ni}_1/\text{SA}$ have better catalytic effects.

3.1.2. Kinetics Analysis. Kinetic analysis, combined with the macroscopic phenomenon of the reaction, reflects the relationship between the energy and the movement of substances and reveals the pyrolysis reaction mechanism so as to control the chemical reaction. Among various analysis models, the

Coats-Redfern (C-R) method has been used to calculate the relevant kinetic parameters of solid fuel pyrolysis [19, 20]. This method was applied to the thermal kinetic calculations in this section to analyze the kinetics in the main pyrolysis stages. After the analysis of the kinetic parameters of the samples adding different $\text{Cu}_m\text{Ni}_n/\text{SA}$, the values of the thermokinetic parameters E , A , and R^2 obtained are shown in Table 4.

Table 4 shows that SA and $\text{Cu}_m\text{Ni}_n/\text{SA}$ reduce the activation energy required for the pyrolysis reaction in the main pyrolysis stage. OS forms asphaltenes in the second stage and then continues to be decomposed and produce volatile substances. A certain amount of energy needs to be absorbed to support the occurrence of related depolymerization cracking reactions in this process. It can be seen from Table 4 that the direct OS pyrolysis needs to absorb approximately 39.2 kJ/mol for the related chemical reactions. Adding SA and $\text{Cu}_m\text{Ni}_n/\text{SA}$, the apparent activation energy-reduced, and the reduction degree of $\text{Cu}_m\text{Ni}_n/\text{SA}$ on activation energy was significantly higher than that of SA. Among them, OS- $\text{Cu}_0\text{Ni}_1/\text{SA}$ reduced the maximum activation energy of 13.8 kJ/mol, accounting for 35.2% of the activation energy required for OS pyrolysis; OS- $\text{Cu}_2\text{Ni}_1/\text{SA}$ is the second and required 13.3 kJ/mol activation energy to reduce pyrolysis, accounting for 33.9% of the activation energy required for the OS pyrolysis. Scholars also believe that metal cations, as a strong polar core, may be embedded into the crystal lattice of macromolecules after interacting with kerogen and other macromolecules, thus deforming the electronic structure on the surface and causing a dynamic induction effect. Such an

TABLE 3: Comparison among thermogravimetric data of different samples.

Samples	Starting temperature/°C	Termination temperature/°C	Maximum weight loss rate /%/min	Temperature at maximum weight loss rate/°C	Sample weight loss rate/wt.%		
					Room temperature~200°C	200~600°C	600~900°C
OS	418.1	520.8	1.609	471.2	0.10	15.07	3.15
OS-SA	413.7	517.4	1.654	470.4	0.11	15.36	3.55
OS-Cu ₁ Ni ₀ /SA	396.5	520.2	1.420	469.0	0.44	16.12	3.99
OS-Cu ₂ Ni ₁ /SA	392.9	519.2	1.589	467.2	0.55	17.05	3.83
OS-Cu ₁ Ni ₁ /SA	398.0	520.0	1.517	467.6	0.20	16.98	3.47
OS-Cu ₁ Ni ₂ /SA	401.8	520.3	1.499	468.0	0.33	16.14	3.85
OS-Cu ₀ Ni ₁ /SA	394.5	515.7	1.586	458.3	0.59	17.35	4.17

TABLE 4: Pyrolysis kinetic parameters calculated via Coats-Redfern method.

Samples	Temperature/°C	Activation ability/kJ/mol	Pre-reference factor/min ⁻¹	Correlation coefficient (R^2)
OS	418.1-520.8	39.2	2.6×10^3	0.9832
OS-SA	413.7-517.4	36.6	1.3×10^3	0.9805
OS-Cu ₁ Ni ₀ /SA	392.9-519.2	26.3	80.3	0.9835
OS-Cu ₂ Ni ₁ /SA	399.5-520.2	25.9	58.0	0.9874
OS-Cu ₁ Ni ₁ /SA	398.0-520.0	27.6	113.3	0.9904
OS-Cu ₁ Ni ₂ /SA	401.8-520.3	28.8	155.3	0.9899
OS-Cu ₀ Ni ₁ /SA	392.5-515.7	25.4	109.7	0.9917

effect reduces the bond energy of the C-C bond, requiring less energy for the reaction, and leading to a decrease of the activation energy. From the kinetic analysis, the order of the samples that reduced the activation energy of the reaction was OS – Cu₀Ni₁/SA > OS – Cu₂Ni₁/SA > OS – Cu₁Ni₀/SA > OS – Cu₁Ni₁/SA > OS – Cu₁Ni₂/SA > OS – SA.

According to the fitting of the C-R model, reactions of the rapid pyrolysis stage of OS belong to the first-order reaction, with a correlation coefficient R^2 of above 0.98. Such a high value proves the reliability of this calculation model. The change of the index factor also demonstrates that Cu_mNi_n/SA might reduce the number of collisions between material particles per unit time. Table 4 shows that the catalytic effect of different samples: OS-Cu₀Ni₁/SA (25.4 kJ/mol) was stronger than OS-Cu₁Ni₀/SA (26.3 kJ/mol), that is, NiCl₂·6H₂O performed better than CuCl₂·2H₂O, but OS-Cu₂Ni₁/SA lied in the middle. However, OS-Cu₁Ni₁/SA and OS-Cu₁Ni₂/SA were relatively poor, and Cu_mNi_n/SA did not increase due to the higher loading of NiCl₂·6H₂O. Therefore the two transition metal salts supported by Cu_mNi_n/SA were complicated in the OS pyrolysis process, rather than catalyzing the OS pyrolysis reaction in their respective ranges.

3.2. Effect of Catalyst on the Output of OS Pyrolysis Products. Figure 6 shows the average yield of the main pyrolysis prod-

ucts of Fushun OS adding Cu_mNi_n/SA. The final pyrolysis temperature was steadily controlled at 520°C. Figure 6 also shows that SC was the main pyrolysis product, accounting for more than 76.1%, which corresponds to the high ash content of Fushun OS. The addition of Cu_mNi_n/SA increased the yield of SC and OS and reduced the yield of exhaust gas, because Cu_mNi_n/SA had changed the chemical constitution and physical structure in the inner of OS during the pyrolysis process. As shown in Figure 7, before the catalytic pyrolysis of OS, the surface structure is compact with only a few small pits (Figure 7(a)); after the catalytic pyrolysis, the surface structure of OS becomes obviously porous and loose (Figure 7(b)). The coke yield increased because higher pyrolysis temperature is conducive for the dissociation of the massive organic matter and their release from the shale, leaving a portion of organic matter being carbonized before separating from the shale [21, 22]. Moreover, such a reaction was enhanced owing to the presence of Cu_mNi_n/SA. Some organic matter, in the meanwhile, combined with metal elements and formed intermediate products, together with which together with coke would adhere to the inner walls of shale pores, also leading to the pore blockage and strengthening the coking reaction [23]. Considering the increase of the SO yield, OS-Cu₀Ni₁/SA and OS-Cu₂Ni₁/SA showed stronger capabilities to a higher oil yield with an increase of 3.5% and 3.1%, respectively.

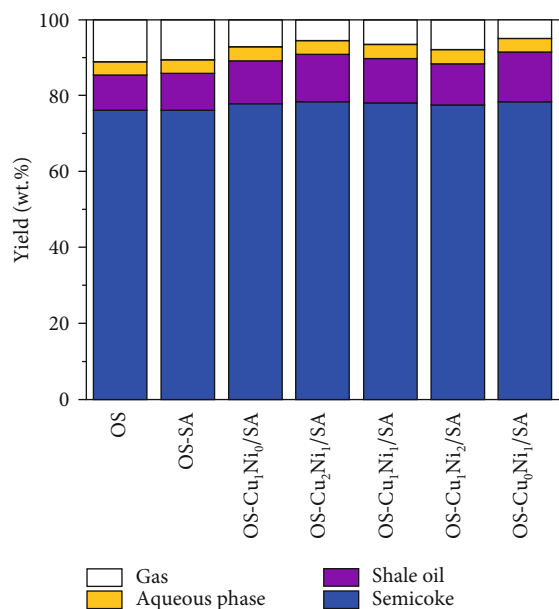


FIGURE 6: The average yield of the catalytic pyrolysis products of OS.

3.3. Component Analysis

3.3.1. Semicoke ATR-FTIR Analysis. Figure 8(a) shows the ATR-FTIR spectrum of the mixed pyrolysis product SC of OS after adding SA and Cu_mNi_n/SA, and Figure 8(b) is the spectrum with the wavenumber of 2300~3300, showing a roughly the same trend of the spectra of several samples. Inorganic minerals were mainly silicate (1022 cm⁻¹), quartz (690 cm⁻¹, 795 cm⁻¹, 777 cm⁻¹), carbonate calcite (1420 cm⁻¹), and silicate kaolinite (3669 cm⁻¹). The spectrum should have included the tensile and flexural vibrations of the aliphatic and aromatic groups of kerogen, but these vibrations overlapped with the peaks of minerals such as carbonate, quartz, and clay [15]. The most obvious absorption peaks—the characteristic absorption peaks of aliphatic hydrocarbons of organic matter—were located at 2920 cm⁻¹ and 2850 cm⁻¹ and were related to aliphatic CH bonds. Therefore, the main component of organic matter in OS was aliphatic hydrocarbons [24, 25]. After the catalytic pyrolysis of OS, the characteristic absorption peaks of the SA spectrum at 2920 cm⁻¹ and 2850 cm⁻¹ appeared obviously lower, indicating that the organic matter in the OS was separated during the pyrolysis process. As it is shown in Figure 8(b), the addition of Cu_mNi_n/SA promoted almost complete pyrolysis of organic matter in OS.

3.3.2. ATR-FTIR Analysis of Shale Oil. Figure 9 shows the ATR-FTIR spectrum of the mixed pyrolysis product SO of OS under SA and Cu_mNi_n/SA, demonstrating an overall identical trend of the spectra of different samples, the main functional groups fluctuating within the wavenumber region of 3000~2800 cm⁻¹, 1600~1000 cm⁻¹, and 900~700 cm⁻¹. The wavenumber 3000~2800 cm⁻¹ mainly corresponded to aliphatic substances and the two most obvious peaks of OS located in this range, mainly near 2920 cm⁻¹ and 2850 cm⁻¹, which corresponded to aliphatic methylene groups (CH₂)

C-H asymmetric and symmetrical vibration [12, 26, 27]. The strong peak at 1460 cm⁻¹ was due to the asymmetric bending of the CH₃ and CH₂ groups, and the peak at 1377 cm⁻¹ appeared rather weak because of the symmetric bending of CH₃, which proved the existence of aliphatics [27]. The addition of SA and Cu_mNi_n/SA may promote the formation of olefins. It is generally believed that when the wavenumber is greater than 3000 cm⁻¹, the vibration is caused by the stretching of the CH bond of ethylene or aromatic groups. The distinct shoulder peak near 3053 cm⁻¹ reveals the presence of unsaturated compounds, corresponding to the vibration of $\nu(C_{sp^2}-H)$. The characteristic absorption peak at 896 cm⁻¹ may represent the out-of-plane bending vibration of the alkene CH (R₁R₂C=CH₂) [28, 29]. In addition, there is a small characteristic peak of bending vibration at about 810 cm⁻¹ of the SO of the seven samples. Davis et al. believes that the peak at 810 cm⁻¹ is an aromatic C-H out-of-plane bending mode, proving the existence of aromatic compounds in SO [30]. The broadened peak group of 1600 cm⁻¹ may represent the aromatic ring C=C group and oxygen-containing functional group stretching vibration. Chi believes that [31], due to the oxygen-containing functional group connected to the aromatic ring, this peak group enhances the nuclear vibration of the aromatic ring. The characteristic absorption peak near 1264 cm⁻¹ may represent the tensile vibration of the aromatic ether C-O, indicating that the addition of SA and Cu_mNi_n/SA may enhance the formation of aromatic compounds [32]. The characteristic peak near 1064 cm⁻¹ may be the characteristic C-O stretching absorption peak of alcohol, phenol, and ester [33]. In addition, it can be found that there is a characteristic peak of 720 cm⁻¹ long chains in the FTIR spectrum of the single OS pyrolysis. Such a small peak was attributed to the swing vibration of the long methylene chains (-CH₂-), which indicated that there was a methylene aliphatic chains with chain lengths greater than 4 during the direct OS pyrolysis. However, after adding SA and Cu_mNi_n/SA, the peak in the FTIR spectrum of SO disappeared and appeared a characteristic peak of short-chain hydrocarbons at 740 cm⁻¹ [34], indicating that both SA and Cu_mNi_n/SA are to a certain extent capable of promoting the decomposition of long-chain hydrocarbons to short-chain hydrocarbons.

The analysis shows that the main component of SO was aliphatic hydrocarbons and a small number of aromatic hydrocarbons. The addition of SA and Cu_mNi_n/SA may not only promote the formation of aliphatic olefins and aromatic compounds in SO but also the decomposition of long-chain aliphatic hydrocarbons to short-chain aliphatic hydrocarbons. Therefore, SA and Cu_mNi_n/SA changed the composition of SO during the OS pyrolysis, providing a basis for improving the quality of SO in the actual industry.

3.3.3. GC-MS Analysis of Shale Oil. Figure 10 shows the GC-MS total ion diagram of the mixed pyrolysis product SO of OS under SA and Cu_mNi_n/SA. As shown in the figure, all chromatograms were dominated by alkanes and alkenes with carbon numbers ranging from 8 to 34. Normal alkenes and normal alkanes with the same carbon number formed a double peak of aliphatic hydrocarbons, and aliphatic

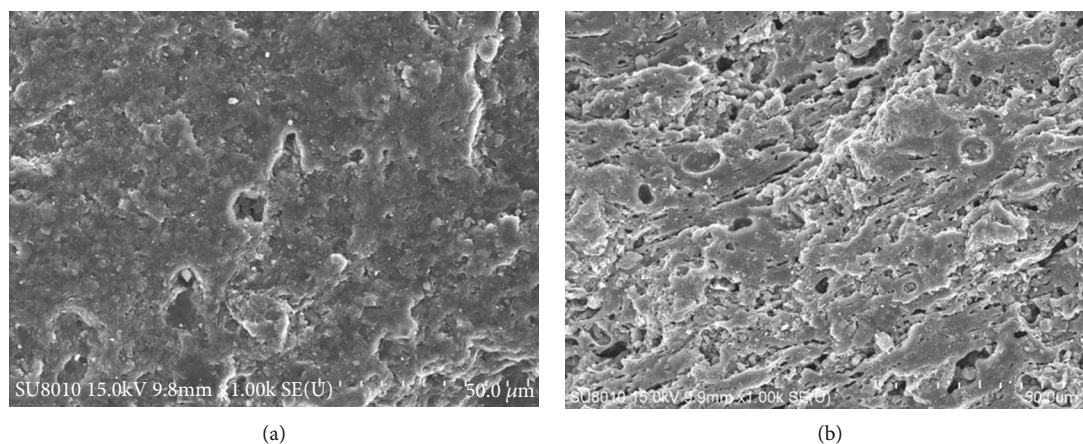


FIGURE 7: SEM image of OS. (a) Before catalytic pyrolysis. (b) After catalytic pyrolysis.

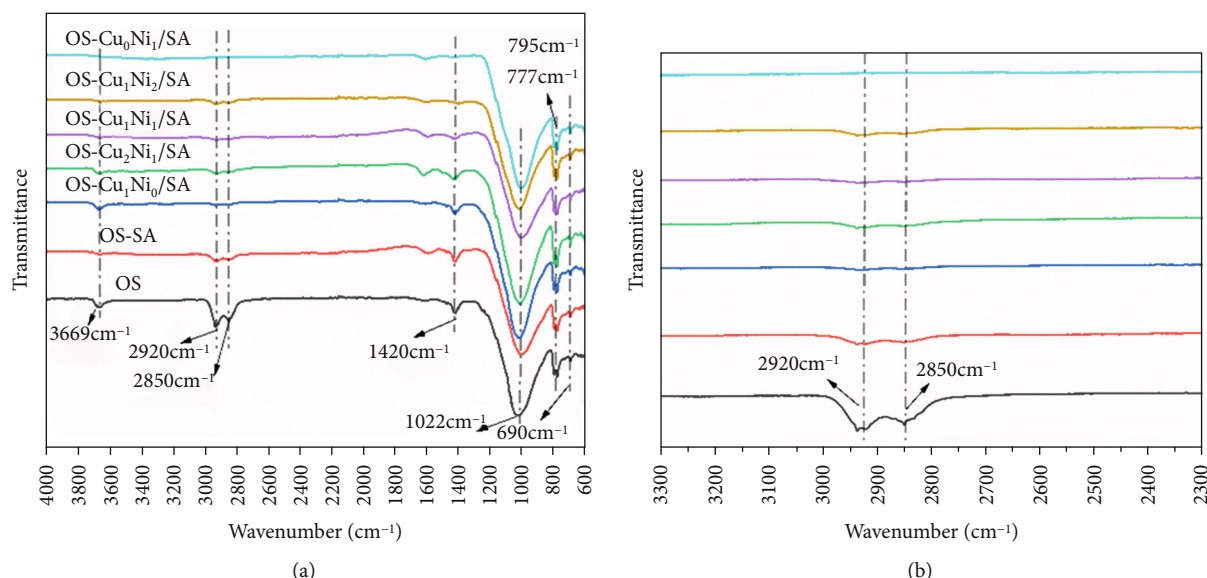


FIGURE 8: ATR-FTIR spectra of OS and pyrolytic SC.

hydrocarbons with adjacent carbon numbers were distributed with branched alkanes, branched alkenes, aromatic hydrocarbons, and oxygen-containing compounds. Oxygen-containing compounds included acids, alcohols, esters, ketones, and phenols, and aromatic hydrocarbons included naphthalene, anthracene, benzene, and benzene series. The relative abundances of *n*-paraffins and *n*-alkenes first increased and then decreased as the carbon number increased and reached the maximum at $C_{16}\sim C_{18}$. These results were of high correspondence to the previous researchers' experimental results [14, 35].

In order to estimate the influence of Cu_mNi_n/SA on SO composition, the relative content of the main components was given by the ion peak area of GC-MS. Figure 11(a) shows the content of the four main components in the pyrolysis product SO. With the change of the Cu-Ni metal salt mixing ratio, the content of each component in SO was slightly different, among which alkanes ranked the most. As the main component of SO, aliphatic compounds played an important

role in improving the quality and quantity of SO. The content of alkanes and olefins in aliphatic hydrocarbons accounted for more than 90% of the relative content of the main components. The addition of SA and Cu_mNi_n/SA reduced the content of alkanes and increased the content of olefins. Among them, the content of alkane in OS- Cu_1Ni_1/SA decreased the most, followed by OS- Cu_0Ni_1/SA ; the content of olefin in OS- Cu_0Ni_1/SA increased the most, followed by OS- Cu_2Ni_1/SA , possibly because the secondary cracking reaction of SO led to a large number of normal types of paraffin to be transferred to cycloalkanes and alkenes. While the existence of Cu_mNi_n/SA strengthened such reaction to a certain extent [36]. Figure 11(b) shows the olefin/alkane ratio. Ballice [37] applies the olefin/alkane ratio to evaluate the cracking reaction of aliphatic hydrocarbons. In his research, it has been shown that the cracking reaction proceeded through a free radical mechanism so that smaller linear alkanes and alkenes were obtained, increasing the alkene/alkane ratio. Therefore, SA and Cu_mNi_n/SA in this study can catalyze the cracking of

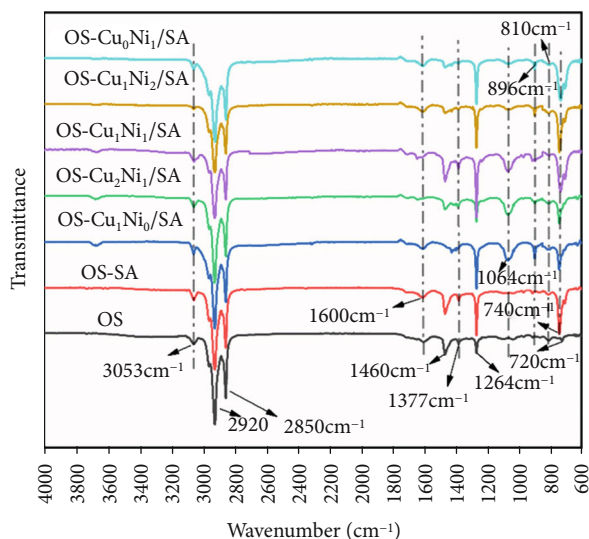


FIGURE 9: ATR-FTIR of mixed pyrolysis product SO of OS under SA and $\text{Cu}_m\text{Ni}_n/\text{SA}$.

aliphatic hydrocarbons. The changes in the OS- $\text{Cu}_0\text{Ni}_1/\text{SA}$ and OS- $\text{Cu}_2\text{Ni}_1/\text{SA}$ samples are more obvious, indicating when Cu and Ni transition metal salt loading mass ratio is 0:1 and 2:1; it has a strong catalytic effect, which is consistent to thermodynamics results.

In addition, as shown in Figure 11(a), the content of aromatic hydrocarbons was affected by the following sequence: OS-SA > OS- $\text{Cu}_1\text{Ni}_2/\text{SA}$ > OS- $\text{Cu}_0\text{Ni}_1/\text{SA}$ > OS- $\text{Cu}_1\text{Ni}_0/\text{SA}$ > OS- $\text{Cu}_1\text{Ni}_1/\text{SA}$ > OS- $\text{Cu}_2\text{Ni}_1/\text{SA}$ > OS, indicating that the presence of SA and $\text{Cu}_m\text{Ni}_n/\text{SA}$ may catalyze the aromatization of aliphatic hydrocarbons to a certain extent and thus produce more aromatic hydrocarbons. The OS-SA samples produced the most aromatic hydrocarbons, which may be because the oil stayed so long time in the pores or on the surface of the OS and SA particles that the subsequent secondary cracking reaction was promoted. Burnham [38] believes that SO cracking occurs through two processes: the coking of hydrogen-depleted materials and the cracking of aliphatic splitting into gases. The reasons for the formation of aromatic hydrocarbons through secondary reactions may include gas-phase cracking of aliphatic compounds or through Diels-Alder type reaction [38–41]. The addition of $\text{Cu}_m\text{Ni}_n/\text{SA}$ may promote the formation of aromatic hydrocarbons to a certain extent because of the abovementioned secondary reactions on the one hand and the low molecular weight (LMW) alkanes and alkenes produced by the cracking of large aliphatic hydrocarbons on the other. The catalysis of strong acidic sites of metal salt cyclized LMW olefins and dienes to form cycloalkenes, and cycloalkanes were dehydrogenated to produce aromatics [39]. However, the sample with $\text{Cu}_m\text{Ni}_n/\text{SA}$ added in this study produced less aromatic hydrocarbons than the sample with SA only. This may be due to the coking reaction of hydrogen-depleted substances during the diffusion in the pyrolysis furnace with the increase of temperature made aromatic hydrocarbon tend to coke before volatilization, forming solid prod-

ucts or coke [42–44]. The presence of $\text{Cu}_m\text{Ni}_n/\text{SA}$ significantly increased the probabilities of the above coking reaction, leading to a reduction of the relative content of aromatic hydrocarbons [14, 45, 46]. The presence of aromatic hydrocarbons weakened the stability of SO and is of toxicity in use [38, 47]. Therefore, based on the stability of SO and safety in use, the order of preference is ranked as OS- $\text{Cu}_2\text{Ni}_1/\text{SA}$ > OS- $\text{Cu}_1\text{Ni}_1/\text{SA}$ > OS- $\text{Cu}_1\text{Ni}_0/\text{SA}$ > OS- $\text{Cu}_0\text{Ni}_1/\text{SA}$ > OS- $\text{Cu}_1\text{Ni}_2/\text{SA}$ > OS-SA. In addition, the presence of SA and $\text{Cu}_m\text{Ni}_n/\text{SA}$ promoted the formation of not only aromatic compounds but also oxygen-containing compounds, with OS- $\text{Cu}_1\text{Ni}_1/\text{SA}$ containing the most oxygen-containing compounds.

According to the GC-MS analysis of SO, *n*-paraffins and *n*-alkenes are the main components in SO samples, which can be further divided into the following categories according to the number of carbon atoms: $\text{C}_8\sim\text{C}_{15}$, $\text{C}_{16}\sim\text{C}_{24}$, and $\text{C}_{25}\sim\text{C}_{34}$. The content of these components based on peak area was normalized to 100%. Figure 12 shows the relative peak areas of different samples at different carbon numbers. The figure shows that the addition of SA and $\text{Cu}_m\text{Ni}_n/\text{SA}$ decreased the content of $\text{C}_{25}\sim\text{C}_{34}$ heavy alkanes and olefins and increased the content of $\text{C}_8\sim\text{C}_{15}$ and $\text{C}_{16}\sim\text{C}_{24}$ light hydrocarbons. This result indicates that SA and $\text{Cu}_m\text{Ni}_n/\text{SA}$ can promote the decomposition tendency of heavy oil fractions to light oil, possibly because the cracking reaction of gas-phase oil is promoted after the SA and SA load transition metal salts so that long-chain aliphatic compounds are converted into short-chain hydrocarbons. In this process, long-chain normal types of paraffin were cracked and formed short-chain alkanes, alkenes, and cycloalkanes, resulting in increasing the content of shorter-chain hydrocarbons. This also firmly proves the $\text{Cu}_m\text{Ni}_n/\text{SA}$ catalyzes aliphatic pyrolysis, which is consistent with the results of ATR-FTIR analysis [36]. In addition, compared with the addition of SA pyrolysis, the content of aliphatic hydrocarbons in the sample with $\text{Cu}_m\text{Ni}_n/\text{SA}$ changed significantly, indicating the strong catalytic activity of SA after being loaded with Cu-Ni double transition metal salt. Therefore, $\text{Cu}_m\text{Ni}_n/\text{SA}$ can significantly affect the composition of SO. Among them, the contents of *n*-paraffins and *n*-alkenes in OS- $\text{Cu}_2\text{Ni}_1/\text{SA}$ and OS- $\text{Cu}_0\text{Ni}_1/\text{SA}$ samples changed the most, that is, the catalytic effect performed better when the Cu-Ni loading mass ratio was 2:1 and 0:1.

4. Conclusion

After analyzing the pyrolysis characteristics of OS containing a different ratio of Cu to Ni with TG-MS technology method then pyrolysis product SO under methods including FTIR and GC-MS, the conclusions are presented as follows:

- (1) The effects of SA and $\text{Cu}_m\text{Ni}_n/\text{SA}$ on the pyrolysis characteristics of Fushun OS were investigated by thermogravimetry. It is found that the addition of SA and $\text{Cu}_m\text{Ni}_n/\text{SA}$ has different effects on the pyrolysis behavior of OS. The total mass loss rate is ranked as OS < OS-SA < OS- $\text{Cu}_m\text{Ni}_n/\text{SA}$; the existence of

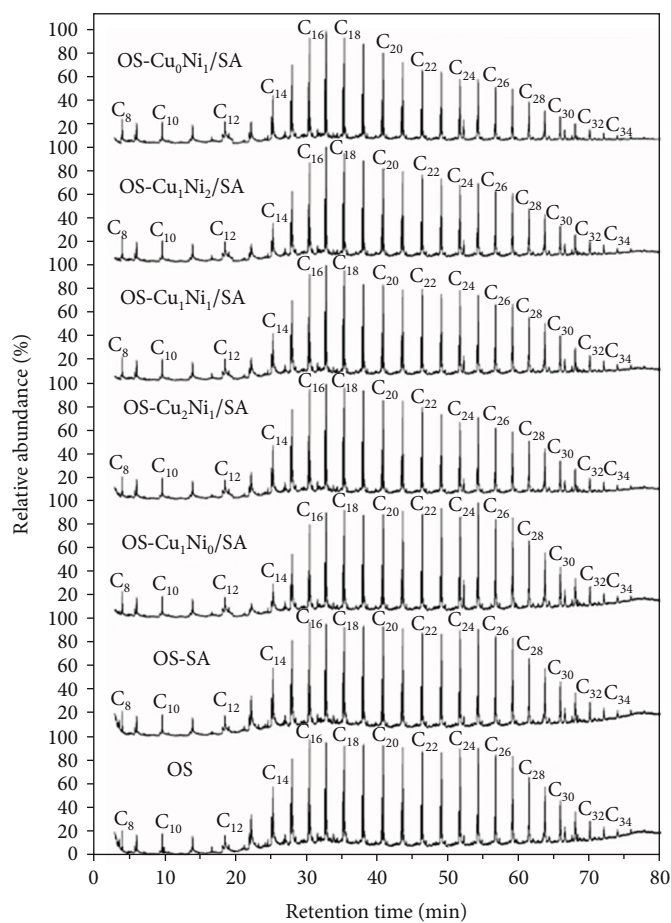
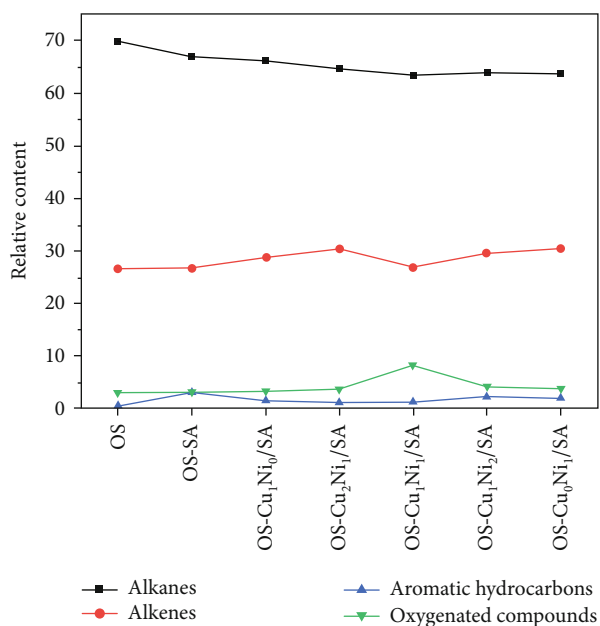
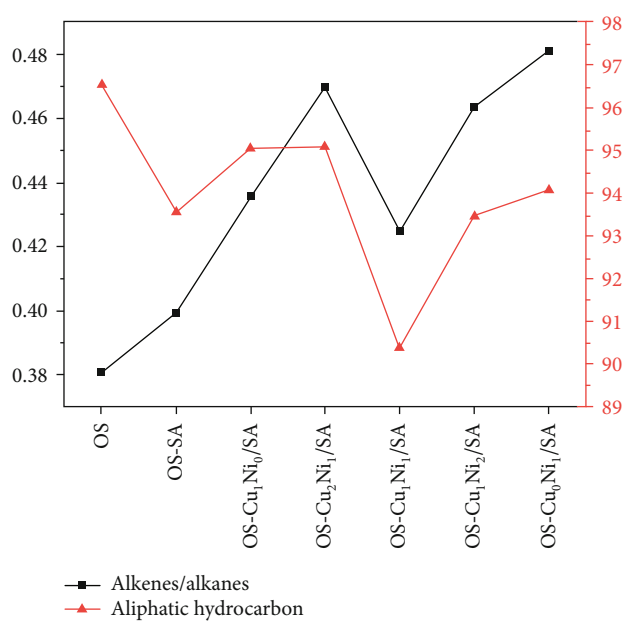


FIGURE 10: GC-MS total ion diagram of mixed pyrolysis product SO of OS under SA and $\text{Cu}_m\text{Ni}_n/\text{SA}$.



(a)



(b)

FIGURE 11: Information on four main components in SO of pyrolysis product. (a) Relative content. (b) Ratio of olefins to alkanes, aliphatic hydrocarbon content.

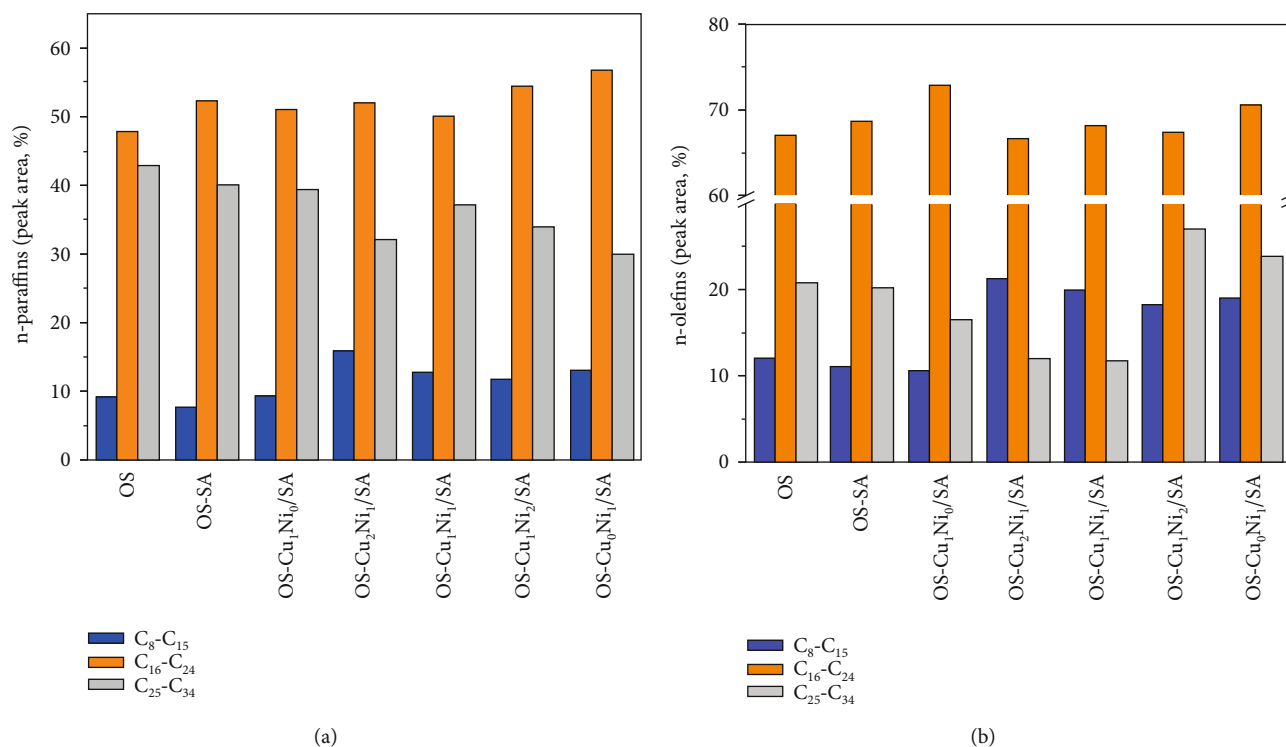


FIGURE 12: Distribution of *n*-paraffins and *n*-olefins in SO: (a) *n*-paraffins, (b) *n*-olefins.

SA and Cu_mNi_n/SA reduces the initial OS Pyrolysis temperature, termination temperature, maximum weight loss rate, and its corresponding temperature (T_{max}). Cu_mNi_n/SA falls further, and the apparent activation energy, combined with kinetic analysis, is ranked as OS > OS - SA > OS - Cu_mNi_n/SA, indicating that the existence of SA promotes the pyrolysis of OS to a certain extent, but the catalytic effect is weaker to that of Cu_mNi_n/SA. OS-Cu₀Ni₁/SA, OS-Cu₂Ni₁/SA, and OS-Cu₁Ni₁/SA in Cu_mNi_n/SA strengthened the catalytic effects, and T_{max} decreased by 12.9°C, 4.0°C, and 3.6°C, respectively, and apparent activation energy decreased by 35.2%, 33.9%, and 29.6%. It was also found that the two transition metal salts supported by Cu_mNi_n may have a complicated effect during the OS pyrolysis process, rather than catalyzing the OS pyrolysis reaction in their respective ranges

- (2) The products of SA-, Cu_mNi_n/SA-, and OS-mixed pyrolysis were analyzed by the pyrolysis device. It is found that the main product of OS pyrolysis is SC, accounting for more than 76.1%; the addition of Cu_mNi_n/SA promotes the coking reaction of OS pyrolysis, leading to an increase in the yield of SC. The existence of Cu_mNi_n/SA also increases the yield of SO and reduces the emissions yield. Among them, OS-Cu₀Ni₁/SA and OS-Cu₂Ni₁/SA further increase the SO yield by 3.5% and 3.1%, respectively
- (3) The analysis of pyrolysis products SC and SO with the FTIR method shows that the inorganic minerals

in SC are mainly composed of silicate, quartz, carbonate calcite, etc.; the main component of organic matter in SO is aliphatic hydrocarbons, a small number of aromatic hydrocarbons, and oxygen-containing compounds as well. The existence of SA and Cu_mNi_n/SA promotes OS pyrolysis secondary cracking, aromatization, and other relevant reactions, forming olefins and aromatic compounds in SO and promoting the decomposition of long-chain aliphatic hydrocarbons to short-chain aliphatic hydrocarbons

- (4) The effects of SA and Cu_mNi_n/SA on different components of SO were further studied by GC-MS. SO is complex and diverse in its composition, mainly dominated by alkanes and alkenes with carbon atoms of 8 to 34; alkanes, alkenes, oxygenates, and aromatics are the main components in SO, with alkanes and alkenes being the majority, accounting for more than 90% of its relative content. The addition of SA and Cu_mNi_n/SA reduces the content of alkanes and increases that of olefins. Among them, the content of alkane in OS-Cu₁Ni₁/SA decreases the most, followed by OS-Cu₀Ni₁/SA. The content of olefin in OS-Cu₀Ni₁/SA increases the most, followed by OS-Cu₂Ni₁/SA. The presence of SA and Cu_mNi_n/SA may also catalyze the aromatization of aliphatic hydrocarbons to a certain extent, increasing the production of aromatic hydrocarbons. The presence of Cu_mNi_n/SA may catalyze aromatization, but at the same time, it also aggravates the coking reaction of hydrogen-poor substances, resulting in Cu_mNi_n/SA

catalytic pyrolysis producing less aromatic hydrocarbons than SA. The aromatic hydrocarbon content is ranked as follows: OS – SA > OS – Cu₁Ni₂/SA > OS – Cu₀Ni₁/SA > OS – Cu₁Ni₀/SA > OS – Cu₁Ni₁/SA > OS – Cu₂Ni₁/SA > OS. In addition, the presence of SA and Cu_mNi_n/SA also promotes the formation of oxygen-containing compounds, and OS-Cu₁Ni₁/SA has the largest content of oxygen compounds

- (5) OS-Cu₀Ni₁/SA and OS-Cu₂Ni₁/SA promote catalysis and effectively increase the SO yield. However, OS-Cu₀Ni₁/SA produces more aromatic hydrocarbons, which weakens the stability of SO and is of toxicity in use

Considering comprehensively the catalytic effect, SO yield, and SO stability, this paper suggests that the Cu-Ni/shale ash-based dual transition metal catalyst Cu-Ni loading ratio preferably be 2:1.

Data Availability

All the data used to support the findings of this study are included within the article.

Conflicts of Interest

The authors declare that they have no conflicts of interest.

References

- [1] N. P. Fossil, *World Energy Outlook 2010*, International Energy Agency, 2014.
- [2] J. L. Hou, Y. Ma, S. Y. Li, and J. S. Teng, "Development and utilization of oil shale resources in the world," *Chemical Progress*, vol. 34, no. 5, pp. 1183–1190, 2015.
- [3] Z. J. Liu, Q. S. Dong, S. Q. Ye et al., "Current situation of oil shale resources in China," *Qinghai Oil*, vol. 36, no. 3, pp. 869–876, 2010.
- [4] H. M. Li, "Current situation and trend of exploitation and utilization of oil shale resources," *Journal of Chengde Petroleum College*, vol. 13, no. 4, pp. 27–29, 2011.
- [5] L. L. Yang, M. H. Chen, J. L. Wang et al., "Microstructure and composition evolution of a single-crystal superalloy caused by elements interdiffusion with an overlay NiCrAlY coating on oxidation," *Journal of Materials Science & Technology*, vol. 45, pp. 49–58, 2020.
- [6] S. Deng, Z. Wang, Q. Gu, F. Meng, J. Li, and H. Wang, "Extracting hydrocarbons from Huadian oil shale by sub-critical water," *Fuel Processing Technology*, vol. 92, no. 5, pp. 1062–1067, 2011.
- [7] R. Gai, L. Jin, J. Zhang, J. Wang, and H. Hu, "Effect of inherent and additional pyrite on the pyrolysis behavior of oil shale," *Journal of Analytical & Applied Pyrolysis*, vol. 105, no. 5, pp. 342–347, 2013.
- [8] Z. D. Cao, "The invention relates to a catalyst and a method for producing light fuel oil," 2005, CN, CN 1644653 A.
- [9] P. T. Williams and H. M. Chishti, "Influence of residence time and catalyst regeneration on the pyrolysis-zeolite catalysis of oil shale," *Journal of Analytical & Applied Pyrolysis*, vol. 60, no. 2, pp. 187–203, 2001.
- [10] P. T. Williams and N. Ahmad, "Influence of process conditions on the pyrolysis of Pakistani oil shales," *Fuel*, vol. 78, no. 6, pp. 653–662, 1999.
- [11] Q. Wang, H. Wu, C. X. Jia, J. X. Shi, and Y. Sui, "Effects of different alkali metal carbonates on oil shale pyrolysis," *Chemical Machinery*, vol. 42, no. 3, pp. 333–340, 2015.
- [12] H. Jiang, L. Song, Z. Cheng et al., "Influence of pyrolysis condition and transition metal salt on the product yield and characterization via Huadian oil shale pyrolysis," *Journal of Analytical and Applied Pyrolysis*, vol. 112, pp. 230–236, 2015.
- [13] D. A. Pulushev and J. R. H. Rossa, "Catalysis for conversion of biomass to fuels via pyrolysis and gasification: a review," *Catalysis Today*, vol. 171, no. 1, pp. 1–13, 2011.
- [14] Z. B. Chang, M. Chu, C. Zhang, S. X. Bai, H. Lin, and L. B. Ma, "Investigation of the effect of selected transition metal salts on the pyrolysis of Huadian oil shale, China," *Oil Shale*, vol. 34, no. 4, pp. 354–367, 2017.
- [15] Y. Sun, F. Bai, B. Liu et al., "Characterization of the oil shale products derived via topochemical reaction method," *Fuel*, vol. 115, pp. 338–346, 2014.
- [16] X. M. Jiang, X. X. Han, and Z. G. Cui, "Mechanism and mathematical model of Huadian oil shale pyrolysis," *Journal of Thermal Analysis & Calorimetry*, vol. 86, no. 2, pp. 457–462, 2006.
- [17] J. G. Na, C. H. Im, S. H. Chung, and K. B. Lee, "Effect of oil shale retorting temperature on shale oil yield and properties," *Fuel*, vol. 95, no. 2, pp. 131–135, 2012.
- [18] P. T. Williams and N. Ahmad, "Investigation of oil-shale pyrolysis processing conditions using thermogravimetric analysis," *Applied Energy*, vol. 66, no. 2, pp. 113–133, 2000.
- [19] F. Bai, Y. Sun, Y. Liu et al., "Kinetic investigation on partially oxidized huadian oil shale by thermogravimetric analysis," *Oil Shale*, vol. 31, no. 4, p. 377, 2014.
- [20] A. Marini, V. Berbenni, and G. Fot, "Kinetic parameters from thermogravimetric data," *Zeitschrift Für Naturforschung A*, vol. 34, no. 5, pp. 661–663, 1979.
- [21] N. V. Dung, "Yields and chemical characteristics of products from fluidized bed steam retorting of Condor and Stuart oil shales: effect of pyrolysis temperature," *Fuel*, vol. 69, no. 3, pp. 368–376, 1990.
- [22] P. R. Solomon, R. M. Carangelo, and E. Horn, "The effects of pyrolysis conditions on Israeli oil shale properties," *Fuel*, vol. 65, no. 5, pp. 650–662, 1986.
- [23] X. Han, X. Jiang, J. Yan, and J. Liu, "Effects of retorting factors on combustion properties of shale char. 2. Pore structure," *Energy & Fuels*, vol. 25, no. 1, pp. 97–102, 2011.
- [24] T. Mongenot, S. Derenne, C. Largeau et al., "Spectroscopic, kinetic and pyrolytic studies of kerogen from the dark parallel laminae facies of the sulphur-rich Orbagnoux deposit (Upper Kimmeridgian, Jura)," *Organic Geochemistry*, vol. 30, no. 1, pp. 39–56, 1999.
- [25] W. T. Shiraishi, M. Sasaki, and M. Goto, "Non-catalytic liquefaction of bitumen with hydrothermal/solvothermal process," *Supercritical Fluids*, vol. 60, pp. 127–136, 2011.
- [26] Q. Wang, Y. Hou, W. Wu et al., "A study on the structure of Yilan oil shale kerogen based on its alkali-oxygen oxidation yields of benzene carboxylic acids, 13 C NMR and XPS," *Fuel Processing Technology*, vol. 166, no. 3, pp. 30–40, 2017.
- [27] J. Tong, X. Han, S. Wang, and X. Jiang, "Evaluation of structural characteristics of Huadian oil shale kerogen using direct

- techniques (Solid-State¹³C NMR, XPS, FT-IR, and XRD)," *Energy & Fuels*, vol. 25, no. 9, pp. 4006–4013, 2011.
- [28] N. Ana, T. Sébastien, and B. Gary, "The oil shale transformation in the presence of an acidic BEA zeolite under microwave irradiation," *Energy & Fuels*, vol. 28, no. 4, pp. 2365–2377, 2014.
- [29] A. Aboulkas, T. Makayssi, L. Bilali, K. El Harfi, M. Nadifiyine, and M. Benchanaa, "Co-pyrolysis of oil shale and high density polyethylene: structural characterization of the oil," *Fuel Processing Technology*, vol. 2012, no. 96, pp. 203–208, 2012.
- [30] P. C. Painter, R. W. Snyder, M. Starsinic, M. M. Coleman, D. W. Kuehn, and A. Davis, "Concerning the application of FT-IR to the study of coal: a critical assessment of band assignments and the application of spectral analysis programs," *Applied Spectroscopy*, vol. 35, no. 5, pp. 475–485, 2016.
- [31] M. Chi, X. Xu, D. Cui, H. Zhang, and Q. Wang, "A TG-FTIR investigation and kinetic analysis of oil shale kerogen pyrolysis using the distributed activation energy model," *Oil Shale*, vol. 33, no. 3, pp. 228–247, 2016.
- [32] Q. Wang, J. B. Ye, H. Y. Yang, and Q. Liu, "Chemical composition and structural characteristics of oil shales and their kerogens using Fourier transform infrared (FTIR) spectroscopy and Solid-State¹³C nuclear magnetic resonance (NMR)," *Energy & Fuels*, vol. 30, no. 8, pp. 6271–6280, 2016.
- [33] M. Kılıç, A. E. Pütün, B. B. Uzun, and E. Pütün, "Converting of oil shale and biomass into liquid hydrocarbons via pyrolysis," *Energy Conversion & Management*, vol. 78, pp. 461–467, 2014.
- [34] Q. Wang, X. C. Xu, M. S. Chi, H. X. Zhang, D. Cui, and J. R. Bo, "FTIR study on the composition of oil shale kerogen and its pyrolysis oil generation characteristics," *Journal of Fuel Chemistry & Technology*, vol. 9, no. 9, pp. 111–126, 2015.
- [35] L. Lin, C. Zhang, H. Li, D. Lai, and G. Xu, "Pyrolysis in indirectly heated fixed bed with internals: the first application to oil shale," *Fuel Processing Technology*, vol. 138, no. 138, pp. 147–155, 2015.
- [36] Y. R. Huang, X. X. Han, and X. M. Jian, "Comparison of fast pyrolysis characteristics of Huadian oil shales from different mines using Curie-point pyrolysis-GC/MS," *Fuel Processing Technology*, vol. 128, pp. 456–460, 2014.
- [37] L. Ballice, "Effect of demineralization on yield and composition of the volatile products evolved from temperature-programmed pyrolysis of Beypazari (Turkey) Oil Shale," *Fuel Processing Technology*, vol. 86, no. 6, pp. 673–690, 2005.
- [38] A. K. Burnham, "Chemistry of shale oil cracking," in *ACS Symposium*, vol. 2, no. 9pp. 39–60, American Chemical Society, 1980.
- [39] J. M. Nazzal, "Influence of heating rate on the pyrolysis of Jordan oil shale," *Journal of Analytical & Applied Pyrolysis*, vol. 62, no. 2, pp. 225–238, 2002.
- [40] R. Cypres, "Aromatic hydrocarbons formation during coal pyrolysis," *Fuel Processing Technology*, vol. 15, pp. 1–15, 1987.
- [41] D. Depeyre, C. Flicoteaux, and C. Chardaire, "Pure n-hexadecane thermal steam cracking," *Industrial & Engineering Chemistry Process Design and Development*, vol. 24, no. 4, pp. 1251–1258, 1985.
- [42] Z. J. Liu and R. Liu, "Analysis of the characteristics, development, and utilization prospects of oil shale in China," *Geoscience Frontiers*, vol. 12, no. 3, pp. 315–323, 2005.
- [43] Advanced Resources International, *EIA/ARI World Shale Gas and Shale Oil Resource Assessment*. Arlington, U.S. Energy Information Administration, Arlington, 2015.
- [44] D. Brown, *IEA's World Energy Outlook 2013: Renewables and Natural Gas to Surge through 2035*, Power, 2014.
- [45] D. Lai, Y. Shi, S. Geng et al., "Secondary reactions in oil shale pyrolysis by solid heat carrier in a moving bed with internals," *Fuel*, vol. 173, pp. 138–145, 2016.
- [46] Y. R. Huang, C. Fan, X. X. Han, and X. Jiang, "A TGA-MS investigation of the effect of heating rate and mineral matrix on the pyrolysis of kerogen in oil shale," *Oil Shale*, vol. 33, no. 2, pp. 125–141, 2016.
- [47] M. Niu, S. Wang, X. Han, and X. Jiang, "Yield and characteristics of shale oil from the retorting of oil shale and fine oil-shale ash mixtures," *Applied Energy*, vol. 111, pp. 234–239, 2013.

Research Article

Effect of Iron Ion on Corrosion Behavior of Inconel 625 in High-Temperature Water

Huiling Zhou¹, Yipeng Chen¹, Yi Sui^{1,2}, Yunfei Lv³, Zhiyuan Zhu¹, Lanlan Yang¹, Zhen He¹, Chengtao Li⁴, and Kewei Fang⁴

¹School of Materials Science and Engineering, Jiangsu University of Science and Technology, Zhenjiang 212003, China

²A. O. Smith (China) Water Heater Co., Ltd., Nanjing 210038, China

³Chengde Petroleum College, Chengde 067000, China

⁴Suzhou Nuclear Power Research Institute, Suzhou 215004, China

Correspondence should be addressed to Huiling Zhou; zhouhl@just.edu.cn, Yunfei Lv; lvyunfei999@sina.com, and Zhiyuan Zhu; salanganazhu@163.com

Received 3 June 2020; Accepted 18 August 2020; Published 22 October 2020

Guest Editor: R. Matthew Asmussen

Copyright © 2020 Huiling Zhou et al. This is an open access article distributed under the Creative Commons Attribution License, which permits unrestricted use, distribution, and reproduction in any medium, provided the original work is properly cited.

The corrosion behavior of an ultralow iron nickel-based alloy Inconel 625 under high-temperature water has been evaluated. The results show that surface oxidation and pitting were the principal corrosion mechanisms of Inconel 625 during the initial immersion period. The surface layer of the oxide film is first Ni-enriched and then Fe-enriched as immersion time increases. The iron ions dissolved from the autoclave could lead to the formation of NiFe_2O_4 and have a great influence on the oxidation behavior of Inconel 625. The oxides nucleated by solid-state reactions with selective dissolution of Fe and Ni and then grew up through precipitation of cations from solution.

1. Introduction

The structure and composition of oxide film formed in primary water of pressurized water reactors (PWR) play a significant role in the degradation processes of material, which have been a special topic for decades [1–4]. Therefore, the oxidation behaviors of materials in PWR as well as the characteristics of the oxide film have always been the focus of attention [5]. It had been reported that the properties of the oxide films are closely related to the corrosion resistance [6–10]. The corrosion behaviors of nickel-based alloys in high-temperature water have been extensively studied [1, 7, 11–16]. The oxide film developed on nickel-based alloys generally presents a multilayer structure with Ni/Fe-rich outer layer and a chromium-rich inner layer [14, 17–19]. The structure and the chemical compositions of the oxide film are closely related to the corrosion properties of nickel-based alloys [20–22]. A couple of materials and environment relevant factors, including chemical composition, microstructure, and thickness, influence the oxide film characteris-

tics [2, 19, 23–25]. The effect of water chemistry is also a key factor that determines the characteristic of the oxide film [10, 12, 19, 23, 26], part from the microstructure and chemical compositions of the materials.

In addition to the oxidation, pitting corrosion has been frequently observed on the nickel-based alloys such as Alloy 625 and Alloy 718 [2]. The dissolved ions in high-temperature water are usually related to the oxidation process [27–29]. Kritzer et al. investigated the corrosion behavior of Alloy 625 in high-temperature and high-pressure sulfate solutions and found that the metal ion concentrations keep increasing at the beginning of the experiment [1]. Kuang et al. [30] investigated the effect of Ni^{2+} from autoclave material on 304 SS in oxygenated high-temperature water and found the dissolved Ni^{2+} promotes the stability of NiFe_2O_4 . Behnamian et al. [31] investigated the oxidation behavior of nickel-based alloys in high-temperature water and observed that the alloys containing Mo, Nb, and Ti were susceptible to pitting. Yang et al. [32] investigated the corrosion behavior of nickel-based alloys in temperature water

TABLE 1: Chemical composition of the tested Inconel 625 (wt%).

C	Cr	Mo	Co	Nb	Fe	Al	Ti	Si	P	S	Ni
0.05	22.4	9.5	0.03	3.66	0.01	0.24	0.23	0.04	0.002	0.001	Bal.

with 6000 ppm NH_4Cl . They found that the oxide film is Fe-enriched oxide deposits, which were mainly resulted from the dissolving of Fe in the autoclave. So it is of great significance to investigate the effect of exotic metallic ions on the oxidation behavior of materials in high-temperature water.

The aim of this work is to clarify the effect of the dissolved iron ion from a 304L SS autoclave on the corrosion behavior of Inconel 625 in high-temperature water. The effects of iron ion on the corrosion behaviors of Inconel 625 were investigated by optical microscopy (OM), scanning electron microscopy (SEM), X-ray diffraction (XRD), and Raman spectra measurements. At the end, the corrosion mechanism is explained briefly.

2. Experimental

The material used in this work is an ultralow iron Inconel 625, the composition of which is listed in Table 1. The microstructure of Inconel 625 has been detailed addressed in literature [33], as is shown in Figure 1. The as-received material was cut into pieces of 30 mm \times 20 mm \times 3 mm. The samples were mechanically polished to 1000# SiC paper, washed by ultrasound with acetone, and dried with hot air. The weight change of samples was obtained using an electric balance (XS105DU) with an accuracy of 0.1 mg. A corrosion test was conducted in a 2.5 L volume autoclave which is made of 304 L stainless steel (SS). The temperature was controlled at 345°C, under a pressure of 15.5 MPa. The samples were immersed in the autoclave for 100 h, 300 h, 500 h, 700 h, 1000 h, and 1500 h, respectively. In order to ensure the accuracy of the experiment, five parallel samples were adopted.

A scanning electron microscope (XL30-FEG ESEM, FEI, Hillsboro, OR, USA) was applied to observe the morphology evolution of the oxide film. Before SEM observation, the sample surface was coated with a thin Ni layer to avoid the sputtering during sample preparation [34]. Phase constituents were identified by an X-ray diffractometer (XRD, Rigaku Corporation, Tokyo, Japan) with $\text{Cu-K}\alpha$ radiation with a wavelength of 1.5 Å at 40 kV. The scan range was 20°–90° with a scan rate of 0.1°/s. A laser Raman spectrometer (Renishaw Micro-Raman, UK) with an excitation source of 532 nm wavelength incident laser was applied to identify the oxide composition in the oxide film.

3. Results and Discussion

3.1. Characteristics of Weight Gain. The result of the weight change with time of Inconel 625 samples in high-temperature water is plotted in Figure 2. The weight gain was negative after immersion in the tested solution for 100 h. The mass loss is $5.09 \times 10^{-4} \text{ mg}\cdot\text{cm}^{-2}$ and this may

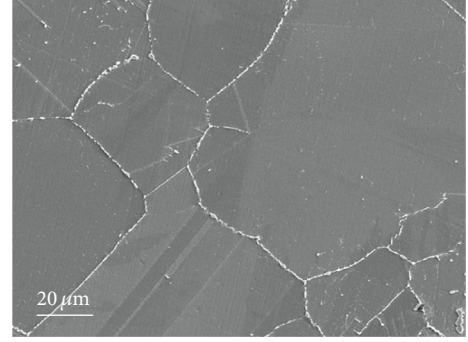


FIGURE 1: Microstructure of ultralow iron Inconel 625.

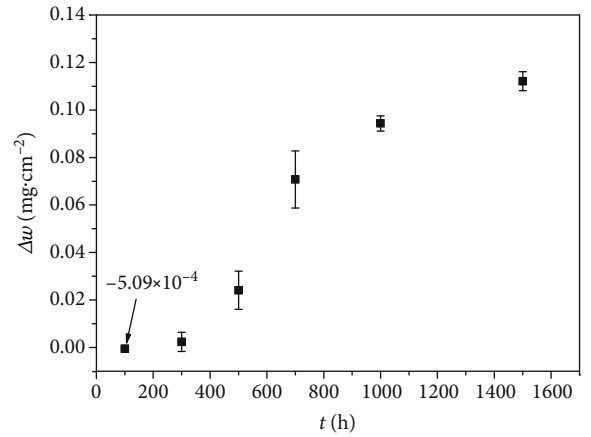


FIGURE 2: Mass gain of Inconel 625 in high-temperature water.

be due to the simultaneous effects of oxidation and material loss due to pitting [17]. In high-temperature water, the fluctuations of the weight change of the Ni-based alloys could be attributed to the pitting corrosion [2, 35]. A detailed explanation of this phenomenon would be conducted by the surface morphology observation later. However, with the exposure time extending, weight gain increased rapidly when the immersion time was longer than 300 h.

After exposing to high-temperature water for different periods, the oxide products formed on Inconel 625 is detected by XRD, as shown in Figure 3. After 300 h immersion, the samples were only slightly oxidized and the characteristic peaks of oxide could be barely discernable. Then, as the immersion time prolonged, the signals of the base alloy tended to weaken, while those for NiCr_2O_4 , NiFe_2O_4 , and NiO gradually dominated.

The surface morphologies of Inconel 625 after exposing for different periods in high-temperature water are shown in Figure 4. The chemical compositions of the oxide film and oxide particles were characterized using EDS at spots

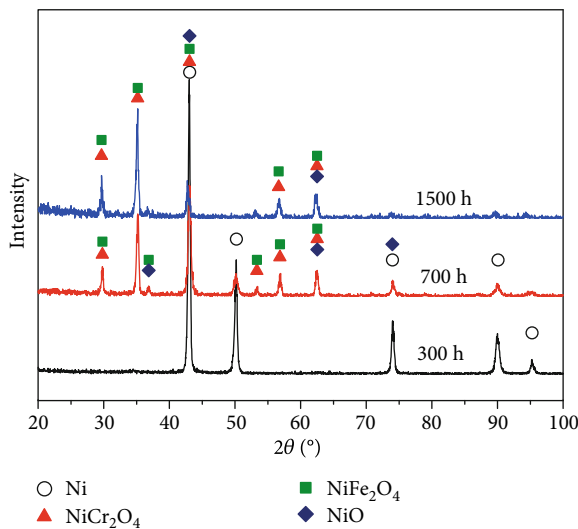


FIGURE 3: The XRD patterns of oxidation film formed on Inconel 625.

1–6 and are listed in Table 2. After immersion under high-temperature water for 100 h, a layer of needle-like oxide and polygonal particle oxide formed on the surface of sample, as shown in Figures 4(a) and 4(a1). As the diffusion rates of typical metal ions followed the order of $\text{Ni} > \text{Cr}$ in Ni-based alloys [12], Ni ions were first detected on the sample surface, which dissolved and precipitated as oxides or hydroxides. The phenomenon is similar to the study of Zhu et al. [15]. From the EDS analysis, it was deduced that these large particles were NiCr_2O_4 . The consideration was also consistent with the finding of Ziemniak and Hanson [16], who reported that the initial oxidation of Inconel 625 in high-temperature water would create NiO and $\text{Ni}(\text{Cr,Fe})_2\text{O}_4$.

After immersion in high-temperature water for 500 h, a layer of dense needle-like oxide film appeared, which has been generally observed in Ni-based alloys in PWR water [15, 20, 36]. As displayed in Figure 2(b1), a decrease in density and thickness of needle-like oxide was evident. A layer of dense continuous oxide layer as well as irregularly shaped oxide particles distributed evenly present on the surface, as shown in Figures 4(c) and 4(c1). These irregularly shaped oxide particles varied greatly in size. These oxide particles are iron-oxides according to the EDS analysis presented in Table 2. Combined with the XRD analysis presented in Figure 3, it could infer that the phase is NiFe_2O_4 . The formation of NiFe_2O_4 can be expressed as [37]



Because the iron content of Inconel 625 in this work was low (0.01%), it was impossible to form iron-containing oxide during the corrosion process. Therefore, it can be deduced that the iron ions may be due to the dissolution of the autoclave material and then deposited

on the sample surface [30, 37]. EDS chemical analyses indicated that the oxide film was mainly composed of Ni and Cr oxides with a small amount of Fe, Nb, and Mo, as shown in Table 2. Consequently, it could be drawn that the oxide film was mainly NiO and $\text{Ni}(\text{Cr,Fe})_2\text{O}_4$. This agreed well with those reported in the literatures for nickel-based alloys [26, 27, 36].

The surface morphology was somewhat similar to that of 1000 h after an immersion period of 1500 h, as shown in Figure 4(d). The irregularly shaped particles developed gradually both in size and in number (Figure 4(d1)). A similar phenomenon had been observed by Clair et al. [27]. The EDS analysis revealed the oxide film as a binary mixture of NiCr_2O_4 and NiFe_2O_4 [27].

3.2. Pitting Corrosion. In addition to the oxidation, pitting corrosion also occurred on the Inconel 625. EDS composition analysis was carried out on the oxide film and corrosion pits at spots 1–7, and the obtained data are presented in Table 3. Pitting corrosion was observed after an immersion period of only 100 h, as shown in Figure 5(a), which was consistent with the results of Behnamian et al. [31] and Yang et al. [32]. The observation strongly supported the result of mass loss presented in Figure 2. In this case, the amount of weight gain caused by the formation of oxide film on the surface was less than the weight loss that is caused by pitting and uniform corrosion. The EDS results suggested that high levels of niobium element accumulated in the corrosion pits. It seemed that the corrosion pits might be determined by inclusions of NbC [31, 38, 39]. In high-temperature water, pitting may be associated with Nb-rich precipitates (likely the γ' -phase) [4, 40] and induced by local potential difference between the matrix and the inclusions [2]. Figure 5(b) showed that the irregularly shaped oxide particles distributed evenly on the surface. Base on the EDS analysis presented in Table 3, the oxide particle was the Nb-rich phase, indicating that the occurrence of the Nb-rich phase and then the dissolved $\text{Nb}^{2+}/\text{Nb}^{3+}$ ion form oxide that deposited in the vicinity of the corrosion pit. Solution treatment can reduce the precipitation of the secondary phases, optimize the microstructure, and improve the pitting corrosion resistance of metallic alloys [41–43].

Figure 6 displays the Raman spectra results of oxide films on Inconel 625. The characteristic peaks located at 485, 550, 695, 1380, and 1590 cm^{-1} indicated that the oxide film mainly consisted of NiO [44], NiCr_2O_4 [44], Cr_2O_3 , and Nb_2O_5 [45]. After 300 hours of immersion, the oxide films were composed of NiO and Nb_2O_5 . The formation of Nb_2O_5 mainly resulted from the pitting corrosion of the NbC phase [31, 32]. After 700 hours of immersion, the peaks of Cr_2O_3 and NiCr_2O_4 gradually appeared. The formation of these continuously dense oxides could protect the alloy effectively. It was reported that NiO was not as stable as the spinel and chromium oxides [2, 34]. Besides, studies showed that element Fe caused solid solution strengthening when added into Ni-based alloy. But others considered that this was due to the low content of oxides produced by iron [17], resulting in the formation of NiCr_2O_4 instead of FeCr_2O_4 . Moreover, the diffusion rate

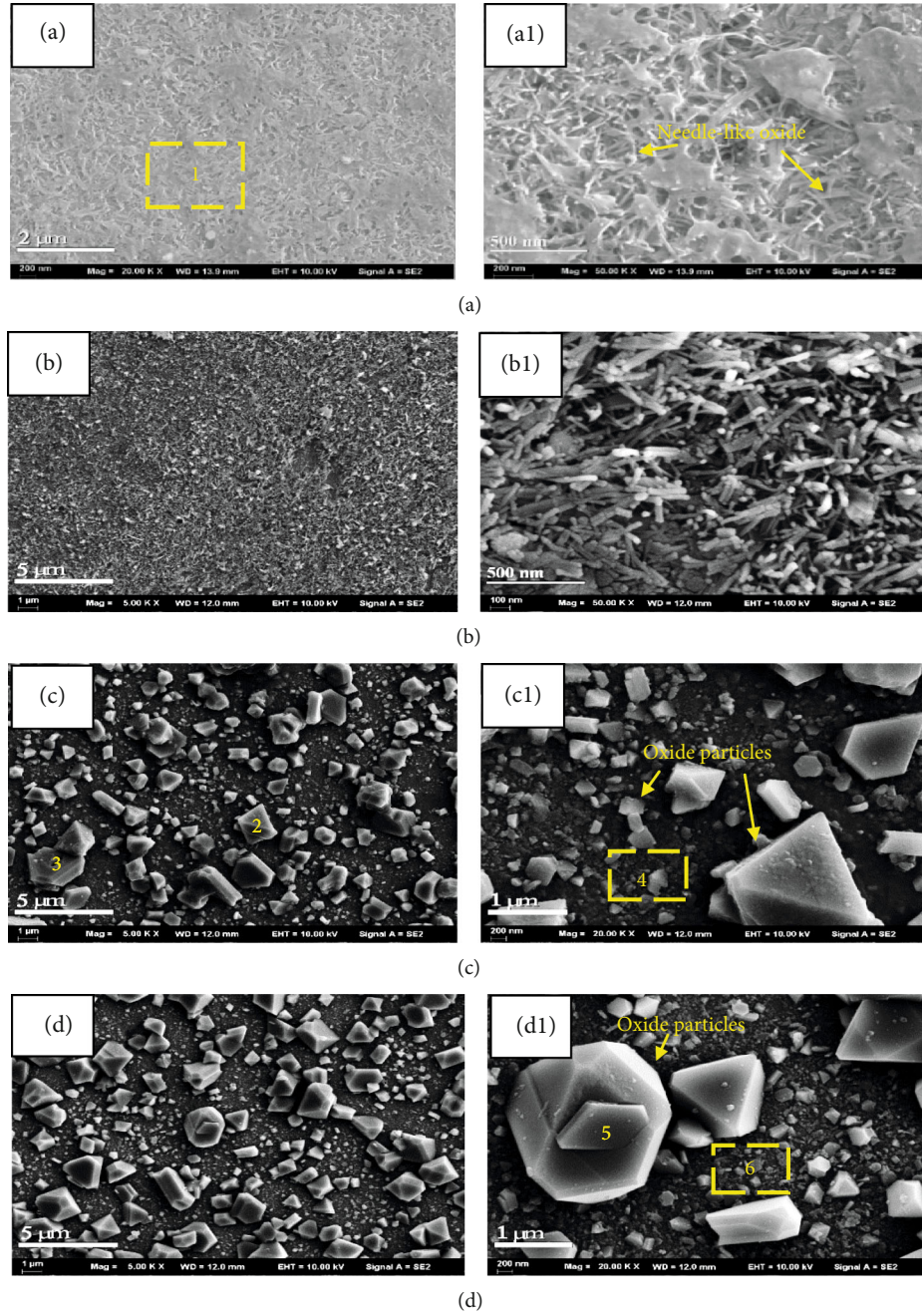


FIGURE 4: Morphologies of the oxide film formed on Inconel 625: (a, a1) 100 h; (b, b1) 500 h; (c, c1) 1000 h; (d, d1) 1500 h.

TABLE 2: The EDS chemical compositions (wt%) of the tested spots presented in Figure 4.

	Ni	Cr	Mo	Nb	Fe	O
1	69.60	18.73	6.15	—	—	5.52
2	12.71	3.44	—	—	59.94	23.91
3	14.87	3.39	—	—	56.17	25.57
4	40.41	20.05	8.13	3.27	15.41	12.71
5	20.91	0.96	—	—	51.97	26.16
6	45.99	18.69	6.99	—	16.72	11.62

TABLE 3: EDS chemical composition of the tested spots presented in Figure 5 (wt%).

Area	Ni	Cr	Mo	Nb	Fe	O
1	39.50	13.84	3.85	31.43	—	11.38
2	22.91	6.39	1.33	54.45	—	14.92
3	22.17	7.79	6.59	1.88	—	7.67
4	69.62	21.55	3.82	—	—	5.00
5	29.16	—	—	21.03	25.82	23.99
6	—	—	—	81.88	—	18.12
7	54.89	20.59	6.61	—	8.81	9.09

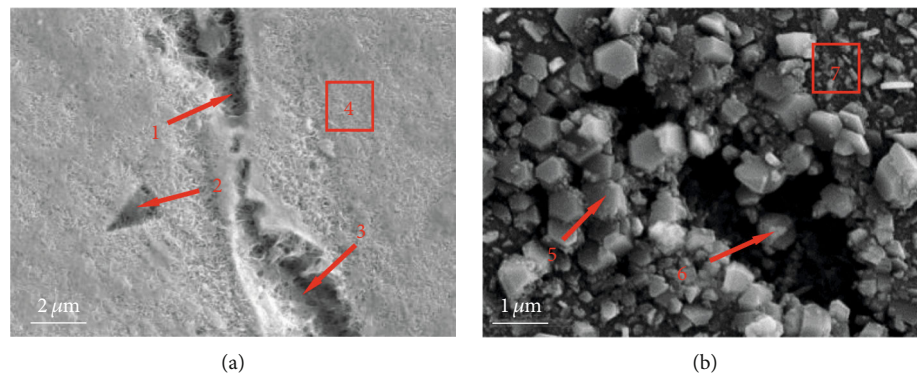


FIGURE 5: Morphologies of pitting corrosion for Inconel 625 in high-temperature water: (a) 100 h; (b) 700 h.

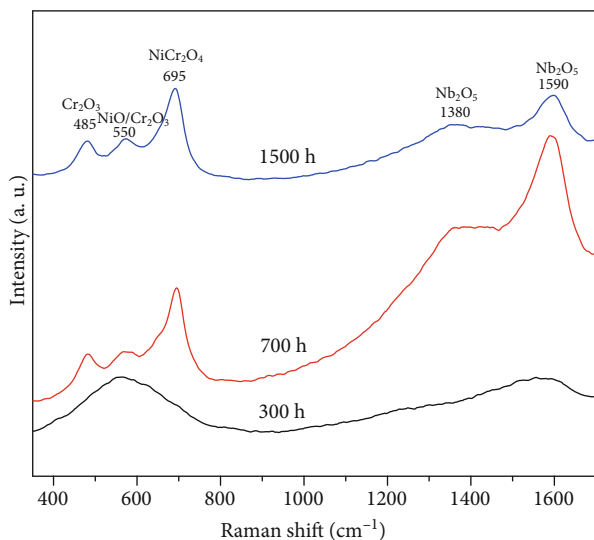


FIGURE 6: Raman spectra of the oxide films formed on Inconel 625 in high-temperature water.

of metal cation Ni^{2+} was much higher than that of Cr^{3+} in oxide film [46]. As a result, the oxide dominated by NiO was formed in the outer layer, while Cr_2O_3 and NiCr_2O_4 formed in the inner layer [17].

The cross-section of Inconel 625 exposed to high-temperature water for 1500 h is shown in Figure 7. The average thickness of the oxide film is about $1.99 \mu\text{m}$. The EDS result of line scanning element distribution is presented in Figure 7(b). It is clear that the oxide film shows a double-layer structure and the thickness of the inner layer is slightly thicker than that of the outer layer. Thus, it is inferred that the inner oxide film is mainly composed of NiCr_2O_4 . In addition, elements Nb and Fe were on the surface of the oxide layer. NiFe_2O_4 formed by iron deposition and Nb oxides formed by NbC detachment are on the surface of the oxide films. Although the alloy was oxidized for 1500 h in high-temperature water, the matrix oxide film formed into a continuously dense layer which was still thin, indicating an excellent corrosion resistance to the alloy.

3.3. Corrosion Mechanism. Inconel 625 exhibited two oxide layers which were coincident with the SEM observation of the surface. Attributes of dense and uniform are showed by the inner layer and randomly oriented grains with rather different compositions that make up the outer layer [33]. The oxide film consists of a combination of NiCr_2O_4 , NiFe_2O_4 , and NiO . On the basis of the evolution of the corrosion process, it is clearly deduced that the elements of 304L SS (autoclave) could be dissolved into the high-temperature water during the immersion test. The dissolved Fe^{2+} could form relatively large, randomly oriented grains of oxide which appeared as polyhedron crystals with sharp edges towards the outermost surface, as shown in Figure 4(c), giving rise to the emerging oxide diffraction peaks. As showed in Table 2 and Figure 4(c), the composition of oxides primarily corresponded to NiFe_2O_4 , and the matrix oxide film was composed of NiCr_2O_4 and NiO according to the diffraction peak. After 1500 h, oxide films adequately covered the alloy surface (Figure 4(d)), leading to the increase of NiCr_2O_4 and NiFe_2O_4 diffraction peaks. Under these conditions, NiO interacted with the chromium ions diffused from the alloy matrix and the iron ions dissolved from the autoclave, thus giving rise to the formation of NiCr_2O_4 and NiFe_2O_4 , respectively. It should be noted that the protective effect brought by NiCr_2O_4 [38] increases along with the increasing corrosion time, as well as the oxidation resistance. This well explains the weight gain trend observed in Figure 1. Figure 8 shows the corrosion mechanism of Inconel 625 in high-temperature water. The outer layer, consisting of relatively large, randomly oriented grains of $\text{Ni}(\text{Fe,Cr})_2\text{O}_4$, is formed by iron dissolve from 304L SS (autoclave) and outward diffusion of ion from the base, which grows on the original surface of the sample.

4. Conclusion

Inconel 625 in $345^\circ\text{C}/15.5 \text{ MPa}$ water of 304 SS autoclave resulted in pitting corrosion on the surface in the early stage of corrosion oxidation, and Nb_2O_5 was deposited in the pit. NiO , Cr_2O_3 was formed as the inner layer, with the progress of corrosion oxidation. Sparse oxide grows preferentially and completely covered the matrix. Fe^{2+} in

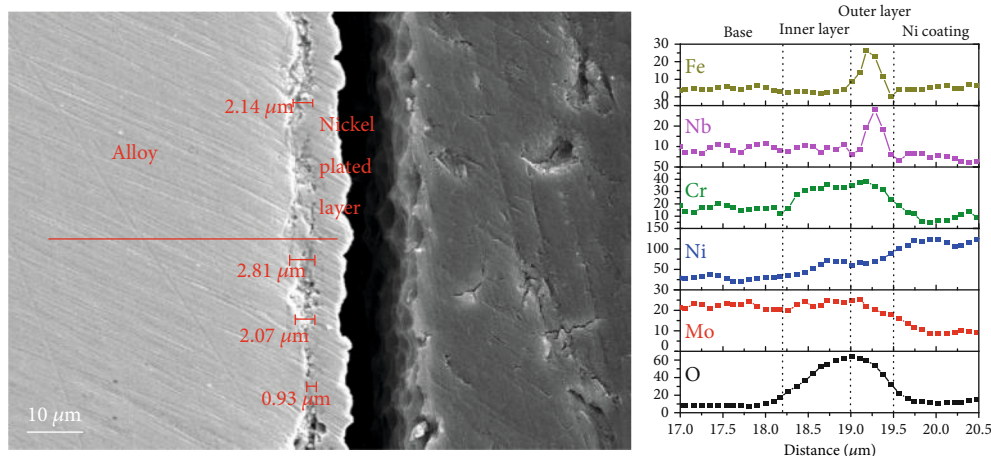


FIGURE 7: Cross-section of Inconel 625 after corrosion oxidation 1500 h and the element distribution line scan.

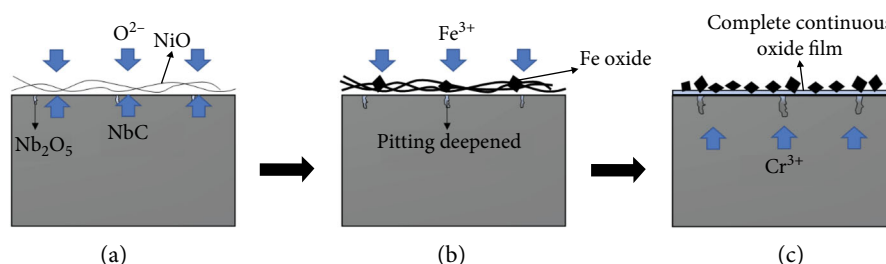


FIGURE 8: Corrosion mechanism of Inconel 625 in high-temperature water.

304 SS autoclave is dissolved in electrolyte and forms the outer layer composed of scattered crystallites, which is granular and very sensitive to the oxidation conditions. In the later stage of corrosion and oxidation, Ni(Fe,Cr)₂O₄ was formed by outward diffusion of Fe and Cr, which is also the components of the outer layer.

Data Availability

The data used to support the findings of this study are available from the corresponding author upon request.

Conflicts of Interest

The authors declare that they have no conflict of interest.

Acknowledgments

This work was supported by the National Natural Science Foundation of China (No. 51401092), the Science and Technology Program of Jiangsu Province (BE2017143), and the Project of Science and Technology Development (No. 2017GDASCX-0117).

References

- [1] P. Kritzer, N. Boukis, and E. Dinjus, "Corrosion of alloy 625 in high-temperature, high-pressure sulfate solutions," *Corrosion*, vol. 54, no. 9, pp. 689–699, 1998.
- [2] L. Tan, X. Ren, K. Sridharan, and T. R. Allen, "Corrosion behavior of Ni-base alloys for advanced high temperature water-cooled nuclear plants," *Corrosion Science*, vol. 50, no. 11, pp. 3056–3062, 2008.
- [3] Z. Tian, L. Song, K. Fang, G. Lin, and H. Zhou, "Corrosion behavior of 304L stainless steel in a B-Li coolant for a nuclear power plant," *Materiali in Tehnologije*, vol. 53, no. 5, pp. 643–647, 2019.
- [4] L. Li, S. Jin, D. Wang et al., "Characterization of oxide film in P92 ferritic-martensitic steel exposed to high temperature and pressure water," *Journal of Nuclear Materials*, vol. 541, article 152406, 2020.
- [5] W. J. Kuang, X. Q. Wu, and E. H. Han, "Effect of Ni²⁺ in occluded volume on the oxidation behavior of 304 stainless steel in high temperature water," *Acta Metallurgica Sinica*, vol. 47, no. 7, pp. 927–931, 2011.
- [6] J. Xu and T. Shoji, "The corrosion behavior of alloy 182 in a cyclic hydrogenated and oxygenated water chemistry in high temperature aqueous environment," *Corrosion Science*, vol. 104, pp. 248–259, 2016.
- [7] L. Xin, B. Yang, J. Li, Y. Lu, and T. Shoji, "Microstructural characteristics of alloy 690TT subjected to fretting corrosion in high temperature water," *Corrosion Science*, vol. 123, pp. 116–128, 2017.
- [8] S. H. Jeon, E. H. Lee, and D. H. Hur, "Effects of dissolved hydrogen on general corrosion behavior and oxide films of alloy 690TT in PWR primary water," *Journal of Nuclear Materials*, vol. 485, pp. 113–121, 2017.
- [9] Z. Wang, J. Xu, J. Li et al., "The synergy of corrosion and fretting wear process on Inconel 690 in the high temperature high

- pressure water environment,” *Journal of Nuclear Materials*, vol. 502, pp. 255–262, 2018.
- [10] W. Kuang, X. Wu, and E. H. Han, “Influence of dissolved oxygen concentration on the oxide film formed on alloy 690 in high temperature water,” *Corrosion Science*, vol. 69, pp. 197–204, 2013.
 - [11] G. Liu, X. Zhang, X. Wang, and Y. Qiao, “Precipitation behavior of the topologically close-packed phase in the DD5 superalloy during long-term aging,” *Scanning*, vol. 2020, Article ID 2569837, 6 pages, 2020.
 - [12] J. Yang, S. Wang, X. Tang, Y. Wang, and Y. Li, “Effect of low oxygen concentration on the oxidation behavior of Ni-based alloys 625 and 825 in supercritical water,” *Journal of Supercritical Fluids*, vol. 131, pp. 1–10, 2018.
 - [13] J. Xu and T. Shoji, “The corrosion behavior of alloy 52 weld metal in cyclic hydrogenated and oxygenated water chemistry in high temperature aqueous environment,” *Journal of Nuclear Materials*, vol. 461, pp. 10–21, 2015.
 - [14] B. Stellwag, “The mechanism of oxide film formation on austenitic stainless steels in high temperature water,” *Corrosion Science*, vol. 40, no. 2–3, pp. 337–370, 1998.
 - [15] Z. Zhu, C. Ouyang, Y. Qiao, and X. Zhou, “Wear characteristic of Stellite 6 alloy hardfacing layer by plasma arc surfacing processes,” *Scanning*, vol. 2017, Article ID 6097486, 7 pages, 2017.
 - [16] S. E. Ziemniak and M. Hanson, “Corrosion behavior of NiCrMo alloy 625 in high temperature, hydrogenated water,” *Corrosion Science*, vol. 45, no. 7, pp. 1595–1618, 2003.
 - [17] X. Ren, K. Sridharan, and T. R. Allen, “Corrosion behavior of alloys 625 and 718 in supercritical water,” *Corrosion*, vol. 63, no. 7, pp. 603–612, 2007.
 - [18] T. Kim, K. J. Choi, S. C. Yoo, and J. H. Kim, “Effects of dissolved hydrogen on the crack-initiation and oxidation behavior of nickel-based alloys in high-temperature water,” *Corrosion Science*, vol. 106, pp. 260–270, 2016.
 - [19] F. Huang, J. Wang, E. H. Han, and W. Ke, “Microstructural characteristics of the oxide films formed on alloy 690 TT in pure and primary water at 325°C,” *Corrosion Science*, vol. 76, pp. 52–59, 2013.
 - [20] J. Xu, T. Shoji, and C. Jang, “The effects of dissolved hydrogen on the corrosion behavior of alloy 182 in simulated primary water,” *Corrosion Science*, vol. 97, pp. 115–125, 2015.
 - [21] P. Y. Guo, H. Sun, Y. Shao et al., “The evolution of microstructure and electrical performance in doped Mn-Co and Cu-Mn oxide layers with the extended oxidation time,” *Corrosion Science*, vol. 172, article 108738, 2020.
 - [22] E. H. Han, J. Q. Wang, X. Q. Wu, and W. Ke, “Corrosion mechanisms of stainless steel and nickel base alloys in high temperature high pressure water,” *Acta Metallurgica Sinica*, vol. 46, no. 11, pp. 1379–1390, 2010.
 - [23] Q. Peng, J. Hou, K. Sakaguchi, Y. Takeda, and T. Shoji, “Effect of dissolved hydrogen on corrosion of Inconel alloy 600 in high temperature hydrogenated water,” *Electrochimica Acta*, vol. 56, no. 24, pp. 8375–8386, 2011.
 - [24] Y. Qiao, J. Huang, D. Huang et al., “Effects of laser scanning speed on microstructure, microhardness and corrosion behavior of laser cladding Ni45 coatings,” *Journal of Chemistry*, vol. 2020, Article ID 1438473, 11 pages, 2020.
 - [25] M. Sun, X. Wu, Z. Zhang, and E. H. Han, “Analyses of oxide films grown on alloy 625 in oxidizing supercritical water,” *Journal of Supercritical Fluids*, vol. 47, no. 2, pp. 309–317, 2008.
 - [26] Q. N. Song, N. Xu, W. Gu et al., “Investigation on the corrosion and cavitation erosion behaviors of the cast and friction stir processed Ni-Al bronze in sulfide-containing chloride solution,” *International Journal of Electrochemical Science*, vol. 12, no. 11, pp. 10616–10632, 2017.
 - [27] A. Clair, M. Foucault, O. Calonne, and E. Finot, “Optical modeling of nickel-base alloys oxidized in pressurized water reactor,” *Thin Solid Films*, vol. 520, no. 24, pp. 7125–7129, 2012.
 - [28] M. Q. Ou, Y. Liu, X. D. Zha, Y. C. Ma, L. M. Cheng, and L. Kui, “Corrosion behavior of a new nickel base alloy in supercritical water containing diverse ions,” *Acta Metallurgica Sinica*, vol. 52, no. 12, pp. 1557–1564, 2016.
 - [29] Z. Ma, D. Xu, S. Guo et al., “Corrosion properties and mechanisms of austenitic stainless steels and Ni-base alloys in supercritical water containing phosphate, sulfate, chloride and oxygen,” *Oxidation of Metals*, vol. 90, no. 5–6, pp. 599–616, 2018.
 - [30] W. Kuang, X. Wu, E. H. Han, and L. Ruan, “Effect of nickel ion from autoclave material on oxidation behaviour of 304 stainless steel in oxygenated high temperature water,” *Corrosion Science*, vol. 53, no. 3, pp. 1107–1114, 2011.
 - [31] Y. Behnamian, A. Mostafaei, A. Kohandehghan et al., “A comparative study of oxide scales grown on stainless steel and nickel-based superalloys in ultra-high temperature supercritical water at 800°C,” *Corrosion Science*, vol. 106, pp. 188–207, 2016.
 - [32] J. Yang, S. Wang, D. Xu, Y. Guo, C. Yang, and Y. Li, “Effect of ammonium chloride on corrosion behavior of Ni-based alloys and stainless steel in supercritical water gasification process,” *International Journal of Hydrogen Energy*, vol. 42, no. 31, pp. 19788–19797, 2017.
 - [33] Z. Y. Zhu, Y. Sui, A. L. Dai et al., “Effect of aging treatment on intergranular corrosion properties of ultra-low iron 625 alloy,” *International Journal of Corrosion*, vol. 2019, Article ID 9506401, 9 pages, 2019.
 - [34] H. Shi, Z. Gao, Z. Fan, Y. Ding, Y. Qiao, and Z. Zhu, “Corrosion behavior of alloy C-276 in supercritical water,” *Advances in Materials Science and Engineering*, vol. 2018, Article ID 1027640, 6 pages, 2018.
 - [35] G. S. Was, S. Teyssere, and Z. Jiao, “Corrosion of austenitic alloys in supercritical water,” *Corrosion*, vol. 62, no. 11, pp. 989–1005, 2006.
 - [36] C. de Araújo Figueiredo, R. W. Bosch, and M. Vankeerberghen, “Electrochemical investigation of oxide films formed on nickel alloys 182, 600 and 52 in high temperature water,” *Electrochimica Acta*, vol. 56, no. 23, pp. 7871–7879, 2011.
 - [37] W. Kuang, X. Wu, E. H. Han, and J. Rao, “Effect of alternately changing the dissolved Ni ion concentration on the oxidation of 304 stainless steel in oxygenated high temperature water,” *Corrosion Science*, vol. 53, no. 8, pp. 2582–2591, 2011.
 - [38] Y. Qiao, D. Xu, S. Wang et al., “Effect of hydrogen charging on microstructural evolution and corrosion behavior of Ti-4Al-2V-1Mo-1Fe alloy,” *Journal of Materials Science & Technology*, vol. 60, pp. 168–176, 2021.
 - [39] N. Q. Zhang, B. R. Li, Y. Bai, and H. Xu, “Oxidation of austenitic steel TP347HFG exposed to supercritical water with different dissolved oxygen concentration,” *Applied Mechanics and Materials*, vol. 148–149, pp. 1179–1183, 2011.
 - [40] S. Barella, A. Gruttadauria, C. Mapelli et al., “Solidification microstructure of centrifugally cast Inconel 625,” *China Foundry*, vol. 14, no. 4, pp. 304–312, 2017.

- [41] Y. Qiao, J. Chen, H. Zhou et al., "Effect of solution treatment on cavitation erosion behavior of high-nitrogen austenitic stainless steel," *Wear*, vol. 424-425, pp. 70-77, 2019.
- [42] G. S. Was, P. Ampornrat, G. Gupta et al., "Corrosion and stress corrosion cracking in supercritical water," *Journal of Nuclear Materials*, vol. 371, no. 1-3, pp. 176-201, 2007.
- [43] Y. Qiao, Z. Tian, X. Cai et al., "Cavitation erosion behaviors of a nickel-free high-nitrogen stainless steel," *Tribology Letters*, vol. 67, no. 1, 2019.
- [44] F. Wang and T. M. Devine, "In-situ surface enhanced Raman spectroscopy investigation of surface film formed on nickel and chromium in high-temperature and high-pressure water," *Atomic Energy Science and Technology*, vol. 47, Supplement 1, pp. 387-393, 2013.
- [45] N. P. de Moraes, R. Bacani, M. L. C. P. da Silva, T. M. B. Campos, G. P. Thim, and L. A. Rodrigues, "Effect of Nb/C ratio in the morphological, structural, optical and photocatalytic properties of novel and inexpensive Nb₂O₅/carbon xerogel composites," *Ceramics International*, vol. 44, no. 6, pp. 6645-6652, 2018.
- [46] L. Yang, M. Chen, J. Wang et al., "Microstructure and composition evolution of a single-crystal superalloy caused by elements interdiffusion with an overlay NiCrAlY coating on oxidation," *Journal of Materials Science & Technology*, vol. 45, pp. 49-58, 2020.

Research Article

Quality Prediction and Control of Assembly and Welding Process for Ship Group Product Based on Digital Twin

Lei Li , Di Liu, Jinfeng Liu, Hong-gen Zhou, and Jiasheng Zhou

School of Mechanical Engineering, Jiangsu University of Science and Technology, Zhenjiang 212003, China

Correspondence should be addressed to Lei Li; lilei0064@sina.com

Received 1 July 2020; Revised 9 August 2020; Accepted 24 August 2020; Published 19 October 2020

Guest Editor: Jian Chen

Copyright © 2020 Lei Li et al. This is an open access article distributed under the Creative Commons Attribution License, which permits unrestricted use, distribution, and reproduction in any medium, provided the original work is properly cited.

In view of the problems of lagging and poor predictability for ship assembly and welding quality control, the digital twin technology is applied to realize the quality prediction and control of ship group product. Based on the analysis of internal and external quality factors, a digital twin-based quality prediction and control process was proposed. Furthermore, the digital twin model of quality prediction and control was established, including physical assembly and welding entity, virtual assembly and welding model, the quality prediction and control system, and twin data. Next, the real-time data collection based on the Internet of Things and the twin data organization based on XML were used to create a virtual-real mapping mechanism. Then, the machine learning technology is applied to predict the process quality of ship group products. Finally, a small group is taken as an example to verify the proposed method. The results show that the established prediction model can accurately evaluate the welding angular deformation of group products and also provide a new idea for the quality control of shipbuilding.

1. Introduction

The current ship production basically adopts the block construction mode, and the block is composed of a large number of typical products (including a large group, middle group, small group, t-type component, and chip component). These group products are the main object of current ship automation and intelligent construction. Due to the large quantity, large batch, and short construction cycle, the construction quality and efficiency are particularly important to improve the overall ship construction capacity. In the process of assembly and welding, a large number of quality data and process data will be generated, which is the key to evaluate the quality and can provide process decision-making support for subsequent quality prediction. Therefore, it is of great significance to realize the quality prediction and control of welding process by collecting and analyzing the data related to the welding process, so as to improve the quality and efficiency of ship product construction.

The prediction and control improve product quality and reduce production cost, which is an indispensable link to realize digital, automatic, and intelligent production. Many

scholars have conducted extensive research on welding quality prediction and control. Öberg and Sikström used arc voltage measurement, CMOS vision, and infrared camera to online monitor the quality characteristics of weld penetration and evaluated the industrial applicability and applicability of the framework [1]. Zhang et al. developed a servo welding experimental system, which can extract the electrode indentation from the servo encoder to reflect the change of welding quality. This online detection method can accurately judge whether the weld meets the requirements of tensile shear strength [2]. Shi et al. made NiTi coating on stainless steel by TIG surfacing process to improve cavitation erosion resistance [3]. Yang et al. established a new welding inspection system based on 3D reconstruction technology. The support vector machine is used to evaluate the welding quality. The experimental results show that the system can complete the welding quality detection quickly and efficiently [4]. Huang and Kovacevic have developed a laser-based nondestructive vision system. By processing the image obtained by the visual sensor, the geometric characteristics of the weld can be obtained. The position and size of welding defects can be accurately identified according to the three-dimensional

contour of weld, so as to realize the nondestructive testing of weld quality [5]. Gu et al. proposed an automatic tracking system for multipass welding of an arc welding robot. The system can accurately track the cap passes, filling passes, and the root pass [6]. Wang et al. proposed a new welding quality inspection framework, which can classify and evaluate welding quality and achieved good welding monitoring performance [7]. According to the literature analysis, online data monitoring and nondestructive quality assessment after welding are the main methods of quality control, which fail to effectively use the real-time data of the production process. The real-time and predictive quality control is poor, and it is difficult to meet the requirements of process online decision-making and future intelligent manufacturing development.

Digital twin technology was proposed by Michael Grieves in 2003 [8]. The current research and applications are mainly focused on product design, product quality analysis, and life prediction in the fields of aerospace and automobile manufacturing. As an emerging technology oriented to intelligent manufacturing, it has attracted wide attention. In 2011, NASN established the virtual twin of the space vehicle to predict the life of the physical vehicle [9]. Subsequently, NASA summarized previous studies on digital twins and proposed a technical route of “modeling-simulation-information technology processing,” which further increased the feasibility of digital twin technology [10]. Cai et al. created a “digital twin” virtual machine tool for physical manufacturing based on sensor data integration and information fusion technology [11]. Söderberg et al. proposed the concept of digital twins for real-time geometric guarantees and the process of how to move from mass production of personalized production [12]. Bilberg and Malik proposed a human-robot assembly system based on digital twin, which was used for industrial applications of variant assembly system to ensure the flexibility and automation of assembly [13]. Roy et al. and Lu et al. summarized the development achievements of digital twinning and pointed out the problems faced by the research of digital twinning of intelligent manufacturing [14, 15]. Park et al. and Leng et al. apply the digital twin technology to the personalized production to increase the flexibility of the manufacturing system [16, 17]. In China, there are more and more researches on digital twin. Fei et al. proposed the concept of digital twin shop-floor, discussed the basic theory and key technology of realizing information physical fusion of digital twin workshop, and then proposed the concept of five-dimension digital twin, which provided a reference for enterprises to practice digital twin [18–21]. Zhuang et al. further elaborated the connotation of digital twins, established the architecture of digital twins, and proposed the development direction of digital twins of products [22]. Qi et al. proposed the digital twin service for intelligent manufacturing and further elaborated the integration process of manufacturing service and digital twin [23]. Xie et al. proposed a virtual monitoring method for hydraulic supports based on digital twins, which simulates the behaviors of the actual hydraulic supports in the whole life cycle to achieve the synchronization of virtual and actual movements [24]. In the field of manufacturing, GE, Sie-

mens, PTC, Dassault, and DNV GL use digital twin technology to meet their respective enterprise needs [25–29]. Through the above analysis, it can be seen that the digital twin technology makes full use of physical models, sensor update, and historical data and integrates multidisciplinary and multiphysical quantities, multiscale, and multiprobability. It can complete the interactive mapping of virtual and physical space, which is an effective means to achieve decision-making and quality control.

In recent years, the research team has deeply studied the dynamic evaluation method and process quality prediction technology of complex product processing technology based on digital twin [30–32], which has improved the timeliness and effectiveness of machining technology evaluation and quality prediction. On the basis of preliminary research, a quality prediction and control method for assembling and welding of group products based on digital twin is proposed. Firstly, a digital twinning model of welding quality prediction and control including physical assembly and welding entity, virtual assembly and welding model, welding quality prediction and control system, and twinning data was established. Then, by means of real-time data collection based on the Internet of Things, twin data organization based on XML, and process quality prediction based on machine learning, the quality control of assembly and welding process of ship group products are realized. Lastly, a small group product of ship is taken as objects for verification.

2. The Quality Factors of Assembly and Welding for Ship Group Products

The assembly and welding process of ship group products mainly include four steps: marking, spot welding, welding, and quality inspection. Hull welding involves physics, chemistry, metal material science, and welding metallurgy. The main defects of the ship welding quality include bulk defects (porosity, slag inclusion, etc.), surface defects (bite edge, welding tumor, welding pit, etc.), and linear defects (incomplete penetration, incomplete fusion, etc.), as shown in Figure 1. The traditional welding process generally carries on quality inspection after welding, which is easy to produce welding defects and affects the welding quality and production efficiency. Hull assembly is the prior process of welding process. High-precision assembly quality can improve welding quality and reduce welding time. Deformation and dimensional deviation are the main quality problems. As the assembly and welding hours account for more than 40% of the total working hours of ship construction, effective control plays a decisive role in improving the quality and efficiency of ship construction.

Although the surface defects can be identified by manual inspection or camera, the defects inside the weld are not easy to identify. With the development of microtechnology, the nondestructive measurement of internal defects of weld can be achieved by using a scanning electron microscope and perspective electron microscope [33, 34]. The scanning electron micrograph of main internal defects is shown in Figure 2 [35]. Nondestructive testing (NDT) is the inspection on whether the weld quality meets the specified requirements

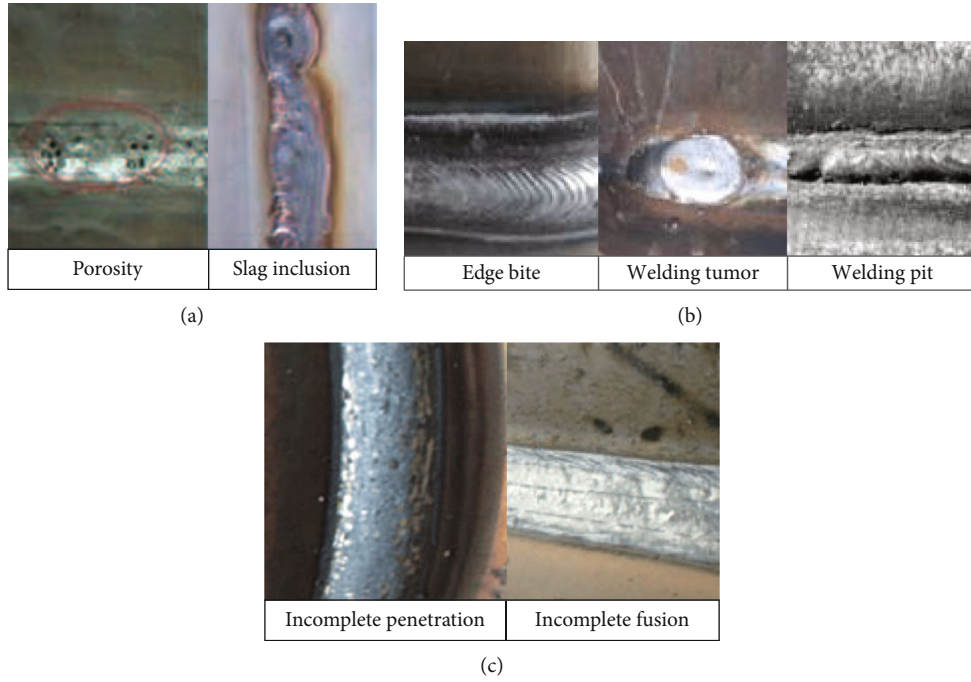


FIGURE 1: Defects of ship surface welding quality: (a) bulk defects; (b) surface defects; (c) linear defects.

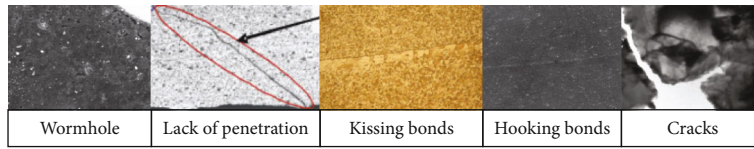


FIGURE 2: Scanning electron micrograph of internal welding defects.

without damaging the performance and integrity of the inspected weld, mainly methods including radiography, ultrasonic testing, eddy current, thermography, and liquid penetrant [36, 37]. NDT can provide rapid and economical methods for evaluating weld quality and has been widely used in various welding tests.

In the analysis of the assembly and welding process, the quality problems mainly are shown in Table 1. Among them, the welding factors include welding voltage, welding current, wire feeding speed, welding speed, bevel angle, weld not cleaned, welding material, and base metal thickness; the assembly factors include assembly sequence, margin, positioning, compensation, and spot welding parameters. Therefore, in order to effectively predict and control the process, it is necessary to complete the corresponding process decision through the process parameters and process data collection, data analysis, fusion, and quality prediction model.

3. Technical Process of Quality Prediction and Control

The traditional ship assembly and welding process quality control is used to compare the quality inspection results with the process requirements after welding to realize the product quality evaluation. In case of quality problems such as deformation, stress concentration and crack, postdeformation cor-

rection, and destress treatment shall be carried out. If cracks or other quality problems occur, the rejection rate will be increased and even the whole batch of products will be scrapped. Due to being time-consuming, high scrap rate, easy rework, low efficiency, high cost, and poor quality control, this method has been unable to meet the current requirements of the digital and intelligent construction of ship products. Therefore, this paper puts forward the quality prediction and control process of assembling and welding of ship group products based on the digital twin technology.

As shown in Figure 3. Firstly, a virtual welding model corresponding to the physical assembly and welding entity is established to realize the high-fidelity mapping between the virtual model and the physical entity. Secondly, the quality data collection is realized by the sensors and data collection system arranged by physical entity. By combining the real-time process data, process design data, and process simulation data, the twin data of welding process were constructed, which realized the virtual model to simulate the welding process of physical entity simultaneously. Then, combined with historical data and real-time data, online prediction of process quality is realized by big data analysis. Auto regression model, support vector machine, artificial neural network, correlation vector machine, random forest, etc. are commonly used in big data analysis. In case of any abnormality, the correction machining parameters shall be

TABLE 1: The quality defects of ship group products.

Type of defect	Quality characteristic	Qualitative factors
Assembly defects	Deformation	(1) Positioning method; (2) assembly sequence; (3) welding parameters
	Size deviation	(1) Assembly margin; (2) assembly compensation amount; (3) positioning method
	Porosity	(1) Welding current; (2) welding speed; (3) welding voltage; (4) the groove is not clean
	Slag inclusion	(1) Slag not cleaned; (2) groove form; (3) welding current; (4) welding speed
	Incomplete penetration	(1) Welding current
Surface welding defects	Incomplete fusion	(1) Groove type; (2) assembly clearance; (3) wire feeding speed; (4) welding current; (5) electrode diameter
	Bite edge	(1) Welding current
	Welding tumor	(1) Welding voltage; (2) welding current; (3) wire feeding speed; (4) welding speed
	Welding pit	(1) Welding speed; (2) welding current; (3) welding voltage
	Wormhole	
Internal welding defects	Lack of penetration	(1) Welding speed; (2) welding current; (3) welding voltage; (4) welding material; (5) base metal thickness
	Kissing bonds	
	Hooking bonds	
	Cracks	

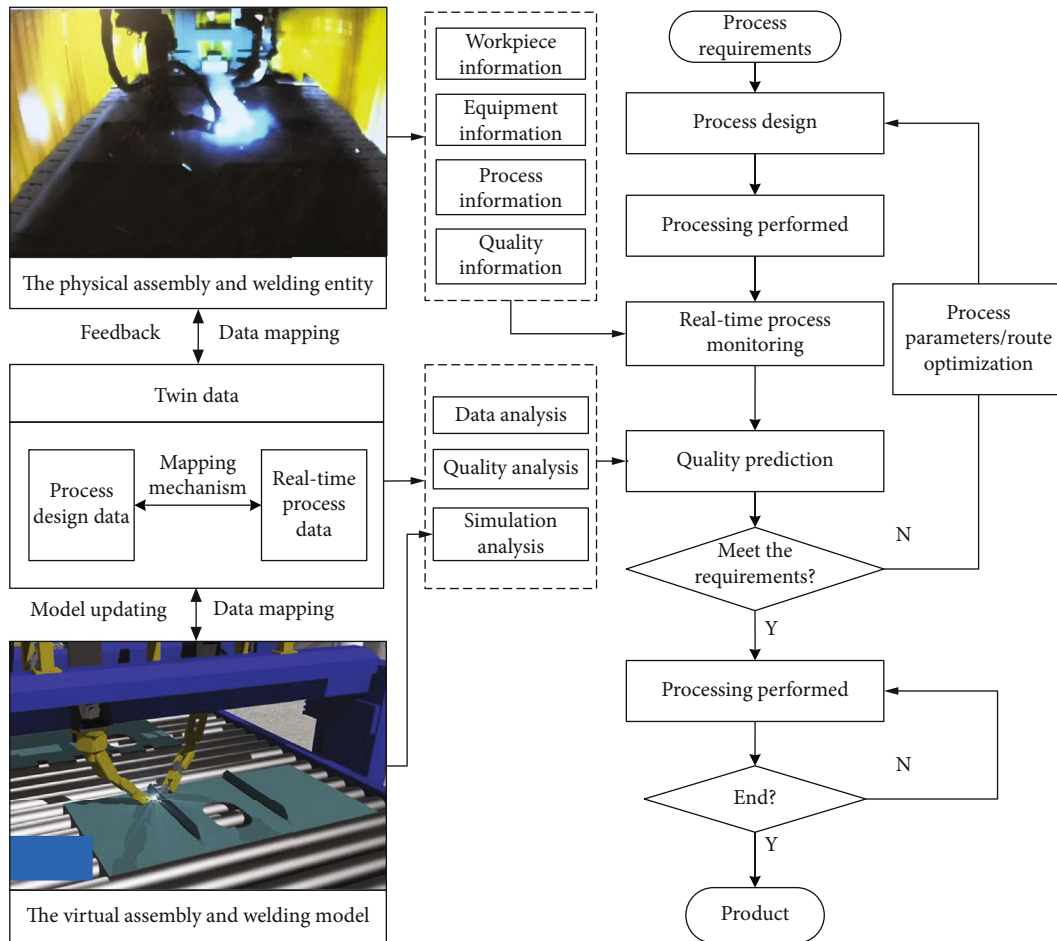


FIGURE 3: Quality prediction and control process of assembly and welding of ship group products based on digital twin.

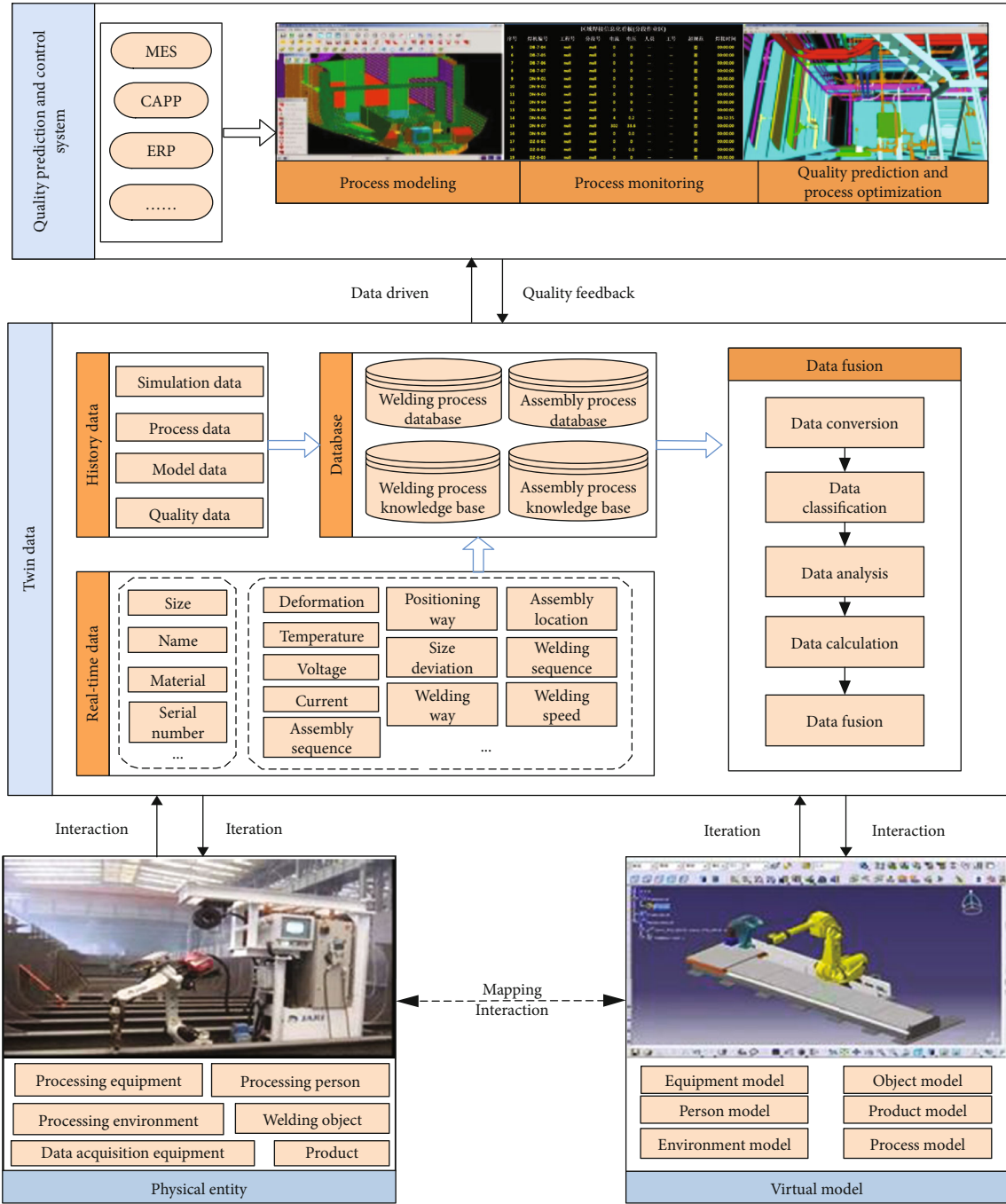


FIGURE 4: Digital twin model for prediction and control of mounting and welding quality of ship group products.

timely carried out and fed back to the physical entity. Thus, the quality prediction and control of welding of ship group products are realized.

4. Establishment of Digital Twinning Model for Product Quality Prediction and Control

In order to meet the synchronous evolution of the virtual model and the physical perception data, a digital twin-based quality prediction and control model was constructed

(as shown in Figure 4). Physical entity (PE), virtual model (VM), and quality prediction and control system (QS) are closely linked by digital twin data (DD). In the quality prediction and control system, the quality data in the physical entity can be collected in real time and stored as twin data; in the virtual model, the twin quality data stored in the quality prediction and control system can be analyzed and predicted, and the prediction results will be fed back to the physical entity for quality monitoring. The interaction and integration of the physical world and the information world of assembly

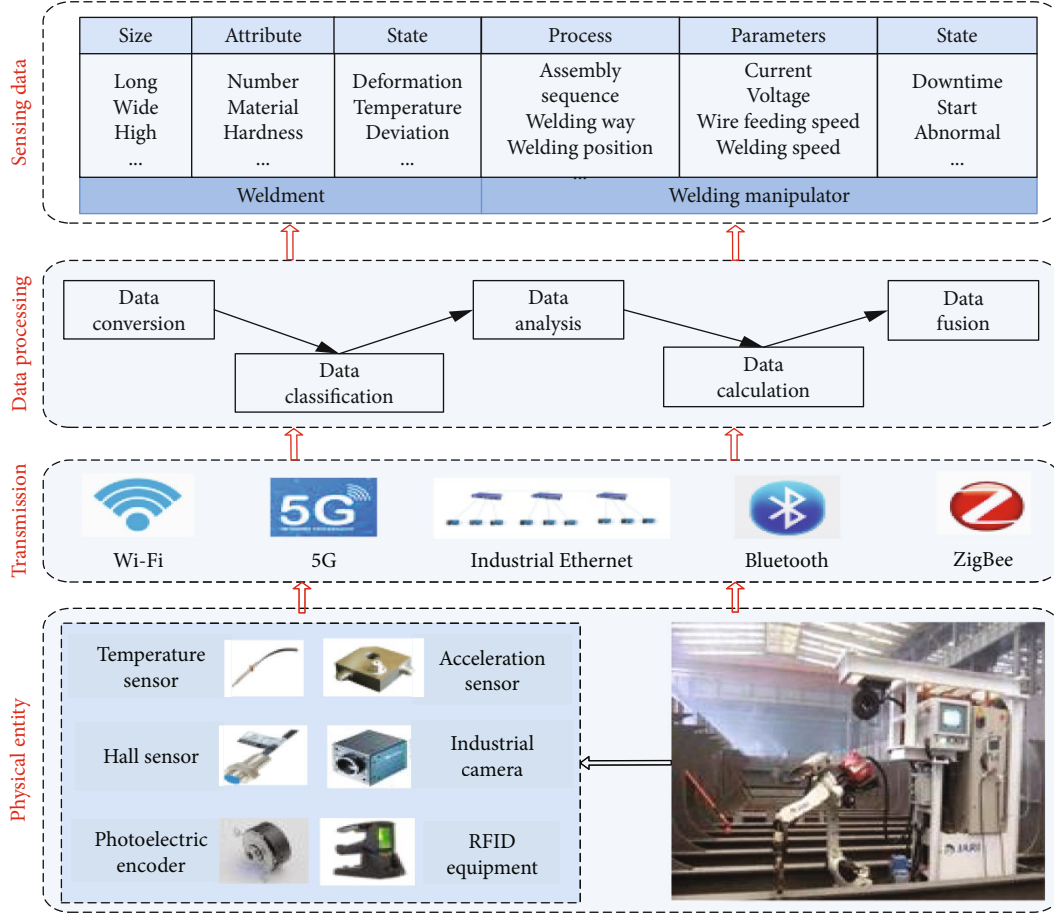


FIGURE 5: Real-time data acquisition of assembly and welding process.

and welding are realized. Define the quality of prediction and control model of ship group products based on digital twin:

$$W_{DT} = PE \cup VM \cup DD \cup QS, \quad (1)$$

where PE refers to the physical assembly and welding entity, VM represents the virtual assembly and welding model, DD stands for the digital twin data, and QS is the quality prediction and control system.

PE is the set of all entities involved in the process. It is responsible for the execution of production activities. It also has the function of real-time collection and fusion of multi-source heterogeneous data and makes dynamic responses according to process requirements, data monitoring, and process quality prediction results. The unified description of physical assembly and welding entity is as follows:

$$PE = [pers, proequis, dcequis, workps, envi, prods]. \quad (2)$$

pers is the processing personnel, proequis is the processing equipment, dcequis is the data acquisition equipment, workps is the welding object, envi is the processing environment, and prods is the product.

VM is a high-fidelity model corresponding to the physical entity, which can reflect the real-time state of the welding site and reproduce the physical assembly and welding entity.

VM is mainly responsible for the simulation, prediction, evaluation, and optimization of the production process. The unified description of the virtual assembly and welding model is as follows:

$$VM = [Mpers, Mequis, Mworkps, Menvi, Mprods, Mpro]. \quad (3)$$

Mpers is the personnel twin model, Mequis is the equipment twin model, Mworkps is the welding object model, Menvi is the environment twin model, Mprods is the product model, and Mpro is the process twin model.

Digital twin data (DD) consists of real-time data and history data. The real-time data is the data generated in the current welding process, and the historical data is the previous relevant welding data. Twin data is the core of digital twin model, which provides data support for welding quality prediction and control. The twin data are uniformly described as

$$DD = [cds, hds],$$

$$cds = wpds \oplus epids, \quad (4)$$

$$hds = simds \oplus prods \oplus molds \oplus quads.$$

cds is real-time data, including weldment data (wpds)

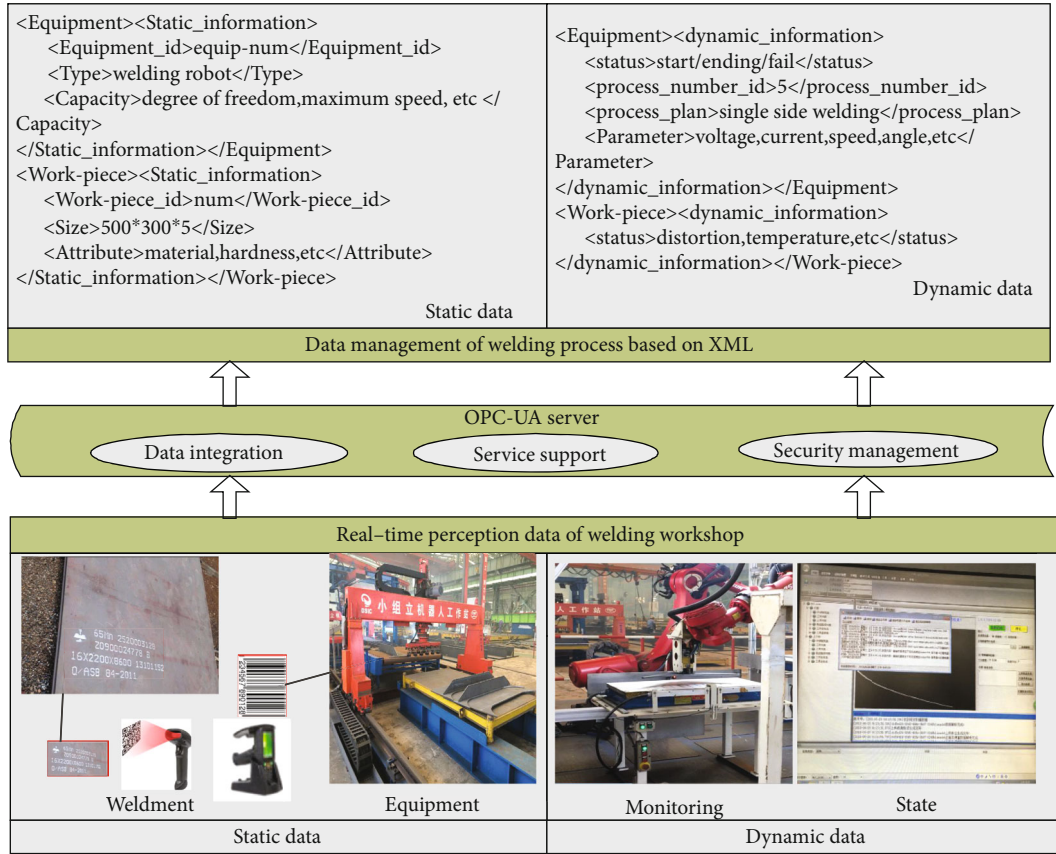


FIGURE 6: Data management and storage.

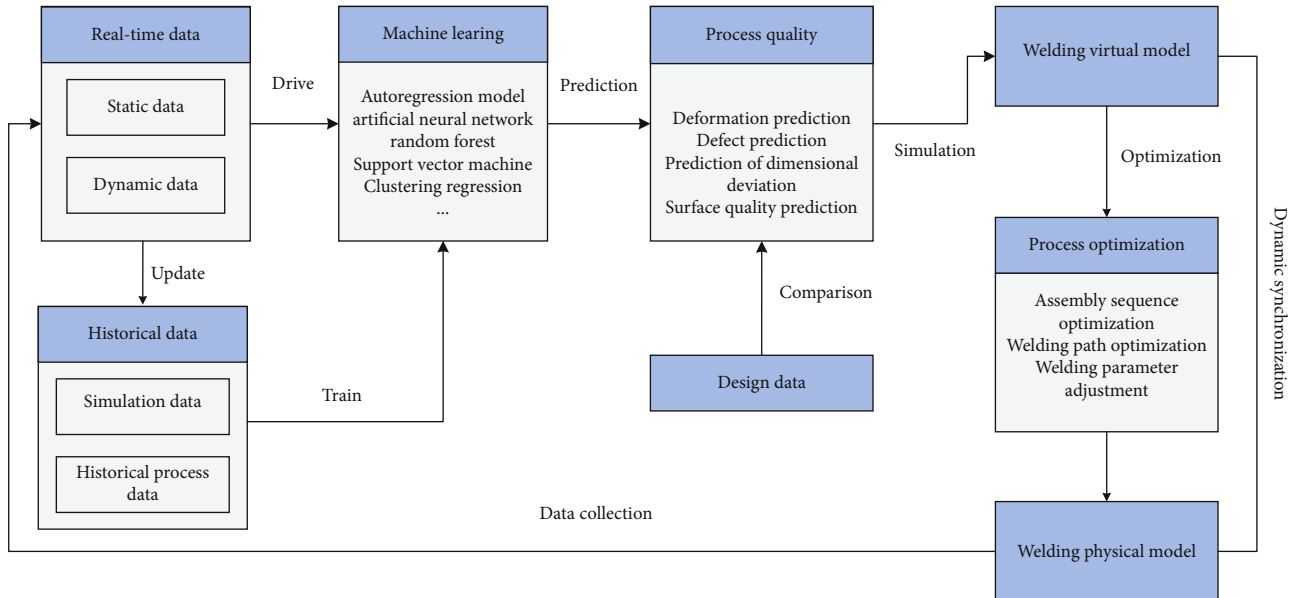


FIGURE 7: Prediction of assembly and welding quality based on machine learning.

and equipment data (epids); hds is history data, including the simulation data (simds), process data (prods), models data (molds), and quality data (quads).

QS is responsible for the monitoring and quality management and is the brain of the twin model. Firstly, the model of welding process is established to realize the synchronous

TABLE 2: Chemical composition and mechanical properties of the material.

C(%)	Mn(%)	Si(%)	S(%)	Yield strength (MPa)	Tensile strength (MPa)	Elongation (%)
≤0.18	0.70~1.60	0.10~0.50	≤0.04	315	440~590	22

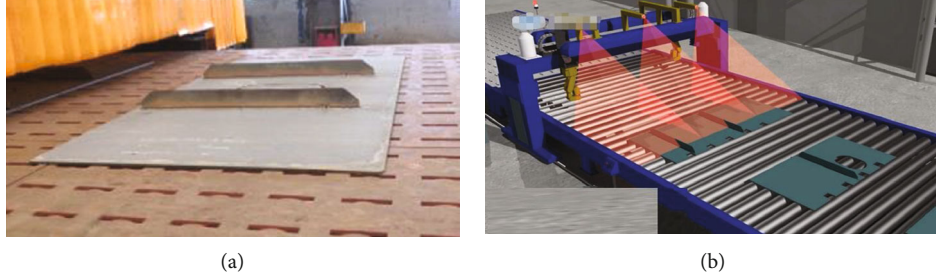


FIGURE 8: Welding process model: (a) product entity of the group; (b) simulation model of the production line.

evolution of virtual and real workshops. Secondly, intelligent sensing devices and systems are used to monitor the real-time state of welding manipulator, welding objects, operators, and environment. Finally, based on twin data, historical data, and machine learning algorithm to predict assembling and welding quality, the optimization scheme of parameters is provided to realize the prediction of loading and welding quality and dynamic adjustment of the process.

5. Real-Time Data Collection and Storage

A large amount of quality data will be generated in the process of assembly and welding, which will serve as an important basis for evaluating the quality of assembling and welding. Therefore, the collection and storage of data are very necessary.

5.1. Real-Time Data Collection. As shown in Figure 5, the real-time data collection process is established. The physical sensor network and intelligent sensing equipment (system) to collect the assembly and welding equipment, welding parts, process, and quality information, such as a RFID device, is used to read the unique identification code of the welding parts and obtain the basic information of the welding parts, including the size, number, and process information of the welding parts. Hall sensor is used to detect welding current, welding voltage, and other data. Welding speed and wire feeding speed are detected by photoelectric code disk and speed sensor. An accelerometer and a gyroscope are used to detect the welding gun angle. The visual sensor is used to extract the information of the molten pool in the welding process, and the image processing technology is used to identify the features. On this basis, data transmission is carried out through a wireless network, 5G, Bluetooth, ZigBee, and industrial Internet, as well as data conversion, grouping, analysis, calculation, and fusion, and finally, valuable information oriented to process decision-making and quality prediction is formed.

5.2. Real-Time Data Storage. As shown in Figure 6, firstly, the real-time data of physical welding process is comprehensively analyzed, which is divided into dynamic data and static

data. Static data refers to the information that will not change with the evolution of weldment in the process of weldment processing, such as equipment basic data and weldment basic data. The basic data of weldment includes weldment name, type, material, and process name; basic data of equipment includes equipment name, equipment model, and equipment processing capacity. Dynamic data refers to the information that will change accordingly as the processing state changes during the processing of weldment, such as the current process, start/completion information, and welding processing parameters of the product. The dynamic data directly reflects the real-time status and quality of the weldment and the operation status of the equipment. Secondly, according to the interface protocol between equipment/system and heterogeneous equipment of different manufacturers/models, the OPC-UA communication framework is used to realize the transmission of multisource heterogeneous data and uses XML text to manage and store real-time data.

6. Machine Learning-Based Ship Group Product Assembly and Welding Quality Prediction

With the rise of artificial intelligence, machine learning has developed rapidly. Machine learning is the use of algorithms to analyze data and learn from it and then make predictions and decisions on events. The machine learning algorithm is used to predict the assembly and welding quality online, which realizes the transformation from passive prevention to active prediction and control.

As shown in Figure 7, real-time data (including dynamic data and static data) and historical data (process design data and simulation data) of the welding process are dynamically acquired by sensors and intelligent sensing devices to build quality twin data. The machine learning prediction model is trained by using the historical big data generated in the welding process. A large number of data are optimized interactively in the training process and packaged into corresponding prediction models. Through the real-time monitoring of digital twin and sensor data in the machining process, the condition monitoring and quality prediction of weldment can be realized. In the process of prediction, the real-time

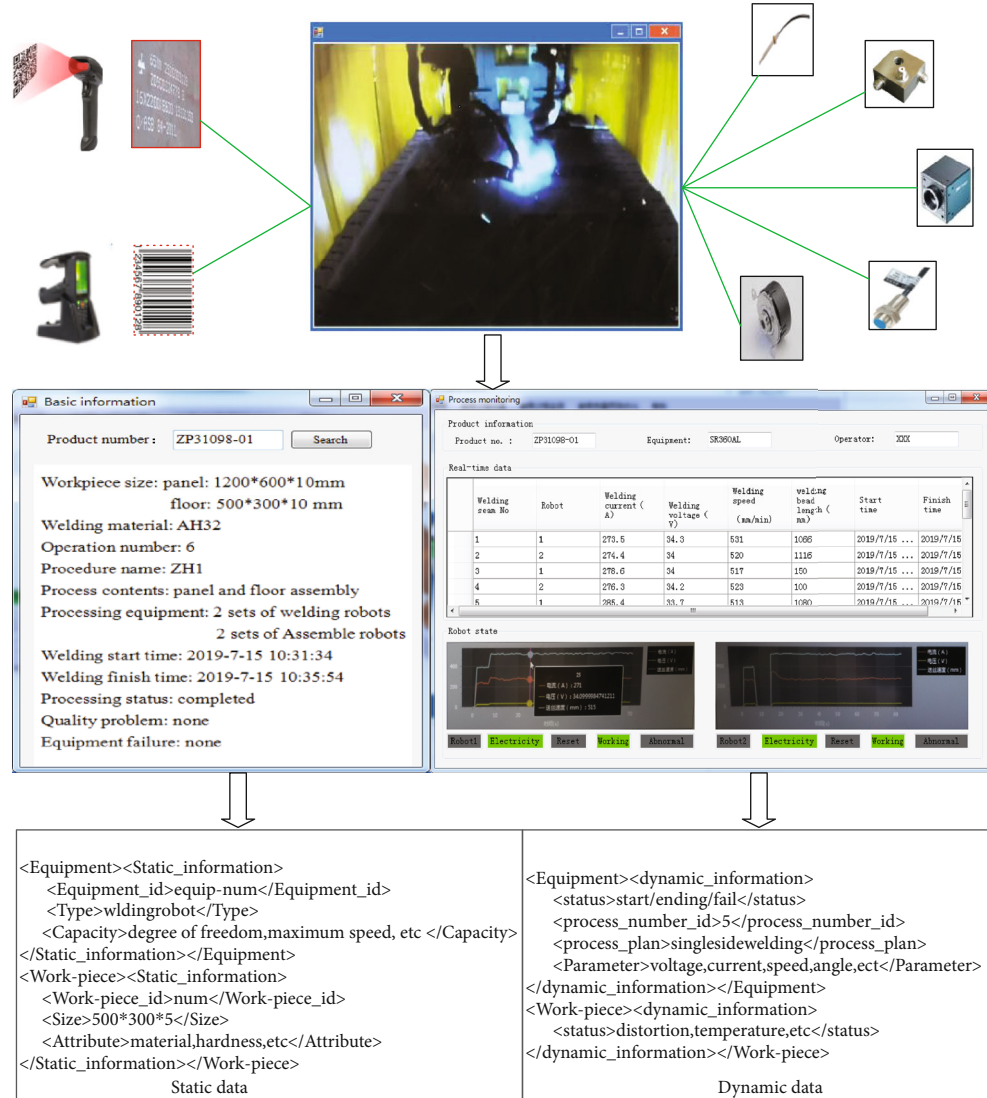


FIGURE 9: Data acquisition and monitoring of small group products.

monitoring data can be tested and corrected according to the historical accumulated data. On the other hand, the historical data can be updated and expanded according to the real-time monitoring data. The welding model in the physical layer dynamically tracks and reflects the latest state of the weldment through its digital twin and optimizes the welding process through simulation, including assembly sequence optimization, welding path optimization, and welding parameter optimization. In this way, we can grasp the trend of quality change in advance, actively prevent quality problems, and achieve dynamic quality assurance. Finally, the fusion and intellectualization of physical information and virtual information in the welding process are realized.

7. Case Analysis

Taking the assembly and welding line of a shipyard as an example, it describes the realization process of the quality prediction and control method of assembly and welding based on digital twin. The production line consists of two

assembly robots, two welding robots, and sensor systems (Hall sensor, optical code plate sensor, acceleration sensor, etc.). The weldment is composed of one panel and two webs, and the material is AH32. The panel size is 500 mm * 400 mm * 12 mm, and the web size is 400 mm * 100 mm * 10 mm. The chemical composition and mechanical properties are shown in Table 2.

The technological process includes the following: the assembly platform determines the assembly position through visual scanning; the assembly manipulator makes the floor plate and panel become positioned vertically; the welding manipulator realizes assembly positioning through spot welding; scanning is done again to determine the position and length of the welding seam, and then installation and welding are performed according to the welding process parameters and process flow imported by the system. During the welding process, the welding processing parameters (welding current, welding voltage, welding speed, etc.) are monitored, and the welding quality is predicted by artificial neural network.

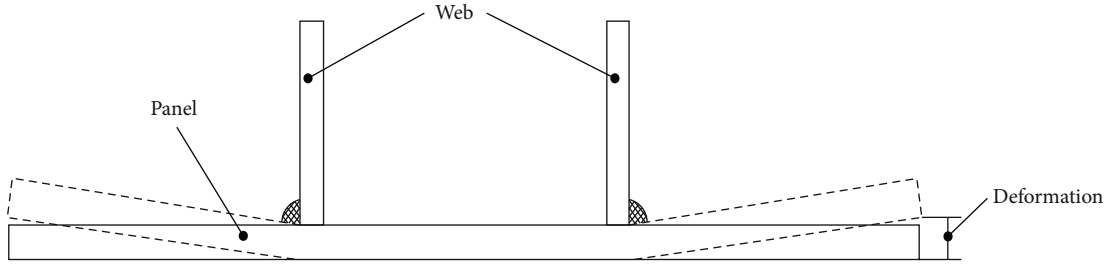


FIGURE 10: Weld angular distortion.

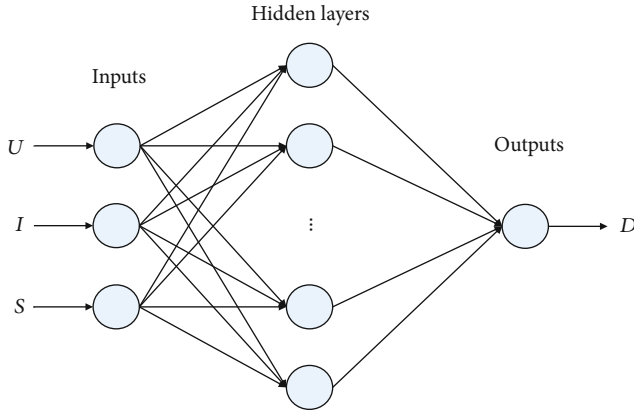


FIGURE 11: BP neural network prediction model.

TABLE 3: Historical data of welding deformation.

Experiment number	U (V)	I (A)	S (mm/s)	D (mm)
1	265	30	4	0.445
2	265	30	6	0.313
3	265	30	8	0.194
4	265	33	4	0.652
5	265	33	6	0.372
6	265	33	8	0.372
7	265	36	4	0.812
8	265	36	6	0.664
9	265	36	8	0.531
10	275	30	4	0.867
11	275	30	6	0.690
12	275	30	8	0.510
13	275	33	4	1.149
14	275	33	6	0.963
15	275	33	8	0.767
16	275	36	4	1.349
17	275	36	6	1.206
18	275	36	8	0.977
19	285	30	4	1.383
20	285	30	6	1.184
21	285	30	8	0.996
22	285	33	4	1.703
23	285	33	6	1.533
24	285	33	8	1.313
25	285	36	4	1.956
26	285	36	6	1.753
27	285	36	8	1.535
28	285	34	7	1.477
29	280	32	5	1.149
30	275	32	5	1.087
31	270	34	7	0.624
32	265	32	5	0.462

7.1. Establishment of a Welding Process Model. The virtual model composed of welding parts and mechanical arm is established. Figure 8(a) shows the product entity of the group, which is composed of a floor plate and two floor plates to complete the welding of the floor plate; Figure 8(b) shows the simulation model of the group production line.

7.2. Real-Time Data Collection and Storage. According to the design requirements, real-time data of the assembly and welding process were collected to dynamically monitor the assembly and welding status of the products. As shown in Figure 9, specific implementation methods include (1) using RFID tags and bar codes to generate static information, such as the size of the welding parts, welding materials, process number, and equipment processing parameters; (2) obtain dynamic information based on multiple intelligent sensors (such as current sensor, speed sensor, temperature sensor, acceleration sensor, and industrial camera), such as equipment parameters, welding deformation, temperature field change, and process execution data; (3) establish data transmission network based on industrial Ethernet to ensure efficient data transmission and data collection; and (4) data storage and management and data related to manufacturing resource status/welding part status are stored in the database in XML format.

7.3. Quality Prediction of Welding Process Based on Artificial Neural Network. A BP neural network is a kind of back propagation neural network. It has strong nonlinear mapping ability, self-learning ability, and self-adaptive ability and has been widely used in nonlinear problems in material engineer-

ing [38–40]. Deformation is one of the main typical problems in welding. Welding deformation has a great impact on the installation accuracy of the structure, and excessive deformation will significantly reduce the bearing capacity of the structure. In this paper, the welding deformation of small group products is predicted by the BP neural network. Since the

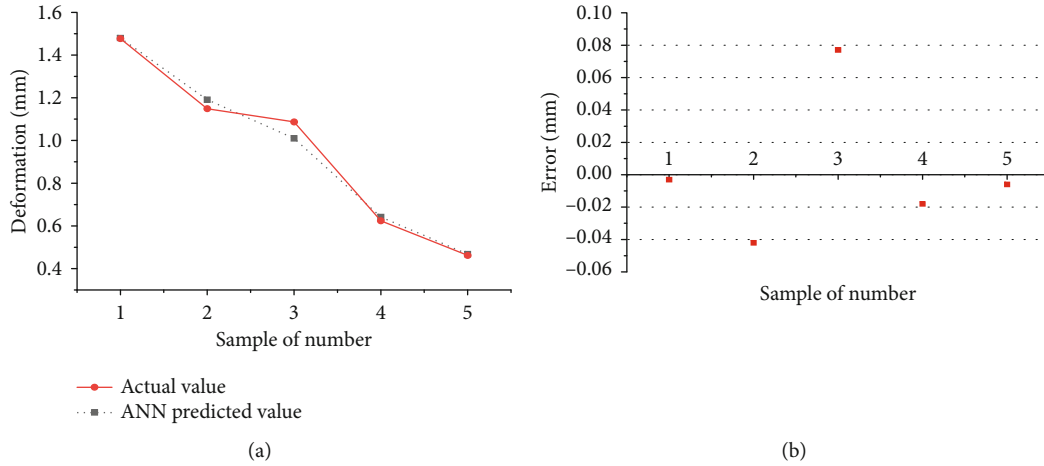


FIGURE 12: Experimental and ANN output: (a) data of deformation; (b) error.

TABLE 4: Comparison of the predicted value and the actual value of welding deformation.

Experiment number	Actual value (mm)	Predicted value (mm)	Error (mm)
1	1.477	1.480	-0.003
2	1.149	1.191	-0.042
3	1.087	1.010	0.077
4	0.624	0.642	-0.018
5	0.462	0.468	-0.006

group product is a symmetrical structure, only the upward deformation of one side of the bottom plate is considered, as shown in Figure 10.

7.3.1. BP Neural Network Model. Through the aforementioned analysis of welding deformation, three quality data of welding voltage (U), welding current (I), and welding speed (S) were selected as the input of the neural network, and the output was the deformation value (D). The learning rate was set at 0.1, the training target was set at 0.01, and the maximum training times was 100, to establish the welding deformation prediction model of the BP neural network. The network topology is “3-10-1,” as shown in Figure 11.

7.3.2. Result Analysis. As shown in Tables 3, 32 sets of data are selected as the basis for analysis. Twenty-seven data were used for training the network, and the remaining 5 data were used for testing the network. The result shows that the predicted value of the artificial neural network is consistent with the actual measured value, as shown in Figure 12. Comparing the predicted value with the actual value, it can be seen that the relative error is small, as shown in Table 4. Therefore, the established prediction model can predict the change trend of welding deformation according to the welding quality parameters and realize the active adjustment of the welding process.

8. Conclusions

The shipping industry is an important strategic industry related to national defense security and national economic development. With the continuous development of industrial Internet, big data, cloud computing, and other information technologies, ship building toward the direction of intelligence and automation has been accelerated. In this paper, digital twin technology is used to solve the problem of assembly and welding quality prediction and control of ship group products. First of all, real-time data acquisition and storage of assembly and welding process are used. Then, the welding quality prediction process based on machine learning is established. Finally, the BP neural network is used to establish the deformation prediction model of group products. The validity and accuracy of the model are verified by comparing the actual value with the predicted value. It can timely grasp the change trend of product processing quality and realize the active control of assembly and welding process quality.

Since welding quality is affected by many factors, it involves multiple data acquisition and fusion and multiobjective quality control, which will be the future research work.

Data Availability

All the data used to support the findings of this study are included within the article.

Conflicts of Interest

The authors declare that they have no conflicts of interests.

Acknowledgments

This work was supported by the Special Funding Project for Key Technologies of Ship Intelligence Manufacturing from the MIIT of China under Grant MC-201704-Z02.

References

- [1] A. E. Öberg and F. Sikström, "Barriers for industrial implementation of in-process monitoring of weld penetration for quality control," *International Journal of Advanced Manufacturing Technology*, vol. 91, no. 5, pp. 1–8, 2017.
- [2] Y. S. Zhang, X. Y. Zhang, X. M. Lai, and G. L. Chen, "Online quality inspection of resistance spot welded joint based on electrode indentation using servo gun," *Science and Technology of Welding and Joining*, vol. 12, no. 5, pp. 449–454, 2013.
- [3] Z. P. Shi, Z. B. Wang, J. Q. Wang et al., "Effect of Ni interlayer on cavitation erosion resistance of NiTi cladding by tungsten inert gas (TIG) surfacing process," *Acta Metallurgica Sinica (English Letters)*, vol. 33, no. 3, pp. 415–424, 2019.
- [4] L. Yang, E. Li, T. Long et al., "A welding quality detection method for arc welding robot based on 3D reconstruction with SFS algorithm," *International Journal of Advanced Manufacturing Technology*, vol. 94, no. 1–4, pp. 1209–1220, 2018.
- [5] H. Wei and K. Radovan, "A laser-based vision system for weld quality inspection," *Sensors*, vol. 11, pp. 506–521, 2011.
- [6] W. P. Gu, Z. Y. Xiong, and W. Wan, "Autonomous seam acquisition and tracking system for multi-pass welding based on vision sensor," *International Journal of Advanced Manufacturing Technology*, vol. 69, no. 1–4, pp. 451–460, 2013.
- [7] X. J. Wang, J. H. Zhou, H. C. Yan, and C. K. Pang, "Quality monitoring of spot welding with advanced signal processing and data-driven techniques," *Transactions of the Institute of Measurement and Control*, vol. 40, no. 6, article 014233121770070, 2017.
- [8] APRISO, *Digital twin: manufacturing excellence through virtual factory replication*, 2014.
- [9] E. J. Tuegel, A. R. Ingraffea, T. G. Eason, and S. M. Spottswood, "Reengineering aircraft structural life prediction using a digital twin," *International Journal of Aerospace Engineering*, vol. 2011, 14 pages, 2011.
- [10] M. Shafto, M. Conroy, R. Doyle et al., *Modeling, simulation, information technology & processing roadmap*, NASA, Washington, D.C., USA, 2012.
- [11] Y. Cai, B. Starly, P. Cohen, and Y.-S. Lee, "Sensor data and information fusion to construct digital-twins virtual machine tools for cyber-physical manufacturing," *Procedia Manufacturing*, vol. 10, pp. 1031–1042, 2017.
- [12] R. Söderberg, K. Wärnefjord, J. S. Carlson, and L. Lindkvist, "Toward a digital twin for real-time geometry assurance in individualized production," *CIRP Annals*, vol. 66, no. 1, pp. 137–140, 2017.
- [13] A. Bilberg and A. A. Malik, "Digital twin driven human-robot collaborative assembly," *CIRP Annals*, vol. 68, no. 1, pp. 499–502, 2019.
- [14] R. B. Roy, D. Mishra, S. K. Pal et al., "Digital twin: current scenario and a case study on a manufacturing process," *International Journal of Advanced Manufacturing Technology*, vol. 107, no. 9–10, pp. 3691–3714, 2020.
- [15] Y. Lu, C. Liu, I. Kevin, K. Wang, H. Huang, and X. Xu, "Digital twin-driven smart manufacturing: connotation, reference model, applications and research issues," *Robotics and Computer-Integrated Manufacturing*, vol. 61, article 101837, 2020.
- [16] K. T. Park, J. Lee, H. J. Kim, and S. Do Noh, "Digital twin-based cyber physical production system architectural framework for personalized production," *International Journal of Advanced Manufacturing Technology*, vol. 106, pp. 1787–1810, 2020.
- [17] J. Leng, Q. Liu, S. Ye et al., "Digital twin-driven rapid reconfiguration of the automated manufacturing system via an open architecture model," *Robotics and Computer-Integrated Manufacturing*, vol. 63, article 101895, 2020.
- [18] F. Tao and M. Zhang, "Digital twin shop-floor: a new shop-floor paradigm towards smart manufacturing," *Computer Integrated Manufacturing System*, vol. 23, pp. 1–9, 2017.
- [19] T. Fei, C. Ying, C. Jiangfeng, Z. Meng, X. U. Wenjun, and Q. I. Qinglin, "Theories and technologies for cyber-physical fusion in digital twin shop-floor," *Computer Integrated Manufacturing System*, vol. 8, pp. 1603–1611, 2017.
- [20] T. Fei, L. Weiran, L. Jianhua et al., "Digital twin and its potential application exploration," *Computer Integrated Manufacturing System*, vol. 24, pp. 1–18, 2018.
- [21] T. Fei, L. Weiran, Z. Meng et al., "Five-dimension digital twin model and its ten applications," *Computer Integrated Manufacturing System*, vol. 25, pp. 1–18, 2019.
- [22] Z. Cunbo, L. Jianhua, X. Hui, D. Xiaoyu, L. Shaoli, and W. Gang, "Connotation, architecture and trends of product digital twin," *Computer Integrated Manufacturing System*, vol. 23, pp. 753–768, 2017.
- [23] Q. Qi, F. Tao, Y. Zuo, and D. Zhao, "Digital twin service towards smart manufacturing," *Procedia CIRP*, vol. 72, pp. 237–242, 2018.
- [24] J. Xie, X. Wang, Z. Yang, and S. Hao, "Virtual monitoring method for hydraulic supports based on digital twin theory," *Mining Technology: Transactions of the Institute of Mining and Metallurgy*, vol. 128, no. 2, pp. 77–87, 2019.
- [25] Warwick Graham, *GE advances analytical maintenance with digital twins*, Aviation Week & Space Technology, 2015, <https://aviationweek.com/special-topics-pages/optimizing-engines-through-lifecycle/ge-advances-analytical-maintenance>.
- [26] J. Olearczyk, M. Al-Hussein, A. Bouferguene, and A. Telyas, "Virtual construction automation for modular assembly operations," *Construction Research Congress*, pp. 406–415, 2009.
- [27] S. H. Han, S. Hasan, A. Bouferguène, M. Al-Hussein, and J. Kosa, "Utilization of 3D visualization of mobile crane operations for modular construction on-site assembly," *Journal of Management in Engineering*, vol. 31, article 04014080, 2014.
- [28] E. Fourgeau, E. Gomez, H. Adli, C. Fernandes, and M. Hagege, "System engineering workbench for multi-views systems methodology with 3D EXPERIENCE platform, the aircraft radar use case," in *Complex Systems Design & Management Asia*, Springer International Publishing, 2016.
- [29] G. L. DNV, *Digital twin at work* <https://www.dnvgl.com/feature/digital-twins.html>.
- [30] L. Jinfeng, Z. Peng, Z. Honggen, L. Xiaojun, and F. Feng, "Digital twin-driven machining process evaluation method," *Computer Integrated Manufacturing System*, vol. 25, no. 6, pp. 1600–1610, 2019.
- [31] J. Liu, H. Zhou, X. Liu et al., "Dynamic evaluation method of machining process planning based on digital twin," *IEEE Access*, vol. 7, pp. 19312–19323, 2019.
- [32] J. Liu, H. Zhou, G. Tian, X. Liu, and X. Jing, "Digital twin-based process reuse and evaluation approach for smart process planning," *International Journal of Advanced Manufacturing Technology*, vol. 100, no. 5–8, pp. 1619–1634, 2019.
- [33] Y. X. Qiao, D. K. Xu, S. Wang et al., "Effect of hydrogen charging on microstructural evolution and corrosion behavior of Ti-

- 4Al-2V-1Mo-1Fe alloy,” *Journal of Materials Science & Technology*, vol. 60, pp. 168–176, 2021.
- [34] Y. X. Qiao, Z. H. Tian, X. Cai et al., “Cavitation erosion behaviors of a nickel-free high-nitrogen stainless steel,” *Tribology Letters*, vol. 67, no. 1, pp. 1–9, 2019.
- [35] H. Taheri, M. Kilpatrick, M. Norvalls et al., “Investigation of nondestructive testing methods for friction stir welding,” *Metals*, vol. 9, no. 6, p. 624, 2019.
- [36] T. Hossein, “Classification of nondestructive inspection techniques with principal component analysis (PCA) for aerospace application,” *26th ASNT Research Symposium*, 2017.
- [37] K. Manjula, K. Vijayarekha, and B. Venkatraman, “Weld flaw detection using various ultrasonic techniques: a review,” *Journal of Applied Sciences*, vol. 14, no. 14, pp. 1529–1535, 2014.
- [38] M. S. Choobi, M. Haghpanahi, and M. Sedighi, “Prediction of welding-induced angular distortions in thin butt-welded plates using artificial neural networks,” *Computational Materials Science*, vol. 62, pp. 152–159, 2012.
- [39] J. Mathew, R. J. Moat, S. Paddea, M. E. Fitzpatrick, and P. J. Bouchard, “Prediction of residual stresses in girth welded pipes using an artificial neural network approach,” *International Journal of Pressure Vessels and Piping*, vol. 150, no. 6, pp. 89–95, 2017.
- [40] Y. Chang, J. Yue, R. Guo, W. Liu, and L. Li, “Penetration quality prediction of asymmetrical fillet root welding based on optimized BP neural network,” *Journal of Manufacturing Processes*, vol. 50, pp. 247–254, 2020.

Research Article

Corrosion Resistance of Waterborne Epoxy Resin Coating Cross-Linked by Modified Tetrabutyl Titanate

Lingli Xu ¹, Zheng Chen,¹ Fei Huang,¹ Yinze Zuo,¹ Xingling Shi ^{1,2,3}
and Xiaowei Zhou ¹

¹School of Materials Science and Engineering, Jiangsu University of Science and Technology, Zhenjiang, China 212003

²Jiuyang Fishing Tackle Co., Ltd., Yangzhou, China 225008

³Jiangsu Gemei High-Tech Development Co., Ltd., Nantong, China 226009

Correspondence should be addressed to Xingling Shi; shixingling1985@hotmail.com
and Xiaowei Zhou; zhouxiaowei901@163.com

Received 15 June 2020; Accepted 21 August 2020; Published 6 October 2020

Guest Editor: Peter G. Keech

Copyright © 2020 Lingli Xu et al. This is an open access article distributed under the Creative Commons Attribution License, which permits unrestricted use, distribution, and reproduction in any medium, provided the original work is properly cited.

The development of waterborne coating is essentially important for environmental protection, and cross-linking agent is of great significance for ensuring corrosion resistance of the coating. In this work, tetrabutyl titanate was modified by ethylene glycol and tris(2-hydroxyethyl) amine and used for the solidification of waterborne acrylic-epoxy resin. Fourier-transform infrared spectroscopy (FTIR) analysis revealed that the agent reacted with OH groups first to cross-link the resin preliminarily, and then, when the amount of agent was further increased, the amino groups opened epoxide rings resulting in a secondary cross-link. Field emission scanning electron microscope (FESEM) observation and electrochemical impedance spectroscopy (EIS) test found that, when the cross-linking agent was used at 6%, the coating remains intact and kept an impedance of as high as $10^8 \Omega \text{cm}^2$ even after being immersed in NaCl solution for 30 days. Copper-accelerated acetic acid-salt spray (CASS) test confirmed that the coating containing 6% cross-linking agent provided the best protection for the carbon steel substrate.

1. Introduction

Due to excellent mechanical properties, mature processing technology, and low price, carbon steel becomes the most widely used engineering material in many fields. Nevertheless, corrosion has long been the problem that has not been well solved, which limits applications of carbon steels, shortens their serving life, and causes accidents and material loss [1–5]. Coating can isolate steel from the aggressive environment and has become an effective method to suppress the corrosion. Nowadays, as the call to protect the environment is growing, the research and application of waterborne coatings have been greatly developed. Among them, the epoxy resin has been widely studied and used due to its high resistance to organic solvents, strong adhesion, high electric insulation, and good thermal shock resistance [6]. However, the waterborne coating still suffers from some weakness. For

example, although waterborne epoxy resin is one of the best developed waterborne coatings, its corrosion resistance is still greatly inferior to that of organic solvent coatings [7, 8]. Studies have shown that a well-designed cross-linking agent could improve the cross-linking density of waterborne resins, enhance their bonding to the matrix, and thus effectively improve the corrosion resistance of the coating. Therefore, the developing of novel cross-linking agent has become one of the research hotspots in the field of waterborne coatings.

In the previous researches on designing of agents, most scholars focused on ring-opening cross-link. For example, Lu et al. prepared a silane-modified waterborne epoxy cross-linking agent and studied the effects of the amount of cross-linking agent on performances of the cured film. They found that hardness, water resistance, and adhesion of the cured film were improved significantly [9]. Sun et al. synthesized a self-emulsified waterborne epoxy cross-linking agent

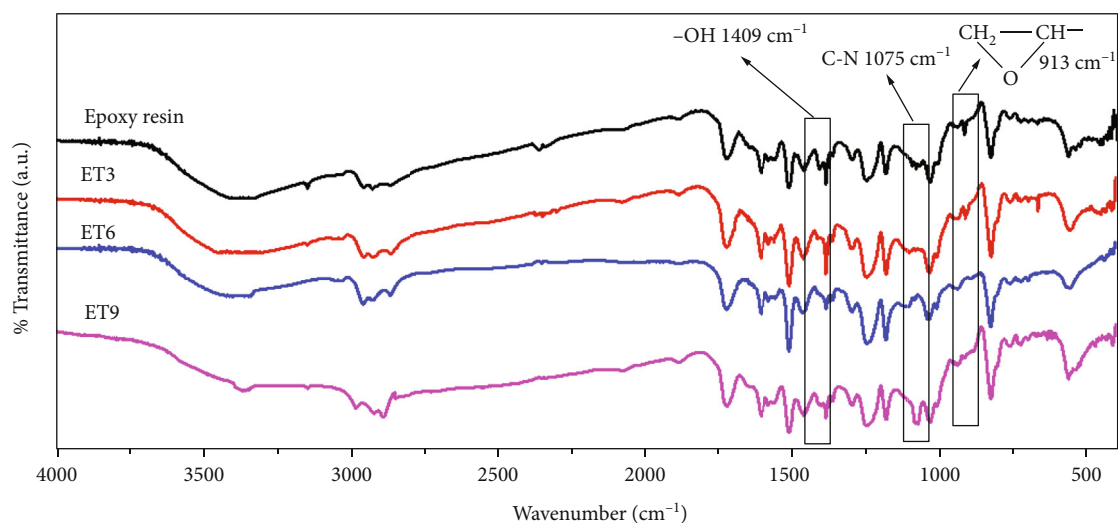


FIGURE 1: FTIR spectra of epoxy resin, ET3, ET6, and ET9 coatings.

of nonionic type using triethylene tetramine (TETA), and they found that epoxy resin film cured by the agent under ambient conditions showed good properties even at high staying temperature [10]. Although films cross-linked through ring-open mode usually showed good water resistance and corrosion resistance within a short period, the durability of the performance needs to be improved urgently.

The molecular structure of the cross-linking agent determines the cross-link mode of the waterborne epoxy resin. Once a proper agent was used, OH groups could also be active groups that could contribute to increasing the cross-link density of the epoxy resin. Given this, our group have developed a novel titanium ion a cross-link agent by modifying tetra-*n*-butyl titanate with ethylene glycol and tris(2-hydroxyethyl) amine and have evaluated its effects on the cure of epoxy ester. It was found that the agent replaced the hydroxyl groups in the epoxy ester and connected cross-link nodes in the coating and, as a consequence, improved the water resistance and corrosion resistance of the coating [11]. Due to excellent solubility in water and excellent long-term storage stability, the acrylic-epoxy emulsion has become the most sophisticated and most widely used waterborne epoxy resin [12, 13]. Therefore, this paper studied the effect of the new cross-linking agent on the cross-link behavior and corrosion resistance of the waterborne acrylic-epoxy coating.

2. Materials and Methods

2.1. Synthesis of the Agent. The titanium ion cross-linking agent was prepared in the same way stated in our previous work [11]. A distillation unit was used for synthesis and pure nitrogen was used for protection. The mole ratio of tetra-*n*-butyl titanate:ethylene glycol:tris(2-hydroxyethyl) amine was 1:1:2.

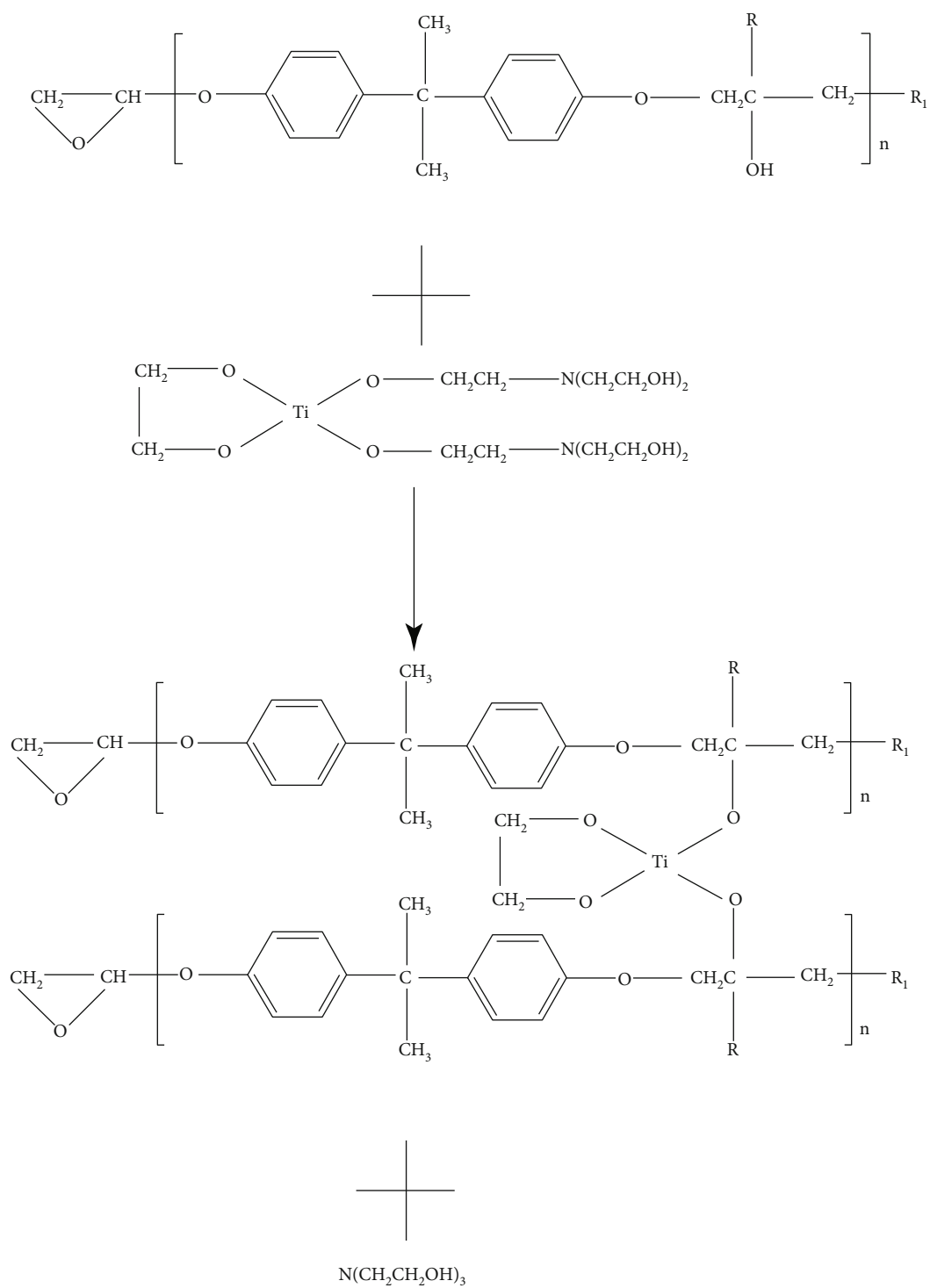
2.2. Cross-Link of Waterborne Epoxy Resin. The cross-linking agent synthesized above was added to the waterborne epoxy resin at a mass ratio of 3%, 6%, and 9%, respectively, and then the mixtures were stirred at a constant speed for 10 min. After adding water of three times the weight of the above mixture, the stirring was conducted again until the resin

was evenly dispersed in the water. Cold rolled A3 mild steel sheets were used as substrate. They were polished by sandpaper of different grades until 1200#, ultrasonically cleaned with acetone and ethanol, and dried in air. The mixtures were coated onto steel sheets, respectively, by the brushing method, and then the coatings were solidified at 80°C for 3 h. Thickness of coatings was monitored by Elcometer Kairda KD 5 and was about 65 μm . Coatings were coded according to the content of a cross-link agent and were ET3, ET6, and ET9 in sequence. Waterborne epoxy resin without a cross-link agent was used as control.

2.3. Characterizations. The FTIR spectra of the coatings were recorded with an ATR-Nicolet iS10 Spectrometer (Thermo Fisher Scientific, USA). The surface morphology of the cured film was characterized by ZEISS Merlin Compact (ZEISS, Germany). Electrochemical impedance spectroscopy (EIS) study was carried out using an electrochemical workstation (PGSTAT302N, Metrohm Autolab, The Netherlands). A standard three-electrode system was used, including sample as a working electrode, a platinum counter electrode (CE), and a saturated calomel electrode (SCE) as reference. The measurement was conducted in 3.5% NaCl solution, and an AC voltage with 10 mV amplitude (vs. SCE) was used as the imposed signal. Immersion test was carried out in 3.5% NaCl solution up to 30 days, and the results were recorded by digital camera. Copper salt-accelerated acetate spray (CASS) test was conducted according to ISO 3770-1976.

3. Results and Discussions

3.1. FTIR Analysis. Figure 1 shows the FTIR spectra of epoxy resin, ET3, ET6, and ET9 coatings. The absorption peak located at 913 cm^{-1} could be assigned to the stretching vibration of the saturated epoxy ring; the one at 1409 cm^{-1} represents O-H bending vibrations in epoxy resin [6, 10]. In the spectrum of the coating without the agent, both peaks could be observed clearly, which meant the cross-linking degree of resin was at a low level. When 3% of agent was used, the signal



(a)

FIGURE 2: Continued.

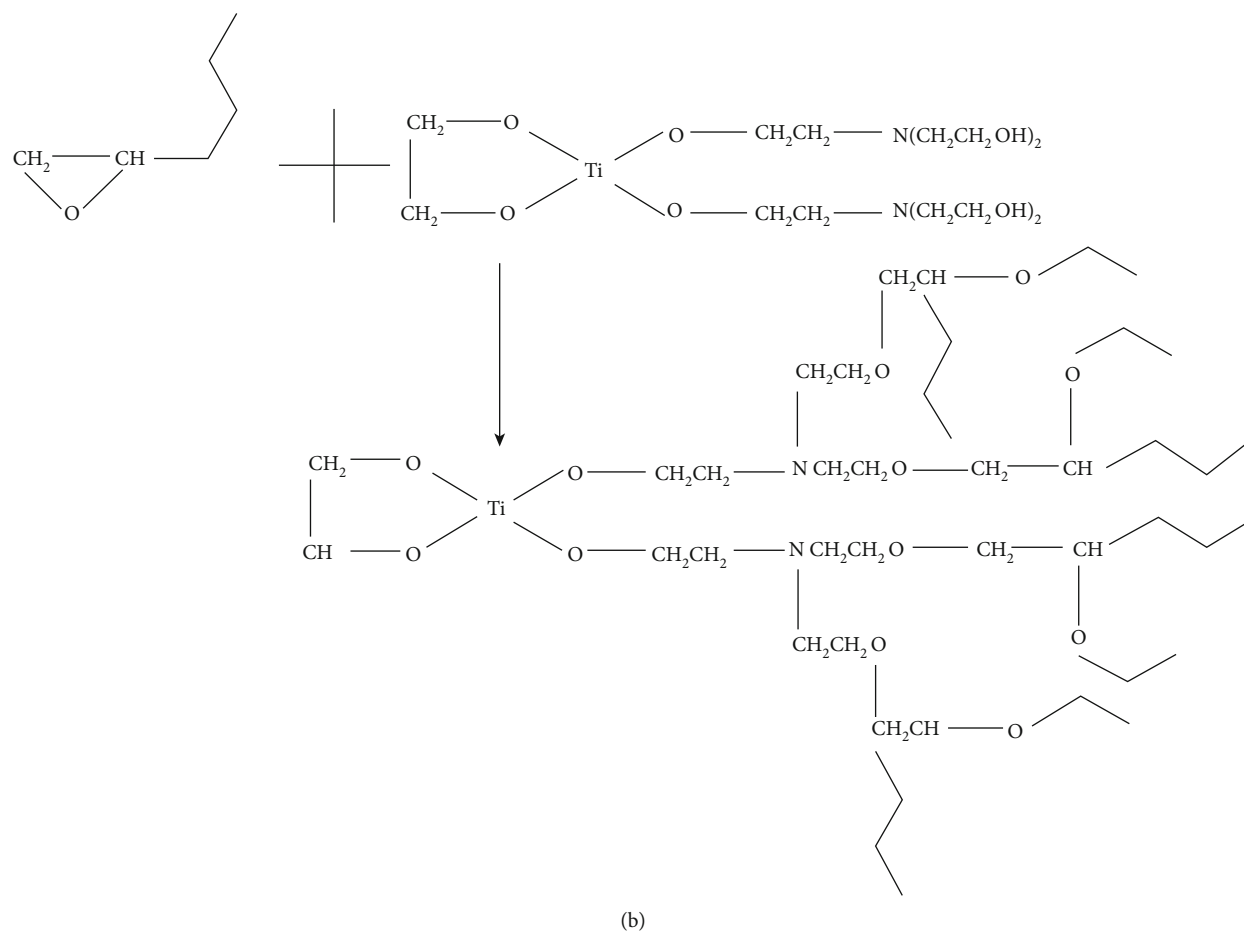


FIGURE 2: Stages involved in the reaction between epoxy ester and titanium ion curing agent. (a) Stage 1 reaction between the -OHs and titanium ion curing agent. (b) Stage 2 Reaction between the epoxide ring of and amino group.

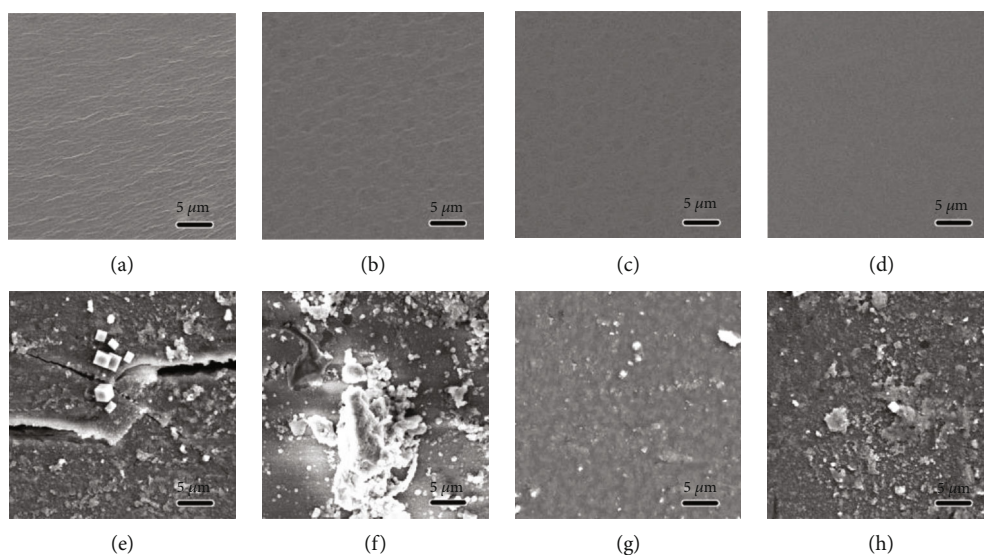


FIGURE 3: FESEM images of coating from epoxy, ET3, ET6, and ET9 before (a-d) after (e-h) 30 days of immersion in 3.5% NaCl solution.

from O-H group disappeared and that from epoxy ring decreased; as amount of agent increased to 6%, both absorption peaks disappeared; when 9% of agent was used, both peaks disappeared while a strong C-N stretching vibration

peak appeared. Those changes indicated that when more agent was added into resin, the cross-linking degree increased as a consequence, and agent of 6% was enough for a sufficient cross-link, whereas, when 9% of agent was used, an excessive

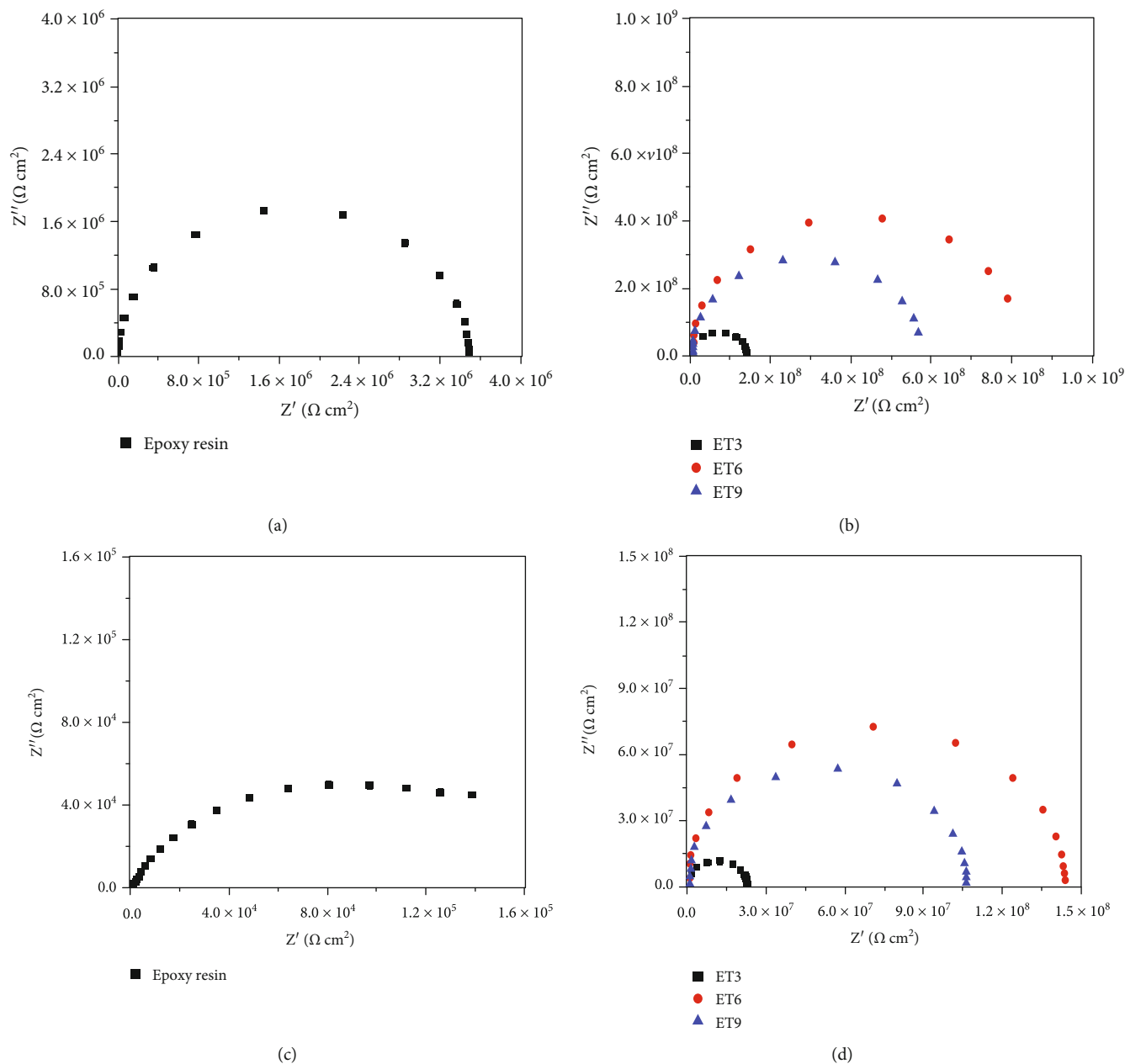


FIGURE 4: Nyquist plots of coatings after 10 days of immersion (a, b) and 30 days of immersion (c, d).

cross-linking agent would remain in the coating. The FTIR results also suggested a chemical reaction as follows: first, the agent reacted with the O-H to cross-link resin primarily, and then, with the further increase of the cross-linking agent, the epoxy ring in the epoxy resin was opened by the $-NH_3$ group, and the resin could be cross-linked further. Based on FTIR results, the reaction scheme is illustrated in Figure 2.

The double cross-linking initiated by the new agent increased cross-linking density and would definitely enhance the shielding properties of the coating, improving the corrosion resistance of the coating [11, 14, 15]. Nevertheless, if excessive cross-linking agent remains in the cured resin, it would impair the shielding property since the agent itself was hydrophilic and tends to adsorb water. Actually, the con-

tact angle of distilled water on epoxy resin, ET3, ET6, and E9 was 61.6, 75.8, 88.0, and 80.5°, respectively.

3.2. Morphologies of Coatings. Figure 3 shows the surface topography of coatings containing different amounts of cross-linking agent before and after immersion. It could be seen that numerous wrinkles formed on the surface of epoxy coating without agent, whereas, as the amount of agent increased, the surface of coating become smoother and smoother. When the cross-linking agent was absent, the cross-link of resin heavily depended on the evaporation of water. Since the evaporation rate of water in the surface and interior of the coating was inconsistent, the cross-link progressed asynchronously and thus caused the formation

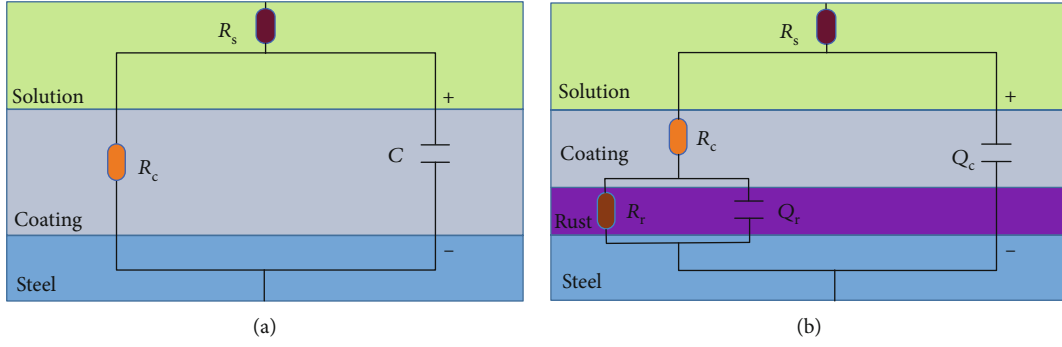


FIGURE 5: Equivalent circuits used to interpret impedance data.

TABLE 1: Parameters gained from fitting of the EIS data after 10 and 30 days of immersion in 3.5% NaCl solution.

Coating	R_c ($\Omega \text{ cm}^2$)	C (F)	Q_c ($\Omega^{-1} \text{ s}^n \text{ cm}^{-2}$)	n	R_r ($\Omega \text{ cm}^2$)	Q_r ($\Omega^{-1} \text{ s}^n \text{ cm}^{-2}$)	n	Equivalent circuit model	Immersion duration/days
Epoxy	3.5×10^6	2.2×10^{-8}	—	—	—	—	—	A	10
ET3	1.0×10^8	1.4×10^{-9}	—	—	—	—	—	A	
ET6	8.3×10^8	2.6×10^{-10}	—	—	—	—	—	A	
ET9	5.7×10^8	2.1×10^{-9}	—	—	—	—	—	A	
Epoxy	1.3×10^5	—	1.8×10^{-9}	0.61	575	1.1×10^{-5}	0.52	B	30
ET3	2.3×10^7	2.5×10^{-9}	—	—	—	—	—	A	
ET6	1.5×10^8	1.1×10^{-9}	—	—	—	—	—	A	
ET9	1.1×10^8	1.3×10^{-9}	—	—	—	—	—	A	

of wrinkles on the surface [16]. With the addition of cross-linking agent, evaporation of water becomes a negligible factor that promotes cross-link, and the cross-link could happen although the coating synchronously, and therefore, the wrinkles and cloud-like pattern disappeared gradually.

After 30 days of immersion, the surface morphology of the coating varied depending on the content of the cross-linking agent. Wide and deep cracks could be seen on the surface of the coating without agent while shallow erosion gullies were found on coating with 3% of agent. When 9% of agent was used, the coating surface became much rougher and showed a tendency of fragmentation. In contrast, the coating containing 6% of agent remained intact although the surface became relatively rough. It could be seen that the addition of the cross-linking agent greatly improved the water resistance of the coating; however, if the initial amount was excessive, the residual agent would cause decrease in durability in corrosive medium.

3.3. EIS Study. EIS data obtained from different coatings are shown in Figure 4. After 10 days of immersion, all the Nyquist plots presented as semicircles, and it meant at this stage, all the coatings remained intact and behaved as a perfect barrier layer to the aggressive medium. The plot could be well fitted by the circuit model (a) in Figure 5, in which, R_s was the solution resistance, C was assigned to the capacitance of the coating, and R_c represented resistance of the coating. The fitting results are presented in Table 1. After 30 days of immersion, two time constants could be noticed

in the Nyquist plot of coating without a cross-link agent, indicating that corrosive medium has reached the interface of coating and steel and rusting had started. At this point, the behavior of epoxy coating without a cross-link agent could be interpreted by the model (b) in Figure 5, where Q_c was assigned to CPE of polymer coating and R_r and Q_r represented resistance and CPE of the rust layer. In contrast, the plots of coating with a cross-link agent kept the shape of semicircle, and therefore, the EIS data were interpreted using the model (a) again. The fitting results are shown in Table 1 as well. According to previous reports, an epoxy coating with a resistance of $10^6 - 10^9 \Omega \text{ cm}^2$ was considered to have a good protection for the substrate [17–19]. It was obvious that the use of cross-linking agent increased impedances of coatings significantly, and more importantly, it could help maintaining the high impedance after 30 days of immersion.

The appearances of the specimens coated with epoxy with different amounts of cross-link agent before and after immersed in 3.5% NaCl solution are shown in Figure 6. All the coatings were intact and almost transparent before immersion, and the freshly polished steel substrate could be seen clearly. After 30 days of immersion, rust was observed all over the steel under coating without a cross-link agent, and serious leakages could also be observed in some regions. Both ET3 and ET9 coatings remained intact, and rust was not observed; however, white cloudy areas could be seen, and this indicated that medium had penetrated into the coating deeply and might reach the substrate shortly. In contrast,

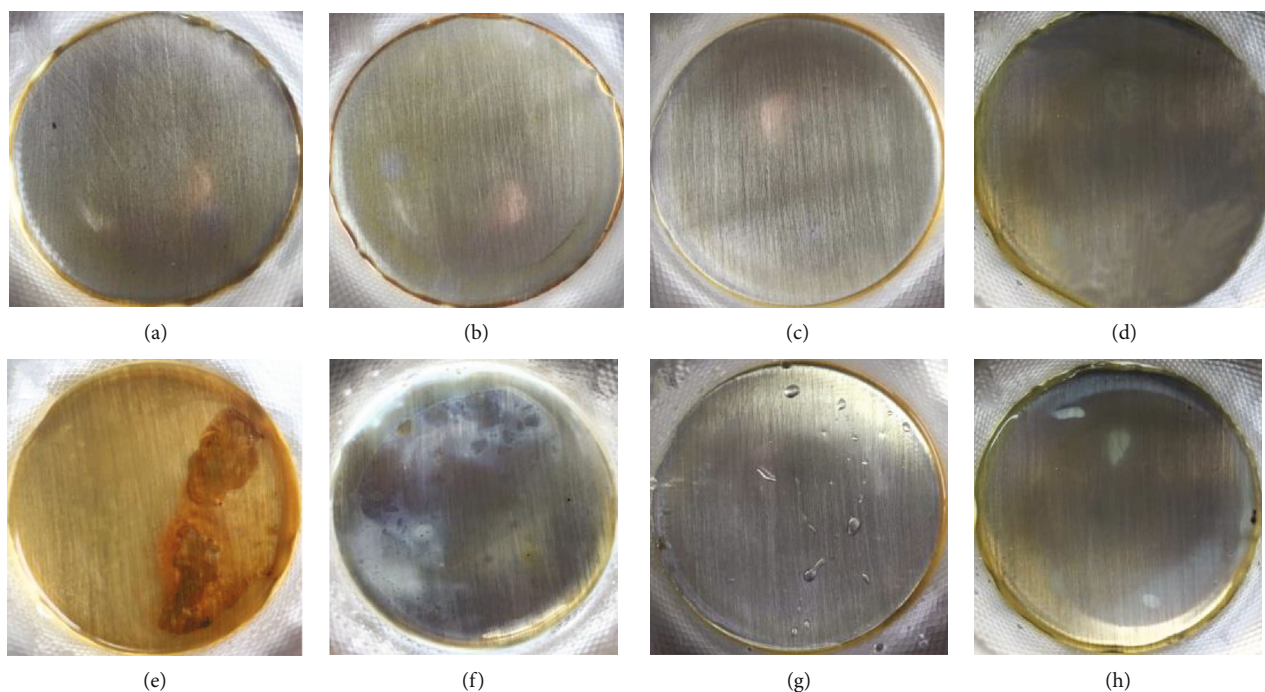


FIGURE 6: Appearance of epoxy resin, ET3, ET6, and ET9 coating before (a–d) and after (e–h) 30 days of immersion in 3.5% NaCl solution.

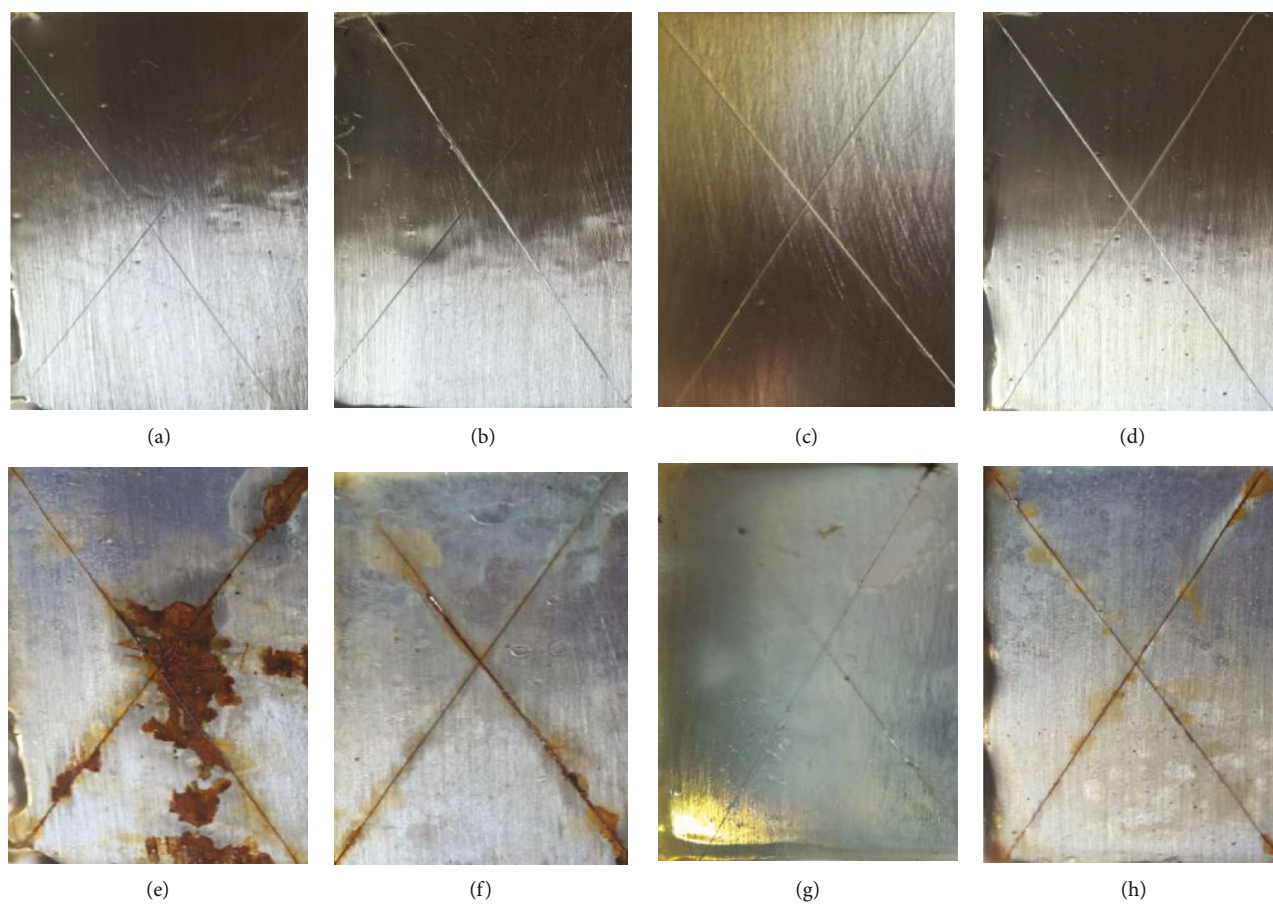


FIGURE 7: Appearances of epoxy, ET3, ET6, and ET9 coatings before (a–d) and after (e–h) 5 days of the CAAS test.

TABLE 2: Corrosion resistance rating of coatings after 5 days of CAAS.

Coatings	Rating
Epoxy resin	1
ET3	4
ET6	6
ET9	5

ET6 coating not only protected the substrate well but also showed excellent stability in the medium that changes in the appearance could hardly be seen. The use of even very small amounts of the agent in the epoxy coating could significantly increase the cross-link density and thus helped blocking invasion of the corrosive medium [20]. However, when the content of the agent exceeds the optimum content, it would increase the water absorbability of the coating and reduce the stability and durability of the coating.

3.4. CAAS Test. The appearances of specimens before and after 5 days of CAAS test are shown in Figure 7. For the specimen coated with epoxy without a cross-link agent, large bubbling areas could be observed, and when coating was peeled off from the steel, severe corrosion along the scratches happened and plenty rust could be seen. For ET3 coating, the corrosion products appeared along the scratches and were accompanied by blisters and slight peeling of the coating. For ET9 coating, only small blisters could be seen along the scratches, while the rest of the coating remained unaffected. It was worth noticing that the ET6 coating kept intact, nor blisters or any corrosion product could be seen along the scratches. From the above observation, the corrosion resistance of coating could be ranked in the following order incontestably: ET6 > ET9 > ET3 > epoxy. Besides, according to a system established by Abhijit et al. [21], the corrosion resistance of the coatings could be also rated clearly as shown in Table 2.

4. Conclusion

A novel cross-link agent was synthesized by modifying etran-butyl titanate with ethylene glycol and tris(2-hydroxyethyl) amine. The agent initiated double cross-link, greatly increased cross-linking density of waterborne acrylic-epoxy resin, and increased the impedance from $10^6 \Omega \text{cm}^2$ to $10^8 \Omega \text{cm}^2$. After 30 days of immersion, NaCl solution passed through the coating without the cross-linking agent, causing the substrate to corrode, while all the coatings with a cross-linking agent could protect the substrate well. The copper-accelerated acetic acid-salt spray test also confirmed that the adding of cross-linking agent had greatly improved protecting function of the coating. In summary, the environmentally friendly and efficient novel cross-linking agent will be promising for the application for waterborne acrylic-epoxy resin coating.

Data Availability

The FTIR, SEM, EIS, and photos used to support the findings of this study are included within the article.

Conflicts of Interest

The authors declare that they have no conflicts of interest.

Acknowledgments

We acknowledge gratefully the financial support from the Natural Science Foundation of the Jiangsu Province (BK20160566) and Open Foundation of Zhenjiang Key Laboratory for High Technology Research on Marine Function Films (ZHZZ2019007).

References

- [1] Z. Liu, X. Gao, L. Du et al., "Comparison of corrosion behaviour of low-alloy pipeline steel exposed to H₂S/CO₂-saturated brine and vapour-saturated H₂S/CO₂ environments," *Electrochimica Acta*, vol. 232, pp. 528–541, 2017.
- [2] Y. Qiao, J. Huang, D. Huang et al., "Effects of laser scanning speed on microstructure, microhardness and corrosion behavior of laser cladding Ni45 coatings," *Journal of Chemistry*, vol. 2020, Article ID 1438473, 11 pages, 2020.
- [3] W. Yao, M. Tebyetekerwa, X. Bian et al., "Materials interaction in aggregation-induced emission (AIE)-based fluorescent resin for smart coatings," *Journal of Materials Chemistry C*, vol. 6, no. 47, pp. 12849–12857, 2018.
- [4] Y. B. Lai, P. Y. Guo, H. Sun, Y. Zhang, L. L. Guan, and Y. X. Wang, "Impedance Spectra Characteristics of Fe-Cr Alloys in the Presence of a Solid K₂SO₄-KCl Mixture at 600°C in air," *International Journal of Electrochemical Science*, vol. 13, pp. 7827–7845, 2018.
- [5] Y. Qiao, D. Xu, S. Wang et al., "Effect of hydrogen charging on microstructural evolution and corrosion behavior of Ti-4Al-2V-1Mo-1Fe alloy," *Journal of Materials Science & Technology*, vol. 60, pp. 168–176, 2021.
- [6] S. Qiu, C. Chen, M. Cui, W. Li, H. Zhao, and L. Wang, "Corrosion protection performance of waterborne epoxy coatings containing self-doped polyaniline nanofiber," *Applied Surface Science*, vol. 407, pp. 213–222, 2017.
- [7] J. Zhang, W. Zhang, J. Lu, C. Zhu, W. Lin, and J. Feng, "Aqueous epoxy-based superhydrophobic coatings: fabrication and stability in water," *Progress in Organic Coatings*, vol. 121, pp. 201–208, 2018.
- [8] S. Xu, N. Girouard, G. Schueneman, M. L. Shofner, and J. C. Meredith, "Mechanical and thermal properties of waterborne epoxy composites containing cellulose nanocrystals," *Polymer*, vol. 54, no. 24, pp. 6589–6598, 2013.
- [9] L. U. Guangqi, J. SUN, and Q. ZHOU, "Synthesis and characterization of waterborne epoxy Curing agent modified by silane," *Chinese Journal of Chemical Engineering*, vol. 15, no. 6, pp. 899–905, 2007.
- [10] H. Sun, W. Ni, B. Yuan et al., "Synthesis and characterization of emulsion-type cross linking agent of water-borne epoxy resin," *Journal of Applied Polymer Science*, vol. 130, no. 4, pp. 2652–2659, 2013.

- [11] Y. Zuo, L. Chen, X. Shi, and Y. Gao, "Study on corrosion resistance of epoxy ester coating cross-linked by a new type of titanium ion curing agent," *Progress in Organic Coatings*, vol. 115, pp. 86–93, 2018.
- [12] C. R. Hegedus, F. R. Pepe, J. B. Dickenson, and F. H. Walker, "Waterborne acrylic-epoxy coatings," *Journal of Coatings Technology*, vol. 74, no. 4, pp. 31–39, 2002.
- [13] H. Bernacki, Z. Fu, B. Li, D. Lindenmuth, and L. Procopio, "Enhancing the uv durability of epoxy coatings: waterborne acrylic-epoxy hybrid coatings for steel," *Journal of Protective Coatings & Linings*, vol. 35, pp. 44–54, 2018.
- [14] T. Okabe, Y. Oya, K. Tanabe, G. Kikugawa, and K. Yoshioka, "Molecular dynamics simulation of crosslinked epoxy resins: curing and mechanical properties," *European Polymer Journal*, vol. 80, pp. 78–88, 2016.
- [15] X. Zhou and C. Ouyang, "Wear and corrosive behaviors of electroless Ni-LaCl₃ composites on nanoporous ATO surface of Ti substrate," *Journal of Materials Engineering and Performance*, vol. 28, no. 5, pp. 2499–2512, 2019.
- [16] V. H. V. Sarmento, M. G. Schiavetto, P. Hammer et al., "Corrosion protection of stainless steel by polysiloxane hybrid coatings prepared using the sol-gel process," *Surface & Coatings Technology*, vol. 204, no. 16–17, pp. 2689–2701, 2010.
- [17] G. P. Bierwagen, L. He, J. Li, L. Ellingson, and D. E. Tallman, "Studies of a new accelerated evaluation method for coating corrosion resistance—thermal cycling testing," *Progress in Organic Coatings*, vol. 39, no. 1, pp. 67–78, 2000.
- [18] L. G. Gray and B. R. Appleman, "EIS: electrochemical impedance spectroscopy," *Journal of Protective Coatings & Linings*, vol. 20, pp. 66–74, 2003.
- [19] Y. Qiao, Z. Tian, X. Cai et al., "Cavitation erosion behaviors of a nickel-free high-nitrogen stainless steel," *Tribology Letters*, vol. 67, no. 1, 2019.
- [20] F. Rafiaei, R. Naderi, and C. Dehghanian, "Impact of curing on the corrosion performance of an eco-friendly silane sol-gel coating on 304l stainless steel," *RSC Advances*, vol. 5, no. 54, pp. 43225–43233, 2015.
- [21] S. Abhijit, P. A. Mahanwar, and V. A. Bambole, "Effect of polypyrrole on the properties of conventional epoxy coatings," *Pigment & Resin Technology*, vol. 42, no. 5, pp. 317–325, 2013.

Research Article

The Effects of Sand Particles on the Synergy of Cavitation Erosion-Corrosion of MIG Welding Stainless Steel Coating in Saline Water

Haodan Pan ¹, Jun Tao,¹ Meng E,^{2,3} Hongxiang Hu ² and Zhengbin Wang²

¹College of Petroleum Engineering, Liaoning Shihua University, Fushun 113001, China

²CAS Key Laboratory of Nuclear Materials and Safety Assessment, Institute of Metal Research, Chinese Academy of Sciences, Shenyang 110016, China

³School of Materials Science and Engineering, Shenyang Aerospace University, Shenyang 110136, China

Correspondence should be addressed to Haodan Pan; panhaodan@126.com and Hongxiang Hu; hxhu@imr.ac.cn

Received 26 August 2020; Revised 6 September 2020; Accepted 15 September 2020; Published 28 September 2020

Academic Editor: Jian Chen

Copyright © 2020 Haodan Pan et al. This is an open access article distributed under the Creative Commons Attribution License, which permits unrestricted use, distribution, and reproduction in any medium, provided the original work is properly cited.

Cavitation erosion (CE) is a common problem troubling many flow-handling equipment such as valves, orifice plate pipes, and propellers. The coating technique is a widely used strategy to resist CE. It is important to understand the CE-corrosion behavior of the coatings in the corrosive solution, especially in the sand-containing saline water. A newly designed MIG welding precipitated hardened martensitic stainless steel (PHMSS) coating was performed, and its silt-CE was investigated in a suspension composed of 3.5 wt.% sodium chloride and 3% silica sand using an ultrasonic vibrator processor. The microstructure of the coating was characterized by optical microscopy and scanning electron microscopy. The effects of the sand particles on the CE-corrosion were analyzed using mass loss measurement, potentiodynamic polarization curve, and surface morphology observation. The results showed that the PHMSS coating was mainly composed of the lath martensitic phase alone. Its mass loss rate was in ascending order in the solution of distilled water alone, sand-containing distilled water, saline water alone, and sand-containing saline water. Sand particles played more roles in the CE in the distilled water than in the saline water. The synergy of CE and corrosion was much less in the sand-free saline than in the sand-containing saline. The maximum component was the erosion enhancement due to the corrosion in the saline without sand particles but was the pure erosion component in the saline with sand particles. The mechanism of the sand particles' effect on the CE was also discussed.

1. Introduction

Cavitation erosion (CE) provokes a high degree of discussion in the fields of flow-handling systems such as impellers, valves, turbines, pumps, and pipes [1–5]. It is mainly due to its complex processes including the bubble nucleation, high-pressure collapsing, and the interaction between the bubble and the material surface. Complex serving conditions also give great difficulty to the investigations including CE and corrosion. The main problem lies in the lack of understanding of the synergy between the mechanical damage caused by the CE and the corrosion caused by corroded ions. Therefore, the clarification to the synergy of the CE and corrosion is essential to the material design and equipment maintenance.

The synergy effect on the CE and corrosion has captured many results. The CE behavior in the corrosive liquid is related to the two main effects of mechanical abrasion and electrochemical corrosion [6–8]. The CE of the materials with good corrosion resistance was less affected by the corrosion-induced damage [9]. Normally, synergy components of the CE and the corrosion were higher than the sum of the pure CE and the pure corrosion [8, 10, 11], while, on some conditions, the minus synergy of the CE and corrosion is less than the pure sum-up of the CE and the corrosion [12, 13]. However, these studies above are obtained in pure liquid solutions. They are doubt to be applied to the conditions with solid particles like the impeller serving in the river with sands. Sand particles can reduce the tensile strength of the solution [14] and affect both the number of the bubble

TABLE 1: Chemical compositions of the welding wire (wt.%).

Comments	C	Cr	Ni	Mo	Nb	Cu	Si	Mn	P	S	Fe
Content	0.024	16.30	4.92	0.40	0.21	3.52	0.45	0.61	0.012	0.03	Bal.

nucleation and the collapse of the bubbles [15]. Even their surface configuration and chemical composition have effects on the CE [16]. Unfortunately, few studies pay attention to the effect of the sand particles on the synergy action of the CE and corrosion. Hu and Zheng [17] investigated the effect of the sand concentration on the CE, but no synergy of the CE and corrosion was referred.

The solid particles have a complex influence on the CEs [14, 17–21]. They affect the CE in the way of changing the solution tensile strength [14], the bubble nucleation and collapse [15], and the erosion direction to the material surface [18]. The CE configurations vary with the surface morphology [16], concentration [17], and size [19, 22] of the solid particles. It can be observed that the understanding of the effect of the solid particles on the corrosion is far less than that on the mechanical damage (CE). For the passive materials, the passive film on the material surface plays an important role in the CE, especially the corrosion [23, 24]. However, the clarification of the effect of the solid particles on the corrosion remains unknown on the condition of CE.

Martensitic stainless steel attracts many investigations due to its higher resistance to the CE than the austenitic and ferritic stainless steel [25]. Metal inert gas (MIG) welding martensitic stainless steel coating is a promising method to resist the CE and corrosion, like the AISI 431 [26], AISI 410 [27], and CA-6NM [28]. Further enhancement in the resistance to the CE was also carried out on the stainless steel by the nitriding process [29, 30], laser surface melting [9], and welding [31, 32]. MIG welding is widely applied in many maintenances to the component suffering slurry erosion and CE due to its convenient operation. In the present study, a newly designed precipitated hardened martensitic stainless steel coating was prepared on 35 forged steel by a MIG welding method. Its CE-corrosion behavior was investigated in a sand suspension of 3.5 wt.% NaCl and 3 wt.% silica sand. The effects of sand particles on the interactions between the CE and the corrosion were also discussed.

2. Experimental

2.1. Coating Preparation. A newly designed wire of precipitated hardened martensitic stainless steel was used as filler wire in the MIG welding process. Its chemical composition is listed in Table 1. The MIG welding precipitated hardened martensitic stainless steel (PHMSS) coating was prepared on a cast steel, ASTM 485-275 (70-40). Before the deposition of the coatings, the substrate surface was derusted and ground to remove the surface oxides and contaminants. The MIG welding process was carried out using a Quinto-GLC403 digitalized MIG welding machine automatically with the protecting gas of argon (98%) and CO₂ (2%). Table 2 lists the other optimized details of the MIG welding.

TABLE 2: Process parameters of the MIG surfacing.

Process parameters	Value
Wire speed (m•min ⁻¹)	12.00
Pulse frequency (Hz)	220
Base current (A)	140
Pulse time (ms)	2.20
Pulse voltage (V)	37
Pulse shape	Steep

2.2. Cavitation Erosion Test. The CE-corrosion experiments were conducted using an ultrasonic vibratory oscillator (Q700 Sonicator) resonating at 20 kHz with a peak-to-peak amplitude of 15 μ m at 25 \pm 1°C. The experimental processes were based on the ASTM G32-10 Standard [33]. A volume of 80 mL of different solution was used as the experimental solution in a stainless beaker including the distilled water with and without 3 wt.% silica sand (200-300 meshes) and the saline water of 3.5 wt.% NaCl with and without 3 wt.% silica sand (200-300 mesh). The test specimen was fixed in a holder as the lower specimen, which was installed coaxially with the horn tip at a constant distance of 0.5 mm. The experimental instrument and its specimen dimensions are sketched in Figure 1. All the specimens were gradually ground to 2000 grit abrasive papers, ultrasonically degreased with ethyl alcohol, and hot air-dried with a blower before the experiments. The weight of the specimens was measured by an analytical balance with an accuracy of 0.1 mg. The average value of at least three experiment data was utilized to make sure the representativeness and reproducibility.

2.3. Electrochemical Measurements. All electrochemical experiments were performed in the saline solution containing 3.5 wt.% NaCl at 25 \pm 1°C. The experiments were carried out with an electrochemical cell (Gamry Interface 1000) accompanied by a traditional three-electrode cell comprising a standard saturated calomel electrode (SCE) as the reference electrode, a platinum slice as the counter electrode, and a sample as the working electrode [34]. The sample was prepared according to the same processes as those for the CE tests and sealed with epoxy with an exposure area of 1.83 cm². Polarization measurements were conducted after 1 h open circuit potential (OCP) tests with a stable potential, and the potential range was from -0.5 V to 0.7 V vs. OCP at a scan rate of 0.5 mV/s. Each experiment was repeated at least three times to ensure reproducibility.

2.4. Surface Observation. X-ray diffraction (XRD, D/Max-2500PC) was employed to identify phase constituents at a Cu K α radiation, a voltage of 40 kV, and a current of 40 mA. Microstructures of the coatings were analyzed by optical microscopy (OM, Carl Zeiss). Before the microstructure observation, the

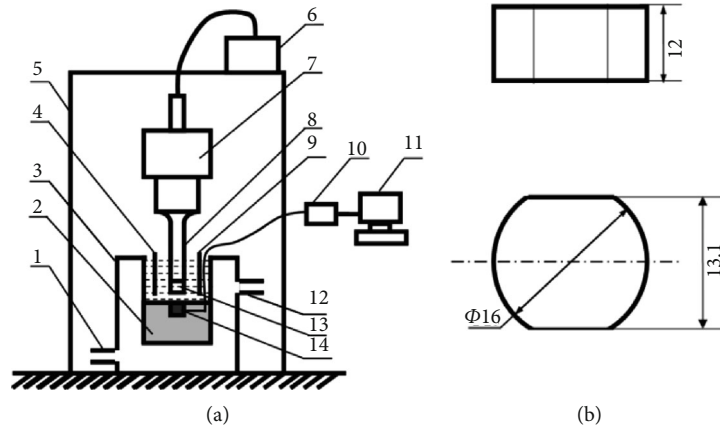


FIGURE 1: Schematic diagram of (a) ultrasonic CE equipment and (b) specimen dimensions. 1: water inlet; 2: nylon support; 3: cooling bath; 4: reference electrode; 5: soundproof enclosure; 6: ultrasonic generator; 7: transducer; 8: horn; 9: counter electrode; 10: electrochemical workstation; 11: computer; 12: water outlet; 13: horn tip; and 14: working electrode.

sample surface was etched with a solution of 5 g FeCl_3 , 50 mL HCl , and 100 mL H_2O . The microhardness of the coating was measured with an automatic microhardness tester at a load of 1.96 N and a duration time of 15 s. Stereomicroscopy (Stemi 2000, Carl Zeiss) and scanning electron microscopy (SEM, XL-30FEG) were employed to reveal the eroded morphologies after tests. The surface roughness was examined by a white light interferometer (MicroXAM).

3. Results and Discussion

3.1. Coating Characterization. Figure 2 shows the X-ray diffraction patterns of the coating surface. It can be seen that the diffraction peaks are located at 42° , 62° , and 81° , respectively, which are typical martensitic peaks. The coating is mainly composed of the martensitic phase with a single body-centered tetragonal (bct) structure without another second phase.

Figure 3 is the cross-sectional microstructure of the stainless steel coating observed by optical microscopy. The thickness of the coating is around 2.5 mm (Figure 3(a)). Three regions are selected to reveal the details of the coating structure in the direction of thickness as labels A, B, and C. Locally magnified images are presented in Figures 3(b)–3(d) corresponding to the regions A, B, and C, respectively. A uniform structure can be observed on the cross-sectional surface of the coating. Almost no difference can be seen in the structure between the region near the top surface (Figure 3(b)), the region in the middle of the coating (Figure 3(c)), and the region near the fusion line (Figure 3(d)). A typical lath structure dominates the entire coating. It is compact with few pores, cracks, and other defects. Moreover, metallurgical bonding is formed in the interface between the coating and the substrate indicating good bonding force (Figure 3(d)).

Figure 4 displays the microhardness distribution in the direction of the thickness. The interval is fixed at 0.2 mm between the adjacent hardness points. The hardness of the coating has few fluctuations in the value suggesting a uniform structure. Its average value is $423.85 \text{ HV}_{0.2}$, which is approximately 3.3 times that of the substrate ($129.31 \text{ HV}_{0.2}$).

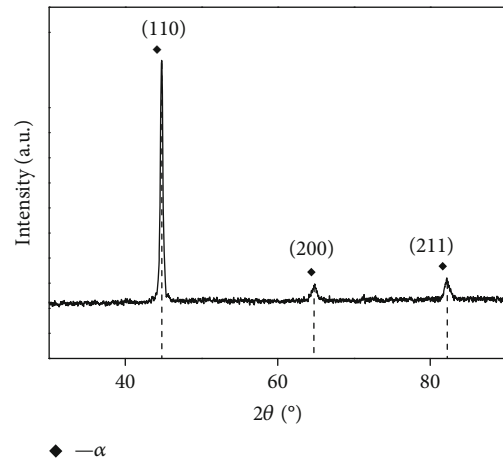


FIGURE 2: XRD pattern of the test coating.

3.2. Mass Loss. Figure 5 shows the variation of the cumulative mass loss and mass loss rate of the target coating with time in distilled water and saline water (3.5 wt.% NaCl) with and without sand (3 wt.%). The cumulative mass loss increases near linearly with test time for all the conditions (Figure 5(a)). No obvious incubation period can be found. They are 1.75 mg, 10.35 mg, 14.2 mg, and 18.2 mg after 25 h CE in distilled water, distilled water with sand, 3.5 wt.% NaCl solutions, and 3.5 wt.% NaCl solutions with 3 wt.% sand, respectively. The cumulative mass loss in the distilled water with 3% sand is nearly 6 times that in the distilled water alone. For the case of saline water with sand, it is approximately 1.3 times that in the saline water alone. Therefore, it can be deduced that adding sand particles can increase the CE in both the distilled water and the saline water. Moreover, the cumulative mass loss in the saline water is higher than that in the distilled water with and without sand particles. It indicates that chloride ions degraded the CE resistance of the coating.

The mass loss rates' variation with time is presented in Figure 5(b). They all increase initially in the first 5 h and then stay in a relatively stable state until the end of the tests in all

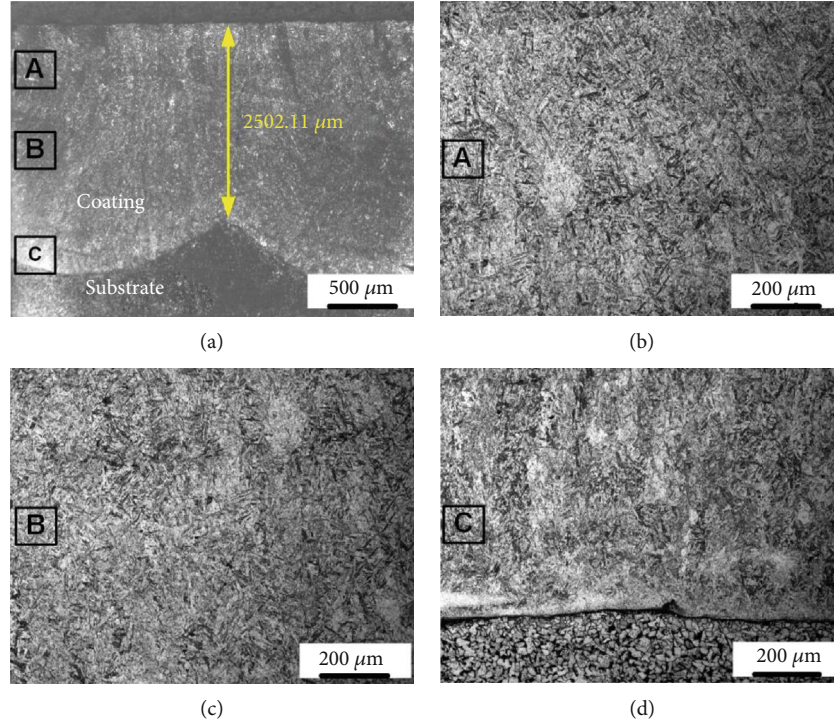


FIGURE 3: The cross-sectional metallographic images of the PHMSS coating.

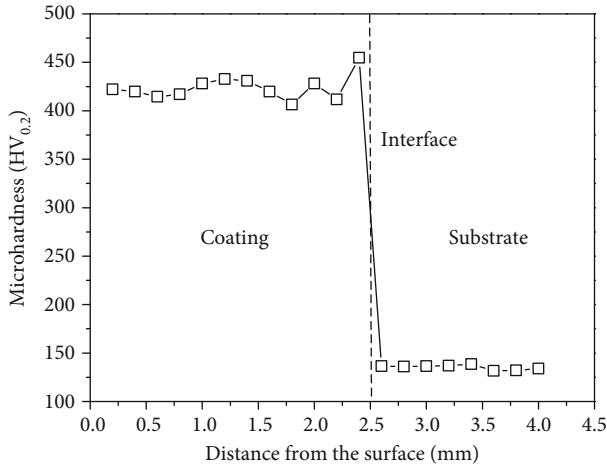


FIGURE 4: Microhardness profiles in the direction of the thickness of the MIG welding PHMSS coating and substrate.

the solutions. However, the mass loss rate is the least in the distilled water and the most in the 3.5 wt.% NaCl solution with sand. The CE resistance (R_{CE}) is determined based on the mean depth of the CE rate [35]. It is expressed as follows:

$$R_{CE} (\text{h} \cdot \mu\text{m}^{-1}) = \frac{1}{\text{MDER}}, \quad (1)$$

$$\text{MDER} (\mu\text{m} \cdot \text{h}^{-1}) = \frac{\Delta m}{10 \rho A \Delta t}, \quad (2)$$

where MDER is the mean depth of the erosion rate, Δm is the cumulative mass loss in mg, ρ is the density of the coating (approximately 7.7 g/cm^3), A is the exposure area of the sample (1.83 cm^2), and Δt is the time interval (25 h). Figure 6 plots the bar graph to compare the CE resistance of the stainless steel coating in different conditions. The trend is the same as that obtained by the cumulative mass loss (Figure 5(a)). It can be conducted that the CE resistance in the distilled water is approximately 5.9 times that in the sand-containing distilled water, whereas in the sand-containing saline water, it is about 1.3 times that in the sand-free saline water. It is reasonable to say that sand particles play a negative role in alleviating the CE damage in both distilled water and saline solution. Furthermore, they have a greater effect on the distilled water than on the saline water. It might be because the chloride ions reduced the influence of the sand particles on the CE.

3.3. Electrochemical Behavior. Figure 7 reveals the potentiodynamic polarization curves of the PHMSS coating on the static and CE conditions with and without sand. Table 3 lists the corrosion current density (I_{corr}) and corrosion potential (E_{corr}) obtained from the Tafel fitting. Under the static condition, the corrosion potential shifts positively by 42.8 mV, and the I_{corr} decreases by $1.7 \mu\text{A/cm}^2$ in the NaCl solution with sand particles compared with the case without sand particles (Figure 7(a)). It indicates that the existence of sand particles can slightly alleviate the corrosion of the PHMSS coating. Moreover, the anodic current density is decreased more obviously in the sand-containing NaCl solution than that in the sand-free NaCl solution on the static condition. It may be caused by the absorption of the fine sand particles to the sample surface, which can isolate the part of the corrosive-

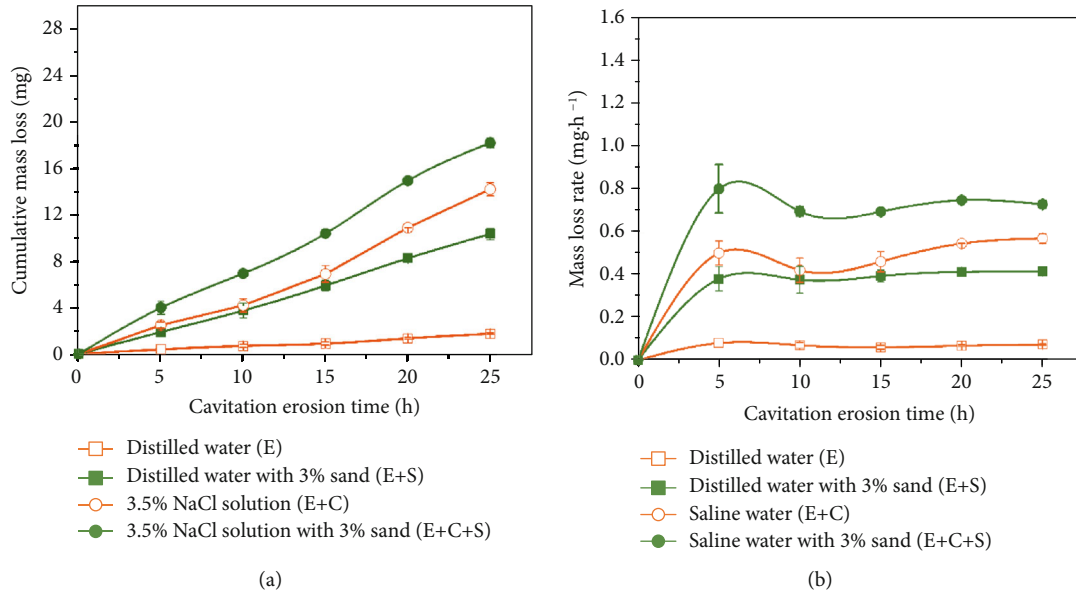


FIGURE 5: (a) Cumulative mass loss and (b) mass loss rate curves of the coating as a function of CE time in distilled water and 3.5 wt.% NaCl solution with and without 3 wt.% sand particles (200-300 mesh).

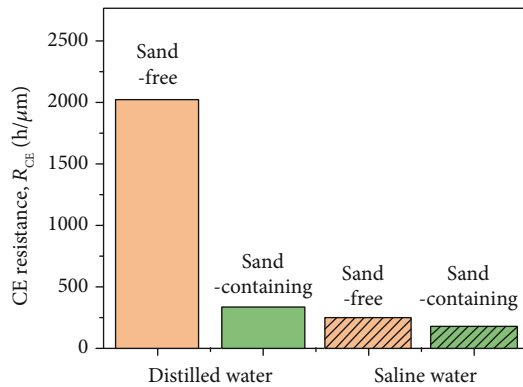


FIGURE 6: CE resistance in the distilled water and saline water with and without sand particles.

reducing anode. However, the corrosion behavior differences are small on a whole between the sand-free saline solution and the sand-containing saline solution. Moreover, passivation can be observed on the static conditions with and without sands, and the passivation current densities are the same in an order of magnitude of approximately $2.0 \times 10^{-5} \text{ A/cm}^2$.

On the CE conditions, the corrosion tendency changes opposite to that in the static conditions with sands (Figure 7(b)). The I_{corr} increases by approximately 6 times after adding sands. The corrosion potential moves negatively from $-167.2 \text{ mV}_{\text{SCE}}$ in the sand-free solution to $-251.8 \text{ mV}_{\text{SCE}}$ in the sand-containing solution. It can be deduced that sand particles accelerate the corrosion process. Besides, the PHMSS coating shows no passivation phenomenon on the CE conditions neither with nor without sand particles. It exhibits an active corrosion status in both CE conditions. Compared with the static condition, the corrosion current density is relatively high on the CE condition independent

on the sand particles. This is mainly due to both the mechanical damage to the passive film and the accelerated mass transfer during CE, which promotes the corrosion of PHMSS coating.

3.4. Morphology. CE can cause two different erosion regions: the center region and the perimeter region [36]. This can be changed by adding sand particles depending on the sand concentration [17], where the boundary between the center region and the perimeter almost disappeared at the concentration of 3 wt.% sand particles. The optical stereomicroscopy was used to reveal the macromorphologies after CE in different solutions.

Figure 8 shows the representative macromorphology of the eroded surface after CSE for 25 h in distilled and saline water with and without sand. It can be observed that the two regions can be distinguished in the distilled water (Figures 8(a) and 8(c)), but it is not as obvious as that caused by different sand particles [17], while the boundary between the center region and the perimeter region cannot be observed in the saline water conditions. Moreover, the CE is more severe in the saline water than in the distilled water, indicating the acceleration of the corrosion. To get an insight into the material removal mechanism, SEM observations were carried out on both the perimeter and center regions.

Figure 9 displays the CE surface morphologies in the center region of the sample after the test for 25 h in the distilled water and saline water with and without sand particles. The surface remains the original surface locally after the test in sand-free distilled water (Figure 9(a)). It indicates that the stainless steel has good CE resistance in the distilled water without sand. In contrast, the erosion is much more severe in the saline water than in the distilled water after the same test time (Figure 9(b)). Only small parts of the original surface can be observed as well as more CE craters. Without

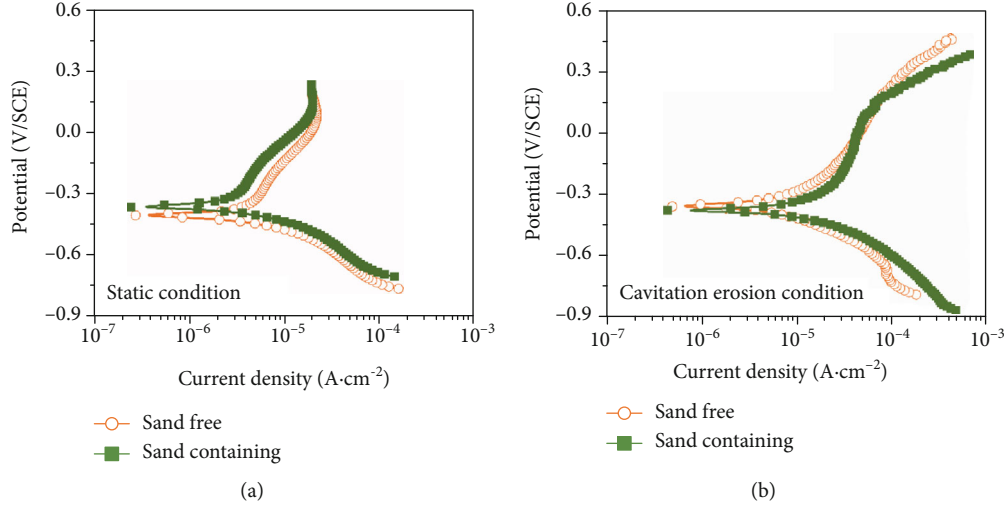


FIGURE 7: Potentiodynamic polarization curves of the PHMSS coating under (a) static and (b) CE conditions in 3.5 wt.% NaCl solution with and without sand particles.

TABLE 3: Comparative summary of electrochemical corrosion results for the PHMSS coating in 3.5 wt.% NaCl solution with and without 3 wt.% sand particles.

Conditions	I_{corr} ($\mu\text{A}/\text{cm}^2$)	E_{corr} (mV vs. SCE)
Sand-free (static)	3.026	-273.6
Sand-containing (static)	1.326	-153.1
Sand-free (CE)	0.582	-167.2
Sand-containing (CE)	3.538	-251.8

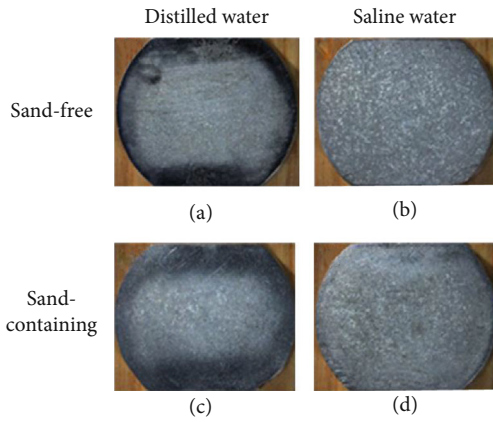


FIGURE 8: Macrographs of the PHMSS coating surface after CE for 25 h in (a) sand-free distilled water, (b) saline water, (c) sand-containing distilled water, and (d) sand-containing saline water.

sand particles, the degradation of the coating resistance to CE is mainly due to the chloride ions.

Compared with the case in the sand-free solution, the CE is accelerated in both distilled water and saline water after adding the sand particles (Figures 9(c) and 9(d)). All the original surfaces have been removed. However, the morphology for the sand-containing distilled water (Figure 9(c)) is different from that for the saline water (Figure 9(d)), indicating

different damage mechanisms. The density of the crater for the former case is less than that for the latter case. It seems that the surface in Figure 9(d) was obtained by the surface in Figure 9(c) after further CE. No big particle-like extrusion can be found on the surface tested in the sand-containing saline (Figure 9(d)). Anode dissolution preferentially occurs on the sharp corners and edges caused by the mechanical cutting of silt-CE resulting in further refinement to the erosion surface. Moreover, the pitting can also increase the bubble nucleation and accelerate the CE. Therefore, the eroded surface in the sand-containing saline is worse than that in the saline water and distilled water.

Micrographs observed by SEM in the perimeter region of the PHMSS coating surface after the CE test in different conditions are shown in Figure 10. The damage in the perimeter region follows the same trend as that in the center region. It is more severe in the sand-containing solution. On the condition of distilled water alone (Figure 10(a)), the original surface can still be seen even after the 25 h test. It only suffers slight plastic deformation due to the microjet flow or shock wave, and the damage degree is relatively low to that in the center region (Figure 9(a)). After adding the sand particles, the erosion regions are enlarged (Figure 10(c)). Local isolated craters connect each other and become bigger craters. Particle impinging due to the collapsing bubbles brings extra mechanical erosion to the coating surface [17]. In the saline solution without sand particles (Figure 10(b)), the original surface can be also observed but with less area than that in the distilled water alone, while no original surface can be found after the same CE time in the solution with sand particles (Figure 10(d)). It indicates that the sand particles affect the CE process in the entire surface of the sample, which is consistent with that observed in the macromorphology observations (Figure 8(d)).

Compared with the CE in the center region (Figure 9), the CE degree is relatively low in the perimeter region in the distilled water but similar in the saline water. It means that the sand particles' effect is more obvious in the distilled

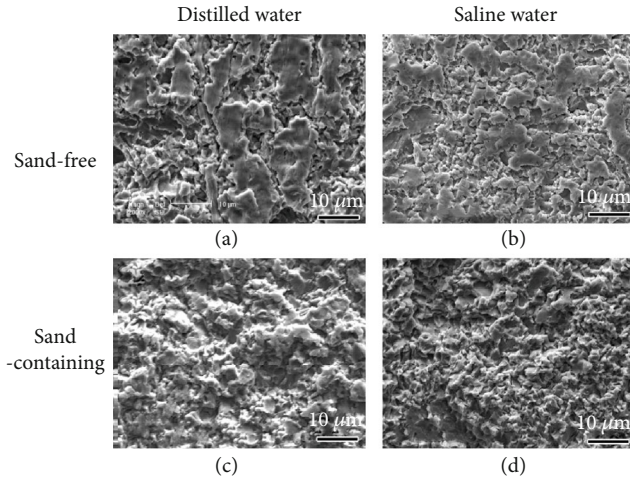


FIGURE 9: SEM micrographs of the CE surface in the central region after CE for 25 h in (a, c) distilled water and (b, d) 3.5 wt.% NaCl solutions (a, b) without and (c, d) with sand.

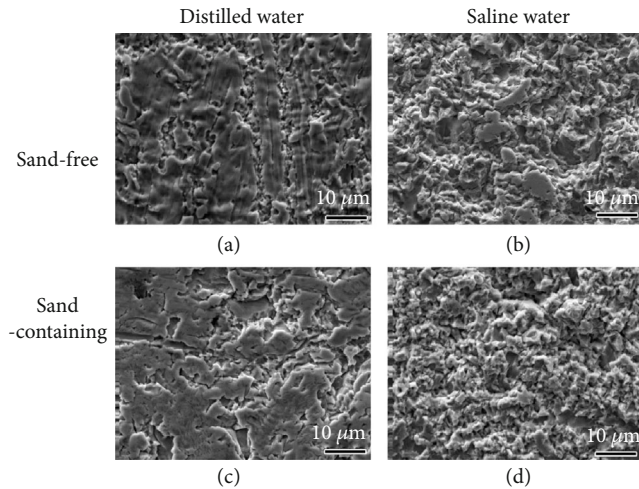


FIGURE 10: SEM micrographs of the CE surface in the perimeter region after CE for 25 h in (a, c) distilled water and (b, d) 3.5 wt.% NaCl solutions (a, b) without and (c, d) with sand.

water than in the saline water, which well agrees with the result obtained from R_{CE} (Figure 6).

Figure 11 displays the roughness profiles of the PHMSS coating surface after CE for 25 h in different solutions. All the areas measured for the roughness are selected within the center region of the surface. In the sand-free distilled water, the eroded surface is uniform and the grinding trace can still be seen (Figure 11(a)), which is consistent with that observed by SEM (Figure 9(d)). No obvious CE craters are detected suggesting little mass loss, which well agrees with the cumulative mass loss in Figure 5(a). Therefore, it can be deduced that the coating resistance to the CE is good in the distilled water alone in the view of roughness. In contrast, the grinding trace is completely removed after the same test time in the distilled water containing sand particles (Figure 11(c)). Local craters exist indicating the sand particles accelerated the CE, which well agrees with the mass loss

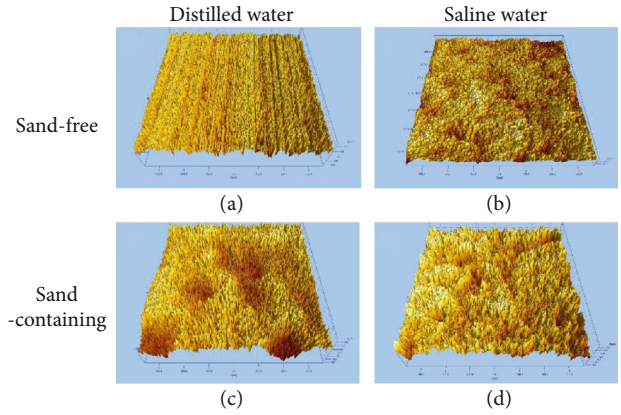


FIGURE 11: Three-dimensional roughness of the center region of the PHMSS coating surface after CE for 25 h in distilled water and saline water with and without sand particles.

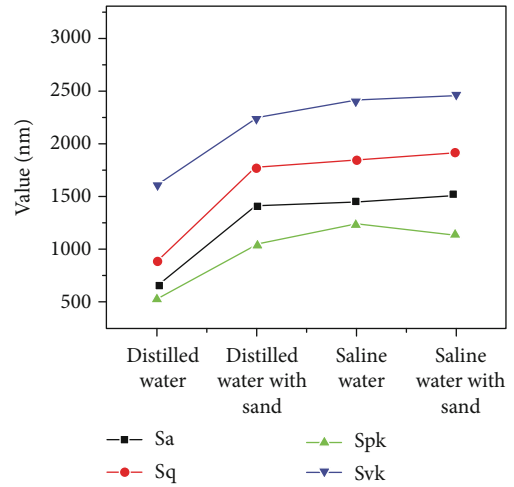


FIGURE 12: Relationship between the surface roughness and the solution conditions after 25 h CE.

measurements (Figure 5(a)), while the variations in the roughness morphologies in the saline water are not as big as those in the distilled water. However, the surface is coarser in the sand-containing saline than in the sand-free saline. The size of the peaks and the craters is larger than that in the sand-free saline.

The quantitative comparison of the surface roughness features after CE for 25 h in different solutions is showed in Figure 12. Sa and Sq are the arithmetical mean height and root mean square height, respectively. Spk is the reduced peak height representing the mean height of peaks above the core surface; Svk expresses the arithmetical mean of the reduced valley depth of the areal material ratio curve. Essentially, this is a measure of the valley depth below the core roughness. It can be observed that all the parameters increase significantly after adding sand to the distilled water. They change in the same way with the changing solution. The values of Sa, Sq, Spk, and Svk slightly rise in the solution adding NaCl alone and the solution adding NaCl+sand. It suggests that the maximum value of the peaks and the valleys increased due to the combined action of the particle

impingement and CE. Sa in the sand-containing saline water is approximately 2.3 times that in the distilled water alone and approximately 1.04 times that in the saline water alone. It indicates that the sand particles degrade the CE resistance of the MIG PHMSS coating more in the distilled water than in the saline water. This may be mainly own to the increase in mechanical damage.

3.5. Synergy Action between CE and Corrosion. It is necessary to understand not only the quantity of synergistic effects [22] but also the sand particles' effect on the synergy. The synergy components were obtained in the solution with and without sand particles, respectively. The total damage of CE can be described in the way of volume loss by the following equations [37–39]:

$$V_{T1} = V_E + V_C + V_{S1} = V_E + V_C + V_{EIC} + V_{CIE}, \quad (3)$$

$$V_{T2} = V_E + S + V_C + V_{S2} = V_E + S + V_C + V_{ESIC} + V_{CIES}, \quad (4)$$

where V_{T1} and V_{T2} are the total volume loss of the coating in the saline solution without and with sand particles, respectively; V_E and V_{E+S} are the pure mechanical erosion components caused by the CE alone in the distilled water without and with sand particles, respectively; V_C is the pure corrosion component measured in the saline water; V_{S1} and V_{S2} are the synergy components of the CE and corrosion in the saline water without and with sand particles, respectively; V_{EIC} and V_{ESIC} are the corrosion enhancements induced by the corrosion in the sand-free and sand-containing saline solutions, respectively; and V_{CIE} and V_{CIES} are the erosion enhancements induced by the corrosion in the sand-free and sand-containing saline solutions, respectively. In the present work, V_E and V_{T1} were measured after CE for 25 h in distilled water and saline water without sand particles, respectively. V_{E+S} and V_{T2} were obtained by the same method but in the sand-containing solution. V_C was calculated from the I_{corr} from the polarization curve in the static saline solution according to Faraday's law. V_{EIC} and V_{ESIC} were determined by the same method but on the CE condition in the saline water without and with sand particles, respectively. It is noted that they are the pure enhancement components due to erosion, which means that the pure corrosion component (V_C) has been deducted.

Table 4 lists the components described above for the MIG welding HPMSS coating. On the sand-free conditions, the biggest component is the erosion enhancement (V_{CIE}) caused by the corrosion with a fraction of 88.14% to the total damage. The next one is the pure CE (V_E , $8.89E-3 \text{ mm}^3/\text{h}$), and the minimum one is the corrosion enhancement due to CE only at the fraction of 0.05%. Compared with the sand-free conditions, a great change occurs due to the existence of the sand particles. Pure mechanical erosion caused by the CE (V_{E+S}) becomes the dominant component followed the erosion enhancement due to the corrosion (V_{CIES}). The pure corrosion component turns out to be the minimum one. All these changes result in the increase of the total damage by approximately 19% compared with that in the sand-

TABLE 4: Component values calculated after 25 h CE in the solution without and with sand.

Conditions	Volume loss rates ($10^{-3} \text{ mm}^3/\text{h}$)/fraction				
Sand-free	V_{T1}	V_E	V_{C1}	V_{EIC}	V_{CIE}
	77.51	8.89	0.26	0.04	68.32
Sand-containing	V_{T2}	V_{E+S}	V_{C2}	V_{ESIC}	V_{CIES}
	92.50	52.60	0.18	0.68	39.04

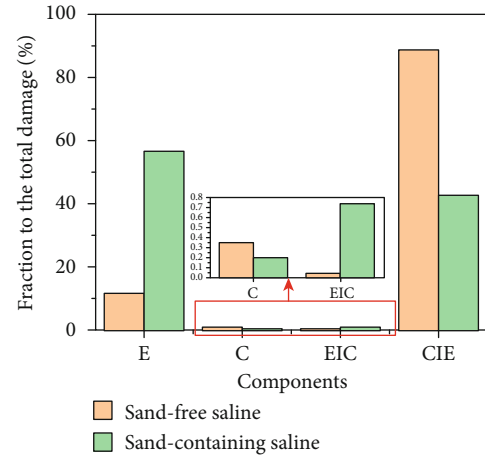


FIGURE 13: Fraction of each component to the total damage.

free saline water. Figure 13 plots the bar graphs of the fraction of each component to the total damage. It can be also observed that the biggest component transforms from V_{CIE} to V_{E+S} due to the adding of the sand particles. The synergy in the sand-free saline is much less than that in the sand-containing saline. Moreover, the corrosion-related components (V_C and V_{EIC}) are significantly less than the erosion-related components (V_E and V_{CIE}) indicating the good corrosion resistance of the coating.

The effect of solid-phase loading on the erosion-corrosion behavior for stainless steel has been examined. It was reported that the increase of charge transfer resulted in a higher contribution to the total weight due to corrosion-related effects [40]. However, the foundation in the present work is different. With the addition of the sand particles, the corrosion-related effect is reduced and the pure mechanical erosion is enhanced. Two aspects may contribute to the decrease of the corrosion effect. One is due to the good corrosion resistance of the MIG welding PHMSS coating itself. The other can result from the sand particles partially preventing the diffusion of chloride into the coating surface. It proved the decrease of the corrosion component (from V_{C1} to V_{C2}) after adding sand particles.

The sand particles affect the silt-CE in many aspects including corrosion, erosion, and synergy. The total damage is increased by adding the sand particles in both the distilled water and the saline water (Figure 5). It is the sum results of each damaged component. On the static distilled water, pure CE is dominant but limited, which can be proved by the small mass loss (Figure 5). Microjet and shock wave do not tear the coating surface (Figures 9(a), 10(a), and 11(a)), while all these

are changed after adding sand particles to the distilled water. The combined action of the sand particle erosion and CE breaks the integrity of the coating resulting in great material removal. In addition to the case in the distilled water, more complex processes occur in the silt-CE and corrosion. The passivation film is peeled off leading to an increase of the I_{corr} . That is why the corrosion enhancement due to erosion becomes higher than that in the sand-free saline water (Table 4). Moreover, the variation of the corrosion component resulted from not only the change of the surface area but also the disturbance of local mass transfer and the concentration due to the moving into and out of the boundary layer. A great change in the pure mechanical erosion occurs when adding the sand particles in the saline water (Table 4), which results in the degradation of the surface morphology (Figures 9(b), 10(b), and 11). It indicates that sand particles play an important role in the mechanical erosion to the coating surface. According to the report carried out by Hu and Zheng [17], the silt-CE was mainly determined by sand erosion on the sand concentration of 3 wt.%. Therefore, it is easy to understand why the pure erosion component becomes the dominant one to the other components.

4. Conclusions

A MIG welding HPMSS coating was newly designed on the cast steel. Its silt-CE resistance was investigated through the mass loss measurement and the micromorphology observation. The synergy of CE and corrosion was discussed in the 3.5 wt.% NaCl solutions without and with sand particles. Some conclusions can be drawn as follows:

- (1) The MIG welding PHMSS coating is mainly composed of the lath martensitic phase alone. It has a single body-centered tetragonal (bct) structure with the microhardness of 423.85 HV_{0.2}.
- (2) The mass loss rate of the coating is in ascending order in the solution of distilled water alone, sand-containing distilled water, saline water alone, and sand-containing saline water.
- (3) The synergy in the sand-free saline is much less than that in the sand-containing saline. The maximum component is the erosion enhancement due to the corrosion in the saline without sand particles but is the pure erosion component in the saline with sand particles.

Data Availability

The data of mass loss, electrochemistry, and hardness used to support the findings of this study are included within the article.

Conflicts of Interest

We declare that we have no financial and personal relationships with other people or organizations that can inappropriately influence our work and there is no professional or other

personal interest of any nature or kind in any product, service, and/or company that could be construed as influencing the position presented in, or the review of, the manuscript entitled.

Acknowledgments

This work was supported by the National Key R&D Program of China (2018YFC0808500) and the National Natural Science Foundation of China (51501206, 51971229).

References

- [1] H. X. Hu, S. L. Jiang, Y. S. Tao, T. Y. Xiong, and Y. G. Zheng, "Cavitation erosion and jet impingement erosion mechanism of cold sprayed Ni-Al₂O₃ coating," *Nuclear Engineering and Design*, vol. 241, no. 12, pp. 4929–4937, 2011.
- [2] Y. Lei, H. Chang, X. Guo, T. Li, and L. Xiao, "Ultrasonic cavitation erosion of 316L steel weld joint in liquid Pb-Bi eutectic alloy at 550°C," *Ultrasonics Sonochemistry*, vol. 39, pp. 77–86, 2017.
- [3] S. Hong, Y. Wu, J. Wu et al., "Effect of flow velocity on cavitation erosion behavior of HVOF sprayed WC-10Ni and WC-20Cr3C2-7Ni coatings," *International Journal of Refractory Metals and Hard Materials*, vol. 92, article 105330, 2020.
- [4] S. Hong, Y. Wu, J. Wu et al., "Microstructure and cavitation erosion behavior of HVOF sprayed ceramic-metal composite coatings for application in hydro-turbines," *Renewable Energy*, 2020.
- [5] S. Hong, J. Lin, Y. Wu et al., "Cavitation erosion characteristics at various flow velocities in NaCl medium of carbide-based cermet coatings prepared by HVOF spraying," *Ceramics International*, 2020.
- [6] Y. Zheng, Z. Yao, X. Wei, and W. Ke, "The synergistic effect between erosion and corrosion in acidic slurry medium," *Wear*, vol. 186–187, pp. 555–561, 1995.
- [7] S. Hong, Y. Wu, J. Zhang, Y. Zheng, Y. Qin, and J. Lin, "Effect of ultrasonic cavitation erosion on corrosion behavior of high-velocity oxygen-fuel (HVOF) sprayed near-nanostructured WC-10Co-4Cr coating," *Ultrasonics Sonochemistry*, vol. 27, pp. 374–378, 2015.
- [8] S. Hong, Y. Wu, J. Zhang, Y. Zheng, Y. Zheng, and J. Lin, "Synergistic effect of ultrasonic cavitation erosion and corrosion of WC-CoCr and FeCrSiBMn coatings prepared by HVOF spraying," *Ultrasonics Sonochemistry*, vol. 31, pp. 563–569, 2016.
- [9] C. T. Kwok, F. T. Cheng, and H. C. Man, "Synergistic effect of cavitation erosion and corrosion of various engineering alloys in 3.5% NaCl solution," *Materials Science and Engineering: A*, vol. 290, no. 1–2, pp. 145–154, 2000.
- [10] J. T. Chang, C. H. Yeh, J. L. He, and K. C. Chen, "Cavitation erosion and corrosion behavior of Ni-Al intermetallic coatings," *Wear*, vol. 255, no. 1–6, pp. 162–169, 2003.
- [11] L. Wang, N. Qiu, D.-H. Hellmann, and X. Zhu, "An experimental study on cavitation erosion-corrosion performance of ANSI 1020 and ANSI 4135 steel," *Journal of Mechanical Science and Technology*, vol. 30, no. 2, pp. 533–539, 2016.
- [12] S. S. Rajahram, T. J. Harvey, and R. J. K. Wood, "Erosion-corrosion resistance of engineering materials in various test conditions," *Wear*, vol. 267, no. 1–4, pp. 244–254, 2009.

- [13] K. S. Tan, J. A. Wharton, and R. J. K. Wood, "Solid particle erosion–corrosion behaviour of a novel HVOF nickel aluminium bronze coating for marine applications—correlation between mass loss and electrochemical measurements," *Wear*, vol. 258, no. 1–4, pp. 629–640, 2005.
- [14] H. B. Marschall, K. A. Mørch, A. P. Keller, and M. Kjeldsen, "Cavitation inception by almost spherical solid particles in water," *Physics of Fluids*, vol. 15, no. 2, pp. 545–553, 2003.
- [15] D. Yan, J. Wang, and L. Fengbin, "Inhibition of the ultrasonic microjet-pits on the carbon steel in the particles-water mixtures," *AIP Advances*, vol. 5, no. 7, 2015.
- [16] B. M. Borkent, M. Arora, and C. D. Ohl, "Reproducible cavitation activity in water-particle suspensions," *Journal of the Acoustical Society of America*, vol. 121, no. 3, pp. 1406–1412, 2007.
- [17] H. X. Hu and Y. G. Zheng, "The effect of sand particle concentrations on the vibratory cavitation erosion," *Wear*, vol. 384–385, pp. 95–105, 2017.
- [18] K. Su, J. Wu, and D. Xia, "Classification of regimes determining ultrasonic cavitation erosion in solid particle suspensions," *Ultrasonics Sonochemistry*, vol. 68, article 105214, 2020.
- [19] J.-h. Wu and W.-j. Gou, "Critical size effect of sand particles on cavitation damage," *Journal of Hydrodynamics*, vol. 25, no. 1, pp. 165–166, 2013.
- [20] D. G. Li, Y. Long, P. Liang, and D. R. Chen, "Effect of micro-particles on cavitation erosion of Ti6Al4V alloy in sulfuric acid solution," *Ultrasonics Sonochemistry*, vol. 36, pp. 270–276, 2017.
- [21] R. Y. Ting, "Polymer effects on microjet impact and cavitation erosion," *Nature*, vol. 262, no. 5569, pp. 572–573, 1976.
- [22] H. Chen, S. Liu, J. Wang, and D. Chen, "Study on effect of microparticle's size on cavitation erosion in solid-liquid system," *Journal of Applied Physics*, vol. 101, no. 10, pp. 103510–103510, 2007.
- [23] Y. X. Qiao, J. Huang, D. Huang et al., "Effects of laser scanning speed on microstructure, microhardness and corrosion behavior of laser cladding Ni45 coatings," *Journal of Chemistry*, vol. 2020, Article ID 1438473, 11 pages, 2020.
- [24] Y. Qiao, D. Xu, S. Wang et al., "Effect of hydrogen charging on microstructural evolution and corrosion behavior of Ti-4Al-2V-1Mo-1Fe alloy," *Journal of Materials Science & Technology*, vol. 60, pp. 168–176, 2021.
- [25] C. J. Heathcock, B. E. Protheroe, and A. Ball, "Cavitation erosion of stainless steels," *Wear*, vol. 81, no. 2, pp. 311–327, 1982.
- [26] K. Ogino and A. Hida, "Cavitation erosion of 431 stainless steel," *Journal of the Faculty of Science Technology Kinki University*, vol. 25, pp. 137–141, 1989.
- [27] R. A. Maftoum, P. C. Borges, and C. M. Marqueze, "Influence of nitrogen on the cavitation erosion resistance of martensitic stainless steel," *Matéria*, vol. 22, 2017.
- [28] A. N. Allenstein, C. M. Lepienski, A. J. A. Buschinelli, and S. F. Brunatto, "Plasma nitriding using high H₂ content gas mixtures for a cavitation erosion resistant steel," *Applied Surface Science*, vol. 277, pp. 15–24, 2013.
- [29] Y. Qiao, J. Chen, H. Zhou et al., "Effect of solution treatment on cavitation erosion behavior of high-nitrogen austenitic stainless steel," *Wear*, vol. 424–425, pp. 70–77, 2019.
- [30] Y. Qiao, Z. Tian, X. Cai et al., "Cavitation erosion behaviors of a nickel-free high-nitrogen stainless steel," *Tribology Letters*, vol. 67, no. 1, 2019.
- [31] J. F. Santa, J. A. Blanco, J. E. Giraldo, and A. Toro, "Cavitation erosion of martensitic and austenitic stainless steel welded coatings," *Wear*, vol. 271, no. 9–10, pp. 1445–1453, 2011.
- [32] Z. P. Shi, Z. B. Wang, J. Q. Wang et al., "Effect of Ni interlayer on cavitation erosion resistance of NiTi cladding by tungsten inert gas (TIG) surfacing process," *Acta Metallurgica Sinica (English Letters)*, vol. 33, no. 3, pp. 415–424, 2020.
- [33] ASTM, *ASTM G32-10 Standard test method for cavitation erosion using vibratory apparatus*, ASTM: USA, 2010.
- [34] M. M. Liu, H. X. Hu, and Y. G. Zheng, "Effects of three sealing methods of aluminum phosphate sealant on corrosion resistance of the Fe-based amorphous coating," *Surface and Coatings Technology*, vol. 309, pp. 579–589, 2017.
- [35] C. T. Kwok, H. C. Man, and F. T. Cheng, "Cavitation erosion of duplex and super duplex stainless steels," *Scripta Materialia*, vol. 39, no. 9, pp. 1229–1236, 1998.
- [36] Y. Wu, S. Hong, J. Zhang et al., "Microstructure and cavitation erosion behavior of WC–Co–Cr coating on 1Cr18Ni9Ti stainless steel by HVOF thermal spraying," *International Journal of Refractory Metals Hard Materials*, vol. 32, pp. 21–26, 2012.
- [37] ASTM, *Annual Book of ASTM Standards 2002*, vol. 3–2, 2002USA: ASTM International, 2002.
- [38] V. A. de Souza and A. Neville, "Corrosion and erosion damage mechanisms during erosion-corrosion of WC-Co-Cr cermet coatings," *Wear*, vol. 255, no. 1–6, pp. 146–156, 2003.
- [39] V. A. D. Souza and A. Neville, "Corrosion and synergy in a WCCoCr HVOF thermal spray coating—understanding their role in erosion–corrosion degradation," *Wear*, vol. 259, no. 1–6, pp. 171–180, 2005.
- [40] J. Basumatary and R. J. K. Wood, "Synergistic effects of cavitation erosion and corrosion for nickel aluminium bronze with oxide film in 3.5% NaCl solution," *Wear*, vol. 376–377, pp. 1286–1297, 2017.

Research Article

Microstructure, Mechanical Properties, and Residual Stress Distribution of AISI 316L Stainless Steel Part Fabricated by Laser Metal Deposition

Jiayang Gu,¹ Ruifeng Li²,² Yi Qiu,² Hangyu Yue,² Bin Liu,² and Heng Gu³

¹Marine Equipment and Technology Institute, Jiangsu University of Science and Technology, Zhenjiang, Jiangsu 212003, China

²School of Materials Science and Engineering, Jiangsu University of Science and Technology, Zhenjiang, Jiangsu 212003, China

³Cardiff School of Engineering, Cardiff University, Cardiff CF24 3AA, UK

Correspondence should be addressed to Ruifeng Li; li_ruifeng@just.edu.cn

Received 30 May 2020; Accepted 30 June 2020; Published 25 July 2020

Guest Editor: Peter G. Keech

Copyright © 2020 Jiayang Gu et al. This is an open access article distributed under the Creative Commons Attribution License, which permits unrestricted use, distribution, and reproduction in any medium, provided the original work is properly cited.

In this paper, AISI 316L stainless steel part is obtained by laser metal deposition additive manufacturing method. The microstructure of the part was observed and analyzed by an optical microscope. The tensile mechanical properties and residual stress distribution of the part were tested by tensile test and the contour method. The results show that the bulk structure is mainly columnar crystal and equiaxed crystal, and the latter layer of laser metal deposition will form a remelted zone and heat-affected zone in the former deposition zone. Tensile test results show that the tensile strength of tensile specimens parallel to laser scanning direction and perpendicular to laser scanning direction is basically the same, but the elongation of the specimens perpendicular to the laser scanning direction is relatively better. The main reason is the different distribution characteristics of columnar crystals and equiaxed crystals in the two directions. Relatively large deformation occurs on the cut surface of the specimen after low-speed wire cut. The residual stress test results indicate that tensile stress is formed in the upper part and it reaches 315 MPa at the top surface. And compressive stress is formed at the part/substrate interface and the substrate.

1. Introduction

316L stainless steel is known as a material with excellent corrosion resistance; it is used for various applications of the petrochemical (oil and gas) and chemical industries and as biomaterial. Additive manufacturing (AM), as an emerging manufacturing technology, has been widely used in aerospace [1, 2], medical [3, 4], construction [5], and other fields. With AM technology, a computer-aided design (CAD) model can be directly transformed into a 3D object, built layer by layer, in a relatively short time and with low cost, avoiding the long processes of conventional fabrication methods [6].

Additive manufacturing process consists of a group of modern manufacturing technologies that are used to produce three-dimensional prototypes from CAD representations [7, 8]. For example, the selective laser melting

(SLM) and laser metal deposition (LMD) techniques are frequently used for stainless steel component production and for regeneration [9, 10]. Compared with SLM, LMD forming size is not limited; in ideal cases, the part size can be very large. In addition, LMD processing efficiency is relatively high; LMD has a great advantage in the case of large part size without accurate part accuracy requirement. The LMD process belongs to the category of laser cladding methods [11]. In recent years, there has been an increasing interest in the LMD process. Ma et al. obtained a well-formed additive manufacturing part using a variation-oriented raster scanning method which can improve the fabrication of precision [12]. Xiang et al. found that the elements of LMD samples were more homogeneously distributed than casting technique samples [13]. Wang et al. found that specimens perpendicular to the build direction had lower elongations than specimens

parallel to the build direction [14]. However, the relation between the microstructure distribution and tensile properties is seldom discussed.

In addition, due to the complex thermal effects in the additive manufacturing process, the residual stress distribution in the part is complicated. The residual stress of the part may exceed the yield strength of the alloy, affecting corrosion resistance, fracture toughness, crack propagation behavior, and fatigue performance [15, 16]. Mukherjee et al. studied the residual stress via finite element method and predicted the part deformation after additive manufacturing [17]. Zhuo et al. carried out heat treatment to eliminate the residual stress and measured the residual stress by X-ray diffraction [18]. Bartlett et al. proposed a new method, the 3D-DIC curvature-RS model, to measure the residual stress of the part which was fabricated by additive manufacturing, and the error was only $\sim 6\%$ for all measured points [19]. Szost et al. studied the residual stress distribution of thin-walled structures using neutron diffraction method which was fabricated by laser additive manufacturing and wire+arc additive manufacturing (WAAM); the results showed that higher residual stress were formed in WAAM samples [20]. In 2001, Prime first proposed the contour method to test the residual stress of components. Prime combined the finite element method with the release technique to propose the original concept of the contour test method and pointed out that this method can completely obtain the stress distribution on a section [21]. Prime et al. studied the contour test method, and the test error of this method is about 25 MPa, which can meet the test requirements of engineering and scientific research. However, few scholars use the contour method to measure the residual stress of parts manufactured by additive manufacturing.

In this paper, AISI 316L stainless steel parts were fabricated by LMD. The microstructures and tensile properties parallel to and perpendicular to the laser scanning direction were observed and tested. Fracture modes were analyzed, and residual stress distribution of the components was measured by the contour method.

2. Materials and Methods

AISI 316L alloy powder obtained by gas atomisation was used in this study. The morphology of the powder is shown in Figure 1, and the chemical composition is listed in Table 1. The powder diameter was ranging between $45\mu\text{m}$ and $75\mu\text{m}$ and had a good degree of sphericity that enabled a smooth powder feeding flow. The substrate was an AISI 1045 medium carbon steel plate with a composition listed in Table 2. The LMD experiment was carried out by using a high-power fiber laser processing system consisting of a high-power fiber laser (YLS-6000-S2T), an ABB robot arm, and a coaxial focusing powder feeding system (DPSF-2). The laser beam was modulated to a $5\text{mm} \times 5\text{mm}$ square spot. The deposition was achieved at a fixed 2kW laser power, an overlapping rate of 30%, a laser scanning speed of 4 mm/s, and a powder feeding rate of 8.8 g/min. A schematic diagram of LMD additive manufacturing process is

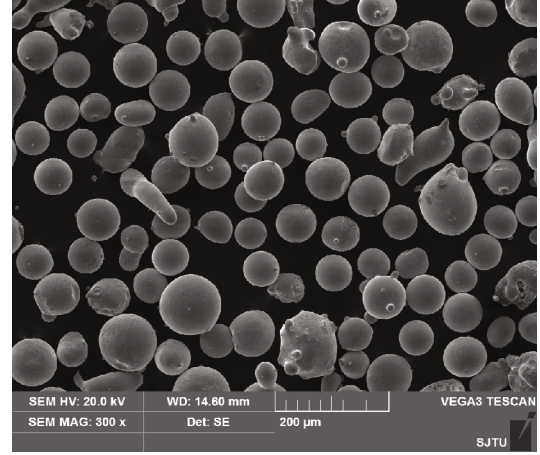


FIGURE 1: SEM picture of AISI 316L stainless steel powders.

TABLE 1: Chemical compositions of AISI 316L stainless steel powder (wt. %).

Element	C	Si	Cr	Ni	S	Fe
Content	<0.08	0.76	17.41	12.04	0.60	Bal.

TABLE 2: Chemical compositions of AISI 1045 substrate (wt. %).

Element	C	Si	Mn	Cr	Ni	Cu	Fe
Content	0.42~0.50	0.17~0.37	0.50~0.80	0.25	0.30	0.25	Bal.

plotted in Figure 2. The distance between the laser head and the substrate was 13 mm. This distance was consistent with the focus of the powder collection to ensure that the powder melts at the same time. When the first layer was finished, the laser head was raised by 0.8 mm in the Z-axis direction, which agrees with the height of each layer of the alloy. The finished alloy serves as a new substrate to carry the new alloy.

After the completion of LMD build, the microstructures of the deposits at different locations were examined after mechanical grinding/polishing and etching by using aqua regia reagent. An optical microscope (OM) was used to observe the microstructure. It is known that an additive manufactured component exhibits anisotropic mechanical properties; therefore, in this study, tensile tests were conducted on specimens taken along both longitudinal and transverse directions. Figure 3(a) illustrates the positions of where the tensile specimens were taken from, and Figure 3(b) shows the dimensions of the samples by following ISO 6892-1:2009 standard. The tensile tests were conducted at room temperature with a stretching speed of 2 mm/min. Each test was repeated 3 times, and an averaged ultimate tensile strength (UTS) and elongation (EL) were thereafter obtained. Finally, the fracture surface was observed by a scanning electron microscope (SEM).

The longitudinal residual stress distribution in the LMD part was analyzed using the contour method [22, 23]. At first, the LMD block was cut into two parts along the direction perpendicular to the laser scanning direction using a slow

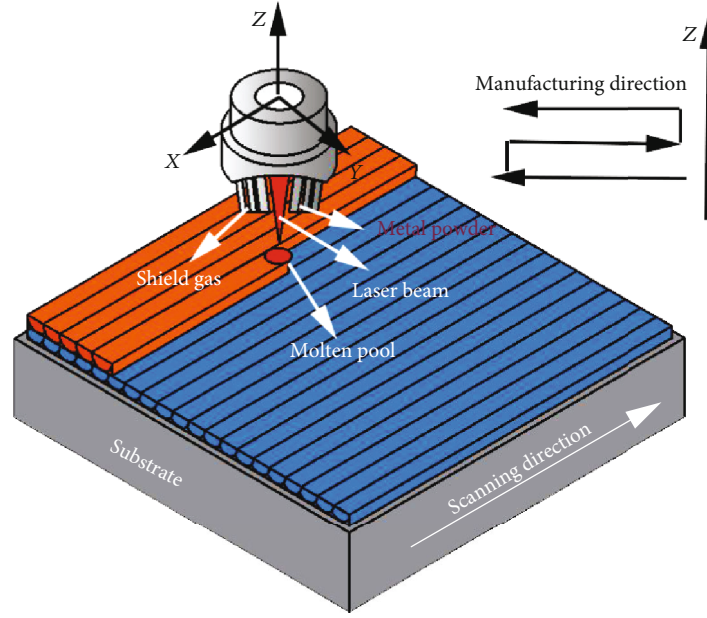


FIGURE 2: Schematic diagram of block part manufacturing.

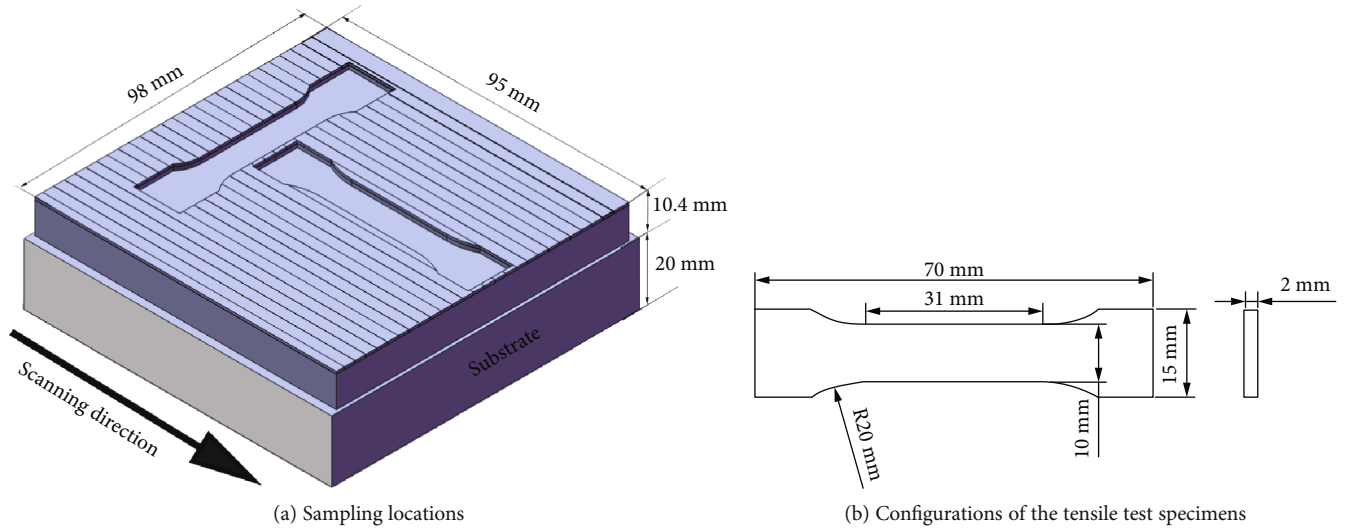


FIGURE 3: Schematic diagram of the samplings of tensile specimens.

wire cutting process as illustrated in Figure 4. The profile of the cutting surface was then deformed due to the release of residual stress. Then, the profiles of two deformed surfaces were determined by a high-precision three-axis coordinate measurement machine (CMM), and the measurement accuracy is $2\ \mu\text{m}$. The acquired contour point clouds from two opposite surfaces were subsequently processed by averaging and bivariate spline fitting to generate a smooth surface and eliminate measurement errors. The representative profile of deformed cutting surface is shown in Figure 5. Finally, the measured contour was used as the boundary condition of the finite element model. The elastic state is used to analyze the stress state of the deformed cutting surface after returning to the plane state before cutting (or changing the cutting surface in the planar state to the deformation contour in the

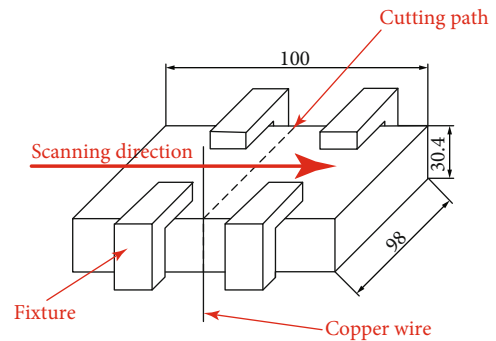


FIGURE 4: Schematic illustration of slow wire cutting process.

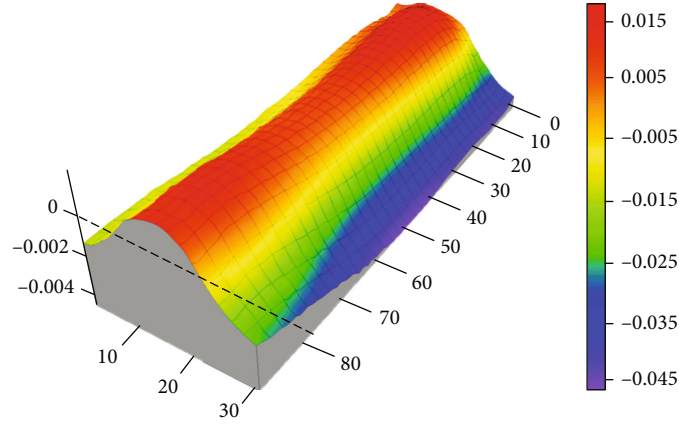


FIGURE 5: Surface contour after linear cutting (mm).

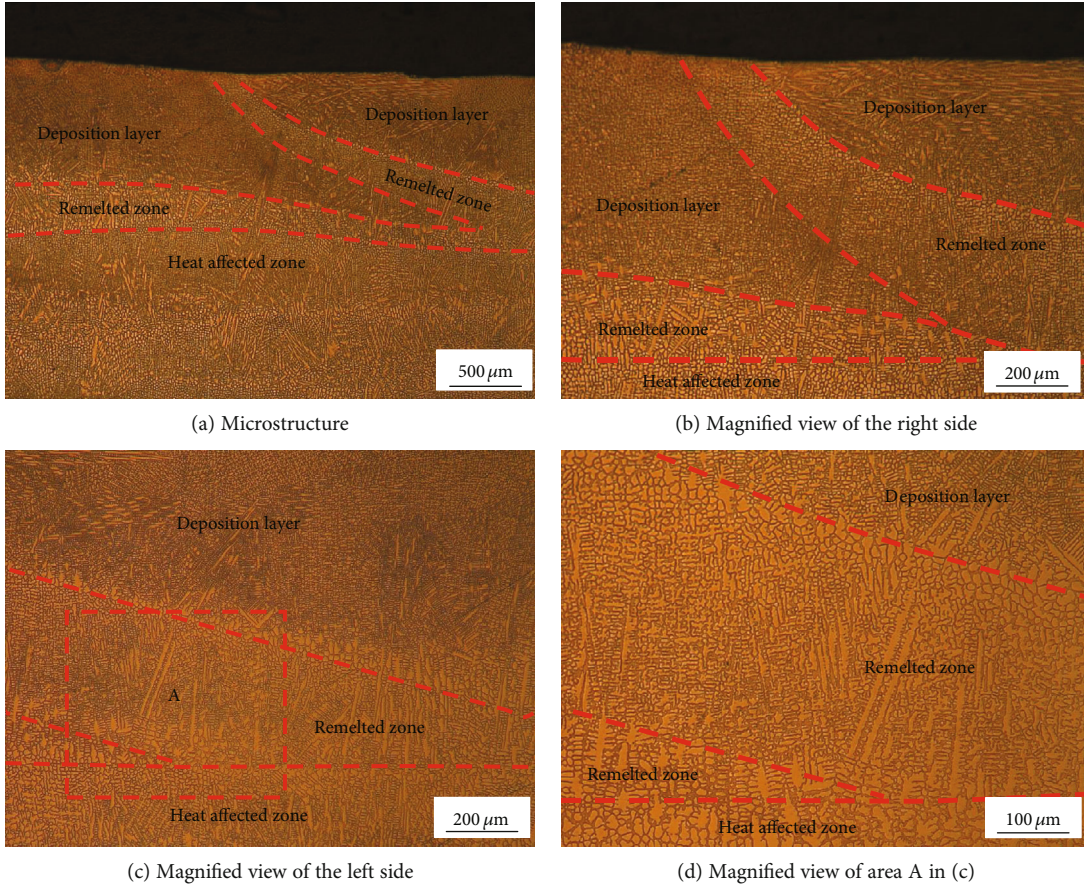


FIGURE 6: Cross-sectional microstructure perpendicular to the laser scanning direction.

opposite direction). It is assumed that no plastic deformation occurs, and the obtained stress on the cutting surface is equivalent to the original stress at the same position before the cutting.

3. Results and Discussion

3.1. Microstructure. Figure 6 shows the microstructure of the cross section perpendicular to the laser scanning direction. Figure 6(a) indicates that the microstructure of the LMD part

consists of a deposition layer zone, remelted zone, and heat-affected zone due to the laser heat input during the latter deposition process. Figures 6(b) and 6(c) indicates that the microstructure of the remelted zone grew from the heat-affected zone of the former layer. The direction of microstructure growth depends on the direction of the structure in the heat-affected zone. In the center zone of the remelted zone, the direction of microstructure growth is no longer the same. This is due to the fact that the remelted

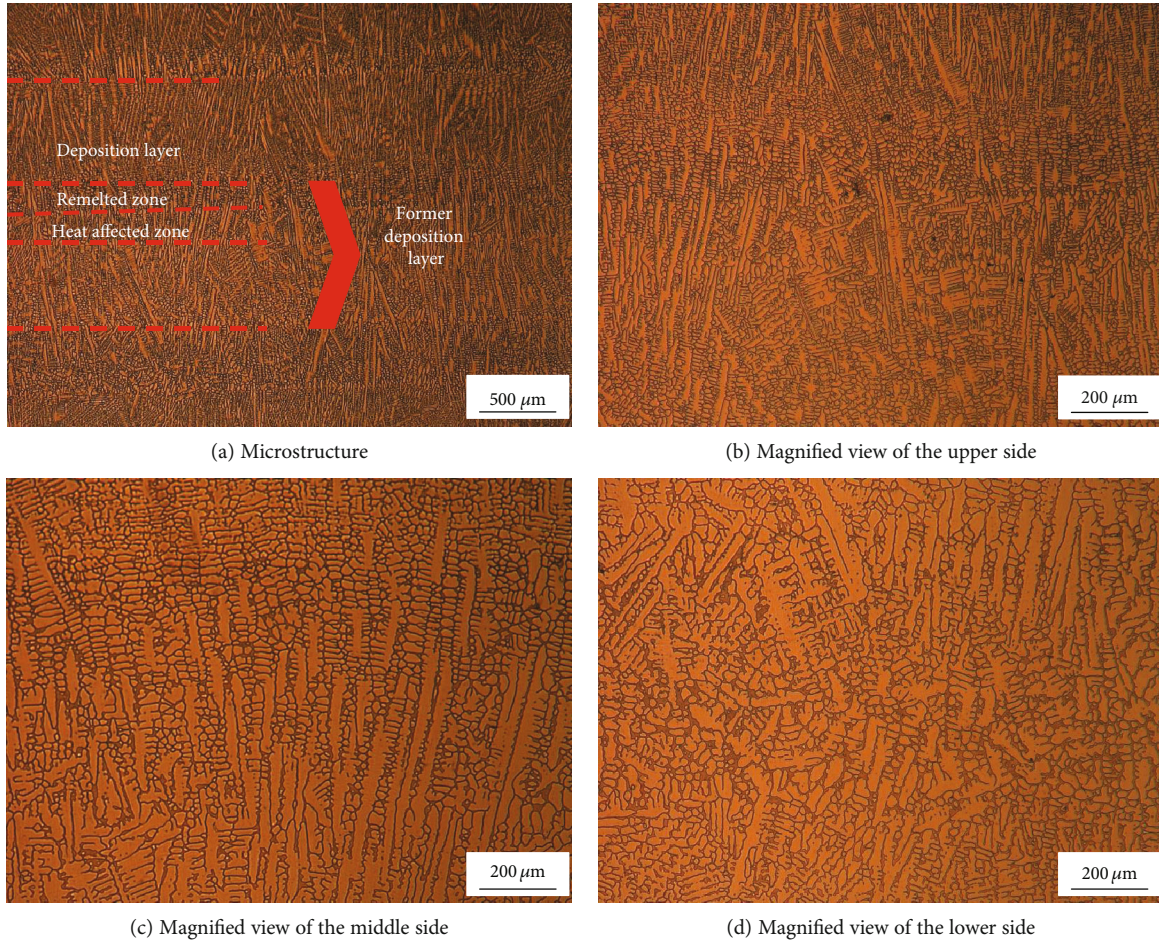


FIGURE 7: Cross-sectional microstructure parallel to the laser scanning direction.

portion has unmelted grains which become the nucleation, resulting in a nonuniform growth direction of the microstructure. In addition, it can be seen that the microstructure of the latter deposited layer is fine, the upper part is equiaxed crystals, and the lower part is fine columnar dendrites. In area A (Figure 6(d)), the microstructure growth direction of this region is consistent, and the growth direction is along the direction with the largest temperature gradient. It can be seen that the microstructure is relatively coarse and some columnar dendrites are formed in it.

Figure 7 shows the microstructure of the cross section parallel to the laser scanning direction. The latter deposition layer zone, remelted zone, and heat-affected zone are also observed in the LMD part. It can be seen that the microstructure in this direction is mainly composed of columnar dendrites. The growth direction of the columnar dendrites is not uniform. This is due to the complicated thermal process of the LMD manufacturing process, which causes the temperature gradient direction of the microstructure to change greatly during the growth, thus causing the growth direction of the columnar crystal to be inconsistent when the part is finally completed. Since the initial cooling rate is low, heterogeneous nucleation starts on the unmelted crystal grains, and relatively coarse columnar crystals are formed, and then, the cooling rate is increased, and the columnar crystals start to

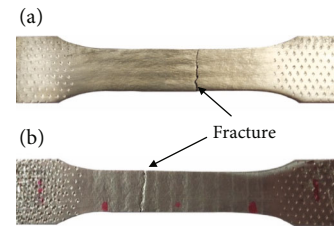


FIGURE 8: Photos of the specimens after tensile tests: (a) perpendicular to laser scanning direction; (b) parallel to laser scanning direction.

grow in a direction in which the temperature gradient is large on the basis of the coarse columnar crystal. As can be seen in Figure 7(b), the direction of microstructure growth in the remelted portion is chaotic, and some columnar crystals grow across the heat-affected zone and the remelted zone. Figure 7(c) indicates that there are columnar crystals before the remelting process. New grains grow from the unmelted short columnar crystals. Figure 7(d) shows that the heat-affected zone is mainly coarse columnar dendrites and the growth direction of the dendrites is basically the same.

3.2. Tensile Properties. Figure 8 shows the photographs of the samples after tensile test. Figure 8(a) is a specimen

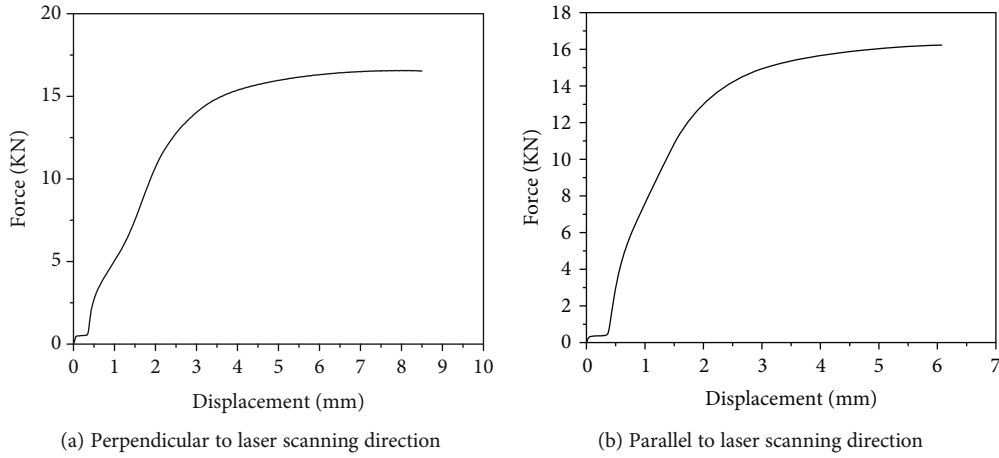


FIGURE 9: Force-displacement curve of the tensile test specimens: (a) perpendicular to laser scanning direction; (b) parallel to laser scanning direction.

TABLE 3: Tensile test results of the 316L LMD part.

Direction	UTS (MPa)	Average value (MPa)	EL	Average value
Perpendicular to laser scanning direction	804	804.3	9%	10.3%
	800		10%	
	809		12%	
Parallel to laser scanning direction	791	791.7	7%	7.3%
	799		8%	
	785		7%	

perpendicular to the laser scanning direction, and Figure 8(b) is a specimen parallel to the laser scanning direction. Figure 8 shows that no “necking” phenomenon happened at the fracture position during the tensile test process. Because the local strains in the neck are large, necking is often closely associated with yielding, a form of plastic deformation associated with ductile materials. The neck eventually becomes a fracture when enough strain is applied. It indicates that the ductility of the 316L LMD part fabricated in this study is not fine. Figure 9 is the force-displacement curve of the tensile specimen obtained in two directions, and it can also be seen from Figure 9 that there was no yielding that happened, and the specimens fractured directly in the tensile test process. Table 3 shows the tensile properties of the two kinds of specimens. Table 3 indicates that the tensile strengths in the two directions are basically the same, about 800 MPa. However, the elongation of the specimen perpendicular to the laser scanning direction is 3.0% larger than that of the specimen parallel to the laser scanning direction. According to the OM results of the LMD part (Figures 6 and 7), a large number of coarse dendrites are found to distribute along the direction parallel to the laser scanning direction, which may decline the mechanical properties of the part. As a result, the elongation of the specimens parallel to the laser scanning direction was only 7.3%. In contrast, the specimen perpendicular to the laser scanning direction displayed higher elongation.

Figure 10 shows the SEM photos of the tensile fracture surface for specimen perpendicular to the laser scanning direction. It can be seen from the macroscopic morphology that the fracture surface of the two regions A and B is different. There is a herringbone pattern in region A. Further enlarged photos of regions A and B are shown in Figures 10(b)–10(e). It can be seen that the cleavage plane can be clearly seen in region A. The fracture mode is the cleavage fracture. The fracture mode is a quasicleavage fracture in region B. Because of the presence of fine microstructures in region B, the quasicleavage facet is not a crystallographic cleavage plane, which is quite different from region A.

Figure 11 shows the SEM photos of the tensile fracture surface for the specimen parallel to the laser scanning direction. It is very different comparing with the fracture morphology of specimens perpendicular to the laser scanning direction in Figure 10. The fracture mode of the tensile specimen is the cleavage fracture. The cleavage facets can easily be seen in Figures 11(b)–11(e), magnified view of regions C and D in Figure 10(a). This is also due to the formation of coarse dendrites in this direction. And the results agree well with the differences of elongation ratio for specimens at two directions.

3.3. Residual Stress Distribution. Figure 12 shows the distribution of longitudinal residual stress after reconstruction, and it can be seen that along the thickness direction, the

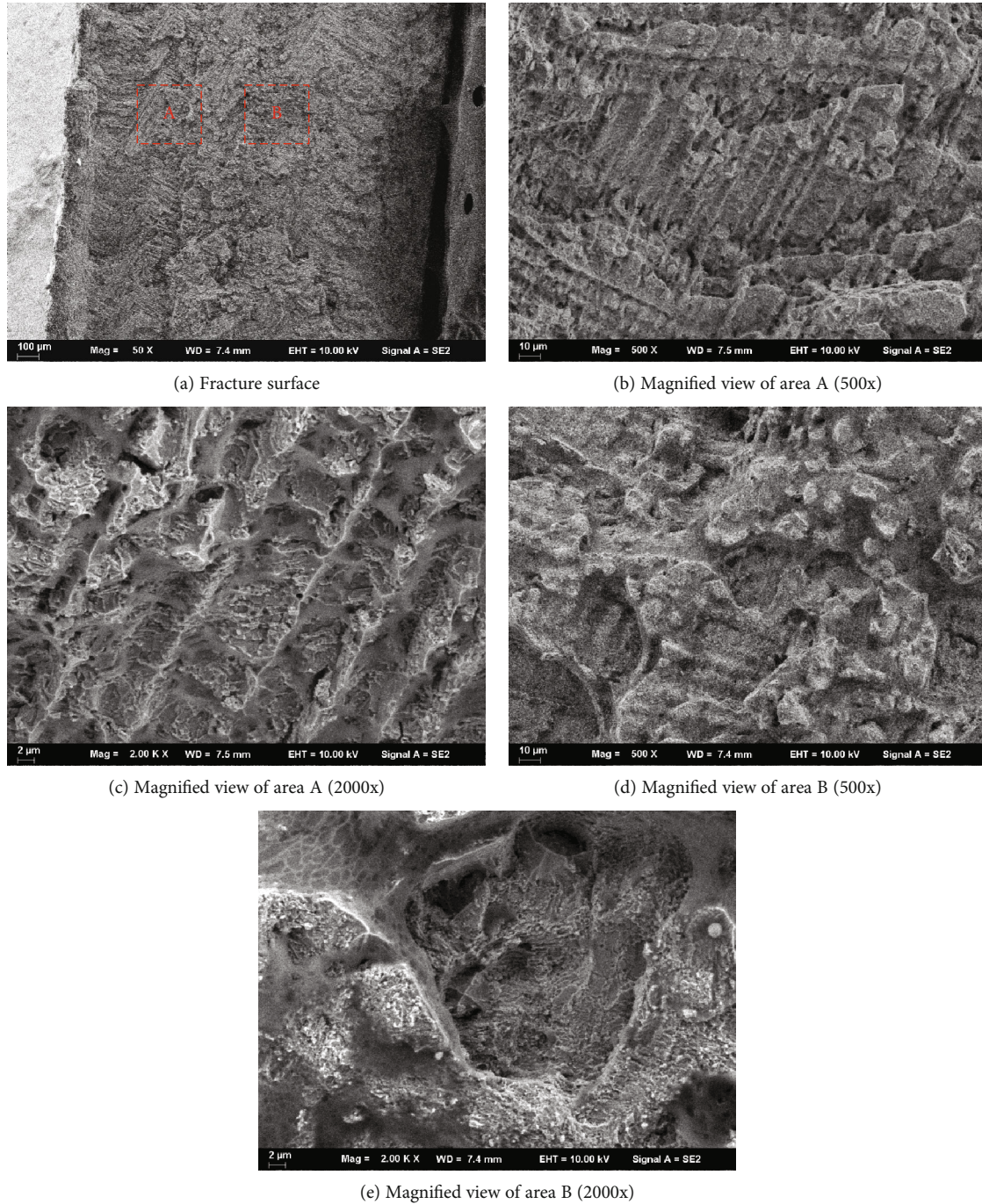


FIGURE 10: SEM photos of the fracture surface.

top region is tensile stress and the middle region is compressive stress. The compressive stress near the interface can reach up to -375 MPa, and the tensile stress in the top region is the largest, and the maximum is 320 MPa. Because additive manufacturing will be accompanied by remelting and the cooling rate of this area is slow, the contraction of this area is stretched by the previous layer of metal, so tensile stress of cracks will appear. Through the progress of the additive manufacturing process, tensile stress will be concentrated in the center zone. With the progress of additive manufacturing, the longitudinal residual stress gradually increases with

the increase of the number of layers, but because the heat effect of the latter layer on the previous layer is equivalent to the heat treatment of the previous layer, the stress increases slowed down.

Figure 13 shows the residual stress line distribution along five typical paths (L1 to L5 in Figure 12). It can be seen from Figure 13(a) that the variation of the three paths (L1, L2, and L3) is almost the same, from the top to the interface; the tensile stress is gradually changed to the compressive stress; and the maximum tensile stress reaches 315 MPa. In the laser metal deposition area, the paths L1 and L3 on both sides of

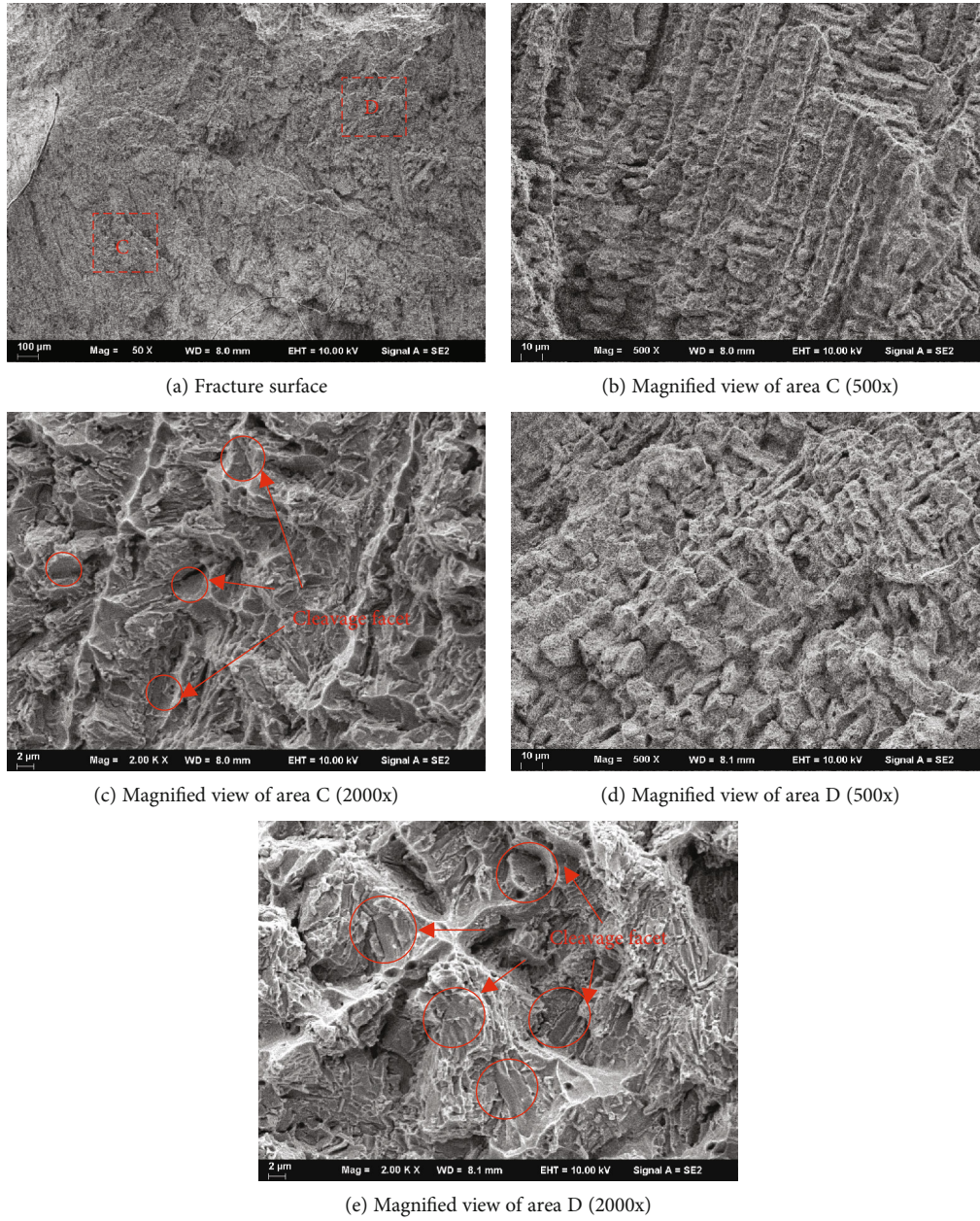


FIGURE 11: SEM photos of the fracture surfaces in parallel to the laser scanning direction.

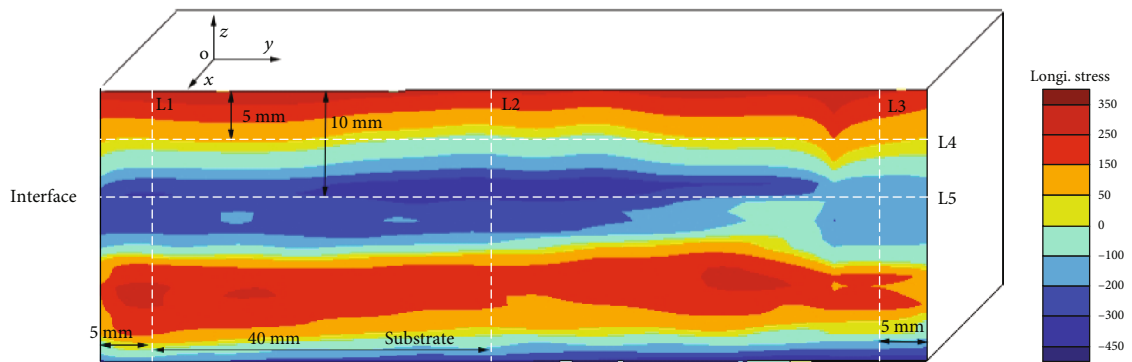


FIGURE 12: Longitudinal residual stress distribution in the LMD part (MPa).

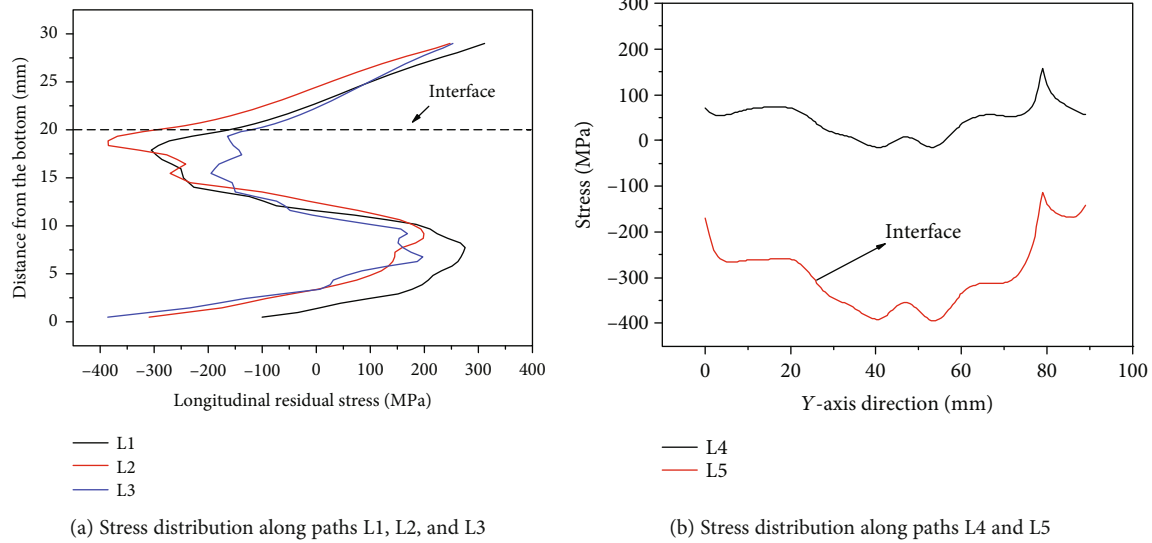


FIGURE 13: Stress distribution along the five typical paths in Figure 12.

the part are more similar, and the areas on both sides are first changed from compressive stress to tensile stress. This is because the areas on both sides of the part can be freely deformed parallel to the scanning direction during the LMD process. In the process of LMD, as the deformation of the part releases the stress, the stress in the two sides changes from compressive stress to tensile stress, and the intermediate zone is restrained by the constraints of the block parts on both sides. The process of changing to tensile stress slows down. Figure 13(b) indicates that the variation of the stress distribution along the paths L4 and L5 (interface) is completely opposite. The small sudden change on the right side of L4 and L5 are due to the oscillation of copper wire during the low-speed wire cut process, making the profile inaccurate, and the actual stress does not mutate. At the same position on the Y-axis, when the compressive stress on the path L5 is the largest, the tensile stress on the path L4 is the smallest. Along the path L4, the tensile stress on both sides is the largest, about 100 MPa, and gradually decreases toward the middle, and it is compressive stress in the middle portion. The compressive stress on both sides of the path L5 is the smallest, about -180 MPa, and the compressive stress in the middle region is the largest, which can reach -375 MPa.

4. Conclusions

The microstructure results show that the LMD 316L parts are mainly composed of columnar crystals and equiaxed crystals. The microstructure distributions perpendicular and parallel to the laser scanning direction are different, resulting in differences of tensile properties in the two directions. The sample elongation of the specimens perpendicular to the laser scanning direction is 3% higher than that in the parallel direction, and the tensile strengths in the two directions are almost the same. The contour stress measurement results show that the tensile stress is observed at the upper side and then changes gradually to compressive stress at the bot-

tom in the LMD part. The maximum tensile stress and compressive stress are 320 MPa and -375 MPa, respectively.

Data Availability

The data used to support the findings of this study are available from the corresponding author upon request.

Conflicts of Interest

The authors declare that they have no conflicts of interest.

Acknowledgments

The authors would like to acknowledge the financial support provided by the National Key Research and Development Program of China (grant number 2018YFC0310400), the National Natural Science Foundation of China (grant number 51911530211), the Natural Science Foundation of Jiangsu Province (grant number BK20191458), and Royal Society International Exchanges 2018 Cost Share (China) Scheme (grant number IEC\NSFC\181278). The authors also thank the assistance from Dr. Chuan Liu for the measurement of residual stress of the LMD part.

References

- [1] E. Kroll and D. Artzi, "Enhancing aerospace engineering students' learning with 3D printing wind-tunnel models," *Rapid Prototyping Journal*, vol. 17, no. 5, pp. 393–402, 2011.
- [2] Y. Qiao, Z. Tian, X. Cai et al., "Cavitation erosion behaviors of a nickel-free high-nitrogen stainless steel," *Tribology Letters*, vol. 67, no. 1, 2019.
- [3] K. Wang, C. Wu, Z. Qian, C. Zhang, B. Wang, and M. A. Vannan, "Dual-material 3D printed metamaterials with tunable mechanical properties for patient-specific tissue-mimicking phantoms," *Additive Manufacturing*, vol. 12, pp. 31–37, 2016.
- [4] Y. Feng, B. Zhan, J. He, and K. Wang, "The double-wire feed and plasma arc additive manufacturing process for deposition

- in Cr-Ni stainless steel,” *Journal of Materials Processing Technology*, vol. 259, pp. 206–215, 2018.
- [5] B. Furet, P. Poullain, and S. Garnier, “3D printing for construction based on a complex wall of polymer-foam and concrete,” *Additive Manufacturing*, vol. 28, pp. 58–64, 2019.
 - [6] T. Abe, D. Mori, K. Sonoya, M. Nakamura, and H. Sasahara, “Control of the chemical composition distribution in deposited metal by wire and arc-based additive manufacturing,” *Precision Engineering*, vol. 55, pp. 231–239, 2019.
 - [7] Y. Qiao, J. Chen, H. Zhou et al., “Effect of solution treatment on cavitation erosion behavior of high-nitrogen austenitic stainless steel,” *Wear*, vol. 424–425, pp. 70–77, 2019.
 - [8] W. Wu, J. Xue, L. Wang, Z. Zhang, Y. Hu, and C. Dong, “Forming process, microstructure, and mechanical properties of thin-walled 316L stainless steel using speed-cold-welding additive manufacturing,” *Metals*, vol. 9, no. 1, p. 109, 2019.
 - [9] J. Cheng, Y. Feng, C. Yan, X. Hu, R. Li, and X. Liang, “Development and characterization of Al-based amorphous coating,” *JOM*, vol. 72, no. 2, pp. 745–753, 2020.
 - [10] K. Zhang, S. Wang, W. Liu, and X. Shang, “Characterization of stainless steel parts by Laser Metal Deposition Shaping,” *Materials & Design*, vol. 55, pp. 104–119, 2014.
 - [11] D. V. Bedenko, O. B. Kovalev, I. Smurov, and A. V. Zaitsev, “Numerical simulation of transport phenomena, formation the bead and thermal behavior in application to industrial DMD technology,” *International Journal of Heat and Mass Transfer*, vol. 95, pp. 902–912, 2016.
 - [12] M. Ma, Z. Wang, D. Wang, and X. Zeng, “Control of shape and performance for direct laser fabrication of precision large-scale metal parts with 316L stainless steel,” *Optics & Laser Technology*, vol. 45, pp. 209–216, 2013.
 - [13] S. Xiang, J. Li, H. Luan et al., “Effects of process parameters on microstructures and tensile properties of laser melting deposited CrMnFeCoNi high entropy alloys,” *Materials Science and Engineering: A*, vol. 743, pp. 412–417, 2019.
 - [14] Z. Wang, T. A. Palmer, and A. M. Beese, “Effect of processing parameters on microstructure and tensile properties of austenitic stainless steel 304L made by directed energy deposition additive manufacturing,” *Acta Materialia*, vol. 110, pp. 226–235, 2016.
 - [15] R. J. Moat, A. J. Pinkerton, L. Li, P. J. Withers, and M. Preuss, “Residual stresses in laser direct metal deposited Waspaloy,” *Materials Science & Engineering A*, vol. 528, no. 6, pp. 2288–2298, 2011.
 - [16] P. Rangaswamy, M. L. Griffith, M. B. Prime et al., “Residual stresses in LENS® components using neutron diffraction and contour method,” *Materials Science and Engineering*, vol. 399, no. 1–2, pp. 72–83, 2005.
 - [17] T. Mukherjee, W. Zhang, and T. DebRoy, “An improved prediction of residual stresses and distortion in additive manufacturing,” *Computational Materials Science*, vol. 126, pp. 360–372, 2017.
 - [18] L. Zhuo, Z. Wang, H. Zhang et al., “Effect of post-process heat treatment on microstructure and properties of selective laser melted AlSi10Mg alloy,” *Materials Letters*, vol. 234, pp. 196–200, 2019.
 - [19] J. L. Bartlett, B. P. Croom, J. Burdick, D. Henkel, and X. Li, “Revealing mechanisms of residual stress development in additive manufacturing via digital image correlation,” *Additive Manufacturing*, vol. 22, pp. 1–12, 2018.
 - [20] B. A. Szost, S. Terzi, F. Martina et al., “A comparative study of additive manufacturing techniques: residual stress and microstructural analysis of CLAD and WAAM printed Ti–6Al–4V components,” *Materials & Design*, vol. 89, pp. 559–567, 2016.
 - [21] M. B. Prime, “Cross-Sectional Mapping of Residual Stresses by Measuring the Surface Contour After a Cut,” *Journal of Engineering Materials and Technology*, vol. 123, no. 2, pp. 162–168, 2001.
 - [22] C. Liu and X. Yi, “Residual stress measurement on AA6061-T6 aluminum alloy friction stir butt welds using contour method,” *Materials & Design*, vol. 46, pp. 366–371, 2013.
 - [23] M. Prime, T. Gnaupelherold, J. Baumann, R. Lederich, D. Bowden, and R. Sebring, “Residual stress measurements in a thick, dissimilar aluminum alloy friction stir weld,” *Acta Materialia*, vol. 54, no. 15, pp. 4013–4021, 2006.